Université de Lille

SCIENCES AND TECHNOLOGIES

DOCTORAL SCHOOL SPI 072

PHD THESIS

to obtain the title of

Doctor of Electronics, Microelectronics, Nanoelectronics and Microwaves

of the University of Lille

Defended by

Tomáš HORÁK

Terahertz Nonreciprocal Effects Using Hexagonal Ferrites

Thesis supervisor: Jean-François LAMPIN

prepared at IEMN, THz PHOTONICS Group

defended on December 12, 2017

Jury :

Reviewers :	Jiří ČTYROKÝ	-	Czech Academy of Sciences-IPE
	Niels KELLER	-	CNRS-GEMaC (Université de Versailles Saint-Quentin)
Supervisor :	Jean-François LAMPIN	-	CNRS-IEMN (Université de Lille)
Co-Supervisor :	Mathias VANWOLLEGHEM	-	CNRS-IEMN (Université de Lille)
President :	Jean-Louis COUTAZ	-	IMEP-LAHC (Université Grenoble Alpes)
Examinators :	Béatrice DAGENS	-	CNRS-C2N (Université Paris-Sud)
	Aloyse DEGIRON	-	CNRS-C2N (Université Paris-Sud)
	Emilie GAMET	-	CNRS-Laboratoire Hubert Curien (Université de Saint-Etienne)

I declare I elaborated this thesis by myself. All literary sources and publications I have used are listed.

Dedicated to my parents

Věnováno mým rodičům.

Děkuji Vám, maminko a tatínku, za obrovskou podporu po celou dobu mého vzdělávání, od základního až po doktorské.

Acknowledgments

It would not have been possible to complete this dissertation thesis without inspirations and continual support of a number of wonderful, intelligent and kind people to whom I would like to express my deepest thanks in the following paragraphs.

First of all, I want to acknowledge the University of Lille which provided me an amazing opportunity to benefit from the scholarship of the university and therefore to have fully financially covered doctoral study in France. I have really enjoyed the time spent in this beautiful country and gained here a lot of scientific knowledge and new life experiences and friends.

My deepest gratitude belongs especially to Dr. Jean-François Lampin and Dr. Mathias Vanwolleghem under whose supervision and leadership I had been working on my dissertation. Dr. Mathias Vanwolleghem was the first person from the IEMN with who I was in contact in 2014. He was looking for a new PhD student for his in that time starting research project ANR TENOR. I want to thank him for choosing me and also helping me with all administration process, paperwork and all necessities after my first arrival to France. During my study and work he introduced me into this beautiful and interesting research area, has given me a lot of experience and I really appreciate his enthusiasm, encouragement and support for solving of scientific problems. I also like his continuous optimism, patience and the fact that we could together talk about science as well as about everyday life and our hobbies. Thank you for everything, Mathias. I express also my warmest gratitude to Dr. Jean-François Lampin who is the leader of the THz Photonics Group in the IEMN. His guidance and enormous knowledge and experience in the THz domain have been a valuable input for my work and this thesis.

My deep thank belongs also to all members of the THz Photonics Group in the IEMN for their friendship, support and creating a pleasant and cooperating working environment. Especially I thank Dr. Guillaume Ducournau for great

help during quasi-optical characterization measurements and Fuanki Bavedila, Dr. Benjamin Walter and Dr. Estelle Mairiaux for well done samples fabrication. I've spent more than 3 years in an one office with my colleague and friend Yann Desmet and I thank him for very nice and friendly atmosphere, frequent scientific and human help and necessary distractions from our research problems. I wish you, Yann, a successful ending of your PhD study and all the best for your future career and life.

I thank Dr. Kamil Postava and his research colleagues at VŠB - Technical University of Ostrava for helpful scientific cooperation during all my study.

My deep gratitude belongs also to my parents for their permanent support and encouragement throughout all my study.

Finally I acknowledge the partial support from projects ANR-14-CE26-0006 TENOR (Agence National de la Recherche) and SP2017/154 (Ministry of Education, Youth and Sports of Czech Republic) and City of Ostrava for the scholarship between years 2014–2017.

Terahertz Nonreciprocal Effects Using Hexagonal Ferrites

Abstract: A key element to protect coherent sources and achieve desired power stability and spectral purity for certain applications is an isolator, which in THz range has still no effective solution. In this thesis, a novel design of THz isolating device based on a one-way reflecting surface is proposed. It combines gyrotropy with surface plasmon (SP) resonance phenomena. A first crucial requirement to realize this is a sufficiently strong THz gyrotropic material. In the last decades new fabrication and material processing methods have enabled to create a new type of ferrite material with a hexagonal magnetoplumbite structure (e.g. $SrFe_{12}O_{19}$). Gyrotropy in this material is a result of gyromagnetic effects occurring when magnetic dipole moments precess nonreciprocally (NR) at Larmor frequency around an internal magnetic field. As a result the permeability acquires a tensorial form and its unequal off-diagonal elements are responsible for NR behavior. The internal field in hexaferrites is particularly strong (up to 20 kOe), resulting in a Larmor frequency close to the mm-wave range. A first important step for the development of the device is complete material characterization of the used hexaferrites. In a first instance the diagonal permittivity and permeability elements have been characterized using time-windowed Vector Network Analyzer (VNA) characterization. Their strong gyrotropic and anisotropic properties in a wide band (0.1-1 THz) are then investigated by an original magneto-optical THz Time-domain spectrometry. The obtained strong gyrotropic spectra of hexaferrites prove their unique potential for THz isolator applications, as will be shown by an original Faraday isolation measurement using a VNA, and consequently by first designs of a NR magnetoplasmonic mirror using the fitted material parameters. This design combines strong gyromagnetic properties of hexaferrites in THz range with SPs resonances formed due to the presence of a metallic grating at the hexaferrite surface. The possibility of SPs excitation at THz frequencies is demonstrated both numerically and experimentally with a strong agreement. Close to these SPs resonances there can appear frequency ranges where the device acts as a one-way mirror.

Keywords: Nonreciprocity, Isolator, Terahertz, Ferrites, Hexaferrites, Gyromagnetism, Plasmonics, Surface plasmons, Magneto-optics, Magneto-plasmonics, Periodic structures, Kerr effect, Extraordinary optical transmission, Time-domain terahertz spectroscopy, Vector network analyzer

Résumé: Aujourd'hui il n'existe pas de solution efficace pour réaliser un isolateur aux fréquences térahertz (THz). Cette fonctionnalité est néanmoins indispensable pour la protection de toute source cohérente et afin de garantir sa stabilité en puissance et sa pureté spectrale. L'objectif de cette thèse de doctorat est d'étudier un nouveau concept d'isolateur THz basé sur une surface réfléchissante unidirectionnelle. Ce comportement est réalisé par une combinaison originale d'une résonance de surface, dite plasmon de surface ("surface-plasmon", SP), avec un phénomène de gyrotropie. Une première brique de base essentielle est de disposer d'un matériau démontrant une gyrotropie suffisamment forte aux fréquences THz. Au cours des dernières décennies, des techniques de fabrication et de traitement améliorées des matériaux ont permis d'élaborer un nouveau type de ferrite de type magnétoplumbite hexagonale (par exemple $SrFe_{12}O_{19}$). La gyrotropie de ce matériau est le résultat d'effets gyromagnétiques se manifestant lorsque les moments magnétiques dipolaires précessent de manière non-réciproque (NR) à la fréquence dite de Larmor autour d'un champ magnétique interne. En conséquence sa perméabilité acquiert une forme tensorielle caractérisée par des contributions hors-diagonales antisymétriques qui induisent une réponse NR. Le champ magnétique interne dans les hexaferrites est particulièrement élevé (jusqu'à 20 kOe) ce qui induit une fréquence de Larmor proche de la gamme des ondes millimétriques. Ainsi, une caractérisation précise des hexaferrites utilisées est un premier pas crucial dans le développement du composant. Dans un premier temps les éléments diagonaux de la permittivité et de la perméabilité ont été déterminés en combinant des mesures dans le domaine fréquentiel (obtenues par analyseur de réseau vectoriel) avec un traitement numérique dans le domaine temporel (”time-gating”). Ensuite, la gyrotropie et l'anisotropie de ces hexaferrites sont étudiées par spectroscopie dans le domaine temporel dans une large bande allant jusqu'à la gamme submillimétrique (0.1-1 THz). Les spectres de gyrotropie obtenus confirment les fortes valeurs attendues et démontrent le potentiel de cette famille de ferrites pour des applications

d'isolation aux fréquences THz. Des mesures par analyseur de réseau vectoriel ont ensuite permis de démontrer un isolateur THz à base de rotateur de Faraday. Finalement, en adaptant ces paramètres mesurés à des modèles de dispersion de type Larmor, des premières conceptions de miroirs magnéto-plasmoniques non-réciproques ont été effectuées. Elles reposent sur la combinaison du gyromagnétisme THz des substrats hexaferrites avec des résonances SP aux fréquences THz qui apparaissent dans la réponse électromagnétique lorsque le métal est structuré avec des dimensions sub-longueur d'onde. L'excitation de ces résonances a été démontrée de manière expérimentale et un bon accord avec les simulations numériques a été obtenu. A proximité des résonances SP des simulations, des bandes de fréquences pour lesquelles le réseau magnéto-plasmonique se comporte comme un miroir unidirectionnel ont été mises en évidence.

Mots-clés: Non-réciprocité, Isolateur, Térahertz, Ferrites, Hexaferrites, Gyromagnétisme, Plasmonique, Plasmons de surface, Magnéto-optique, Magnéto-plasmonique, Structures périodiques, Effet magnéto-optique de Kerr, Transmission optique extraordinaire, Spectroscopie dans le domaine temporel, Analyseur de réseau vectoriel

---

Contents

CHAPTER 1

Introduction

Contents

This dissertation thesis named *Terahertz nonreciprocal effects using hexagonal ferrites* is focused on research and development of nonreciprocal devices, particularly isolators, for terahertz (THz) frequency range, study of suitable material candidates and their quasi-optical and magneto optical characterization.

1.1 Nonreciprocal Effects

At the beginning it is necessary to introduce a reader generally into the matters of nonreciprocal effects. The basic principle of reciprocity includes the fact, that the amplitude of an electromagnetic (EM) wave scattered from an object does not change when the source and the detector are mutually exchanged, as presented by Deák and Fülöp [1]. This scattering experiment, as shown in Fig. 1.1, is indeed a convenient description of many existing physical processes. It also allows to interchange the incoming wave and corresponding outgoing one without any

observable resulting amplitude change. Such a scattering system can be therefore considered as symmetrical [2]. However, the cases of the time-reversal symmetry or the invariance under rotation, exchanging the positions of the source and the detector, are just special ones as the fundamental reciprocity feature is rather complex. First indication of the reciprocity theorem was given already by Stokes [3] in 1849. For EM waves the theory was well described and extended in 1866 by Helmholtz [4] and later in 1905 by Lorentz [5]. A recent high quality review of reciprocity with particular focus on optics was presented in 2004 by Potton [6] showing that predictions based on reciprocity can be made even under less restrictive conditions than those that apply to time-reversibility.

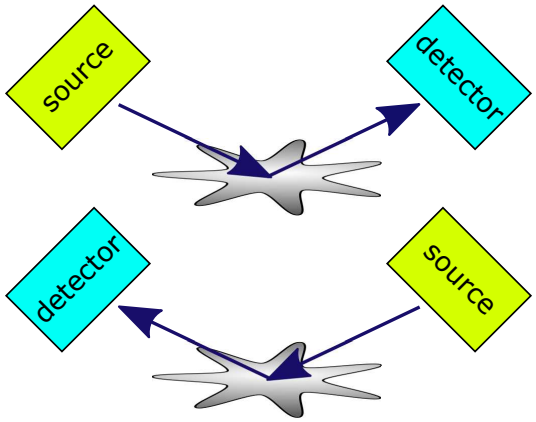

Figure 1.1: Original (top) and reversed (bottom) arrangements of the scattering experiment.

Devices which are considered to be *nonreciprocal* (NR) must therefore operate in a way in which the well-known *Lorentz reciprocity* of Maxwell's equations is broken [7]. The easiest way how to understand the reciprocity is by considering the time-inversion symmetry of Maxwell's equations. It is well known that the source-free Maxwell's curl equations:

$$\nabla \times \mathbf{E} = -\frac{\partial \mathbf{B}}{\partial t}, \qquad \nabla \times \mathbf{H} = \frac{\partial \mathbf{D}}{\partial t}, \tag{1.1}$$

are invariant under the following time-reversal transformation:

$$\begin{cases} \mathbf{E}(t,x,y,z) & \longrightarrow & \mathbf{E}(-t,x,y,z) \\ \mathbf{H}(t,x,y,z) & \longrightarrow & -\mathbf{H}(-t,x,y,z) \end{cases} . \tag{1.2}$$

The time-inversion symmetry therefore says, that out of a forward propagating solution a backward propagating solution with the same properties can be generated by the transformation (1.2). This symmetry is kept unless any external source is present. Several different methods for breaking of the reciprocity theorem have been already presented, for example based on modulation of refractive index [8], where the time-reversal symmetry has been broken dynamically by inducing indirect photonic transitions in an appropriately designed photonic structure; by nonlinear optical processes (NOP), as shown by Dong *et al.* [9], where Brillouin scattering process gives rise to the breaking of the relevant reversal symmetry, leading to nonreciprocal nonlinear optical processes that are switchable by the control laser, or as studied also by other authors [10, 11]; by NOP together with resonators [10]; or with use of angular momentum-biased metamaterials [12], in which a tailored spatiotemporal modulation is azimuthally applied to subwavelength Fano-resonant inclusions, producing largely enhanced NR response; by using coupled photonic systems [13]; by spintronics [14], where a strongly nonreciprocal transmission of a low-loss silica nanophotonic waveguides is controlled by the internal state of spin-polarized atoms; or by direct temporal modulation of waveguiding material properties [15, 16]. In summary, all of the above presented structures or devices therefore use different approaches for infraction of time-inversion symmetry of Maxwell's equations by processes which can be understood as introducing of sources into (1.1), leading thus into breaking the Lorentz reciprocity. However, most of the work was done on study of breaking of the reciprocity via magneto-optical material response, since a presence of a fixed magnetic field breaks as well the time-reversal invariance of Maxwell's equations and hence makes the transformation (1.2) impossible.

1.1.1 Role of Magnetization

Magneto-optical (MO) effects deal with an interaction of electromagnetic radiation with a matter subjected to a magnetic field. The presence of magnetization (**M**) leads to a reduction of system symmetry and an artificial creation of the material anisotropy or its variation. Generally, the principal effect of magnetized medium on an interacting EM wave is a change of its polarization state. In the optical range of EM spectrum a medium can be described by complex electric susceptibility tensor $\bar{\bar{\chi}}_e$, relating to the relative permittivity tensor in Maxwell's equations. This susceptibility tensor characterizes a local response of the medium to a monochromatic EM wave and expresses a relation between the electric field vector $\mathbf{E}(\mathbf{r})$ in the medium and the induced electric dipole moment density $\mathbf{P}(\mathbf{r})$ at the position given by the vector $\mathbf{r}$, in Cartesian coordinates in the form:

$$\begin{pmatrix} P_x \\ P_y \\ P_z \end{pmatrix} = \varepsilon_0 \underbrace{\begin{pmatrix} \chi_{xx} & \chi_{xy} & \chi_{xz} \\ \chi_{yx} & \chi_{yy} & \chi_{yz} \\ \chi_{zx} & \chi_{zy} & \chi_{zz} \end{pmatrix}}_{\bar{\bar{\chi}}_e} \begin{pmatrix} E_x \\ E_y \\ E_z \end{pmatrix}, \tag{1.3}$$

where ε_0 is the permittivity of vacuum. If we now choose the principal axis (the direction of a magnetization vector) in the direction of the z axis, the symmetry group operations, including all proper rotations about the principal axis and the rotations times reflection in a plane normal to this axis, require $\bar{\bar{\chi}}_e$ to be invariant under the operation of the group represented by matrix transformations:

$$\begin{pmatrix} \cos\alpha & \sin\alpha & 0 \\ -\sin\alpha & \cos\alpha & 0 \\ 0 & 0 & \pm 1 \end{pmatrix} \begin{pmatrix} \chi_{xx} & \chi_{xy} & \chi_{xz} \\ \chi_{yx} & \chi_{yy} & \chi_{yz} \\ \chi_{zx} & \chi_{zy} & \chi_{zz} \end{pmatrix} \begin{pmatrix} \cos\alpha & -\sin\alpha & 0 \\ \sin\alpha & \cos\alpha & 0 \\ 0 & 0 & \pm 1 \end{pmatrix}, \tag{1.4}$$

where α represents an arbitrary rotation angle about the magnetization z-axis for the proper $(+1)$ and improper (-1) rotations. The resulting complex electric

susceptibility tensor is in the form:

$$\bar{\bar{\chi}}_e = \begin{pmatrix} \chi_{xx} & \chi_{xy} & 0 \\ -\chi_{xy} & \chi_{xx} & 0 \\ 0 & 0 & \chi_{zz} \end{pmatrix}. \tag{1.5}$$

The same operations are valid also for magnetic susceptibility tensor, for complex permittivity tensor, complex conductivity tensor and complex permeability tensor with similar results. The symmetry operations of reflection in planes containing the principal axis and represented by matrix transformations:

$$\begin{pmatrix} -\cos\beta & \sin\beta & 0 \\ \sin\beta & \cos\beta & 0 \\ 0 & 0 & 1 \end{pmatrix} \begin{pmatrix} \chi_{xx} & \chi_{xy} & 0 \\ -\chi_{xy} & \chi_{xx} & 0 \\ 0 & 0 & \chi_{zz} \end{pmatrix} \begin{pmatrix} -\cos\beta & \sin\beta & 0 \\ \sin\beta & \cos\beta & 0 \\ 0 & 0 & 1 \end{pmatrix}, \tag{1.6}$$

produce the magnetization reversal represented by the following rules for the tensor elements:

$$\chi_{xx}(M_z) = \chi_{xx}(-M_z) \tag{1.7a}$$

$$\chi_{zz}(M_z) = \chi_{zz}(-M_z) \tag{1.7b}$$

$$\chi_{xy}(M_z) = -\chi_{xy}(-M_z) = -\chi_{yx}(M_z). \tag{1.7c}$$

The result of the transformation (1.6) does not depend on the angle specifying the orientation of the reflection planes. From this we can conclude that the diagonal and off-diagonal elements of the complex electric susceptibility tensor of a magnetized medium, which was isotropic before turning on the magnetization, are even and odd functions of the magnetization, respectively. This is a particular case of a generalized Onsager relation [17] giving for an arbitrary $\mathbf{M}$ orientation:

$$\chi_{ij}(\mathbf{M}) = \chi_{ji}(-\mathbf{M}). \tag{1.8}$$

Since an interaction of a polarized EM wave with a magnetized medium is an essence of our work, it was necessary to understand all the above presented properties of the susceptibility tensor. The unequal off-diagonal elements, which arise also in the permeability tensor characterizing ferrite materials, are responsible for NR effects, as will be later demonstrated in Chapters 2 and 3.

An interaction of an EM wave with a magnetized medium can be explained in terms of a particular MO effect. First MO effect was discovered in 1845 by M. Faraday. By measuring an interaction of linearly polarized light passing through a piece of heavy glass placed in strong magnetic field in a way that the propagation direction was parallel to the field direction, he observed a rotation of the polarization plane [18]. The angle of this rotation is proportional to the applied field and the propagation length, and, as will be shown in Chapter 3, is nonreciprocal, since the sense of the rotation depends on the magnetization direction. This effect has been since that time known as the *Faraday effect* or magnetic circular birefringence. In general, all magneto-optical effects can be divided into two main categories according the interaction of radiation with a magnetized medium. MO effects in transmission cover the above described Faraday effect as well as the similar Voigt (or Cotton-Mouton) effect in which the light travels perpendicularly to the field direction ($\mathbf{k} \perp \mathbf{H}$). Voigt effect is proportional to the square of magnetization. When radiation is reflected from a magnetized medium, MO effects in reflection, which are commonly named *Kerr effects* (MOKE) manifest themselves. There are three known Kerr effects: Polar, Longitudinal and Transverse, each of them differs by orientation of magnetization in the medium. The polar Kerr effect (PMOKE) was discovered in 1876 by J. Kerr by observing a rotation of the polarization plane of linearly polarized light upon reflection from the surface of a piece of iron magnetized perpendicularly to its surface [19, 20]. Two years later, Kerr discovered a similar MO phenomenon in the reflection from an in-plane magnetized piece of iron [21], nowadays known as longitudinal Kerr effect (LMOKE). The last one, transverse Kerr effect (TMOKE), in which the sample is magnetized in-plane, perpendicularly to the plane of incidence, was later,

in 1896, experimentally demonstrated by Zeeman [22]. All MO effects are essentially consequences of splitting of system energy levels in the presence of a magnetic field, what is know as *Zeeman effect*, discovered by Zeeman in 1897 [23].

Magneto-optically active materials can be familiarly separated into several groups according to their magnetic ordering. It is possible to distinguish three main groups of magnetic order: ferromagnetic, anti-ferromagnetic, and ferrimagnetic. Fe, Co, Ni, Mn, Cr and many of their alloys are typical members of ferromagnetic materials, which have been studied already for decades [24]. They have a strong net magnetization even without presence of an external magnetic field. This comes from the parallel ordering of magnetic moments due to a strong exchange interaction between atoms. The ferromagnetic materials have strong MO properties, but also exhibit very high absorption losses. Therefore, they are mostly used for Kerr effect measurements and applications. Another well-known group of MO materials are rare earth garnets [25, 26] and spinels [27, 28, 29]. These are ferrimagnetic oxides with a complex cubic structure and two mutually anti-parallel lattice sites of magnetic moments. Their net magnetization is a result of an unequal number of ions and magnitudes of their magnetic moments. Most of the ferrimagnetic materials have strong MO properties and low absorptions in wide spectral range and therefore have found a lot of applications in MO technologies [30, 31, 32, 33, 34, 35]. The third group of MO materials are anti-ferromagnetic compounds including transition metal oxides and fluorides (e.g. FeO, MnF_2, CoF_2 etc.). In these materials, each individual atom has an unbalanced magnetic moment, but all the moments form two sublattices with an anti-parallel arrangement and thus the net magnetization is completely canceled. They can provide strong faraday rotation, but one has to minimize their high natural birefringence using them in the form of polycrystalline films or bulks. Moreover, their characteristic magnetic ordering is controlled by a temperature and is limited below the Neel temperature around 70 K [36, 37].

Most of the above presented materials are MO active at optical and infrared frequencies and are characterized by a gyrotropic form of electric susceptibility

(1.5) (and permittivity) and a scalar form of permeability. These media are therefore called gyroelectric (electrically gyrotropic). Magneto-optically active materials at THz frequencies can be semiconductors e.g. InAs or InSb [38, 39, 40] due to the cyclotron-frequency motion of carriers, graphene [41] due to the presence of defects in the lattice structure or hexagonal ferrite materials where the origin of the permeability tensor is the Larmor-frequency precession motion of magnetic dipole moments, as will be studied in Chapter 3. These ferrites with a tensorial form of permeability and a scalar form of permittivity, are typically called gyromagnetic (magnetically gyrotropic).

1.1.2 Nonreciprocal Devices

Using the above described effects and materials breaking the Lorentz reciprocity can lead to fabrication of a nonreciprocal device, from which the most known and important are: an optical isolator and a circulator. An isolator, shown in Fig. 1.2a, is a device which allows radiation to pass in one direction, preferably with low insertion losses and blocks it in the opposite one. A circulator, shown in Fig. 1.2b, is basically a three-port isolator which reroutes a backward radiation and can serve for "duplexing" two signals into one channel (e.g. transmit and receive into an antenna). Energy can be made to flow from the transmitter (port 1) to the antenna (port 2) during transmit, and from the antenna (port 2) to the receiver (port 3) during receive. These devices when incorporated into an optical system can greatly increase power stability and spectral purity and assure protection of other coherent components in optical communication systems. If we consider the simplest case of an isolator, including two single-mode waveguide ports, from the definition of the isolator arises that there must exist a pair of modes (I, II) for which the transmission from mode I in port 1 to mode II in port 2 is non-zero and the transmission from mode II in port 2 to mode I in port 1 is close to zero. This existence of at least one pair of modes with the asymmetrical transmission properties must be kept also for a general isolator having a port with multiple

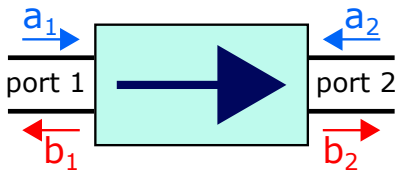

(a) An isolator

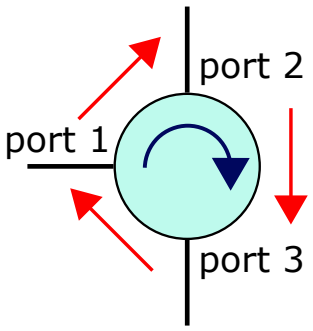

(b) A circulator

Figure 1.2: The simplest isolator (a) and circulator (b) with two and three single-mode waveguide ports, respectively.

modes. Therefore, it is possible to express a corresponding scattering matrix **S**, characterizing the transmission properties of the isolator, which for the two-port case of isolation must be in the asymmetrical form [7]:

$$\begin{pmatrix} b_1 \\ b_2 \end{pmatrix} = \underbrace{\begin{bmatrix} 0 & 0 \\ 1 & 0 \end{bmatrix}}_{\mathbf{S}-\text{matrix}} \begin{pmatrix} a_1 \\ a_2 \end{pmatrix}, \tag{1.9}$$

where a_1, a_2 are the complex amplitudes of the waves traveling into the isolator and b_1, b_2 are the amplitudes of the waves propagating in the reverse direction. The **S** matrix of a perfect circulator, as shown in Fig. 1.2b, is then in the form:

$$\mathbf{S} = \begin{pmatrix} 0 & 0 & 1 \\ 1 & 0 & 0 \\ 0 & 1 & 0 \end{pmatrix}. \tag{1.10}$$

It denotes that an isolator and a circulator must have the scattering matrices in asymmetric forms, where:

$$\mathbf{S} \neq \mathbf{S}^{\mathrm{T}}, \tag{1.11}$$

and hence, they can be built only from devices which break the Lorentz reciprocity. One of the most widely known isolator is based on the nonreciprocal MO

Faraday effect [42, 43, 44], as will be in detail explained in Chapter 2. Faraday isolation measurement with magnetized hexagonal ferrites are then presented at the end of Chapter 3.

1.2 State of the Art in THz Nonreciprocal Devices

Terahertz (THz) band is commonly defined as a part of spectrum with frequencies between 0.1–10 THz. A continuously rising research interest within this range allowed in the last decades a development of high-performance sources and detectors [45] and new active devices for polarization control [46], filters [47] or modulators [48], and therefore opened doors for high number of useful applications such as improved wireless communication [49], security and process imaging [50], quality monitoring or various spectroscopic and microscopy techniques [51, 52]. Besides these domains there is yet insufficient progress in a development of competitive THz nonreciprocal components. Despite the useful properties of isolators and circulators, still no effective solution for nonreciprocity in THz range has been developed and thus performance of THz systems is persistently limited by noise and instabilities (or even destruction of active devices) originating from scattering and reflection echoes.

As it was already mentioned, the key requirement for obtaining an isolation is a breaking of Lorentz reciprocity of Maxwell's equations, which is often realized using of gyrotropic materials. It is exactly the lack of low-loss materials with sufficiently strong gyrotropic properties which has inhibited the development of THz nonreciprocal devices (NRD). Some of good isolating properties of microstructured devices based on semiconductor magneto-plasmonics were presented by Fan *et al.* [53], Hu *et al.* [54], and Chen *et al.* [55], all basically showing how MO effects can be significantly enhanced via plasmonic resonance phenomena and thus also how MO effects will lead to the splitting of the plasmonic resonance giving thereupon strong nonreciprocal transmission. The latter considers a periodically patterned InSb semiconductor layer coated on the silica substrate layer,

as shown in Fig. 1.3. Because the off-diagonal elements of the InSb permittivity

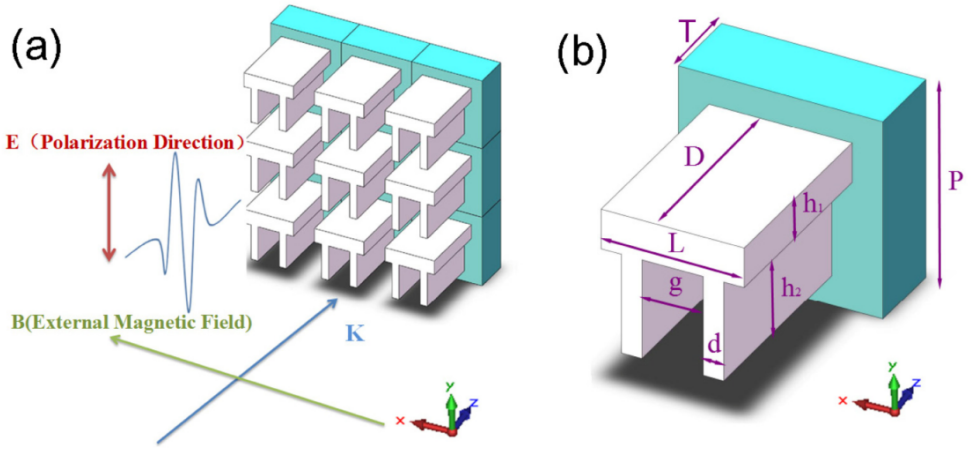

Figure 1.3: Schematic structure of the proposed isolator as presented by Chen *et al.* [55]. (a) The 3D view of the device including the directions of the wave polarization and external magnetic field and the coordinate system in this work; (b) The geometry of the unit cell structure, $D = 10\,\mu m$, $T = 40\,\mu m$, $L = 70\,\mu m$, $P = 100\,\mu m$, $h_1 = 100\,\mu m$, $h_2 = 21\,\mu m$, $d = 10\,\mu m$, and $g = 30\,\mu m$.

tensor, which are responsible for NR behavior, strongly depend on the applied magnetic field and temperature, numerical simulations show that a strong gyrotropic behavior of InSb in the THz range can be induced by external magnetic field of $0 - 0.5\,T$ in the temperature range $160 - 205\,K$. The magnetic field applied in the perpendicular direction to the propagation of linearly polarized EM wave causes in an ordinary bulk medium MO Cotton-Moutton effect (discussed in detail in Section 2). The asymmetry of the metasurface structure along the incident polarization leads to the magnetoplasmon mode splitting and to the nonreciprocal resonance enhancement, because the effective refractive indexes of the left and right rotating magnetoplasmon modes become different, and hence the resonance frequencies of the forward and backward waves move to a higher and lower frequency respectively. The resonance frequency and intensity are mainly determined by the width of InSb stick orthogonal to the polarization direction of incident waves when material parameters are fixed. Numerical simulations

show a maximum isolation of 43 dB under an external magnetic field of 0.3 T, as displayed in Fig. 1.4. Besides the fabrication difficulties of all the above men-

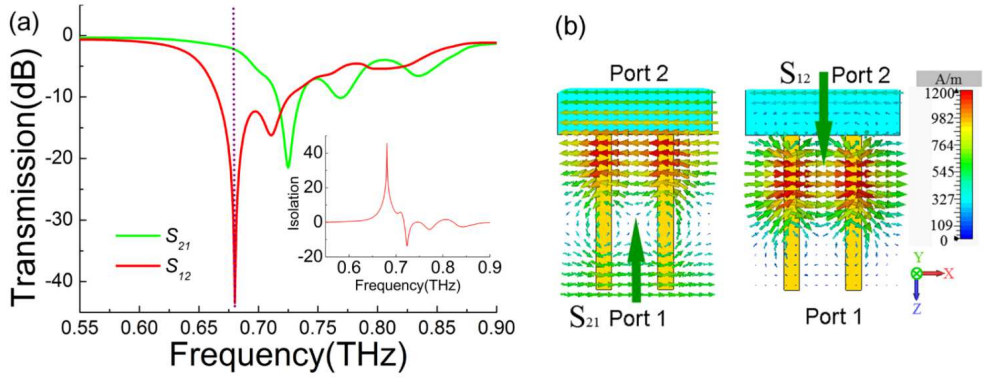

Figure 1.4: (a) The transmission spectrum of the forward waves $|S_{21}|^2$ and backward waves $|S_{12}|^2$, when $T = 195\,\mathrm{K}$, $B = 0.3\,\mathrm{T}$, the inset picture is the isolation spectra of the isolator. (b) Steady magnetic field of the isolator at 0.68 THz when $T = 195\,\mathrm{K}$, $B = 0.3\,\mathrm{T}$ in the $x - z$ cut plane. [55]

tioned micro-structured devices, the strongest isolating mode is obtained either at low temperatures or with high external magnetic field or with a combination of these, what makes them useless at normal conditions. Nevertheless, it proves that small-gap, high mobility semiconductors can achieve plasma frequencies and cyclotron frequencies close to THz range by controlling the applied magnetic field as well as the temperature and their carrier density [56].

Another member of gyroelectric materials which has attracted a lot of research attention in the recent years is graphene. This material has been studied intensively for its promising nonreciprocal properties, e. g. Faraday rotation in single and multilayer graphene [57] or just recently presented isolation obtained by a NR reflecting device [58]. Here, the device operation is based on reflecting incident left hand circularly polarized (LHCP) plane waves as right hand circularly polarized (RHCP) ones, while absorbing RHCP incident waves. It exploits Fabry-Perot resonances in the silicon substrate layer to increase light-matter interaction in graphene. As a result, three monolayers of graphene are sufficient to obtain

near perfect isolation. The principle of the isolator consists in creating for clockwise rotating waves a total surface impedance equal to the impedance Z of free space, causing total absorption. On the contrary, for counter-clockwise ones the impedance is mismatched, and waves are reflected. This effect is based on different conductivity for both circular polarizations, when graphene is magnetized. It is again exactly the necessity of high applied magnetic field (up to 7 T) what hinders a development of real graphene-based NR devices.

One of other approaches how to overcome the technological gap in this frequency range is an extension of techniques used in microwave band to higher frequencies. These are based on gyromagnetism caused by a precession motion of magnetic dipole moments. A number of authors [59, 60, 61, 62, 63, 64] have reviewed and published various applications of ferrite materials in microwave nonreciprocal devices. These materials can serve as strong absorbers or electromagnetic shielding materials close to their natural magnetic resonance or above and below this range as low-loss NRD due to their intrinsic magnetism. First real applications of ferrites in microwave and millimeter-wave range were studied by Snoek *et al.* [65, 66]. They usually exist in highly symmetric cubic structures including spinels and garnets with low values of magnetic anisotropy fields. The Larmor frequency of the precession motion can be expressed in the form $\omega_0 = \mu_0 \gamma H_0$, where $\gamma = 2\pi \times 28\,\mathrm{rad\,GHz\,T^{-1}}$, where H_0 is the ferrite internal magnetic field $H_0 = H_A + H_{ext} + H_d$. This includes the internal anisotropy field H_A keeping the magnetization along certain crystallographic directions, the external applied field H_{ext} and the demagnetization field H_d expressing an anisotropy caused by a material shape. Because the value of the ferromagnetic resonance (FMR) strongly depends on the internal magnetic anisotropy, the gyrotropic properties of these magnetic oxides until recent decades had not reached higher frequencies then 100 GHz. This makes them unusable in THz range without application of high external magnetic field [67, 68].

Nevertheless, recent advances in magnetic materials processing allowed to create complex magnetic iron oxides with hexagonal structure, i.e. hexaferrites

[62, 63, 69] with significantly higher magnetocrystalline anisotropy energies and magnetic anisotropy field and therefore higher FMR frequencies. Most of these popular hexaferrites are derived from Ba M–type hexaferrite, $BaFe_{12}O_{19}$, and have become technologically and commercially very important materials with numerous scientific and real-life applications [64, 69]. A strong gyrotropic potential of Sr–M polycrystalline hexaferrite (Ferroxdure 330) for free-space NR components in W-band has been presented in 1991 by M. R. Webb [70] and later also by Smith *et al.* [71]. In 1994 M. Raum [72] demonstrated Faraday rotation measurements of the same material at 290 GHz and following work of Smith *et al.* [73] includes characterization measurements up to 550 GHz. Some years later, the promising gyrotropic properties of ceramic hexaferrite were characterized by Hunter *et al.* [74] and by Yang *et al.* [75, 76] who focused on specific ceramic Sr- hexaferrite FB6H which also found an application in circulators (as shown in Fig. 1.5) in the 2009 ESA mission PLANCK telescope to measure the cosmic microwave background up to 320 GHz [77]. This ceramic possesses high value of

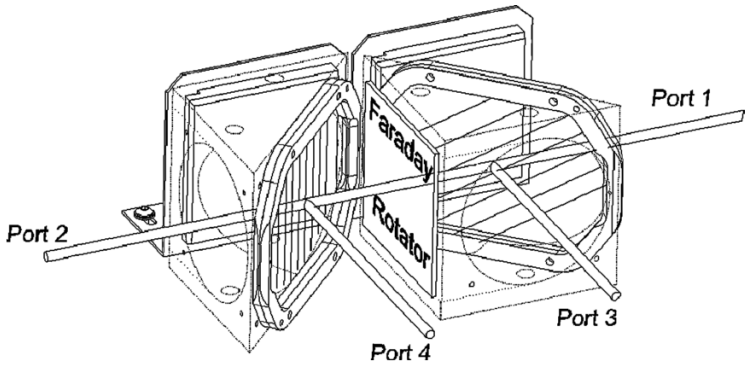

Figure 1.5: Quasi-optical Faraday-rotation circulator as presented by D. H. Martin and R. J. Wylde [77]

H_A as well as high remanence magnetization and therefore showed up itself as a very promising material for THz NRDs. The Faraday-rotator plate at the center of the circulator is of a nonmetallic magnetic material, fully magnetized normally to its surfaces, with surface layers of dielectric material to match a normally inci-

dent plane-polarized signal beam into the plate, and out of it following a single pass of the plate. The thickness of the plate is such that the signal beam suffers a 45° Faraday rotation of its plane of polarization in the single pass. This Faraday-rotator plate is located between two wire-grids set with their planes at 45° to the lines of the signal beams. The directions of the closely spaced wires in the two grids (as indicated in Fig. 1.5 by a few-lines drawing the plane of each grid), when projected onto a transverse plane, are at 45° to each other. Planar power dumps are provided as indicated at the rear of the diagram. This circulator becomes an isolator if further power dumps are placed in Ports 3 and 4.

Consequently, first THz isolator working without application of an external magnetic field and thus confirming strong gyrotropic properties of hexagonal ferrites in mm-wave range was published by Shalaby *et al.* [78]. The exploited medium allowed a broadband rotation, up to 194 °/T, obtained using a 3 mm thick permanently magnetized $SrFe_{12}O_{19}$. The value of $\mathbf{B} = 1$ T is strong enough to saturate the ferrite. For a characterization of the hexaferrite a typical THz Time-domain spectrometry has been used. Thanks to the coherent nature of the used terahertz detection techniques, one can record a time trace of the terahertz field amplitude. Its Fourier transform reveals both the amplitude and the phase of the terahertz pulse spectrum, as will be described in Section 2. The functionality of the proposed terahertz isolator has been tested using the backward-waves characterization setup shown in Fig. 1.6, where a flat mirror is normally placed after the sample to allow for the terahertz wave to back-propagate through the same sample. Two polarizers are used in the configuration following the typical Faraday isolator design: WGP4 is set to 0° and WGP5 is set to 45°. Corresponding measured THz back-reflected pulses for magnetized and non-magnetized sample are depicted in Fig. 1.7a.

Performance of this nonreciprocal (NR) component was however at higher frequencies hindered by high insertion losses of used Sr-hexaferrite, as is shown in Fig. 1.7b. Moreover, this figure also indicates high values of measured refractive index, which have not been published anywhere else.

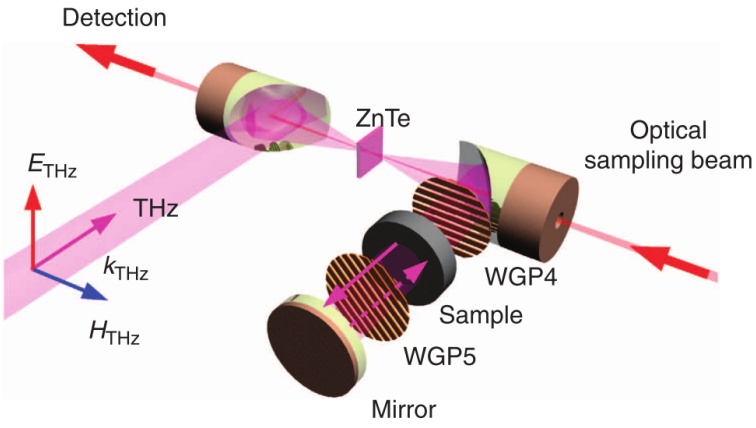

Figure 1.6: Isolator characterization setup. A two-polarizer (WGP4 and WGP5) configuration is employed. WGP4 is set to 0° to ensure a vertical polarization of both the generated and detected signals. [78]

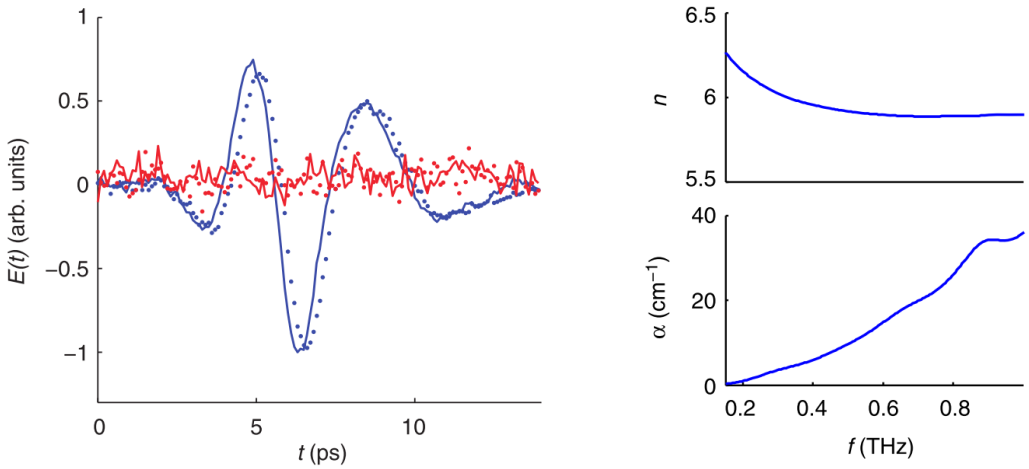

(a) THz time pulse.

(b) Refractive index and absorption coeff.

Figure 1.7: The back-reflected terahertz pulse was measured using the isolator setup. The comparison is made between a 45°-magnetized sample (the isolator case, shown in red) and an demagnetized one (shown in blue). Solid/dotted lines refer to the cases where WPG5 was removed/placed, respectively. (b) Refractive index and absorption coefficient of $SrFe_{12}O_{19}$ measured by THz-Time-domain spectroscopy [78]

1.3 Objective of This Work

The main objective of this thesis is a study of nonreciprocal effects at THz frequencies. By this work we will take up on recently demonstrated results, as summarized in the State of the Art section (Sec. 1.2), with particular focus on NR properties of hexagonal ferrites.

The first part of the study is hence devoted to the precise full-tensor magneto-optical characterization of several types of hexagonal ferrites, including single crystal Ba- and Sr- hexaferrites and two types of commercially available hexaferrite ceramics FB6H and FB6N. The experimental data were obtained by VNA-controlled frequency multipliers and mixers Rohde and Schwarz ZVA 24 with millimeter-wave heads and THz Time-domain Spectrometer TPS Spectra 300 of TeraView Company with rotating polarizers.

The biggest drawback of the hexagonal ferrites, otherwise ideal candidates for NRD, are indeed their expected high insertion losses. Because there is currently a lack of precise characterization of hexaferrites in mm- and sub-mm-wave range and existing sources [73, 76, 78] report conflicting values of optical index and losses, we first aimed to help resolve this confusion. Our latest research [79] shows that values of losses can vary between different M-type hexaferrites and small differences in real parts of optical indices have been also observed, however we have never measured as high values as published by Shalaby *et al.* [78] and all our results have been in good agreement with these measured by Yang *et al.* [75, 76]. However, we confirmed that losses of hexaferrites are indeed their big disadvantage and one has to therefore limit the propagation length through used hexaferrite in order to obtain still acceptable losses and thus decrease also a performance of the proposed NRD. That is, of course, usually not desirable.

In order to solve this issue of high insertion losses we therefore propose a novel design of THz isolator which works as a one-way NR mirror. This isolator represents a complex device which consists of two basic elements: A gyrotropic substrate on which a structured metallic layer is deposited. The substrate is rep-

resented by a transversely magnetized hexagonal ferrite which, upon reflection of a linearly polarized EM wave, gives rise to the transverse magneto-optical Kerr effect. This MOKE provides a change of intensity and phase of incident linearly polarized light and is, as will be studied in Chapter 2, fundamentally nonreciprocal. However, this effect is at an ordinary planar interface not strong enough to provide a reasonable isolation. As we have seen already at the presented microstructures (Fig. 1.3), plasmonic resonance phenomena can greatly enhance otherwise weak MO effects. Because hexagonal ferrites do not support excitation of surface plasmons themselves, we have to for this purpose introduce a second element of the isolator: a metallic layer structured by sub-wavelength motifs. The presence of the otherwise opaque metallic layer enables the excitation of surface plasmons at the interface between the metal and substrate manifesting themselves as the extraordinary transmission (EOT) phenomena. The resonance between the incident EM wave and excited surface plasmons causes a presence of strong dip in reflection spectrum, and when coupling with the gyrotropy of the substrate, the resonance frequencies move to higher and lower energies, according the magnetization direction. Consequently, radiation incident from at an angle on the device can be almost perfectly reflected, while the one incident from the angle in the same plane of incidence passes through the metallic layer into the substrate.

The whole concept builds on recently demonstrated NR reflecting surface for near-infrared (NIR) spectral range [80, 81]. This magnetoplasmonic structure consisting of a 1D periodic grating of gold fabricated on the surface of a magneto-optic garnet substrate, as shown in Fig. 1.8, supports an enhancement of the transverse MO Kerr effect and therefore can have strong isolating properties close to the plasmonic frequencies, as depicted via TMOKE spectrum in Fig. 1.9. This isolator from its principle works in a reflection configuration with no need to propagate through the gyrotropic medium and therefore might significantly reduce insertion losses.

Design of a similar NR device for THz frequencies brings up several new chal-

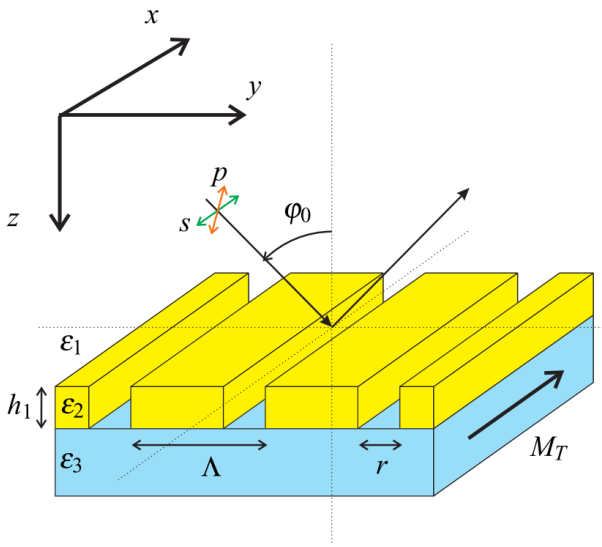

Figure 1.8: Coordinate system and schematic representation of studied structure as presented by Halagačka *et al.* [80] : gold grating with a period Λ and a thickness h_1 on a magneto-optic garnet substrate in transversal configuration with incident plane wave in $y-z$ plane at the incident angle ϕ_0 and with s- or p-polarization.

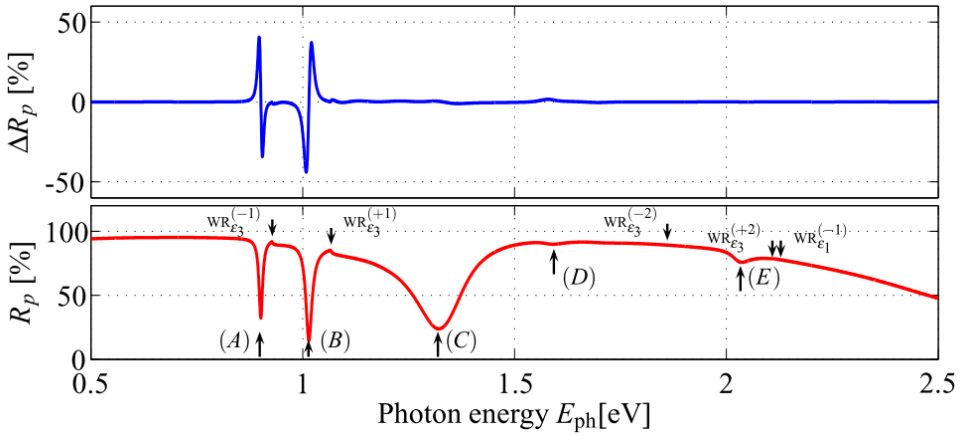

Figure 1.9: Specular reflectivity (bottom line) and associated TMOKE spectrum (top line) of p-polarized light incident on the grating structure in Fig. 1.8 with $\Lambda = 500\,\text{nm}$, $h_1 = 150\,\text{nm}$ and $r = 20\,\text{nm}$. [80]

lenges which we have to solve. First of them is the question of existence of extraordinary transmission effect in THz range. Plasmonics in the THz range has attracted research interest in recent years even with the fact that THz range is far from plasmonic frequencies of most real metals whose properties approach these of a perfect electric conductor (PEC) with negative real part and large imaginary part of permittivity. Therefore, surface plasmons (SPs), which are collective electron oscillations, can not be in THz directly excited at ordinary metal/dielectric interface and metals must be for this purpose patterned. One of the first predictions of a surface electromagnetic modes excitation at THz frequencies by structuring of the metal surface was done by group of Pendry *et al.* [82, 83]. The structured metallic surface can be, according to the theory, described by an effective dielectric function which is now different from the one of PEC, and enables the excitation of evanescent surface modes at the metal/substrate interface. These SPPs-like surface modes have been since that time named *spoof SPPs* or *designer plasmons*. In the same year O'Hara *et al.* [84] published successful coupling of THz radiation into surface plasmon polaritons on metallic gratings. Couple of years latter a guiding of surface plasmons polaritons on structured metal surfaces was confirmed by Williams *et al.* [85] and analytical description of spoof plasmons in real metals was developed by Rusina *et al.* [86]. In following years a propagation of SPPs was intensively studied [87, 88, 89] and plasmons were used in a number of THz applications such as near-field sensing [90], switches [91, 92], sensitive sensing devices [93, 94, 95] or waveguiding structures [96]. A high-quality review of THz plasmonics in subwavelength holes on conducting films was published in 2013 by Azad *et al.* [97]. It did not take a long time and plasmonics found a way into first NR devices. THz isolator using structured semiconductors magneto-plasmonics and requiring high magnetic field and low temperatures was presented by Fan *et al.* [98]. Just few years ago Degiron *et al.* [99] presented combination of ferrite gyrotropy and surface plasmons for microwave nonreciprocal materials.

Another challenge for the THz NR device comes from the fact, that hexafer-

rites, as potential candidates for the device substrate material, are in the THz range characterized by a tensorial form of the permeability, unlike the MO garnet in the work of Halagačka *et al.*, which is characterized by a permittivity tensor. Considering this exchange of permittivity for permeability and taking into account a duality of Maxwell's equations $\bar{\bar{\varepsilon}} \leftrightarrow \bar{\bar{\mu}} \Rightarrow \mathbf{E} \leftrightarrow \mathbf{H}$, it implies, that the EOT effect and thus also the SPPs excitation must occur for TE-polarized wave, instead of TM polarization active in Fig. 1.9. This is possible only when a second dimension of grating periodicity is introduced, as will be shown in chapter 2.

The last part of the thesis is thus focused on a study of a completely novel design of THz isolating device consisting of a thin 2D periodic structure of gold fabricated on a surface of the transversely-magnetized hexaferrite substrate, as depicted in Fig. 1.10. We primarily focused on the isolation in the millimeter-wave range, therefore close to 300 GHz.

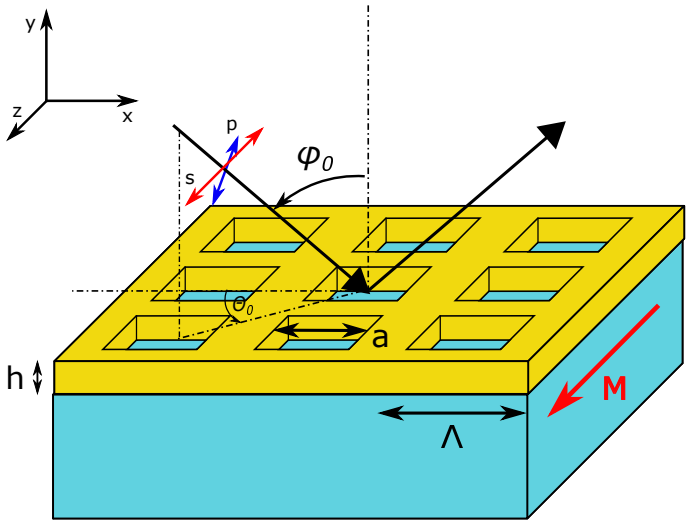

Figure 1.10: Schematic representation of the studied THz nonreciprocal isolator: gold layer patterned by 2D periodic structure with period Λ, holes size a and thickness h on a magneto-optical hexaferrite substrate magnetized in transverse configuration with incident s- or p-polarized plane wave at an angle of incidence ϕ_0 and an azimuthal angle θ_0.

1.4 Organization of the Thesis

This thesis is organized in four chapters.

Chapter 2 summarizes general properties of electromagnetic radiation with focus on THz frequency range. The THz time-domain spectroscopy is presented, its principle and benefits. It also introduces formulation of Maxwell's equations and polarization properties of electromagnetic radiation. Material parameters are presented in a form of permittivity and permeability tensors as well as their forms for different anisotropy examples. Next part is focused on an interaction of EM wave with a magnetized medium, and therefore on all types of magneto-optical effects. Transverse Kerr effect, Faraday effect and Cotton-Mouton effect are described more in detail because of their application in other parts of the thesis. Subsequently, the effect of extraordinary optical transmission is presented. We introduce two possible channels of EOT with focus on surface plasmon polaritons, their excitation and coupling mechanisms. The last part of the chapter studies possibility of SPPs presence in THz range and an excitation by *TE*-polarized radiation.

Chapter 3 is focused on magneto-optical ferrites with hexagonal lattice structure. In the first instance we summarize their general properties, including their chemical composition, anisotropy, crystal structure. Surface of several samples was studied by scanning electron microscopy and atomic force microscopy techniques. Subsequently their magnetic properties and origin of permeability tensor are described together with hysteresis curve measurement by vibrating sample magnetometry. The next part of the chapter describes the free-space characterization of non-magnetized hexaferrites by quasi-optical setup using VNA. The whole procedure of data processing technique and extraction of parameters is presented. Final obtained parameters give first indication of ideal candidates for THz transmissive nonreciprocal devices. The following part of the chapter is devoted to complete magneto-optical characterization of hexaferrite ceramics. This

was done in remanent magnetization of the sample and measuring by THz Time-domain spectroscopy. Obtained gyrotropic spectra show strong magneto-optical behavior of the ceramics in the THz range, as proved by an original free-space Faraday-isolation measurement done by the VNA-controlled setup.

Chapter 4 introduces the novel design of the THz isolator based on magneto-plasmonic reflecting surface. First, the optical properties of gold in THz range obtained from well-known Drude model are presented. This optical function will be used for the following numerical studies. The presence of SPPs in the millimeter-wave range is in the first instance demonstrated experimentally by a gold structure fabricated on a quartz substrate, as the lower refractive index of quartz provides stronger resonance effect. Then the isolator design combining the gold periodic structure and hexaferrite substrate is presented. The nonreciprocal properties of this device are confirmed numerically both by RCWA calculations via Python code and finite elements method (FEM) simulations in CST Studio Suite software.

CHAPTER 2

Theoretical Background

Contents

This chapter introduces theory used in the following parts of the thesis. In the first place we describe the THz range, its position in the spectrum, advantages of using THz technologies and principle of Time-domain THz spectrometry. This part is followed by a description of light polarization and material properties including Jones formalism which will be used in Chapter 3 for description of radiation polarization state during material characterization measurements, with focus on material tensors. The MO effects are introduced afterwards with a particular focus on the Faraday and TMOKE effects as the essential effects used in THz nonreciprocity. The last part of the chapter is focused on the effect of extraordinary optical transmission and its two possible channels followed by a study of surface plasmon polaritons and their excitation options in the THz range and by an *s*-polarized wave.

2.1 The Electromagnetic Spectrum

All electromagnetic (EM) radiation travels in vacuum at the speed of light c and we can characterize it by its wavelength λ measured often in mm, µm, or nm, by its wavenumber $\tilde{\nu}$ $\left(\mathrm{cm}^{-1}\right)$, or frequency ν (GHz, THz, ...). It includes, in addition to what is usually referred to as *light*, radiation of longer and shorter wavelengths. In vacuum the wavelength is defined as:

$$\lambda_{\mathrm{vac}} = \frac{c}{\nu} = \frac{1}{\tilde{\nu}}. \tag{2.1}$$

The velocity of propagation in vacuum is constant for all regions of the spectrum and has the value $c = 299\,792\,458\,\mathrm{m\,s^{-1}}$.

Fig. 2.1 shows the electromagnetic spectrum from low-frequency (long-wave) radiation to high-frequency (short-wave) radiation. The red-highlighted part de-

notes the THz region. As it is obvious it is located between electronic and photonic spectral parts which have been named according the dominant used technology at corresponding frequencies. Optical frequencies occupy a band of the electromagnetic spectrum that extends from the infrared (IR) through the visible to the ultraviolet (UV) region. In energy scale the photon energy is also very often

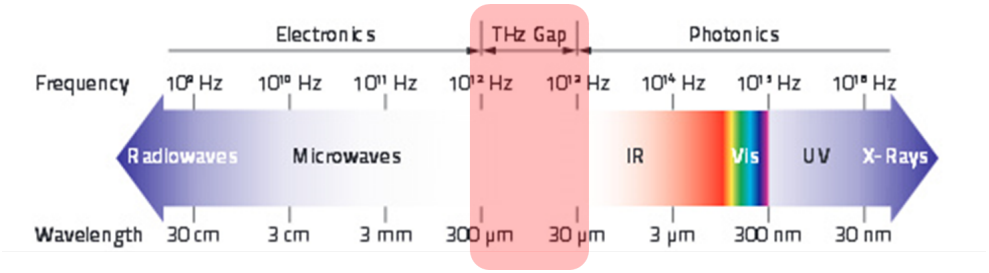

Figure 2.1: The electromagnetic spectrum from low-frequency to high-frequency radiation.

indicated in electron volts (eV), where:

$$\begin{aligned} E &= hc\tilde{\nu} \\ \frac{1\,\mathrm{eV}}{hc} &= 8065.54\,\mathrm{cm}^{-1} \end{aligned} \tag{2.2}$$

and $h \doteq 4.1357 \times 10^{-15}\,\mathrm{eV\,s}$ is Planck's constant. Radiation at a frequency of 1 THz has a wavelength of 300 µm, a photon energy of 4.14 meV and a wavenumber of $33.3\,\mathrm{cm}^{-1}$. We can summarize processes occurring in atoms or molecules exposed to the EM radiation. An atom can undergo only an electronic transition or ionization, because it has no rotational or vibrational degrees of freedom. But a molecule can undergo rotational, vibrational, electronic or ionization processes, in order of increasing energy. A molecule can also scatter light in a Raman effect, and the light source for such an experiment is usually in the visible or near-ultraviolet region [100]. The division into the various regions is useful to indicate the different experimental techniques. The mechanism leading to terahertz absorption in molecular and biomolecular systems is dominated by the excitation of intramolecular as well as intermolecular vibrations between weakly

bound molecular entities with hydrogen bonds and weak interactions such as van der Waals forces playing an important role [101]. The modes at THz frequencies are, for example, associated with collective intramolecular vibrations (e.g. torsional modes in large molecular chains) or with intermolecular vibrations between neighboring molecules (e.g. in molecular crystals).

The electromagnetic spectrum and the various interactions between the radiation and many forms of matter can be considered in terms of classical or quantum theories. The nature of the various radiations shown in Fig. 2.1 have been interpreted by Maxwell's classical theory of electro- and magneto-dynamics - herefrom, the term *electromagnetic radiation*. According to this theory, radiation is considered as two mutually perpendicular electric and magnetic fields. The electric component of the radiation is in the form of an oscillating electric field of strength **E** and the magnetic component is in the form of an oscillating magnetic field **B**. These oscillating fields are perpendicular to each other, as shown in Fig. 2.2 . The magnitudes of the electric and magnetic vectors are represented by E and B, respectively [102].

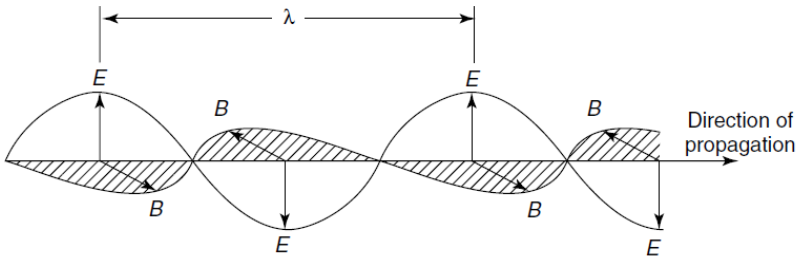

Figure 2.2: Representation of an electromagnetic wave. [102]

2.2 Terahertz Radiation and Spectroscopy

Generation, utilization and detection of terahertz (THz) radiation represent another milestone in science and technologies. The term *terahertz radiation* is usually used for an electromagnetic radiation with frequencies between 0.1 THz and

10 THz. Another terminology utilized for this range is *T-rays*, where *T* stands for terahertz. As we can see in Fig. 2.1, it corresponds to the range between the IR and microwave bands. It includes as well some neighboring spectral bands such as the millimeter-wave and sub-millimeter-wave bands. Due to its central spectral position between electronic and photonic technologies this part of electromagnetic spectrum has been for a long time perhaps the least explored region. None of the technologies of the neighboring bands was developed enough to be extended into the lower or higher frequencies and the development of either efficient, powerful and applicable THz sources or sufficiently sensitive detectors was complicated. The increase of the frequency of electronic synthesizers [103] was not possible anymore and Planck's law confirms that the brightness of optical sources rapidly decreases towards longer wavelengths. This range was therefore for a long time entitled the *THz gap*, but in the last two decades scientists have registered significant progress in the development. The first dated experiments in the THz range originate from the end of 19th century [104]. In following decades, besides the first attempts on THz spectroscopy, the THz technologies were initially used by astronomers for the study of cosmic far-infrared radiation background. Later, researchers focused mainly on development in generation and detection of THz waves. Nowadays, as a result of rapidly developing technology of ultrafast lasers, THz radiation has widespread potential applications in medicine, spectroscopy, information and communication technology, security, microelectronics, agriculture, forensic science, and many other fields. The general properties of the THz radiation are summarized in the following points [105]:

- According to the used source, THz radiation can be generated as pulsed (used for example in THz spectroscopy) or continuous-wave (CW, used in free-space quasi-optical applications). [51]

- THz waves have longer wavelengths in comparison to IR waves. Most of dry dielectric materials (plastic, paper...) are transparent to THz waves. Therefore the THz waves are considered to be very promising in nonde-

structive evaluation applications such as security imaging or process monitoring.

- Many molecules exhibit strong absorption and dispersion at THz frequencies. Due to specific molecule rotational and vibrational transitions there is spectroscopic fingerprinting present in the THz range. THz radiation strongly interacts mainly with metals and with polar molecules, e.g. water.

- THz waves are generally considered as safe for the samples and the operator, because they have lower photon energy compared to X-rays, hence they cannot lead to photoionization. They also cannot penetrate into the human body unlike microwaves.

Detection of THz radiation can be classified either as coherent or incoherent. Incoherent detection measures only intensity and can be represented by thermal sensors such as pyroelectric devices, bolometers or Golay cells. Coherent detection scheme can record both amplitude and phase of the field.

Typical coherent detector is a photoconductive (PC) antenna of which a schematic representation is shown in Fig. 2.3. The PC antenna uses an effect

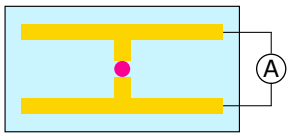

Figure 2.3: Schematic representation of a photoconductive antenna

of increased electrical conductivity of semiconductors and insulators whey they are exposed to radiation. Here, incident THz radiation induces a current in the photoconductive gap between two electrodes when a probe pulse creates photocarriers. The photon energy of the probe pulse must be sufficiently large to overcome a bandgap of the used material. The resulting induced photocurrent lasts for the carrier lifetime, is proportional to amplitude of the THz field, and the

THz pulse shape is recorded by measuring the photocurrent during variation of the time delay between THz and probe pulses. The measurement of a THz pulse by a PC antenna is schematically depicted in Fig. 2.4. The current amplifier is used in order to amplify a typically weak photocurrent signal.

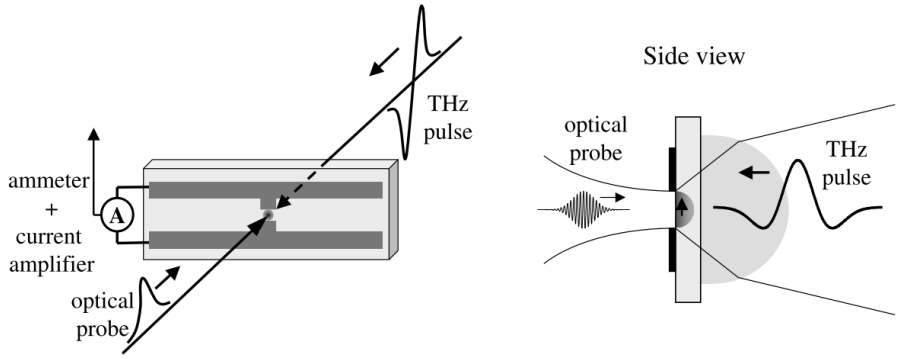

Figure 2.4: Schematic representation of THz pulse detection by a photoconductive antenna [51]

Other well-known members of the coherent detectors group are nonlinear crystals measuring broadband THz pulses in time domain using Pockels effect. An incident THz field induces crystal's birefringence proportional to the field amplitude. This birefringence is then measured by the probe pulse as a function of a time delay between the THz and probe pulses leading to a determination of an entire waveform. All the most used techniques of the coherent detection are summarized in Fig. 2.5.

A setup combining both broadband THz generation and detection can be used for measurement of amplitude and phase changes of the THz beam provided by a measured sample. This technique is well-known as THz time-domain spectroscopy (TDS) which will be presented in following section, since it has been widely used during material and device characterization presented in Chapters 3 and 4.

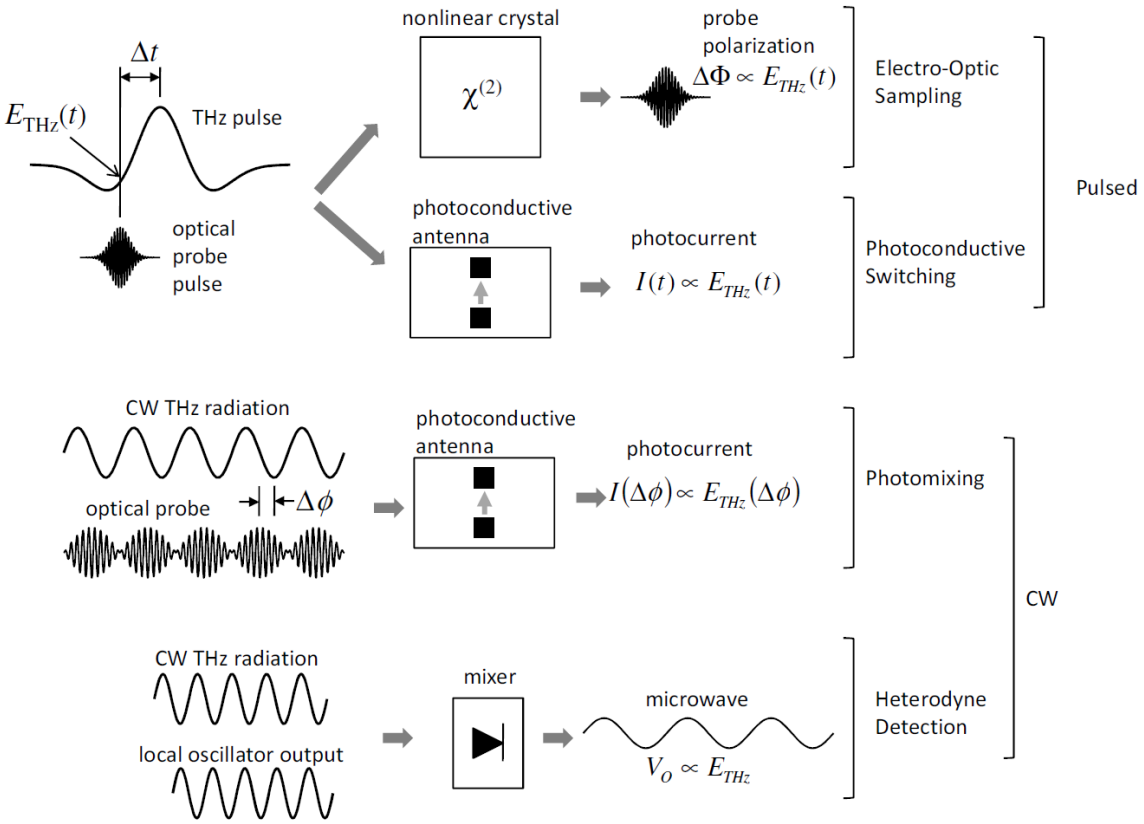

Figure 2.5: Coherent detection techniques of THz radiation [51]

2.2.1 Terahertz Time-domain Spectroscopy

Terahertz time-domain spectroscopy is one of the most successful and widespread fields of THz optoelectronics. It is the leader of most of the spectroscopic measurements performed in the THz range and provides a powerful tool with ultrawide bandwidth for studying and characterizing material properties as well as IR spectroscopy. Due to the high sensitivity of THz waves to water molecules and unique molecular vibrations and rotational energy levels of molecules of many chemical and biological samples, these can have direct spectral response in this band. This makes a THz beam a powerful tool for examination of samples and agents in a wide scientific range including physics, chemistry, biology, astronomy or medicine. Despite these real useful applications TDS systems are still being developed as there is high demand for making them even

faster, smaller, more stable and less expensive [52].

TDS uses pulsed THz wave which means that the waveform of THz pulse is detected by temporally sampling the THz pulse using probe laser pulses. We can see the basic experimental scheme of the typical TDS setup on Fig. 2.6.

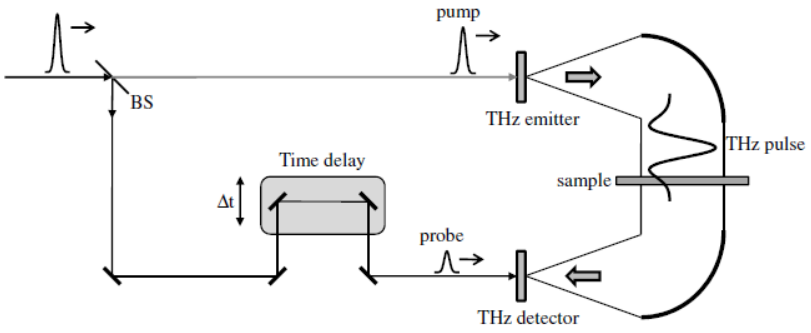

Figure 2.6: The basic experimental scheme of a typical THz-TDS setup. [51]

The optical beam from the femtosecond (fs) laser is split into two segments. The first of them generates the THz pulse from a THz emitter, which can be a nonlinear crystal or a PC antenna. This THz pulse then continues through the sample into the detector represented by an electro-optic crystal or another PC antenna. The second segment of the beam continues into a translational stage, providing a time delay. This part is used to detect those THz pulses. The two segments have a defined time relationship, because they originate from the same source. The temporal profile of the THz pulse with subpicosecond time resolution can be measured by progressively changing of the arrival time of the second pulse. Two waveforms, with and without sample, are measured in the time domain and they are Fourier-transformed (FT) into the complex amplitudes in the frequency domain (FD). The signal is detected in the form of an electric field and by using the Fourier transformation of the pulse signal we can obtain both amplitude and phase of the radiation. Hence, since the electric field is directly measured, one of the biggest advantage in comparison to IR spectroscopy is the possibility to obtain the absorption and even the dispersion of the sample without necessity of using Kramers-Kronig relations [106]. Moreover, the fact that THz pulses are cre-

ated and detected using short-pulsed lasers opens possibility for high-temporal-resolution study of dynamics [107].

As it was already mentioned, the time-delay between the THz and the optical pulse triggering the detector is varied by using an optical delay line. As the result of this varying delay the THz pulse is recorded in the time-domain. Because any change of the positioning stage position by Δx introduces a change of the total path equal to $2\Delta x$, as one can see in Fig. 2.6, we can express the discrete temporal steps Δt which correspond to discrete spatial steps Δx as:

$$\Delta t = \frac{2\Delta x}{c}\,, \tag{2.3}$$

where c denotes the speed of light. A discretely sampled signal $E(t)$ is obtained by recording a data point at every position of the delay line. Therefore, the frequency spectrum of the radiation is obtained by the Fourier transformation of the electric field [108]:

$$\hat{E}\left(\omega\right) = \frac{1}{2\pi}\int_{-\infty}^{+\infty} e^{i\omega t} E\left(t\right) dt = A\left(\omega\right) e^{i\phi(\omega)}\,, \tag{2.4}$$

where $\omega = 2\pi\nu$ is the angular frequency, $\phi\left(\omega\right)$ is the phase and $A\left(\omega\right)$ denotes the measured amplitude. The temporal scanning range ΔT determines a spectral resolution $\delta\omega$ of THz-TDS in the form:

$$\delta\omega = \frac{2\pi}{\Delta T}. \tag{2.5}$$

Mathematically is the spectrum measured within a bandwidth:

$$\Delta B = \frac{2\pi}{2\delta t} = \frac{\pi}{\delta t}, \tag{2.6}$$

where δt is the temporal sampling interval, and 2 in the denominator comes from the fact, that the spectrum is after FT mirrored also into negative frequencies. Real frequency range of the spectrometer is however limited by the source and

detector responses and length of optical delay line. Figures 2.7a and 2.7b show the THz waveform and transmission spectrum of a transmission through a glass plate. The waveform shows two detected peaks - in the TD. The first one (at $t = 855\,\text{ps}$) corresponds to the first pass through the glass plate and the other one at $\approx 873\,\text{ps}$ corresponds to the second pass of the THz pulse after a round-trip inside the sample (echo). This multi-pass detection, also known as *Fabry-Perot* oscillations, then manifests itself as pronounced minima and maxima in the FD spectrum (visible in the range 0–30 cm^{-1}). These can be removed by a technique called time-domain gating, which corresponds to a selection of a region of interest and multiplying all remaining unwanted responses by zero, which leads to artificially numerically performing a single-pass experiment. This technique of TD gating will be widely used later during a free-space characterization, presented in Chapter 3.

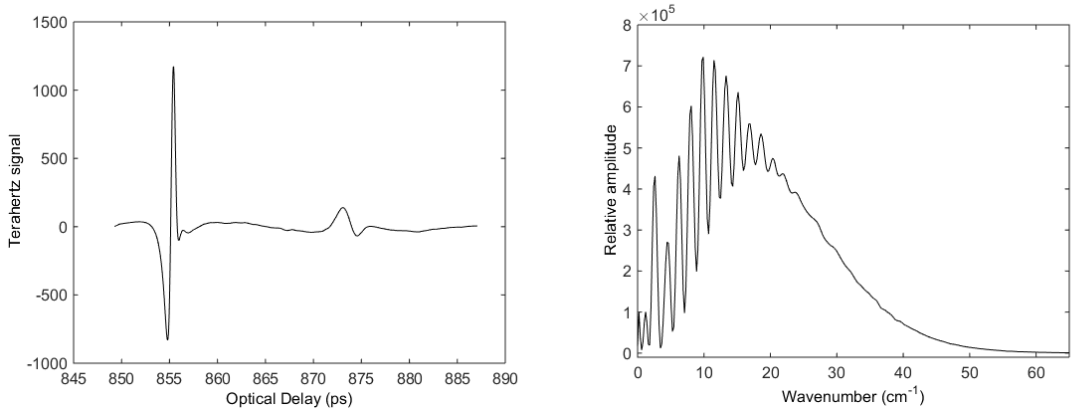

(a) THz waveform (b) Frequency spectrum

Figure 2.7: Examples of THz signal and spectrum after transmission through a glass sample.

2.3 Material Properties and Constitutive Relations

This section is devoted to material properties and constitutive relations which will be used through all the research. We will show the principle of duality in

classical EM theory and a derivation of the important Lorentz reciprocity theorem which was already mentioned in Chapter 1 and which plays a crucial role in the subject of this research.

As it was mentioned in Section 2.1, the electromagnetic field consists of two orthogonal components, the electric and the magnetic, perpendicular to the direction of travel of the photon (Fig. 2.2). Therefore, all EM waves can be described by the vectors of the electric-field intensity **E**, the electric displacement **D**, the magnetic-field intensity **H**, and the magnetic flux density **B**. The time and spatial evolution of electric and magnetic fields is described by Maxwell's equations [109]:

$$\nabla \times \mathbf{E} = -\frac{\partial \mathbf{B}}{\partial t}, \qquad \nabla \cdot \mathbf{D} = \rho, \qquad \nabla \times \mathbf{H} = \mathbf{j} + \frac{\partial \mathbf{D}}{\partial t}, \qquad \nabla \cdot \mathbf{B} = 0, \tag{2.7}$$

where **j** represents the electric current density and ρ stands for the volume electric charge density. The boundary conditions at an interface between two media with different material properties, when $\mathbf{n}_{12}$ is the normal vector from medium 1 to medium 2, can be expressed as [110]:

$$\mathbf{n}_{12} \times (\mathbf{E}_{1t} - \mathbf{E}_{2t}) = 0, \tag{2.8a}$$

$$\mathbf{n}_{12} \times (\mathbf{H}_{1t} - \mathbf{H}_{2t}) = \mathbf{J}, \tag{2.8b}$$

$$\mathbf{n}_{12} \cdot (\mathbf{B}_{1n} - \mathbf{B}_{2n}) = 0, \tag{2.8c}$$

$$\mathbf{n}_{12} \cdot (\mathbf{D}_{1n} - \mathbf{D}_{2n}) = \sigma, \tag{2.8d}$$

where **J** is the surface current density at the interface, and σ is the surface charge between the media. In other words the conditions says, that the tangential component of **E** is continuous across the interface and the tangential component of **H** is continuous across the surface if there is no surface current present; the normal component of **B** is continuous across the interface and the normal component of **D** has a step of surface charge on the interface surface. If there is no surface charge on the interface, the normal component of **D** is continuous. These boundary con-

ditions will be widely used especially during description of magneto-optical effects in Section 2.5.

2.3.1 Permittivity and Permeability

The relation between the macroscopic fields **B** and **D** and the fundamental fields **E**, **H** can be expressed in different medium as following

1. In free-space:

$$\mathbf{D} = \varepsilon_0 \mathbf{E}, \qquad \mathbf{B} = \mu_0 \mathbf{H}, \tag{2.9}$$

where ε_0 is the vacuum permittivity and $\mu_0 = 4\pi \times 10^{-7}\,\mathrm{N\,A^{-2}}$ is the vacuum permeability. If $c = 299\,792\,458\,\mathrm{m\,s^{-1}}$ representing the speed of light, then:

$$\varepsilon_0 = \frac{1}{c^2 \mu_0} = 8.85 \times 10^{-12}\,\mathrm{A^2\,s^4\,kg^{-1}\,m^{-3}}. \tag{2.10}$$

2. For an isotropic material, in which the physical properties in the neighborhood of an interior point are the same in all directions, we obtain:

$$\mathbf{D} = \varepsilon \mathbf{E}, \qquad \mathbf{B} = \mu \mathbf{H}. \tag{2.11}$$

The dimensionless ratios:

$$\varepsilon_r = \frac{\varepsilon}{\varepsilon_0}, \quad \mu_r = \frac{\mu}{\mu_0} \tag{2.12}$$

are called the relative permittivity and relative permeability, respectively.

Now we consider the solution of the Maxwell's equations (2.7) in the form of planar monochromatic waves:

$$\mathbf{E}(\mathbf{r}, t) = \mathbf{E}_0 \exp\left[i\left(\omega t - \mathbf{k} \cdot \mathbf{r}\right)\right], \tag{2.13}$$

$$\mathbf{H}(\mathbf{r}, t) = \mathbf{H}_0 \exp\left[i\left(\omega t - \mathbf{k} \cdot \mathbf{r}\right)\right], \tag{2.14}$$

where $\mathbf{k} = \mathbf{n}\,(\omega/c)$ is the wavevector and $\omega = 2\pi\nu$. The permittivity and

permeability of the medium are generally complex functions of angular frequency ω: $\hat{\varepsilon}(\omega) = \varepsilon'(\omega) - i\varepsilon''(\omega)$, $\hat{\mu}(\omega) = \mu'(\omega) - i\mu''(\omega)$ and the complex refractive index of a material is defined as:

$$\hat{n}(\omega) = n(\omega) - ik(\omega) = \sqrt{\hat{\varepsilon}(\omega)\,\hat{\mu}(\omega)}. \tag{2.15}$$

3. The material properties of anisotropic medium vary in a different manner along different directions at a given point. Therefore, for a dielectric material we obtain:

$$\begin{aligned} D_x &= \varepsilon_{xx}E_x + \varepsilon_{xy}E_y + \varepsilon_{xz}E_z, \\ D_y &= \varepsilon_{yx}E_x + \varepsilon_{yy}E_y + \varepsilon_{yz}E_z, \\ D_z &= \varepsilon_{zx}E_x + \varepsilon_{zy}E_y + \varepsilon_{zz}E_z, \end{aligned} \tag{2.16}$$

where E_x, E_y, E_z are the Cartesian components of $\mathbf{E}$ and D_x, D_y, D_z the Cartesian components of $\mathbf{D}$. Eq. (2.16) can be expressed in a matrix formulation:

$$\begin{pmatrix} D_x \\ D_y \\ D_z \end{pmatrix} = \underbrace{\begin{pmatrix} \varepsilon_{xx} & \varepsilon_{xy} & \varepsilon_{xz} \\ \varepsilon_{yx} & \varepsilon_{yy} & \varepsilon_{yz} \\ \varepsilon_{zx} & \varepsilon_{zy} & \varepsilon_{zz} \end{pmatrix}}_{\bar{\bar{\varepsilon}}} \begin{pmatrix} E_x \\ E_y \\ E_z \end{pmatrix}, \tag{2.17}$$

where $\bar{\bar{\varepsilon}} = \varepsilon_0 \bar{\bar{\varepsilon}}_r$ is the permittivity tensor and the whole relation can be simplified into:

$$\mathbf{D} = \bar{\bar{\varepsilon}}\mathbf{E}. \tag{2.18}$$

Analogously it is possible to express relation for magnetic field between $\mathbf{B}$ and $\mathbf{H}$ as following:

$$\mathbf{B} = \bar{\bar{\mu}}\mathbf{H}, \tag{2.19}$$

where $\bar{\bar{\mu}} = \mu_0 \bar{\bar{\mu}}_r$ represents the permeability tensor, which exhibits itself in (hexagonal) ferrite materials, as a result of a precession motion of magnetic dipole moments, and as will be in detail analyzed in Chapter 3.

2.3.1.1 Permittivity and Permeability Tensors

The optical and magneto-optical properties of an anisotropic material are within the macroscopic theory described in the form of the $\bar{\bar{\varepsilon}}$ and $\bar{\bar{\mu}}$ tensors (Eqs. (2.18), (2.19)). Their general forms (for triclinic system) are shown in (2.20) and (2.21), respectively:

$$\bar{\bar{\varepsilon}} = \begin{pmatrix} \varepsilon_{xx} & \varepsilon_{xy} & \varepsilon_{xz} \\ \varepsilon_{yx} & \varepsilon_{yy} & \varepsilon_{yz} \\ \varepsilon_{zx} & \varepsilon_{zy} & \varepsilon_{zz} \end{pmatrix} \tag{2.20}$$

$$\bar{\bar{\mu}} = \begin{pmatrix} \mu_{xx} & \mu_{xy} & \mu_{xz} \\ \mu_{yx} & \mu_{yy} & \mu_{yz} \\ \mu_{zx} & \mu_{zy} & \mu_{zz} \end{pmatrix}. \tag{2.21}$$

A material is said to be anisotropic when some of its crystallographic directions are not identical (in terms of physical, mechanical, etc. properties). It is also possible to distinguish some special anisotropy cases and therefore simplify the material tensor, for electrical anisotropy as follows:

Isotropic material

All crystallographic directions in an isotropic material are identical. Therefore it has a rotation symmetry around all crystal's axes (cubic system):

$$\bar{\bar{\varepsilon}} = \begin{pmatrix} \varepsilon_{xx} & 0 & 0 \\ 0 & \varepsilon_{xx} & 0 \\ 0 & 0 & \varepsilon_{xx} \end{pmatrix} \tag{2.22}$$

in this case the material property can be represented by a scalar value (ε, μ).

Uniaxial anisotropy

The material has a rotation symmetry around one symmetry axis (tetragonal, trigonal and hexagonal systems). The principal axis that is different (displays the

anisotropy) is called the *optical axis*; here presented for the z-axis:

$$\bar{\bar{\varepsilon}} = \begin{pmatrix} \varepsilon_{xx} & 0 & 0 \\ 0 & \varepsilon_{xx} & 0 \\ 0 & 0 & \varepsilon_{zz} \end{pmatrix} \tag{2.23}$$

Biaxial anisotropy

If $\varepsilon_{xx} \neq \varepsilon_{yy} \neq \varepsilon_{zz}$, the material is called *biaxial* (orthorhombic, monoclinic, and triclinic systems):

$$\bar{\bar{\varepsilon}} = \begin{pmatrix} \varepsilon_{xx} & 0 & 0 \\ 0 & \varepsilon_{yy} & 0 \\ 0 & 0 & \varepsilon_{zz} \end{pmatrix} \tag{2.24}$$

Similar simplifications stands also for magnetically anisotropic materials, therefore for $\bar{\bar{\mu}}$ tensor.

2.3.2 Polarization and Magnetization

Application of an electric field to a dielectric material leads to a separation of the negative portions of charge provided by electrons and the positive portion of charges of atomic nuclei. This causes a consequent electrical distortion. This polarization of the medium can be described by an introduction of the electric polarization **P**:

$$\mathbf{P} = \varepsilon_0 \bar{\bar{\chi}}_e \mathbf{E}, \tag{2.25}$$

where $\bar{\bar{\chi}}_e = \bar{\bar{\varepsilon}}_r - 1$ is the electric susceptibility tensor, as presented in Chapter 1 (1.3). Analogously, an applied magnetic field on a medium will cause a change in the magnetic dipole moment **m**. Total magnetization of the material will be $\mathbf{M} = N\mathbf{m}$, where N denotes the number of magnetic dipoles per unit volume. This magnetization is related to the magnetic field in the following form:

$$\mathbf{M} = \mu_0 \bar{\bar{\chi}}_m \mathbf{H}, \tag{2.26}$$

where $\bar{\bar{\chi}}_m = \bar{\bar{\mu}}_r - 1$ is the magnetic susceptibility tensor. The vectors **P** and **M** contain information about the electromagnetic properties of the matter and considering (2.25) and (2.26) we can express the relation between the fundamental fields **E**, **H** and the macroscopic fields **B** and **D** in the following form:

$$\mathbf{D} = \varepsilon_0 \mathbf{E} + \mathbf{P} = \bar{\bar{\varepsilon}} \mathbf{E}, \qquad \mathbf{B} = \mu_0 \left(\mathbf{H} + \mathbf{M} \right) = \bar{\bar{\mu}} \mathbf{H}. \tag{2.27}$$

2.3.3 Duality of Maxwell's Equations

Assuming now a case when no electric charges or currents are present and the medium is characterized by a scalar permittivity ε and scalar permeability μ. Then the Maxwell's equations take a form:

$$\nabla \times \mathbf{E} = -\mu \frac{\partial \mathbf{H}}{\partial t}, \qquad \nabla \cdot \varepsilon \mathbf{E} = 0, \qquad \nabla \times \mathbf{H} = \varepsilon \frac{\partial \mathbf{E}}{\partial t}, \qquad \nabla \cdot \mu \mathbf{H} = 0. \tag{2.28}$$

For any solution of these equations it is possible to find a new physical system in which the **E** and **H** fields are mutually interchanged and will be again a solution of the Maxwell's equations. This is a basic principle of *duality* in classical EM theory, discovered by Heaviside [111], and showing the invariance of the Maxwell's equations under following transformations:

$$\begin{cases} \mathbf{E} & \longrightarrow & \mathbf{H} \\ \mathbf{H} & \longrightarrow & -\mathbf{E} \\ \varepsilon & \Longleftrightarrow & \mu \end{cases}. \tag{2.29}$$

and therefore the Maxwell's equations in (2.28) can be transformed as follows:

$$\nabla \times \mathbf{E} = -\mu \frac{\partial \mathbf{H}}{\partial t} \quad \longrightarrow \quad \nabla \times \mathbf{H} = \varepsilon \frac{\partial \mathbf{E}}{\partial t} \tag{2.30a}$$

$$\nabla \times \mathbf{H} = \varepsilon \frac{\partial \mathbf{E}}{\partial t} \quad \longrightarrow \quad \nabla \times \mathbf{E} = -\mu \frac{\partial \mathbf{H}}{\partial t} \tag{2.30b}$$

$$\nabla \cdot \varepsilon \mathbf{E} = 0 \quad \longrightarrow \quad \nabla \cdot \mu \mathbf{H} = 0 \tag{2.30c}$$

$$\nabla \cdot \mu \mathbf{H} = 0 \quad \longrightarrow \quad \nabla \cdot \varepsilon \mathbf{E} = 0 \tag{2.30d}$$

The transformed set of equations in (2.30) (right) is the same as the original set (left), except its sequencing. As a result, any solution of Maxwell's equations is also a solution to the dual problem where the variables and boundary conditions are all transformed as indicated in (2.29). This is an important statement which has an essential impact on the whole concept of the proposed isolator device. As will be shown in Section 2.5.2, the ordinary magneto-optical Kerr effect occurs typically for *p*-polarized EM wave, when the magnetized medium is characterized by permittivity tensor. However, as will be described in Chapter 3, the permittivity of hexagonal ferrites acquires a scalar form, whereas a precession motion of magnetic dipole moments causes the permeability to be in a tensorial form. Therefore the above presented duality denotes that in order to obtain a transverse MO Kerr effect at ordinary hexaferrite surface, the incident EM wave must necessarily be *s*-polarized.

2.3.4 Reciprocity Theorem

Since the Lorentz reciprocity theorem plays the very central role in the subject of this research, we will in this section focus on its derivation. Let us now consider a volume containing two sets of sources: $\mathbf{j}_1$, producing fields $\mathbf{E}_1$, $\mathbf{H}_1$, and $\mathbf{j}_2$, producing fields $\mathbf{E}_2$, $\mathbf{H}_2$. Consider the quantity:

$$\nabla \cdot (\mathbf{E}_1 \times \mathbf{H}_2 - \mathbf{E}_2 \times \mathbf{H}_1), \tag{2.31}$$

using a vector identity, (2.31) can be expanded into:

$$(\nabla \times \mathbf{E}_1) \cdot \mathbf{H}_2 - (\nabla \times \mathbf{H}_2) \cdot \mathbf{E}_1 - (\nabla \times \mathbf{E}_2) \cdot \mathbf{H}_1 + (\nabla \times \mathbf{H}_1) \cdot \mathbf{E}_2. \tag{2.32}$$

From time-harmonic Maxwell's equations (2.7) we can write:

$$\nabla \times \mathbf{E}_1 = -i\omega\bar{\bar{\mu}}_1\mathbf{H}_1 \tag{2.33}$$

$$\nabla \times \mathbf{H}_1 = i\omega\bar{\bar{\varepsilon}}_1\mathbf{E}_1 + \mathbf{j}_1 \tag{2.34}$$

$$\nabla \times \mathbf{E}_2 = -i\omega\bar{\bar{\mu}}_2\mathbf{H}_2 \tag{2.35}$$

$$\nabla \times \mathbf{H}_2 = i\omega\bar{\bar{\varepsilon}}_2\mathbf{E}_2 + \mathbf{j}_2 \tag{2.36}$$

and therefore:

$$\begin{aligned}\nabla \cdot (\mathbf{E}_1 \times \mathbf{H}_2 - \mathbf{E}_2 \times \mathbf{H}_1) = -i\omega\mathbf{E}_1 \cdot \left(\bar{\bar{\varepsilon}}_2 - \bar{\bar{\varepsilon}}_1^T\right) \cdot \mathbf{E}_2 - \mathbf{j_2} \cdot \mathbf{E}_1 + \\ + i\omega\mathbf{H}_1 \cdot \left(\bar{\bar{\mu}}_2 - \bar{\bar{\mu}}_1^T\right) \cdot \mathbf{H}_2 + \mathbf{j_1} \cdot \mathbf{E}_2.\end{aligned} \tag{2.37}$$

If the materials tensors satisfy the following conditions:

$$\bar{\bar{\varepsilon}}_2 = \bar{\bar{\varepsilon}}_1^T \tag{2.38a}$$

$$\bar{\bar{\mu}}_2 = \bar{\bar{\mu}}_1^T \tag{2.38b}$$

then Eq. (2.37) can be reduced into:

$$\nabla \cdot (\mathbf{E}_1 \times \mathbf{H}_2 - \mathbf{E}_2 \times \mathbf{H}_1) = \mathbf{j_1} \cdot \mathbf{E}_2 - \mathbf{j_2} \cdot \mathbf{E}_1. \tag{2.39}$$

This is an important result known as the differential form of the Lorentz reciprocity theorem in the frequency domain. Now we can integrate the divergence over the volume of interest, hence we obtain:

$$\iiint_V \nabla \cdot (\mathbf{E}_1 \times \mathbf{H}_2 - \mathbf{E}_2 \times \mathbf{H}_1)\mathrm{d}v = \iiint_V (\mathbf{j}_1 \cdot \mathbf{E}_2 - \mathbf{j}_2 \cdot \mathbf{E}_1)\mathrm{d}v, \tag{2.40}$$

the left side can be worked out using the divergence theorem into:

$$\oiint_S (\mathbf{E}_1 \times \mathbf{H}_2 - \mathbf{E}_2 \times \mathbf{H}_1)\mathrm{d}s = \iiint_V (\mathbf{j}_1 \cdot \mathbf{E}_2 - \mathbf{j}_2 \cdot \mathbf{E}_1)\mathrm{d}v. \tag{2.41}$$

If we now observe the **E** and **H** fields from an infinite distance, they can be considered as plane waves. Therefore, $\mathbf{E} \times \mathbf{H}$ points in the direction of the normal **n**, and **E** and **H** are related through $\mathbf{H} = (\mathbf{n} \times \mathbf{E})/\eta$, and it is possible to express the left side of (2.41) into:

$$\begin{aligned}(\mathbf{E}_1 \times \mathbf{H}_2 - \mathbf{E}_2 \times \mathbf{H}_1) \cdot \mathbf{n} \mathrm{d}S &= (\mathbf{n} \times \mathbf{E}_1) \cdot \mathbf{H}_2 - (\mathbf{n} \times \mathbf{E}_2) \cdot \mathbf{H}_1 \\ &= \eta(\mathbf{H}_1 \cdot \mathbf{H}_2 - \mathbf{H}_2 \cdot \mathbf{H}_1) \\ &= 0.\end{aligned} \tag{2.42}$$

And therefore we obtain:

$$\iiint_V \mathbf{j_1} \cdot \mathbf{E_2} \mathrm{d}v = \iiint_V \mathbf{j_2} \cdot \mathbf{E}_1 \mathrm{d}v, \tag{2.43}$$

which is the Lorentz reciprocity theorem in its integral form. This reciprocity theorem says, that a reaction of a reciprocal system is insensitive of the interchange of source and measurement locations. We can also conclude, that a medium is called reciprocal, if all materials creating the medium are reciprocal, meaning that the material properties satisfy the following conditions:

$$\bar{\bar{\varepsilon}} = \bar{\bar{\varepsilon}}^T, \qquad \bar{\bar{\mu}} = \bar{\bar{\mu}}^T. \tag{2.44}$$

Here it is tacitly assumed that they do not depend on the fields, i.e., linear media.

As was already explained in Chapter 1, a presence of magnetization reduces the isotropic spherical symmetry of the material to an uniaxial rotation symmetry around one axis. As a result, the $\bar{\bar{\varepsilon}}$ and $\bar{\bar{\mu}}$ tensors possesses unequal off-diagonal components, which are responsible for breaking of the Lorentz reciprocity, and hence are also responsible for non-reciprocal effects during interaction with an EM wave.

2.4 Polarization of Radiation

Polarization of EM radiation is one of its fundamental properties, together with its intensity, frequency and coherence. Because the study of fundamental behavior of polarized radiation and its interaction with a (magnetized) matter creates the principal part of this research, we will now devote this section to its description and classification and also to a matrix formalism for treating of the polarization evolution upon propagation through an optical system.

Polarization describes behavior of one of the field vectors with time observed at a given point in space. For definition of polarization of light waves the electric-field strength vector is commonly used. It is due to the fact that mainly the **E**-field vector of an EM wave interacts with the vibrational modes of the molecules in a medium and the force exerted on electrons by the electric field of light wave is bigger than the one exerted on electrons by the magnetic field. The polarization plane is the plane containing both **E** and **k** vectors. Due to the condition $\nabla \cdot \mathbf{D} = 0$, the **D**-vector always lies in the plane perpendicular to the wave vector direction. Polarization generally plays an important role in the interaction of light with a matter, which can be summarized in following points:

- Polarization of an incident wave influences the amount of reflected light at the interface of two media.
- Polarization influences the amount of light which is absorbed by an anisotropic material.
- Light scattering from a media is polarization dependent.
- The refractive index of anisotropic materials depends on the polarization.

Because polarization of EM wave plays important role within magneto-optical effects we will now describe particular cases of polarization, some basic polarization components and Jones formalism for description of evolution of polarization during EM wave propagation through an optical system. This formalism will be

used later in Chapter 3 during magneto-optical characterization and Faraday isolation measurements.

Two special cases of the polarization states of light are *linear* and *elliptical* (or *circular*) polarization and these are described in the following paragraphs.

2.4.1 Linear Polarization

If the electric fields are distributed in the same plane, the radiation is called *linearly* (or *plane*) polarized. The representation of a linearly polarized wave is illustrated in Fig. 2.8.

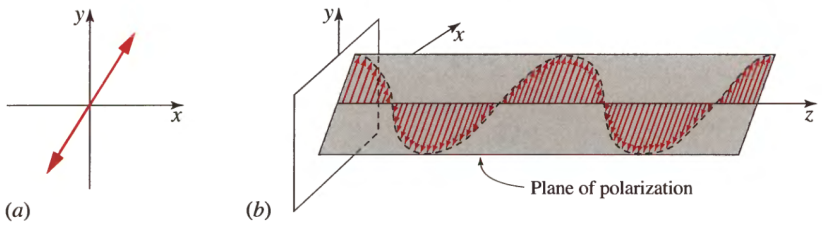

Figure 2.8: Representation of linearly polarized light. (a) Time course at a fixed position z. (b) A snapshot (fixed time t). [109]

If radiation is polarized in two perpendicular directions, any measured sample can reflect them in different way. In the field of the spectrometry and ellipsometry, there are usually recognized two perpendicular polarizations. Radiation with its plane of polarization parallel to the plane of incidence is usually named *p*–polarized. The other one is *s*–polarized radiation and it denotes, that the plane of its polarization is perpendicular to the plane of incidence. If two polarizations are absorbed differently by a sample, the phenomena is said to be a *linear dichroism*.

2.4.2 Circular and Elliptical Polarization

Radiation is said to be *circularly* polarized, if the electric field vector of a wave rotates when it travels through a medium. The difference in absorption of radi-

ation that is circularly polarized in opposite directions (left-polarized and right-polarized) by a sample is called *circular dichroism*. The representation of circularly left- and right- polarized wave is illustrated in Fig. 2.9.

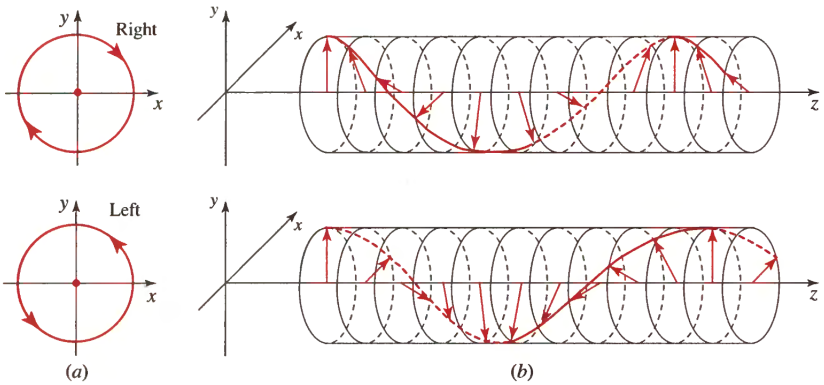

Figure 2.9: Trajectories of the endpoint of the electric-field vector of a circularly polarized plane wave. (a) Time course at a fixed position z. (b) A snapshot at a fixed time t. [109]

We can imagine a monochromatic planar wave of the angular frequency ω traveling with the velocity c in the direction of axis z. The vector $\mathbf{E}$ lies in $x-y$ plane and one of the solutions of the Maxwell's equations (2.7) is in the form:

$$\mathbf{E}(z,t) = \Re\left\{\mathbf{A}\exp i\omega\left(t-\frac{z}{c}\right)\right\}, \tag{2.45}$$

where $\Re$ represents the real part of a complex number and $\mathbf{A}$ represents the complex envelope:

$$\mathbf{A} = A_x\mathbf{i} + A_y\mathbf{j} = a_x\exp(i\varphi_x)\mathbf{i} + a_y\exp(i\varphi_y)\mathbf{j}. \tag{2.46}$$

If we express A_x and A_y in terms of their magnitudes and phases and substitute into (2.45), we obtain:

$$\mathbf{E}(z,t) = \underbrace{a_x\cos\left[\omega\left(t-\frac{z}{c}\right)+\varphi_x\right]}_{E_x}\mathbf{i} + \underbrace{a_y\cos\left[\omega\left(t-\frac{z}{c}\right)+\varphi_y\right]}_{E_y}\mathbf{j}. \tag{2.47}$$

The components of the vector **E** in (2.47) correspond to the equation of an ellipse:

$$\frac{E_x^2}{a_x^2} + \frac{E_y^2}{a_y^2} - 2\frac{E_x}{a_x}\frac{E_y}{a_y}\cos\varphi = \sin\varphi^2, \tag{2.48}$$

where $\varphi = \varphi_y - \varphi_x$ is the phase difference.

From the Eq. (2.48) is obvious, that the monochromatic wave is fully elliptically polarized (Fig. 2.10). This is the general polarization state of the light. The polarization ellipse is described by two parameters: the azimuth θ end the ellipticity ε. The azimuth θ describes the rotation angle of the ellipse major axis and the $\tan\varepsilon$ denotes the ratio between the major and minor axes of the ellipse. If

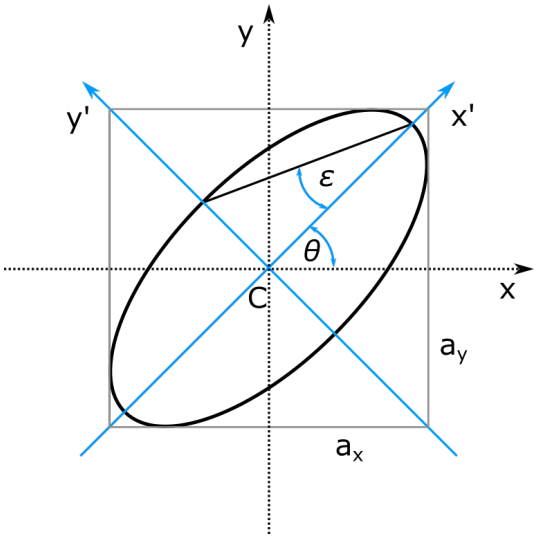

Figure 2.10: Polarization ellipse showing the orientation angle θ and ellipticity ε.

one of the components a_x, a_y is equal to zero or $\varphi = 0$ or π, the light is linearly polarized. If $a_x = a_y$ and $\cos\varphi = 0$, the light is circularly polarized. Therefore, circularly (or elliptically) polarized light is produced by retarding the phase of one polarization state [112].

2.4.2.1 Polarization Components - Linear Polarizer

A linear polarizer is an optical element which produces linearly-polarized radiation from an unknown or uncontrolled polarized beam. The most used types

of polarizers in terahertz applications are wire-grid polarizers, also called free-standing wire polarizers. These polarizers are fabricated usually with 5 or 10 µm diameter wire, the grid period is in the range of 20 µm–200 µm, and are available on aluminium, stainless steel, or invar frames as standard. Wire-grids are usually made of tungsten because it has the highest tensile strength among metals and excellent corrosion resistance [51]. Typical wire-grid polarizer is shown in Fig. 2.11.

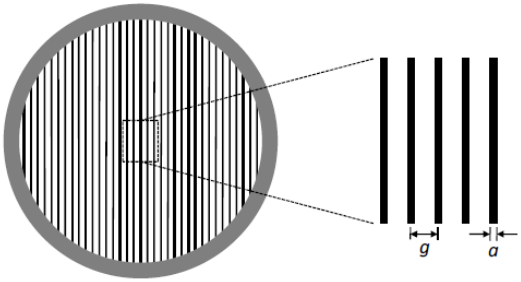

Figure 2.11: Wire-grid polarizer; g denotes the grid period and a denotes the wire diameter [51]

The mechanism of the polarization selectivity is simple. If the electric field is parallel to the wires, the electrons can move in the wires and in this case the wire grid acts as a metal surface reflecting almost all radiation polarized along the wires. If the electric field is perpendicular to the direction of wires, the electrons are localized in the wires and the wave passes through the polarizer.

2.4.3 Jones Formalism

A well-known technique to treat the evolution of the polarization state of the light is use of Jones formalism [109]. This formalism makes use of the perpendicular component of the electric field vector and provides a very powerful tool for the description of the light polarization characteristic and moreover is simple to use. However, it can be used only for description of totally polarized light. This Jones formalism is particularly used in Chapter 3 for transformation of measured lin-

early polarized transmittances into circularly polarized transmittances and also for description of the transmission Faraday isolation experiment.

The Jones vector representing complex quantities of an EM wave is transformed by 2×2 Jones matrix of an optical component into another Jones vector. In this case the complex quantities $A_x = a_x \exp(i\varphi_x)$, $A_y = a_y \exp(i\varphi_y)$ of a planar monochromatic wave are written in the form of the Jones vector, which describes polarization state of the wave:

$$\mathbf{J} = \begin{bmatrix} A_x \\ A_y \end{bmatrix}. \tag{2.49}$$

The total intensity of the wave can be expressed in the form:

$$I = \frac{|E|^2}{2\eta} = \frac{|A_x|^2 + |A_x|^2}{2\eta} = \frac{1}{2\eta}\mathbf{J}^+\mathbf{J}, \tag{2.50}$$

where η represents the impedance of the medium and $\mathbf{J}^+ = \begin{bmatrix} A_x^* A_y^* \end{bmatrix}$ is the Hermitian conjugated vector. Table 2.1 summarizes the Jones vectors of some basic polarization states.

Table 2.1: Jones vectors of basic polarization states

Linearly polarized light in $x-$ direction	$\mathbf{J}_x = [1, 0]^T$
Linearly polarized light in $y-$ direction	$\mathbf{J}_y = [0, 1]^T$
Linearly polarized light at angle α	$\mathbf{J}_{x'} = [\cos\alpha,\ \sin\alpha]^T$
Linearly orthogonally polarized light at angle α	$\mathbf{J}_{y'} = [-\sin\alpha,\ \cos\alpha]^T$
Right-circularly polarized light	$\mathbf{J}_R = \frac{1}{\sqrt{2}}[1, i]^T$
Left-circularly polarized light	$\mathbf{J}_L = \frac{1}{\sqrt{2}}[1, -i]^T$
Elliptically polarized light with ellipticity ε	$\mathbf{J} = [\cos\varepsilon, i\sin\varepsilon]^T$

Two polarization states $\mathbf{J}_1$, $\mathbf{J}_2$ are orthogonal, if:

$$\mathbf{J}_1^+ \mathbf{J}_2 = A_{1x}^* A_{2x} + A_{1y}^* A_{2y} = 0 \tag{2.51}$$

The examples of orthogonal Jones vectors are:

- linearly polarized waves in orthogonal directions
- left– and right–circularly polarized waves.

The transformation of the Jones vector by rotation of coordinate system can be expressed by matrix $\mathbf{R}(\alpha)$:

$$\mathbf{J'} = \underbrace{\begin{pmatrix} \cos\alpha & \sin\alpha \\ -\sin\alpha & \cos\alpha \end{pmatrix}}_{\mathbf{R}(\alpha)} \mathbf{J}. \tag{2.52}$$

When the polarized plane wave passes through some linear system, the polarization of wave is changed, because the system linearly transforms the components of complex amplitude in terms of linear combination:

$$\begin{aligned} A'_x &= T_{11} A_x + T_{12} A_y \\ A'_y &= T_{21} A_x + T_{22} A_y, \end{aligned} \tag{2.53}$$

where T_{11}, T_{12}, T_{21} and T_{22} are elements of a 2×2 matrix $\mathbf{T}$. If the input and output waves are described by Jones vectors $\mathbf{J}$ and $\mathbf{J'}$, respectively, it's possible to write:

$$\mathbf{J'} = \underbrace{\begin{pmatrix} T_{11} & T_{12} \\ T_{21} & T_{22} \end{pmatrix}}_{\mathbf{T}} \mathbf{J}, \tag{2.54}$$

where $\mathbf{T}$ represents the Jones matrix describing the polarization properties of the system. The response in a single layer sandwiched between two different isotropic half spaces (0) and (2), is characterized by Jones transmission and reflec-

tion matrices of the system:

$$\mathbf{T} = \begin{pmatrix} t_{xx}^{(02)} t_{xy}^{(02)} \\ t_{yx}^{(02)} t_{yy}^{(02)} \end{pmatrix} \qquad \text{and} \qquad \mathbf{R} = \begin{pmatrix} r_{xx}^{(02)} r_{xy}^{(02)} \\ r_{yx}^{(02)} r_{yy}^{(02)} \end{pmatrix}, \tag{2.55}$$

where the components $t_{ii}^{(02)}$ and $r_{ii}^{(02)}$ include multiple reflections inside the layer.

If we want to describe the optical system containing N components, we use the multiplication of **T** matrices and the resulting Jones matrix will be in the form:

$$\mathbf{T} = \mathbf{T}_N \cdot \mathbf{T}_{N-1} \cdot \ldots \cdot \mathbf{T}_2 \cdot \mathbf{T}_1, \tag{2.56}$$

where $\mathbf{T}_i$, $i = 1, 2, \ldots, N$ represent Jones matrices of each component in the system. Therefore, as we can see, even complicated optical system can be simply described using this tool. Now, let's take a look on some basic components which can compose an optical system.

2.4.3.1 Jones matrices of basic polarization components

Linear polarizer in $x-$direction

$$\mathbf{T} = \begin{pmatrix} 1 & 0 \\ 0 & 0 \end{pmatrix} \tag{2.57}$$

The linear polarizer described by **T** matrix in (2.57) transforms the wave components (A_x, A_y) into the wave components $(A_x, 0)$, so the output wave is completely polarized in $x-$ direction.

Polarization rotator

$$\mathbf{T} = \begin{pmatrix} \cos\theta & -\sin\theta \\ \sin\theta & \cos\theta \end{pmatrix} \tag{2.58}$$

Polarization rotator rotates the plane of polarization by a angle θ and keeps the linear polarization.

2.5 Magneto-Optical Effects

The proposed NR isolator consists of a metal grating deposited on a magnetized substrate. It is therefore important to study the interaction of an incident polarized EM wave with a magnetized medium. In this section we will focus on magneto-optical effects upon reflection and also in the transmission since the well-known Faraday effect plays a key role in NR devices as well.

Magneto-optical (MO) effects are phenomena describing an interaction of radiation and a medium subjected to a magnetic field. For some magnetically ordered materials (ferromagnets, ferrites) they can be present even without influence of an external magnetic field. The description of MO effects is based on the consideration of the magnetic field influence on the material tensor of the medium. The anisotropy variation is a direct result or a consequence of a energy levels splitting, usually known as Zeeman effect [23]. It is well-known that left- and right-circularly polarized photons excite electronic transitions which, according to the law of angular momentum conservation, change the appropriate projection of the quantum system's angular momentum by $\Delta m = \pm 1$. The Zeeman effect causes a difference in the frequencies of the right- and left- transitions resulting in a difference in the polarizibility of the system for left- and right- circularly polarized wave. In general, all magnetooptical effects are consequences of the Zeeman effect.

If the tensor is symmetric, any presence of the magnetization in a medium reduces its symmetry to the uniaxial one. Taking as an example a ferromagnetic medium which is in demagnetized state at optical frequencies optically isotropic, now being magnetized in the direction of z-axis. The presence of magnetization reduces its symmetry to an uniaxial rotational symmetry around the z-axis and the permittivity tensor of this magnetized medium acquires the form:

$$\bar{\bar{\varepsilon}} = \varepsilon_0 \begin{pmatrix} \varepsilon_{xx} & 0 & 0 \\ 0 & \varepsilon_{xx} & 0 \\ 0 & 0 & \varepsilon_{zz} \end{pmatrix} + \varepsilon_0 \begin{pmatrix} 0 & ig & 0 \\ -ig & 0 & 0 \\ 0 & 0 & 0, \end{pmatrix} \tag{2.59}$$

where ε_0 is the permittivity of the vacuum, ε_{zz} the relative permittivity of the medium in demagnetized state, i.e when $M = 0$ and $g(\mathbf{M})$ is the gyroelectric constant, a linear function of $\mathbf{M}$. In a general case taking into account absorptions all tensor components are complex. The magneto-optical (Voigt) parameter for the permittivity tensor is then defined as follows:

$$Q = Q' - iQ'' = g/\varepsilon_{xx}, \tag{2.60}$$

and usually $|Q| \ll 1$.

Since the hexaferrites used in the THz range are usually characterized by a scalar form of ε and a tensorial form of $\bar{\bar{\mu}}$ (as will be more deeply described in the next Chapter 3), we have to introduce also the permeability tensor, analogously to (2.59). The $\bar{\bar{\mu}}$ tensor can be expressed as a sum of a symmetric and an antisymmetric tensors giving for the z-axis the following form:

$$\bar{\bar{\mu}} = \begin{pmatrix} \mu & 0 & 0 \\ 0 & \mu & 0 \\ 0 & 0 & \mu_0 \end{pmatrix} + \begin{pmatrix} 0 & i\kappa & 0 \\ -i\kappa & 0 & 0 \\ 0 & 0 & 0, \end{pmatrix} \tag{2.61}$$

where the components μ and κ are generally complex. The magneto-optical (Voigt) parameter for the permeability tensor is then defined as follows:

$$Q_m = Q'_m - iQ''_m = \kappa/\mu, \tag{2.62}$$

and usually $|Q_m| \ll 1$. For *bi-gyrotropic* MO medium both Q and Q_m are generally non-zero.

According to the interaction of EM radiation with a matter all magneto-optical effects can be divided into three main categories [113]:

- MO effects in reflection
- MO effects in transmission

- MO effects in absorption

Let's take a look at all these categories of MO effects more closely.

2.5.1 Normal Modes and Fresnel Equation

First we have to find a solution for normal modes of EM field. They are generally solutions of the Maxwell's equations (2.7) with a harmonic dependence on **k** and on the time, for **E** field as:

$$\mathbf{E} = \mathbf{E}_0 \exp\left[i\left(\omega t - \mathbf{k}\cdot\mathbf{r}\right)\right]. \tag{2.63}$$

From the Maxwell's equations we can derive the main wave equation for the **E** field:

$$-\nabla^2\mathbf{E} + \nabla\left(\nabla\cdot\mathbf{E}\right) = -\frac{1}{c^2}\frac{\partial^2\mathbf{D}}{\partial t^2} \tag{2.64}$$

and for the normal modes given by (2.63) this wave equation can be expressed as:

$$n^2\mathbf{E} - \mathbf{n}\left(\mathbf{n}\cdot\mathbf{E}\right) = \bar{\bar{\varepsilon}}\mathbf{E}, \tag{2.65}$$

where $\mathbf{n} = \left(\frac{c}{\omega}\right)\mathbf{k}$ represents the refraction vector. This eigenvalue problem has a non-trivial solution when the determinant of the coefficients vanishes:

$$\det\left|n^2\delta_{ij} - n_i n_j - \varepsilon_{ij}\left(\omega\right)\right| = 0. \tag{2.66}$$

Considering $\mathbf{k} = \boldsymbol{\imath}_x k_x + \boldsymbol{\imath}_y k_y + \boldsymbol{\imath}_z k_z$, Eq. (2.65) can be expressed via matrix multiplication as:

$$\begin{pmatrix} (k_y^2+k_z^2) & -k_x k_y & -k_x k_z \\ -k_y k_x & (k_z^2+k_x^2) & -k_y k_z \\ -k_z k_x & k_z k_y & (k_x^2+k_y^2) \end{pmatrix} \begin{pmatrix} E_x \\ E_y \\ E_z \end{pmatrix} = \frac{\omega^2}{c^2} \begin{pmatrix} \varepsilon_{xx} & \varepsilon_{xy} & \varepsilon_{xz} \\ \varepsilon_{yx} & \varepsilon_{yy} & \varepsilon_{yz} \\ \varepsilon_{zx} & \varepsilon_{zy} & \varepsilon_{zz} \end{pmatrix} \begin{pmatrix} E_x \\ E_y \\ E_z \end{pmatrix}. \tag{2.67}$$

The propagation vector can be expressed as $\mathbf{k} = \frac{\omega}{c}\left(\boldsymbol{\imath}_x\hat{n}_x + \boldsymbol{\imath}_y\hat{n}_y + \boldsymbol{\imath}_z\hat{n}_z\right)$ and (2.67) therefore takes the form:

$$\begin{pmatrix} (\hat{n}_y^2 + \hat{n}_z^2) - \varepsilon_{xx} & -\hat{n}_x\hat{n}_y - \varepsilon_{xy} & -\hat{n}_x\hat{n}_z - \varepsilon_{xz} \\ -\hat{n}_y\hat{n}_x - \varepsilon_{yx} & (\hat{n}_z^2 + \hat{n}_x^2) - \varepsilon_{yy} & -\hat{n}_y\hat{n}_z - \varepsilon_{yz} \\ -\hat{n}_z\hat{n}_x - \varepsilon_{zx} & \hat{n}_z\hat{n}_y - \varepsilon_{zy} & (\hat{n}_x^2 + \hat{n}_y^2) - \varepsilon_{zz} \end{pmatrix} \begin{pmatrix} E_{0x} \\ E_{0y} \\ E_{0z} \end{pmatrix} = 0. \quad (2.68)$$

Equation (2.66) is called the Fresnel equation and defines the refraction vectors $\mathbf{n} = \mathbf{n}(\omega)$ of the normal modes. Substituting of its solution into Eq. (2.65) one can obtain the corresponding eigenvectors of each mode. In a general case the modes are elliptically polarized. In a gyrotropic medium ($g \neq 0$ and/or $\kappa \neq 0$) the refraction vector depends on the tracing direction of the ellipse. This right-left anisotropy ($n_+ \neq n_-$) is called the gyrotropy of the medium.

2.5.2 Magneto-Optical Effects in Reflection

These MO effects occur when EM radiation is reflected from a magnetized medium. They are all known as *Kerr effects* and can be divided into three groups according a mutual orientation of **M**, **k** and the sample surface: Polar, Longitudinal and Transversal, as displayed in Fig. 2.12.

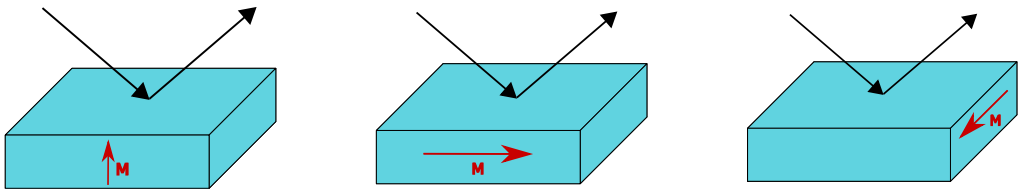

(a) Polar (b) Longitudinal (c) Transversal

Figure 2.12: Three configurations of MO Kerr effects

In the polar and longitudinal configurations the gyrotropy of the material causes a difference in optical indices $\hat{n}$ for left- and right-circularly polarized light. This difference creates an amplitude or a phase shift of these two modes forming the incident polarization. The magnetization **M** has in these two configurations

a non-zero component along **k** which causes an appearance of ellipticity in the reflected light and, as a consequence, the polarization plane will be rotated. The polar Kerr effect has nowadays a great importance for optical data storage, since it creates bases for reading information from MO disks. In the transverse configuration, for a purely p-polarized EM wave, the magnetization vector is oriented perpendicularly to the plane of incidence of the EM wave and this MO Kerr effect causes an amplitude or a phase change of the reflected light, whereas the polarization stays unchanged. This effect is odd in magnetization and is widely used in magnetic investigations, for example for observations of magnetic domains at the surface of a magnetized sample. It is also often used for designing of nonreciprocal devices [80, 114, 115].

The reflection coefficients for the reflected elliptically-polarized EM wave $(\mathbf{E}_r)$ can be calculated with using of the electric field $\mathbf{E}_i$ of the incident wave and boundary conditions at the interface:

$$\begin{bmatrix} E_r^s \\ E_r^p \end{bmatrix} = \underbrace{\begin{pmatrix} r_{ss} & r_{ps} \\ r_{sp} & r_{pp} \end{pmatrix}}_{\mathbf{R}} \begin{bmatrix} E_i^s \\ E_i^p \end{bmatrix}, \tag{2.69}$$

where the reflection matrix **R** describes the total optical response of the reflecting system. The Kerr rotation $\Theta_{s,p}$ and ellipticity $\varepsilon_{s,p}$ for s $(TE - \text{transverse electric})$ and p $(TM - \text{transverse magnetic})$ polarizations can be defined with use of the reflection coefficients:

$$\Theta_s + i\varepsilon_s = \frac{r_{sp}}{r_{ss}}, \quad \Theta_p + i\varepsilon_p = -\frac{r_{ps}}{r_{pp}}. \tag{2.70}$$

For transverse Kerr effect $r_{ps} = r_{sp} = 0$.

2.5.2.1 Transverse Kerr Effect

Because the transverse configuration is relevant for the proposed isolator design, in the following paragraphs we will take a look at the transverse MO Kerr effect

(TMOKE) more in detail and formulate the strength of this effect on an ordinary plain surface.

We consider first a TM-polarized plane wave (electric field vector **E** present in the plane of incidence, magnetic field vector **H** perpendicular to the plane of incidence) incident at angle ϕ_0 at an interface between non-magnetic (1) and transversely magnetized (2) media (as displayed in Fig. 2.13). We assume the permittivity of the magnetic substrate to be in tensorial form and permeability equal to 1.

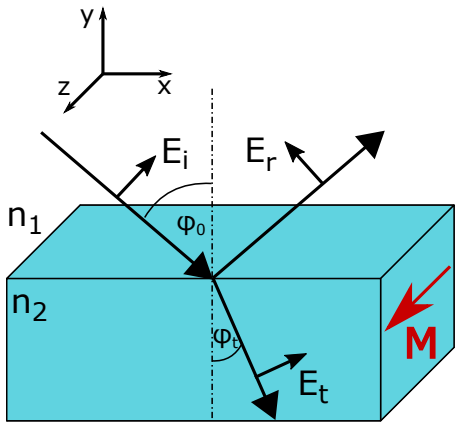

Figure 2.13: Transmission of p-polarized EM wave through an interface between non-magnetic (1) and transversely magnetized (2) media

Considering the $\bar{\bar{\varepsilon}}$ components, Eq. (2.68) can be simplified into:

$$\begin{pmatrix} \hat{n}_y^2 - \varepsilon & -\hat{n}_x\hat{n}_y - ig & 0 \\ -\hat{n}_y\hat{n}_x + ig & \hat{n}_x^2 - \varepsilon & 0 \\ 0 & 0 & \left(\hat{n}_x^2 + \hat{n}_y^2\right) - \varepsilon_0 \end{pmatrix} \begin{pmatrix} E_{0x} \\ E_{0y} \\ E_{0z} \end{pmatrix} = 0. \tag{2.71}$$

The solution of (2.71) when the determinant vanishes is the solution for normal

modes:

$$\left(\hat{n}_y^2-\varepsilon\right)\left(\hat{n}_x^2-\varepsilon\right)\left[\left(\hat{n}_x^2+\hat{n}_y^2\right)-\varepsilon_0\right]- \\ -\left(-\hat{n}_y\hat{n}_x+ig\right)\left(-\hat{n}_x\hat{n}_y-ig\right)\left[\left(\hat{n}_x^2+\hat{n}_y^2\right)-\varepsilon_0\right]=0 \tag{2.72a}$$

$$\hat{n}_x^2\hat{n}_x\varepsilon+\hat{n}_y^4\varepsilon-\hat{n}_y^2\varepsilon\varepsilon_0+\hat{n}_x^4\varepsilon+\hat{n}_x^2\hat{n}_y^2\varepsilon-\hat{n}_x^2\varepsilon\varepsilon_0- \\ -\hat{n}_x^2\varepsilon^2-\hat{n}_y^2\varepsilon^2+\hat{n}_x^2g^2-\hat{n}_y^2g^2+\varepsilon^2\varepsilon_0-g^2\varepsilon_0=0 \tag{2.72b}$$

$$\left[\hat{n}_x^2-\left(\varepsilon_0-\hat{n}_y^2\right)\right]\left[\hat{n}_x^2-\left(\varepsilon-\hat{n}_y^2\right)+\frac{g^2}{\varepsilon}\right]=0. \tag{2.72c}$$

Eq. (2.72c) has solutions for waves polarized in z-direction independent on the off-diagonal permittivity tensor element g and solutions for waves polarized parallel to the plane of incidence which are influenced by the term g^2. Propagation vectors in the plane of incidence are given by:

$$\mathbf{k}_{1,2}=\frac{\omega}{c}\left(\boldsymbol{\imath}_x\hat{n}_{x(1,2)}+\boldsymbol{\imath}_y\hat{n}_y\right)=\frac{\omega}{c}\left[\pm\boldsymbol{\imath}_x\sqrt{\left(\varepsilon-\hat{n}_y^2-\frac{g^2}{\varepsilon}\right)}+\boldsymbol{\imath}_y\hat{n}_y\right]. \tag{2.73}$$

Therefore, for transverse orientation the normal modes are p-polarized (TM), where:

$$H_x=0,\quad H_y=0,\quad H_z\neq 0 \tag{2.74}$$

with

$$\hat{n}_x^2=\left(\varepsilon-\hat{n}_y^2\right)-\frac{g^2}{\varepsilon}, \tag{2.75}$$

which can be simplified into:

$$n_p^2=\varepsilon\left(1-Q^2\right), \tag{2.76}$$

and s-polarized (TE), where:

$$H_x\neq 0,\quad H_y\neq 0,\quad H_z=0 \tag{2.77}$$

with

$$\hat{n}_x^2 = \left(\varepsilon_0 - \hat{n}_y^2\right), \tag{2.78}$$

which can be simplified into

$$n_s^2 = \varepsilon_0. \tag{2.79}$$

The electric field vectors of the incident and reflected waves are written in terms of the projections on the coordinate axis as:

$$\mathbf{E}_i = E_i \left(\cos\phi_0,\ \sin\phi_0,\ 0\right) \exp\left\{i\left[\omega t - (\omega/c)\,\mathbf{n}_i \cdot \mathbf{r}\right]\right\}, \tag{2.80}$$

$$\mathbf{E}_r = E_r \left(-\cos\phi_0,\ \sin\phi_0,\ 0\right) \exp\left\{i\left[\omega t - (\omega/c)\,\mathbf{n}_r \cdot \mathbf{r}\right]\right\}, \tag{2.81}$$

where:

$$\mathbf{n}_i = n_i \left(\sin\phi_0,\ -\cos\phi_0,\ 0\right), \tag{2.82}$$

$$\mathbf{n}_r = n_r \left(\sin\phi_0,\ \cos\phi_0,\ 0\right). \tag{2.83}$$

Besides the reflected wave there is obviously present also a transmitted wave traveling through the magnetized medium. If the incident wave is p-polarized, this transmitted wave is according Eq. (2.74) the p-polarized normal mode of this medium with the refraction vector:

$$\mathbf{n}_t = n_t \left(\sin\phi_t,\ -\cos\phi_t,\ 0\right), \tag{2.84}$$

where, with respect to the Eq. (2.76):

$$n_t = n_2\sqrt{(1-Q^2)} \approx n_2 \qquad \text{(linear approximation in - } Q\text{)} \tag{2.85}$$

and $\sin\phi_t$ can be obtained with use of the Snell's law:

$$\sin\phi_t = \frac{n_1}{n_2}\sin\phi_0, \quad \cos\phi_t = \sqrt{\left(1 - \left(\frac{n_1}{n_2}\right)^2 \sin^2\phi_0\right)}. \tag{2.86}$$

The electric field of the transmitted wave can be derived from the wave equation (2.71), where we take into account the linear approximation in magnetization, because $|Q| \ll 1$:

$$E_{tx} = E_t \cos\phi_t, \tag{2.87}$$

and the component E_{ty} is therefore in the form:

$$0 = \left(-n_{ty}n_{tx} + ig\right) E_{tx} + \left(n_{tx}^2 - \varepsilon\right) E_{ty} \tag{2.88a}$$

$$E_{ty} = \frac{n_{ty}n_{tx} - ig}{n_{tx}^2 - \varepsilon} E_{tx} \tag{2.88b}$$

$$E_{ty} = \frac{-n_t \sin\phi_t \cos^2\phi_t - ig\cos\phi_t}{n_t^2 \sin^2\phi_t - \varepsilon} E_{tx} \tag{2.88c}$$

$$E_{ty} = \left(\sin\phi_t + \frac{iQ}{\cos\phi_t}\right) E_t. \tag{2.88d}$$

Hence for electric field we can write

$$\mathbf{E}_t = E_t \left(\cos\phi_t,\ \sin\phi_t + iQ/\cos\phi_t,\ 0\right) \exp\left\{i\left[\omega t - (\omega/c)\,\mathbf{n}_t \cdot \mathbf{r}\right]\right\}. \tag{2.89}$$

This wave described in (2.89) is elliptically polarized in the plane of incidence, in addition to the ordinary transverse component present in the absence of magnetization, it contains a longitudinal component along the y-direction, shifted in phase and proportional to Q, therefore to the magnetization. It is this component in the field vector that leads to the magnetooptical effects and gives rise to non-reciprocity of the reflection and transmission coefficients of the light at the interface between a magnetic and non-magnetic medium.

The magnetic fields of the three waves can be derived from the Maxwell equation:

$$\nabla \times \mathbf{E} = -i\omega\mu_0 \mathbf{H}, \tag{2.90}$$

which in this case takes form:

$$c\varepsilon_0 \mathbf{n} \times \mathbf{E} = \mathbf{H}. \tag{2.91}$$

From this and Eqs. (2.80), (2.81) and (2.89) the magnetic fields acquire the form:

$$\mathbf{H}_{i,r,t} = (0, 0, H_{i,r,t}) \exp\{i\left[\omega t - (\omega/c)\,\mathbf{n}_{i,r,t} \cdot \mathbf{r}\right]\}, \tag{2.92}$$

where:

$$H_i = c\varepsilon_0 n_1 E_i, \quad H_r = c\varepsilon_0 n_1 E_r, \quad H_t = c\varepsilon_0 n_2 (1 + iQ\tan\phi_t) E_t. \tag{2.93}$$

The boundary conditions of Maxwell equations (2.8) indicate that the tangential components of **E** and **H**-fields are continuous:

$$E_{ix} + E_{rx} = E_{tx}, \quad H_{iz} + H_{rz} = H_{tz}. \tag{2.94}$$

Substitution of Eqs. (2.80), (2.81) and (2.89) into (2.94) we obtain:

$$\cos\phi_0\,(E_i - E_r) = E_t \cos\phi_t \tag{2.95a}$$

$$n_1\,(E_i + E_r) = n_2 E_t (1 + iQ\tan\phi_t). \tag{2.95b}$$

This set of equations can be worked out into:

$$\frac{\cos\phi_0\,(E_i - E_r)}{\cos\phi_t} = \frac{n_1\,(E_i + E_r)}{n_2(1 + iQ\tan\phi_t)}, \tag{2.96}$$

and from (2.96) we can determine the formulas for the reflection coefficient at the interface:

$$\hat{r}_p = \frac{E_r}{E_i} \tag{2.97a}$$

$$\frac{E_r}{E_i} = \frac{\rho^2\cos^2\phi_0 - \cos^2\phi_t + 2iQ\rho\cos\phi_0\sin\phi_t + \cancel{Q^2\rho^2\cos^2\phi_0\tan^2\phi_t}}{(\rho\cos\phi_0 + \cos\phi_t)^2 + \cancel{Q^2\rho^2\cos^2\phi_0\tan^2\phi_t}} \tag{2.97b}$$

where $\rho = n_2/n_1$. Using the linear approximation in Q, the magnetic and non-

magnetic contributions can be separated:

$$\hat{r}_p = \hat{r}_{p0} + i\delta\hat{r}_p = \hat{r}_p\left(1 + i\hat{\varsigma}_p\right) \tag{2.98}$$

where:

$$\hat{r}_{p0} = \frac{\rho\cos\phi_0 - \cos\phi_t}{\rho\cos\phi_0 + \cos\phi_t}, \quad \delta\hat{r}_p = \frac{2\cos\phi_0\sin\phi_0}{\left(\rho\cos\phi_0 + \cos\phi_t\right)^2}Q, \quad \hat{\varsigma}_p = \frac{\hat{r}_{p0}\sin\phi_0}{2\sqrt{\left(\rho^2 - \sin^2\phi_0\right)}}Q \tag{2.99}$$

One can see that the MO effect modifies the conventional Fresnel reflection coefficient $\hat{r}_{p0}$ at the interface between a non-magnetic and a magnetic medium. This change is linear in Q, it means also linear in magnetization. As a consequence, a switching of the direction of magnetization changes the sign of $\delta\hat{r}_p$. The relative change in the reflected intensity can be therefore expressed as:

$$\Delta_p = \frac{(I - I_0)}{I_0} = 2\Im\left(\hat{\varsigma}_p\right), \tag{2.100}$$

where I and I_0 represent the intensity of light after reflection from a magnetized and a non-magnetized medium, respectively, and $\Im$ denotes the imaginary part of a complex number. Equation (2.100) leads to another important conclusion. If Q is purely real, then $\Im\left(\hat{\varsigma}_p\right) = 0$ and thus no change in the reflected intensity appears. Therefore, in a case when the magnetic medium has negligible losses, the MO Kerr effect is not apparent.

Until now we have considered the incident wave to be TM-polarized. If the wave is TE-polarized, the electric field vectors of the incident and reflected wave become:

$$\mathbf{E}_i = E_i\,(0, 0, 1)\exp\left\{i\left[\omega t - (\omega/c)\,\mathbf{n}_i\cdot\mathbf{r}\right]\right\} \tag{2.101a}$$

$$\mathbf{E}_r = E_r\,(0, 0, 1)\exp\left\{i\left[\omega t - (\omega/c)\,\mathbf{n}_r\cdot\mathbf{r}\right]\right\}, \tag{2.101b}$$

where $\mathbf{n}_i$ is given by (2.82) and $\mathbf{n}_r$ by (2.83). The electric field vector of the transmitted wave propagating through the magnetized medium can be found from

the wave equation (2.65) and takes the form:

$$\mathbf{E}_t = E_t\,(0,0,1)\exp\{i\,[\omega t - (\omega/c)\,\mathbf{n}_t\cdot\mathbf{r}]\}, \tag{2.102}$$

where $\mathbf{n}_t$ is given by (2.84). We can therefore conclude, that when the MO media is characterized by a permittivity tensor, the transmitted and reflected waves are purely TE-polarized and the presence of the magnetization, in a linear approximation in Q has no influence on the TE-polarized light. The corresponding reflection coefficient is therefore equal to the conventional Fresnel coefficient.

This situation however changes when gyrotropic effects arising from the permeability tensor (Q_m) must be taken into account, which is exactly the case of hexaferrites, as will be shown in detail in Chapter 3.

From the Heaviside duality (2.29) it is apparent, that in order to obtain the TMOKE effect for $\bar{\bar{\mu}}$ tensor, we have to consider a TE-polarized EM wave (electric field vector **E** perpendicular to the plane of incidence, magnetic field vector **H** in the plane of incidence) incident at angle ϕ_0 at an interface between non-magnetic (1) and transversely magnetized (2) media (as displayed in Fig. 2.14). We therefore assume the permittivity of the magnetic substrate to be equal to 1

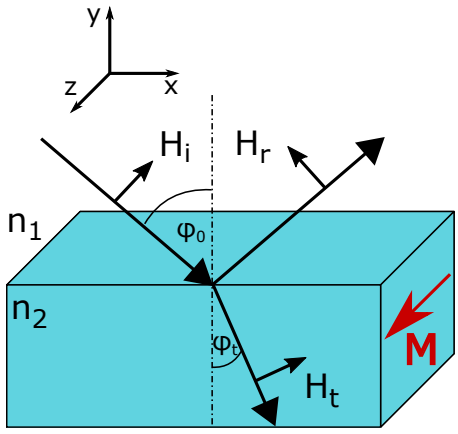

Figure 2.14: Transmission of s-polarized EM wave through an interface between non-magnetic (1) and transversely magnetized (2) media

and permeability to be in tensorial form (2.61). Here the solution for the normal

modes gives p-polarized (TM) modes, where:

$$H_x = 0, \quad H_y = 0, \quad H_z \neq 0 \tag{2.103}$$

with

$$n_p^2 = \mu_0, \tag{2.104}$$

and s-polarized (TE) modes, where:

$$H_x \neq 0, \quad H_y \neq 0, \quad H_z = 0 \tag{2.105}$$

with

$$n_s^2 = \mu \left(1 - Q_m^2\right). \tag{2.106}$$

The vectors of magnetic field of the incident ($\mathbf{H}_i$) and reflected ($\mathbf{H}_r$) waves can be written in terms of projections to the chosen coordinate system (Fig. 2.14):

$$\mathbf{H}_i = H_i \left(\cos\phi_0,\ \sin\phi_0,\ 0\right) \exp\left\{i\left[\omega t - (\omega/c)\,\mathbf{n}_i \cdot \mathbf{r}\right]\right\}, \tag{2.107}$$

$$\mathbf{H}_r = H_r \left(-\cos\phi_0,\ \sin\phi_0,\ 0\right) \exp\left\{i\left[\omega t - (\omega/c)\,\mathbf{n}_r \cdot \mathbf{r}\right]\right\}, \tag{2.108}$$

where $\mathbf{n}_i$ is given by (2.82) and $\mathbf{n}_r$ by (2.83). The incident s-polarized wave on the gyrotropic medium excites the propagating transverse normal mode with the refraction vector $\mathbf{n}_t$ given by (2.84). where, with respect to the Eq. 2.106:

$$n_t = n_2\sqrt{(1 - Q_m^2)} \approx n_2 \qquad \text{(linear approximation in - } Q_m) \tag{2.109}$$

and $\sin\phi_t$ can be obtained with use of the Snell's law: $n_2 \sin\phi_t = n_1 \sin\phi_0$. With use of the wave equation (2.65) for $\mathbf{H}$ field we can express the magnetic field vector of this propagating mode:

$$\mathbf{H}_t = H_t \left(\cos\phi_t,\ \sin\phi_t + iQ_m/\cos\phi_t,\ 0\right) \exp\left\{i\left[\omega t - (\omega/c)\,\mathbf{n}_t \cdot \mathbf{r}\right]\right\}. \tag{2.110}$$

The electric fields of the three waves can be derived from the Maxwell equation:

$$\nabla \times \mathbf{H} = i\omega\varepsilon_0\mathbf{E}, \tag{2.111}$$

which in this case takes the form:

$$-c\mu_0\mathbf{n} \times \mathbf{H} = \mathbf{E}. \tag{2.112}$$

Considering Eqs. 2.107–2.110 the electric fields acquire the form:

$$\mathbf{E}_{i,r,t} = (0, 0, E_{i,r,t}) \exp\{i\left[\omega t - (\omega/c)\,\mathbf{n}_{i,r,t} \cdot \mathbf{r}\right]\}, \tag{2.113}$$

where:

$$E_i = -cn_1H_i, \quad E_r = -cn_1H_r, \quad E_t = -cn_2(1 + iQ_m \tan\phi_t)H_t. \tag{2.114}$$

The boundary conditions of Maxwell equations (2.8) indicate that the tangential components of **E** and **H**-fields are continuous:

$$H_{ix} + H_{rx} = H_{tx}, \quad E_{iz} + E_{rz} = E_{tz}. \tag{2.115}$$

Analogously to the previous case with TM polarization, substitution of Eqs. (2.107), (2.108) and (2.110) into (2.115) lead to determination of the formulas for the reflection coefficient at the interface for s-polarized wave in the form:

$$\hat{r}_s = \frac{E_r^s}{E_i^s} \tag{2.116a}$$

$$\frac{E_r^s}{E_i^s} = \frac{\zeta^2\cos^2\phi_0 - \cos^2\phi_t + 2iQ_m\zeta\cos\phi_0\sin\phi_t + \cancel{Q_m^2\zeta^2\cos^2\phi_0\tan^2\phi_t}}{\left(\zeta\cos\phi_0 + \cos\phi_t\right)^2 + \cancel{Q_m^2\zeta^2\cos^2\phi_0\tan^2\phi_t}} \tag{2.116b}$$

where $\zeta = n_1/n_2$. Using the linear approximation in Q_m, the magnetic and non-

magnetic contributions can be separated:

$$\hat{r}_s = \hat{r}_{s0} + i\delta\hat{r}_s = \hat{r}_s\left(1 + i\hat{\varsigma}_s\right) \tag{2.117}$$

where:

$$\hat{r}_{s0} = \frac{\zeta\cos\phi_0 - \cos\phi_t}{\zeta\cos\phi_0 + \cos\phi_t},\ \delta\hat{r}_s = \frac{2\zeta\cos\phi_0\sin\phi_t}{\left(\zeta\cos\phi_0 + \cos\phi_t\right)^2}Q_m,\ \hat{\varsigma}_s = \frac{\hat{r}_{s0}\sin\phi_0}{2\sqrt{\left(\zeta^2 - \sin^2\phi_0\right)}}Q_m \tag{2.118}$$

One can again see that the MO effect modifies the conventional Fresnel reflection coefficient $\hat{r}_{s0}$ at the interface between a non-magnetic and a magnetic medium, characterized by $\bar{\bar{\mu}}$. This change is linear in Q_m, it means also linear in magnetization. As a consequence, a switching of the direction of magnetization changes the sign of $\delta\hat{r}_s$, which gives rise to nonreciprocal effects.

Finally, the relative change of light intensity after the reflection from the interface is:

$$\Delta_s = \frac{(I - I_0)}{I_0} = 2\Im(\hat{\varsigma}_s), \tag{2.119}$$

where the I and I_0 are the light intensities after reflection from magnetized and non-magnetized substrate, respectively.

2.5.3 Magneto-Optical Effects in Transmission

The second category of MO effects describes the interaction of an EM wave propagating through a magnetized matter. Two basic configurations according the mutual orientation of $\mathbf{k}$ and $\mathbf{M}$ can be distinguished:

- Faraday geometry ($\mathbf{k} \parallel \mathbf{M}$)

- Voigt geometry ($\mathbf{k} \perp \mathbf{M}$)

2.5.3.1 Faraday Geometry

In the Faraday configuration EM light passes through a medium in parallel direction to its magnetization. The magnetization causes a splitting of energy levels and shifting of the original resonant frequency of an absorption line. From Kramers-Kronig relations follows that the splitting of the absorption coefficient is connected with the splitting of the dispersion curves of the refractive index. As a result these two polarizations propagate at different speeds due to different optical indices of refraction (hence, the Faraday effect is also sometimes called *magnetic circular birefringence* - MCB):

$$n_+ \neq n_- \tag{2.120}$$

The circular anisotropy of a magnetized medium is explained by the fact that the splitting of the energy levels of the ground and excited states by magnetic field creates energy inequality of quantum states with different eigenvalues of the angular momentum. Phenomenologically, the Faraday effect is explained by the fact that the refractive indices n_+, n_- in the case of an originally inactive medium, become different after placing the latter into a magnetic field. The mechanism for the Faraday effect in the case of ferrite materials is the magnetic-field induced Larmor precession motion of magnetic-dipole moments, as will be later explained in Chapter 3. The magnetic field creates a preferred direction for magnetic dipole precession, and one sense of circular polarization causes precession in this preferred direction while the other sense of polarization causes precession in the opposite direction. These materials are characterized by a tensorial permeability $\bar{\bar{\mu}}$ and scalar permittivity ε. Because the EM wave propagation through magnetized (hexagonal) ferrites is essential for the study of NR effects we will now take a look closely at the particular Faraday rotation in these materials.

Faraday rotation in ferrites Let us consider an infinite ferrite medium with a DC bias field given in z-direction by $\mathbf{H}_0 = H_0 \boldsymbol{\imath}_z$, where $\boldsymbol{\imath}_z$ represents the unit vector

in the z-axis direction, with a permeability tensor $\bar{\bar{\mu}}$ given by (2.61). Maxwell's equations for a source-free medium can be expressed as:

$$\nabla \times \mathbf{E} = -i\omega\bar{\bar{\mu}}\mathbf{H}, \qquad \nabla \times \mathbf{H} = i\omega\varepsilon\mathbf{E}, \qquad \nabla \cdot \mathbf{D} = 0, \qquad \nabla \cdot \mathbf{B} = 0. \quad (2.121)$$

We consider a plane wave propagating in the z-direction and hence the electric and magnetic field are in the following form:

$$\mathbf{E} = \mathbf{E}_0 \exp\left(-i\beta z\right) \quad (2.122a)$$

$$\mathbf{H} = \mathbf{H}_0 \exp\left(-i\beta z\right) \quad (2.122b)$$

Considering the $\bar{\bar{\mu}}$ components μ and κ and the curl equations in (2.121), the components of the **E** and **H** fields can be expressed as:

$$-i\beta E_x = -i\omega\left(-i\kappa H_x + \mu H_y\right) \quad (2.123a)$$

$$i\beta E_y = -i\omega\left(\mu H_x + i\kappa H_y\right) \quad (2.123b)$$

$$0 = -i\omega\mu_0 H_z \quad (2.123c)$$

$$-i\beta H_x = i\omega\varepsilon E_y \quad (2.123d)$$

$$i\beta H_y = i\omega\varepsilon E_x \quad (2.123e)$$

$$0 = i\omega\varepsilon E_z \quad (2.123f)$$

From Eqs. (2.123d) and (2.123e) we obtain relations between the transverse field components in the form:

$$Y = \frac{H_y}{E_x} = -\frac{H_x}{E_y} = \frac{\omega\varepsilon}{\beta}, \quad (2.124)$$

where Y represents the wave admittance. Now we use (2.124) for elimination of H_x and H_y components in (2.123a) and (2.123b) leading to the wave equation in

the form:

$$i\omega^2\varepsilon\kappa E_x + \left(\beta^2 - \omega^2\mu\varepsilon\right) E_y = 0 \tag{2.125a}$$

$$\left(\beta^2 - \omega^2\mu\varepsilon\right) E_x - i\omega^2\varepsilon\kappa E_y = 0 \tag{2.125b}$$

which has a nontrivial solution for E_x, E_y when its determinant vanishes, as was discussed in Section 2.5.1, and therefore:

$$\omega^4\varepsilon^2\kappa^2 - \left(\beta^2 - \omega^2\mu\varepsilon\right)^2 = 0 \tag{2.126}$$

leading to the expressions for two possible propagation constants in the form:

$$\beta_\pm = \omega\sqrt{\varepsilon\left(\mu \pm \kappa\right)}. \tag{2.127}$$

The fields **E** associated with both propagation constants can be found by substituting (2.127) into the wave equations (2.125a) or (2.125b). For β_+ we obtain:

$$E_y = -iE_x, \tag{2.128}$$

and the **E** field must therefore be in the form:

$$\mathbf{E}_+ = E_0\left(\boldsymbol{\imath}_x - i\boldsymbol{\imath}_y\right)\exp\left(-i\beta_+ z\right), \tag{2.129}$$

which represents a right-hand circularly polarized wave. The associated **H** field can be obtained by using (2.124) as:

$$\mathbf{H}_+ = E_0 Y_+\left(i\boldsymbol{\imath}_x + \boldsymbol{\imath}_y\right)\exp\left(-i\beta_+ z\right), \tag{2.130}$$

where Y_+ is the right-hand wave admittance:

$$Y_+ = \frac{\omega\varepsilon}{\beta_+} = \sqrt{\frac{\varepsilon}{\mu + \kappa}}. \tag{2.131}$$

The fields associated with β_- are obtained in a similar way and are left-hand circularly polarized:

$$\mathbf{E}_- = E_0 \left(\boldsymbol{\imath}_x + i\boldsymbol{\imath}_y\right) \exp\left(-i\beta_- z\right) \tag{2.132a}$$

$$\mathbf{H}_- = E_0 Y_- \left(-i\boldsymbol{\imath}_x + \boldsymbol{\imath}_y\right) \exp\left(-i\beta_- z\right), \tag{2.132b}$$

where Y_- is the left-hand wave admittance:

$$Y_- = \frac{\omega\varepsilon}{\beta_-} = \sqrt{\frac{\varepsilon}{\mu - \kappa}}. \tag{2.133}$$

We can therefore conclude that both circularly polarized waves are the normal modes of the $\boldsymbol{\imath}_z$- magnetized ferrite medium, and these waves propagate through the ferrite with different propagation constants. One can also see that for the right-hand circularly polarized wave the ferrite material is represented by an effective permeability $\hat{\mu}_+ = (\mu + \kappa)$ and for the left-hand circular polarization is represented by $\hat{\mu}_- = (\mu - \kappa)$. These effective permeabilities, or β_+, β_- are normal modes or eigenvalues of the system of wave equations (2.125a), (2.125b) and $\mathbf{E}_\pm$ are the associated eigenvectors.

Now we consider a linearly polarized electric field at $z = 0$, represented as the sum of both counter-rotating circularly polarized waves:

$$\mathbf{E}|_{z=0} = \boldsymbol{\imath}_x E_0 = \frac{E_0 \left(\boldsymbol{\imath}_x - i\boldsymbol{\imath}_y\right)}{2} + \frac{E_0 \left(\boldsymbol{\imath}_x + i\boldsymbol{\imath}_y\right)}{2}. \tag{2.134}$$

Due to the different propagation constants $\beta_+ \neq \beta_-$ both circularly polarized

waves propagate at different speeds, so the total field propagate as:

$$\mathbf{E} = \frac{E_0\left(\boldsymbol{\imath}_x - i\boldsymbol{\imath}_y\right)}{2}\exp\left(-i\beta_+ z\right) + \frac{E_0\left(\boldsymbol{\imath}_x + i\boldsymbol{\imath}_y\right)}{2}\exp\left(-i\beta_- z\right) \tag{2.135a}$$

$$= \frac{E_0}{2}\boldsymbol{\imath}_x\left[\exp\left(-i\beta_+ z\right) + \exp\left(-i\beta_- z\right)\right] - i\frac{E_0}{2}\boldsymbol{\imath}_x\left[\exp\left(-i\beta_+ z\right) - \exp\left(-i\beta_- z\right)\right] \tag{2.135b}$$

$$= E_0\left[\boldsymbol{\imath}_x\cos\left(\frac{\beta_+ - \beta_-}{2}\right)z - \boldsymbol{\imath}_y\cos\left(\frac{\beta_+ - \beta_-}{2}\right)z\right]\exp\left(-i\frac{(\beta_+ + \beta_-)}{2}z\right) \tag{2.135c}$$

Eq. (2.135) represents a linearly polarized wave whose polarization rotates as the wave propagates along the direction of the z-axis. At a given point along this axis a direction of polarization measured from the x-axis is given by:

$$\Theta_F = \tan^{-1}\frac{E_y}{E_x} = \tan^{-1}\left[-\tan\left(\frac{\beta_+ - \beta_-}{2}\right)z\right] = -\left(\frac{\beta_+ - \beta_-}{2}\right)z. \tag{2.136}$$

Considering $\beta_\pm = \left(\omega\hat{n}_\pm\right)/c$, the angle of rotation can be also expressed with use of the optical indices for two orthogonal polarizations ($\hat{n}_+$, $\hat{n}_-$):

$$\Theta_F = -\frac{\left(\hat{n}_+ - \hat{n}_-\right)\pi l}{\lambda}, \tag{2.137}$$

where l represents the length of the gyrotropic material and λ the wavelength of the EM wave in vacuum.

One can see that the resulting phase difference for left- and right-circularly polarized waves will cause a rotation of a polarization plane of any incident elliptically (or linearly) polarized EM wave by an angle Θ_F, commonly called *Faraday rotation*. A schematic representation of the Faraday effect is shown in Fig. 2.15.

For $\omega < \omega_0$, where ω_0 is the Larmor frequency of the ferrite, $\mu > 0$ and $\kappa > 0$ and $\mu > \kappa$. Then $\beta_+ > \beta_-$ and according Eq. (2.136), Θ_F becomes more negative with propagation along z. This means that the polarization plane rotates counterclockwise with respect to the $+z$ direction. Reversing the magnetic field changes sign of κ and the polarization plane will rotate clockwise. Therefore, a

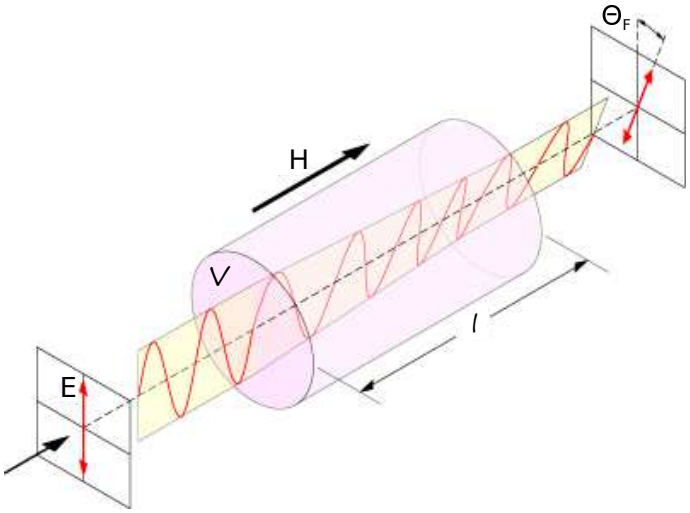

Figure 2.15: Schematic representation of the Faraday effect

wave traveling from $z = 0$ to $z = l$ and back to $z = 0$ undergoes a total polarization rotation of $2\Theta_F$, where Θ_F is obtained from (2.136) for $z = l$. We can therefore conclude from this, that the **Faraday rotation is a nonreciprocal effect**, since the the polarization angle is not zeroed, but doubled.

This a clear distinction from the effect of natural optical activity and is used in well-know Faraday isolator with combination of 2 polarizers, typically rotated by 45° with respect to each other, as displayed in Fig. 2.16 [78, 116]. Here a wave linearly-polarized by the first polarizer passes through the gyrotropic faraday rotator which is typically designed in order to rotate the wave polarization by 45°. Then the wave passes easily through the second polarizer turned by 45° as well. In the backward direction the wave is polarized by the polarizer 2 at 45° and rotated during transmission through the gyrotropic material by other 45° which makes the wave polarization to be perpendicular to the transmission channel of the first polarizer. Therefore the backward wave is completely isolated due to the crossed polarizations.

The Faraday rotation is in the simplest case proportional to the length l of the

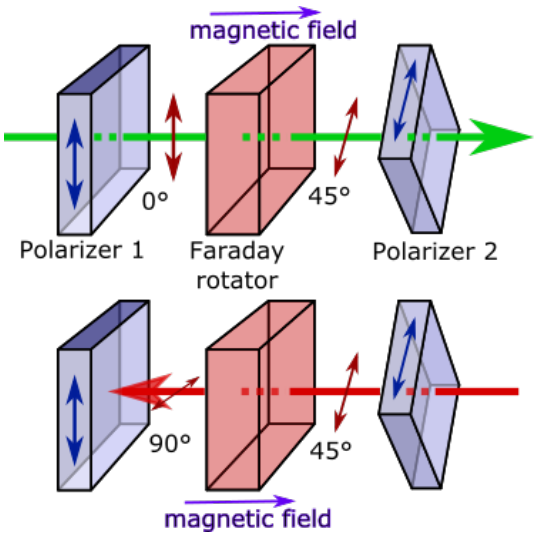

Figure 2.16: Schematic representation of the Faraday isolator

magnetized matter and strength of the total magnetic field **H**:

$$\Theta_F = VHl, \tag{2.138}$$

where V represents the Verdet constant, defined as the rotation per length unit per unit of field strength. This Verdet constant depends on material properties of the medium, the frequency of EM radiation and the temperature. As was already mentioned above, the sign of the angle Θ_F depends on the orientation of **H**.

2.5.3.2 Voigt Geometry

When an EM wave propagates through a magnetized medium in perpendicular direction to **M**, the configuration is called the Voigt effect (or Cotton-Moutton effect). This effect causes a change of ellipticity of an elliptically polarized light propagating through the magnetized medium. The polarization component parallel with the magnetization is not affected by the field, while two perpendicular components interact with it. As a result a difference in the refractive index appear $\left(\Delta n_V = \|n_{\|} - n_{\perp}\|\right)$ and therefore a *magnetic linear birefringence* (MLB) for the two mutually perpendicular components. Light linearly polarized at an an-

gle with respect to the magnetization becomes after the propagation through the medium elliptically polarized.

Analogously to the Faraday rotation in a ferrite medium we can now study a propagation of an EM wave in the transverse direction to the magnetization of a ferrite. Let us consider a case when an infinite ferrite region is magnetized in x-direction, transversely to the propagation direction. The permeability tensor for magnetization in x- direction is given by:

$$\bar{\bar{\mu}} = \begin{pmatrix} \mu & 0 & 0 \\ 0 & \mu & i\kappa \\ 0 & -i\kappa & \mu_0 \end{pmatrix}. \tag{2.139}$$

The **E** and **H** fields are in the form:

$$\mathbf{E} = \mathbf{E}_0 \exp\left(-i\beta z\right) \tag{2.140a}$$

$$\mathbf{H} = \mathbf{H}_0 \exp\left(-i\beta z\right) \tag{2.140b}$$

and considering the $\bar{\bar{\mu}}$ components μ and κ and the curl equations in (2.121), the components of the **E** and **H** fields can be expressed as:

$$-i\beta E_x = -i\omega\left(\mu H_y + i\kappa H_z\right) \tag{2.141a}$$

$$i\beta E_y = -i\omega\mu_0 H_x \tag{2.141b}$$

$$0 = -i\omega\left(-i\kappa H_y + \mu H_z\right) \tag{2.141c}$$

$$-i\beta H_x = i\omega\varepsilon E_y \tag{2.141d}$$

$$i\beta H_y = i\omega\varepsilon E_x \tag{2.141e}$$

$$0 = i\omega\varepsilon E_z \tag{2.141f}$$

From Eqs. (2.141d) and (2.141e) we obtain relations between the transverse field

components in the form:

$$Y = \frac{H_y}{E_x} = -\frac{H_x}{E_y} = \frac{\omega\varepsilon}{\beta}. \tag{2.142}$$

Now we use (2.142) for elimination of H_x and H_y components in (2.141a) and (2.141b) and (2.141c) in (2.141a) what leads to the wave equation in the form:

$$\beta^2 E_y = \omega^2 \mu_0 \varepsilon E_y \tag{2.143a}$$

$$\mu\left(\beta^2 - \omega^2\mu\varepsilon\right) E_x = -\omega^2\varepsilon\kappa^2 E_x. \tag{2.143b}$$

This set of equations gives two particular solutions. First solution gives:

$$\beta_o = \omega\sqrt{\mu_0\varepsilon}, \tag{2.144}$$

with $E_x = 0$. From (2.142) implies that $H_y = 0$ when $E_x = 0$ and from (2.141c) implies that $H_z = 0$ when $H_y = 0$ and, therefore, the **E** and **H** fields are then in the form:

$$\mathbf{E}_0 = \boldsymbol{\imath}_y E_0 \exp\left(-i\beta_o z\right) \tag{2.145a}$$

$$\mathbf{H}_0 = -\boldsymbol{\imath}_x E_0 Y_o \exp\left(-i\beta_o z\right), \tag{2.145b}$$

with the admittance:

$$Y_o = \frac{\omega\varepsilon}{\beta_o} = \sqrt{\frac{\varepsilon}{\mu_0}}. \tag{2.146}$$

This is a solution for an ordinary wave, since it is not affected by the magnetization of the ferrite. It is caused by the fact that the magnetic field components transverse to the magnetization direction are zero ($H_z = H_y = 0$). This wave hence propagates either in $+z$ or $-z$ with the same propagation constant, independently on H_0. The second solution of (2.143) gives:

$$\beta_e = \omega\sqrt{\mu_e\varepsilon}, \tag{2.147}$$

where μ_e is the effective permeability in the form:

$$\mu_e = \frac{\mu^2 - \kappa^2}{\mu} = \mu - \frac{\kappa^2}{\mu}, \tag{2.148}$$

signifying a reciprocal propagation, since $\mu_e \sim \kappa^2$. This is a solution for an extraordinary wave, since it is affected by the magnetization of the ferrite. The electric field of this wave is in the form:

$$\mathbf{E}_e = \boldsymbol{\imath}_x E_0 \exp(-i\beta_e z). \tag{2.149}$$

From (2.141d) it implies that $H_x = 0$ when $E_y = 0$. The **H** field components H_z and H_y can be found from Eqs. (2.141c) and (2.141e), respectively:

$$\mathbf{H}_e = E_0 Y_e \left(\boldsymbol{\imath}_y + \boldsymbol{\imath}_z \frac{i\kappa}{\mu}\right) \exp(-i\beta_e z), \tag{2.150}$$

where:

$$Y_e = \frac{\omega\varepsilon}{\beta_e} = \sqrt{\frac{\varepsilon}{\mu_e}}. \tag{2.151}$$

The proportionality to κ denotes, that the field component H_z is nonreciprocal.

These **E** and **H** fields creates a linearly polarized wave with a magnetic field component in the propagation direction. The extraordinary wave has **E** and **H** fields components perpendicular to the corresponding fields of the ordinary wave. Therefore, for the here presented case, the ordinary wave with the propagation constant β_o is polarized in y-direction, whereas the extraordinary wave with the propagation constant β_e is polarized in the x-direction. The propagation constants depend here on the polarization direction and this effect is called *birefringence*.

Both Faraday and Cotton-Mouton effects manifest themselves during propagation of an EM wave through a magnetized (hexagonal) ferrite medium and play therefore important roles in the magneto-optical material characterization presented in the Chapter 3.

2.5.4 Magneto-Optical Effects in Absorption

A difference in absorption coefficients for left- or right-circularly polarized EM wave or in two perpendicular linear polarizations is called the *magnetic circular dichroism* (MCD) or the *magnetic linear dichroism* (MLD), respectively. MCD changes an incident linear polarization into an elliptical one. The presence of the MLD causes a rotation of the elliptically polarized wave by an angle. These effects generally result in a change in the absorption spectrum of a magnetized sample giving information about the band structure of crystals.

Besides the above presented MO effects which will be active during the complete characterization of hexagonal ferrites in Chapter 3 and where TMOKE represents one of the key effect for the proposed isolating device, we also have to introduce the extraordinary transmission effect caused by a presence of a metal grating on the hexaferrite surface. This will be therefore described in the following sections.

2.6 Extraordinary Optical Transmission

Extraordinary optical transmission (EOT) is a phenomenon describing a transmission of EM wave through an otherwise opaque (typically metallic) layer which has been patterned by subwavelength motifs. This transmission is much stronger than one would expect by considering typical ray optics effects or a phenomena of a transmission through single apertures. Since the proposed isolating device consists of a metallic grating deposited on the hexaferrite surface, it is important to study the conditions for proper obtaining of the EOT effect at THz frequencies, and this creates the subject of this section.

The effect of EOT through sub-wavelength hole arrays was first described in 1998 by Ebbesen *et al.* [117] and since that time it has been studied intensively by many authors [83, 118, 119]. The important characteristics of the EOT is a sharp single peak (or a set of peaks) in the transmission spectrum and corresponding sharp dip in the reflection spectrum, as displayed in Fig. 2.17. The interesting

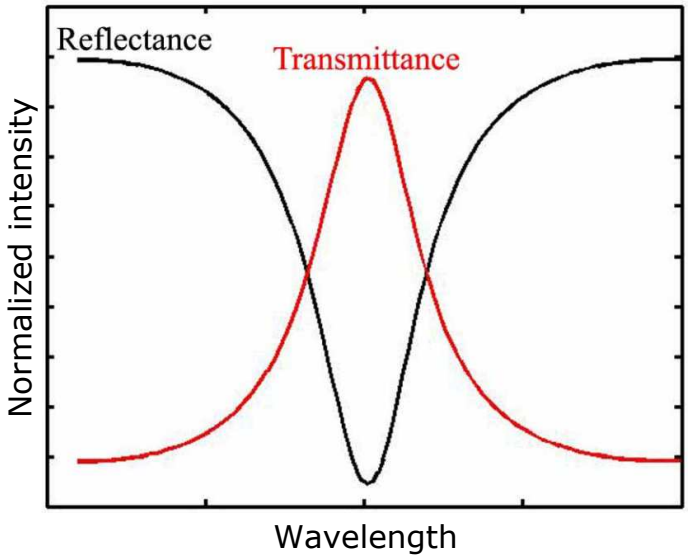

Figure 2.17: Zero-order transmittance (red) and reflectance (black) characterizing an EOT in a periodically structured metal

feature of this effect is that such a transmission through a periodically patterned layer can be as high as 100% which is much more than a transmission through a

single hole with a size corresponding to the sum of all the sub-wavelength holes sizes. This fact signifies that the perforated layer acts in the EOT more like an active member which boosts the transmission process than like a mirror. Due to intensive studies of a transmission through single apertures with various shapes [120, 121, 122, 123, 124, 125, 126] a large difference in the optical response of one-dimensional (1D) slits or two-dimensional (2D) rectangular patterns under *TE*- or *TM*-polarized illumination was found. The EOT effect started to be therefore linked with the excitation of surface plasmons (SPs) at corrugated metal surfaces and coupling of incident EM radiation into them. This coupled state including EM modes bound to the metal surface is known as surface plasmons polaritons (SPPs) [127, 128, 129]. Later studies of periodic arrays of 1D slits confirmed the fact, that the transmission resonances appear only for *TM*-polarized radiation (**H** field parallel to the slits), because only the *TM*-polarized wave can be coupled into the SPs [130]. In 1999, Porto *et al.* [131] showed that there exist two possible ways of enhanced transmission of *p*-polarized light through a periodic array of slits. The well-known coupling of EM wave to the surface modes (SPs) on both sides of the grating (Fig. 2.18a) was supplemented by a coupling of the incident EM wave with cavity resonances (also know as *Fabry-Perot* resonances) located inside the slits (Fig. 2.18b). These two possible channels of the EOT and their mutual mixing were studied in the following years in several publications with various gratings parameters [132, 133, 134, 135, 136] and it became apparent that the physics of the EOT is rich and complex [137].

After the description of the Fabry-Perot resonances for *p*-polarized wave, the similar case for *s*-polarized incident wave was studied theoretically by Schouten *et al.* [138]. Unlike the *TM* modes, these *TE*-polarized waveguide modes present a cut-off at $\lambda_c = 2a$ (a corresponds to the slit size). The resonances similar to those found for *p*-polarized light appear in the spectrum when $\lambda < \lambda_c$. The transmission process is therefore dominated by the existence of a cutoff wavelength for *TE*-mode. For $\lambda > \lambda_c$ and thick enough films, the transmission is in this case strongly attenuated due to the evanescent character of the EM fields in-

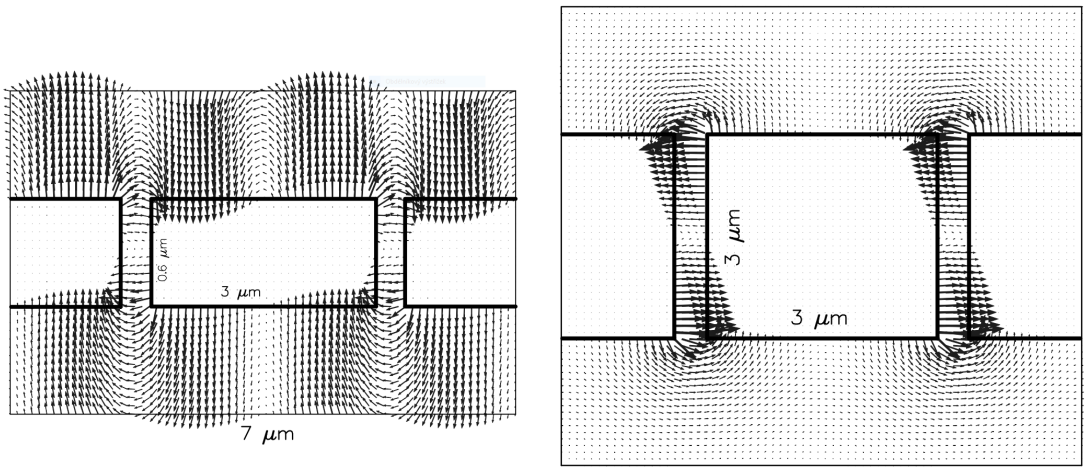

(a) Coupled SPPs

(b) Waveguide resonance

Figure 2.18: Two possible ways of transferring light from the upper surface to the lower one: by the excitation of coupled SPPs on both surfaces of the metallic grating or by the coupling of incident plane waves with waveguide resonances located in the slits. [131]

side the slit [119]. This signifies that the *TE* polarization is unattractive in the EOT phenomenon in the subwavelength regime for the 1D structures as was also confirmed by a rigorous numerical analysis performed by Fiala and Richter [139] who concluded that waveguide modes are responsible for energy transfer through the 1D slits only for *TM* polarization. Another deep study of polarization independent EOT in 1D gratings and its applications were presented by Course [140].

Focusing now on the THz frequencies, one of the first experimental studies of enhanced transmission properties of THz radiation pulses through 1D metallic gratings was done by Xing *et al.* [141] followed by demonstrations of EOT of THz radiation through gratings of subwavelength apertures structured in indium antimonide (InSb) semiconductor [142, 143].

Two-dimensional grating structures have been however studied more in detail since the first EOT demonstration given by Ebbesen *et al.* [117]. Already in the same year Ghaemi *et al.* [144] studied 2D periodic array of holes and showed that

the zero-order transmission spectra show well-defined maxima and minima of which the positions are determined by the geometry of the hole array. It was concluded that the maxima are the result of a resonant excitation of SPPs from both surfaces of the metallic film, which indicated an anomalously strong coupling between the two sides of the metal. Therefore, it meant that maximum transmission occurs for those frequencies for which the parallel component of the wave vector of a SPP is equal to a wave vector of the 2D reciprocal lattice associated with the geometry of the array. In a mathematical expression it means that the transmission maxima satisfied the following condition:

$$\mathbf{k}_{SPP} = \mathbf{k}_x \pm i\mathbf{G}_x \pm j\mathbf{G}_z, \tag{2.152}$$

where $\mathbf{k}_{SPP}$ is the wave vector of the SPP, $\mathbf{k}_x$ represents the parallel component of the wave vector of the incident wave and $\mathbf{G}_x$, $\mathbf{G}_z$ are the reciprocal lattice vectors for the square lattice where $|\mathbf{G}_x| = |\mathbf{G}_z| = 2\pi/\Lambda$, Λ stands for the lattice period and i, $j \in \mathbb{Z}$. Eq. 2.152 is called the *resonance condition* and relates also the spectral positions of the minima and maxima and the angle of incidence of the EM wave. Moreover, the absence of an enhanced transmission in hole arrays fabricated in Germanium films points to the importance of the metallic film. The confirmation of the fact the EOT effect at periodic array of holes is caused by excitation of SPPs at the metallic film interfaces was also later presented by Barnes *et al.* [145] and Lalanne *et al.* [146]. In summary, we can classify two different approaches responsible for the EOT as their effect is dominant under little different conditions. In the case when $\lambda \approx \Lambda$, in other words, when wavelength of the incident EM wave is comparable to the periodicity of the structure, it is believed, that the SPPs are mainly responsible for the EOT. In the other case when $\lambda \ll \Lambda$, the resonances result mostly from coupling between guided and grating modes given with the Fabry-Perot resonance condition [147]. A complex description of different types of resonances, changing their dominance and their mutual coupling by varying the thickness of the metallic layer was presented by Roszkiewicz *et al.* [148]. It

was therefore proven that by proper structuring the metal surface one can control the EOT phenomena source.

2.6.1 Surface Plasmon Polaritons

Surface plasmon polaritons (SPPs) are electromagnetic waves propagating at an interface between a dielectric and a conductor, typically a metal. They are evanescently confined in the perpendicular direction to the interface and arise by coupling of the EM wave represented by free photons to oscillations of the conductor's electron plasma (free electrons) [127]. The term *surface plasmon polariton* thus explains the hybrid coupled state of the charge motion in the metal (surface plasmons) and photons from EM waves in the air or dielectric.

As we could see in the previous paragraphs, a number of publications reported the SPPs as the dominant responsible member for effect of EOT (together with the FP resonances). We will now therefore focus more on the general properties of SPPs, the excitation and coupling mechanism and the possibility of their presence and use at THz frequencies.

Surface waves were for the first time mathematically described already at the turn of 19th and 20th century [149, 150] in the context of radio waves propagating along a surface of a conductor with finite conductivity. The propagation of radio waves on the Earth surface was studied already in 1907 by Zenneck [150]. In 1902 Wood [151] observed anomalous intensity drops in spectra of visible light reflecting from metallic gratings which were however not connected to the theoretical calculations before 1941 [152]. Ritchie in 1957 [153] predicted the existence of self-sustained collective excitations at metal surfaces during pioneering treatment of characteristic energy losses of fast electrons passing through thin metal films. The term *surface plasmons* was for the first time used by Stern and Ferrel [154] who used it for observed surface collective excitations. First unified description of SPPs was given by Kretschmann and Raether [155, 156] after successful coupling of visible light into surface waves via a coupling prism. In the

following decades, the plasmonics became to be a popular research area and surface plasmons found use in high number of applications especially thank to the development of nanotechnology and nanophotonics.

2.6.1.1 Drude model for dielecric constants of metals

In order to describe dielectric functions of metals one can use the well-known Drude model which was originally proposed by Drude in 1900 [157, 158] for description of the transport properties of electrons in materials, particularly in metals. During development of THz technologies it was also proved that the Drude model fits well for noble metals also at THz frequencies [159, 160].

For derivation of optical function of a metal we consider free valence electrons in the metal which are not bound to a particular nucleus. For these free electrons we can therefore express an equation of motion in the form:

$$m_e \frac{\mathrm{d}\mathbf{v}}{\mathrm{d}t} + m_e \gamma \mathbf{v} = -e\mathbf{E}, \tag{2.153}$$

where $\gamma = \frac{1}{\tau}$ is the decay constant, τ the electron relaxation time and $m_e = 9.109 \times 10^{-31}$ kg is the electron effective mass, e electron charge and $\mathbf{v}$ its speed. The current density can be defined as:

$$\mathbf{j} = -Ne\mathbf{v}, \tag{2.154}$$

where N represents the electron density and after a substitution into the Eq. (2.153) we obtain:

$$\frac{\mathrm{d}\mathbf{j}}{\mathrm{d}t} + \gamma \mathbf{j} = \left(\frac{Ne^2}{m_e}\right) \mathbf{E}. \tag{2.155}$$

Assuming a harmonic time-dependence of the applied electric field $\mathbf{E} = \mathbf{E}_0 \exp(i\omega t)$ and the conduction current density $\mathbf{j} = \mathbf{j}_0 \exp(i\omega t)$, the equation (2.155) takes the form:

$$i\omega \mathbf{j}_0 \exp(i\omega t) + \gamma \mathbf{j}_0 \exp(i\omega t) = \left(\frac{Ne^2}{m_e}\right) \mathbf{E}_0 \exp(i\omega t). \tag{2.156}$$

This equation can be multiplied by $\exp(-i\omega t)$ giving then a simplified form:

$$(\gamma + i\omega)\,\mathbf{j} = \left(\frac{Ne^2}{m_e}\right)\mathbf{E} \tag{2.157}$$

and therefore:

$$\mathbf{j} = \left(\frac{\sigma}{1 + i\frac{\omega}{\gamma}}\right)\mathbf{E} = \sigma_m \mathbf{E}, \tag{2.158}$$

where σ_m is the dynamic conductivity and $\sigma = (Ne^2)/(m_e\gamma)$ is the static conductivity, giving for static fields $(\omega = 0)$:

$$\mathbf{j} = \left(\frac{Ne^2}{m_e}\right)\mathbf{E} = \sigma\mathbf{E}, \tag{2.159}$$

The Eq. (2.158) denotes that at very low frequencies ($\omega \ll \gamma$) the dynamic conductivity acquires purely real values and hence the electrons are in a phase with the electric field, whereas with increasing frequency the dynamic conductivity becomes complex and the electrons react on the **E** field with a phase delay (kinetic inductance).

The wave equation for metals can be derived from the Maxwell's equations (2.7) considering $\mathbf{j} \neq 0$ and $\mathbf{P} = 0$:

$$\nabla^2\mathbf{E} = \frac{1}{c}\frac{\partial^2\mathbf{E}}{\partial t^2} + \frac{1}{c^2\varepsilon_0}\frac{\partial\mathbf{j}}{\partial t}. \tag{2.160}$$

Substituting (2.158) into (2.160) this wave equation takes the form:

$$\nabla^2\mathbf{E} = \frac{1}{c}\frac{\partial^2\mathbf{E}}{\partial t^2} + \frac{1}{c^2\varepsilon_0}\left(\frac{\sigma}{1 + i\frac{\omega}{\gamma}}\right)\frac{\partial\mathbf{E}}{\partial t}, \tag{2.161}$$

where the solution is in the form $\mathbf{E} = \mathbf{E}_0 \exp[-i(\mathbf{k}\cdot\mathbf{r} - \omega t)]$, where:

$$k^2 = \frac{\omega^2}{c^2} - i\left(\frac{\mu_0\sigma\omega}{1 + i\frac{\omega}{\gamma}}\right). \tag{2.162}$$

Then we can express the complex refractive index of a metal as:

$$\hat{n}^2 = \frac{c^2}{\omega^2}k^2 = 1 - i\left[\frac{\mu_0\sigma c^2}{\omega\left(1 + i\frac{\omega}{\gamma}\right)}\right] \tag{2.163}$$

$$\hat{n}^2 = 1 - \frac{\gamma\mu_0\sigma c^2}{\omega^2 - i\omega\gamma} \tag{2.164}$$

$$\hat{n}^2 = 1 - \frac{\omega_p^2}{\omega^2 - i\omega\gamma}, \tag{2.165}$$

where $\omega_p^2 = \mu_0\sigma\gamma c^2$ is the *plasma frequency*. For high frequencies where $(\omega \gg \gamma)$ the optical index can be simplified into:

$$\hat{n}^2 = 1 - \frac{\omega_p^2}{\omega^2} \tag{2.166}$$

and $\hat{n}$ becomes pure imaginary when $\omega < \omega_p$ thus this implies that the EM wave cannot propagate inside the metal and is in the direction perpendicular to the interface exponentially decayed. When $\omega > \omega_p$, $\hat{n}$ is real and this implies that metals are transparent to EM radiation only above the plasma frequency.

The plasma frequency is a frequency of the electron oscillation in a plasma caused by its displacing from a uniform background of ions. When an electron is moved out from its initial position by an element δx an electrostatic field will be built up as a result of a charge separation, in the form:

$$\mathbf{E} = \frac{\sigma_0}{\varepsilon_0} = \frac{Ne\,(\delta x)}{\varepsilon_0}. \tag{2.167}$$

The oscillation of the electron around its equilibrium position can be expressed as $\delta x = \delta x_0 \exp(i\omega_p t)$. Considering a force acting on the electron and combining it with Newton's second law we obtain an equation of motion for the electron with the effective mass m_e in the form:

$$m_e\frac{\mathrm{d}^2\,(\delta x)}{\mathrm{d}t^2} = (-e)\,\mathbf{E} \tag{2.168}$$

$$m_e\omega_p^2 = -\frac{Ne^2}{\varepsilon_0} \tag{2.169}$$

with the plasma frequency $\omega_p^2 = Ne^2/m_e\varepsilon_0$.

2.6.1.2 SPPs at a planar interface

Let's take a look first at the simplest geometry supporting the SPPs, which is a planar interface between a dielectric half space $(y > 0)$ characterized by a positive real part of the dielectric constant ε_2 and conducting half space $(y < 0)$ described by a strongly dispersive dielectric function $\varepsilon_1(\omega)$, as shown in Fig. 2.19.

Figure 2.19: Sketch of the geometry for SPPs propagation at a planar interface between a metal and a dielectric medium.

The fields **E** and **H** in media (1) and (2) can be for TM polarization described in the form:

$$\text{for } y > 0 \quad \mathbf{E}_2 = (E_{x2}, E_{y2}, 0)\exp\left[-i\left(k_{x2}x + k_{y2}y - \omega t\right)\right] \tag{2.170a}$$

$$\mathbf{H}_2 = (0, 0, H_{z2})\exp\left[-i\left(k_{x2}x + k_{y2}y - \omega t\right)\right] \tag{2.170b}$$

and:

$$\text{for } y < 0 \quad \mathbf{E}_1 = (E_{x1}, E_{y1}, 0)\exp\left[-i\left(k_{x1}x - k_{y1}y - \omega t\right)\right] \tag{2.171a}$$

$$\mathbf{H}_1 = (0, 0, H_{z1})\exp\left[-i\left(k_{x1}x - k_{y1}y - \omega t\right)\right]. \tag{2.171b}$$

Analogously also for TE polarization in the form:

$$\text{for } y > 0 \quad \mathbf{H}_2 = \left(H_{x2}, H_{y2}, 0\right) \exp\left[-i\left(k_{x2}x + k_{y2}y - \omega t\right)\right] \tag{2.172a}$$

$$\mathbf{E}_2 = \left(0, 0, E_{z2}\right) \exp\left[-i\left(k_{x2}x + k_{y2}y - \omega t\right)\right] \tag{2.172b}$$

and

$$\text{for } y < 0 \quad \mathbf{H}_1 = \left(H_{x1}, H_{y1}, 0\right) \exp\left[-i\left(k_{x1}x - k_{y1}y - \omega t\right)\right] \tag{2.173a}$$

$$\mathbf{E}_1 = \left(0, 0, E_{z1}\right) \exp\left[-i\left(k_{x1}x - k_{y1}y - \omega t\right)\right] \tag{2.173b}$$

The **E** and **H** fields must fulfill boundary conditions (2.8) at the interface:

$$TM: \quad E_{x1} = E_{x2}, \quad H_{z1} = H_{z2}, \quad \varepsilon_1 E_{y1} = \varepsilon_2 E_{y2} \tag{2.174a}$$

$$TE: \quad H_{x1} = H_{x2}, \quad E_{z1} = E_{z2}, \quad H_{y1} = H_{y2} \tag{2.174b}$$

With use of Maxwell's equations (2.7) we can for source-free dielectric medium write:

$$\nabla \times \mathbf{H}_i = \frac{\varepsilon_i \partial \mathbf{E}_i}{\partial t}, \quad \nabla \times \mathbf{E}_i = -\frac{\partial \mathbf{H}_i}{\partial t}, \tag{2.175}$$

where $i = 1, 2$ for metal and dielectric medium, respectively. Eq. (2.175) give for TM polarization:

$$k_{y1} H_{z1} = \omega \varepsilon_1 E_{x1} \tag{2.176a}$$

$$-k_{y2} H_{z2} = \omega \varepsilon_2 E_{x2} \tag{2.176b}$$

and with taking into account the boundary conditions (2.174) we obtain:

$$\frac{k_{y1}}{\varepsilon_1} + \frac{k_{y2}}{\varepsilon_2} = 0 \tag{2.177}$$

which is a condition for existence of surface plasmons. Because $\varepsilon_2 > 0$, Eq. (2.177) gives a requirement for existence of SPs in the form $\Re(\varepsilon_1) < 0$ which is for metals accomplished below their plasma frequency ω_p. This condition denotes that the

surface waves can exist only at interfaces between materials with opposite sign of real parts of the permittivity. Further we can for any EM wave write:

$$k^2 = \varepsilon_i \left(\frac{\omega}{c}\right)^2 = k_x^2 + k_{yi}^2 \tag{2.178}$$

and combining (2.177) and (2.178) we obtain:

$$\frac{\varepsilon_1^2}{\varepsilon_2^2} = \frac{k_x^2 - \varepsilon_1 \left(\frac{\omega}{c}\right)^2}{k_x^2 - \varepsilon_2 \left(\frac{\omega}{c}\right)^2} \tag{2.179a}$$

$$k_x^2 \left(\varepsilon_2^2 - \varepsilon_1^2\right) = \left(\frac{\omega}{c}\right)^2 \left(\varepsilon_1 \varepsilon_2^2 - \varepsilon_1^2 \varepsilon_2\right) \tag{2.179b}$$

$$\beta = k_x = \frac{\omega}{c} \sqrt{\frac{\varepsilon_1 \varepsilon_2}{\varepsilon_1 + \varepsilon_2}}. \tag{2.179c}$$

where (2.179c) is the *dispersion relation* of propagating SPPs at the planar interface [129]. The strongest localization and accompanying field enhancement at the interface is in the case when $\beta > nk_0$, where n is the refractive index of the dielectric. Analogously for TE polarization Eq. (2.175) give:

$$k_{y1} E_{z1} = -\omega H_{x1} \tag{2.180a}$$

$$k_{y2} E_{z2} = \omega H_{x2} \tag{2.180b}$$

a from the boundary conditions implies condition:

$$k_{y1} + k_{y2} = 0. \tag{2.181}$$

which doesn't have any real solution. Therefore, no real solution exists for the TE modes, signifying that SPPs at the planar interface can exist only for the p-polarization (TM modes).

2.6.1.3 Excitation of SPPs and coupling mechanisms

Fig. 2.20 shows a dispersion relation of a metal/dielectric system with a dielectric function of the metal described by Drude model when $\omega > \omega_p$:

$$\varepsilon_1(\omega) = 1 - \frac{\omega_p^2}{\omega^2}. \tag{2.182}$$

As we can see, excitations of SPPs corresponds to the part of dispersion curve below the light line of air. Therefore, if an EM wave hit this metal surface at an angle ϕ_0, the external radiation dispersion line will never intersect the SPPs line. In other words, the projection along the interface of the photons momentum $k_x = k \sin \phi_0$ to the surface normal will be always smaller than the propagation constant β of the SPPs. Hence, at perfectly flat surfaces the SPs are always *non-*

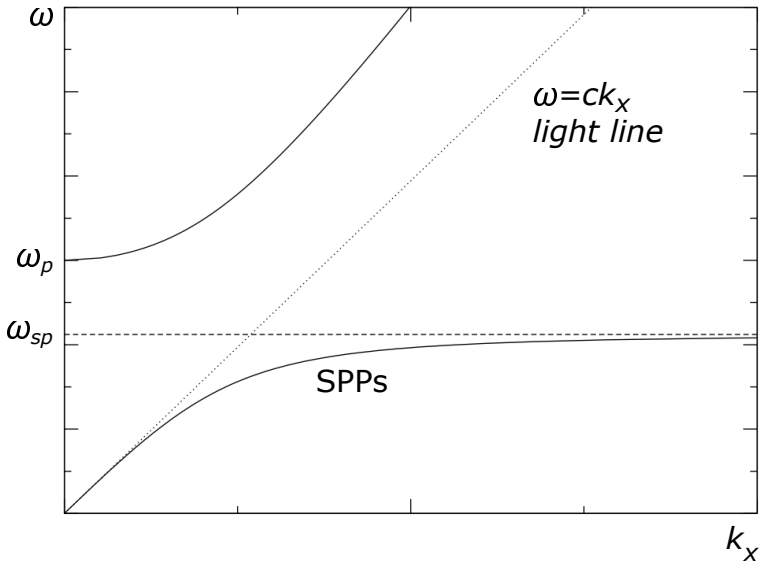

Figure 2.20: Dispersion relation of a system metal/dielectric with dielectric function of the metal described by Drude model. Upper line corresponds to the dispersion of light in the solid and the lower line to the SPPs.

radiative, meaning that they do not couple with an incident EM wave and it is necessary to find a suitable way for proper coupling. This is required for successful excitation of SPPs. Combination of Eqs. (2.179c) and (2.182) gives dispersion

relation for a metal described by Drude model in the form:

$$k_x = \frac{\omega}{c}\sqrt{\frac{\left(\omega^2 - \omega_p^2\right)\varepsilon_2}{\omega^2\left(1+\varepsilon_2\right) - \omega_p^2}}. \tag{2.183}$$

For small wave vectors at low frequencies, the propagation constant of SPPs is close to the light line and the waves extend over many wavelengths into the dielectric space. The SPPs in this range are known as *Sommerfeld-Zenneck waves* [161] acquiring the nature of a grazing-incidence light field [129] with:

$$k_x \approx \frac{\omega}{c}\sqrt{\varepsilon_2}. \tag{2.184}$$

For large wave vectors $k_x \to \infty$ we obtain $\Re(\varepsilon_1) \to -\varepsilon_2$ and therefore from the Drude metal permittivity description given by Eq. (2.182) it is possible to show that the SPPs approach the characteristic frequency of surface plasmons:

$$-\varepsilon_2 = 1 - \frac{\omega_p^2}{\omega^2} \tag{2.185a}$$

$$\frac{\omega_p^2}{\omega^2} = 1 + \varepsilon_2 \tag{2.185b}$$

$$\omega = \omega_{sp} = \frac{\omega_p}{\sqrt{1+\varepsilon_2}}. \tag{2.185c}$$

Due to the hybrid optical-electronic nature of SPPs, we can distinguish two main branches of excitation schemes: by *photon coupling* or by *electron coupling*. The electron coupling including methods of fast electron coupling [162, 163, 164], electron tunneling [165, 166] and hot electron coupling [167] are using electrons with specific energy for generation of bulk and surface plasmons. The well-used technique is a combination of the electron tunneling with the near-field scanning optical microscopy (NSOM) [168].

We are however primarily interested in techniques of coupling incident photons into the surface plasmons. There exist several methods for compensation of the momentum mismatch between SPPs and free-propagating photons

(phase-matching), e.g. excitation upon charged particle impact, highly-focused beam, near-field, end-fire or step-gap leakage coupling [129, 168]. The well-know Kretschmann [155] and Otto [169] configurations are examples of a prism coupling based on an increasing of optical index (permittivity) of a media from which the photons are coming. Thus the metal will have in this case an in-plane momentum $k_x = k\sqrt{\varepsilon}\sin\phi_0$ which is now sufficient for SPPs excitation at the metal-dielectric interface (as displayed in Fig. 2.21)

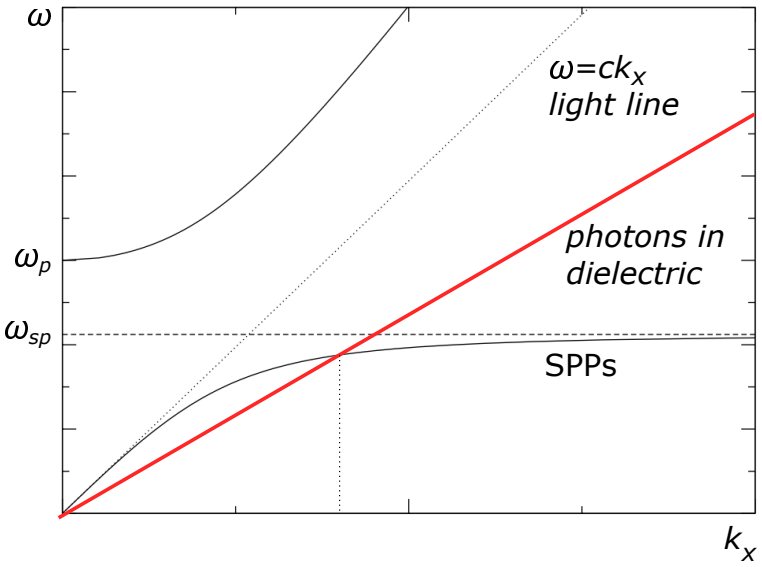

Figure 2.21: Prism (dielectric) provides a phase-matching technique. The excited propagation constants are within the prism light cone (red)

Another way how to overcome the mismatch between in-plane momentum of incident photons and SPPs' propagation constant β is by use of gratings on metal surfaces. In the case of a 1D grating with periodicity Λ, as shown in Fig. 2.22, the reciprocal vector $G = 2\pi/\Lambda$ gives the necessary momentum for excitation of SPPs. Therefore, the coupling is effective when the following condition is accomplished:

$$\beta = k\sin\phi_0 \pm nG, \tag{2.186}$$

where $n = (1, 2, 3\ldots)$. It corresponds to the multiplication of the dispersion curves by grating vectors as displayed in Fig. 2.23.

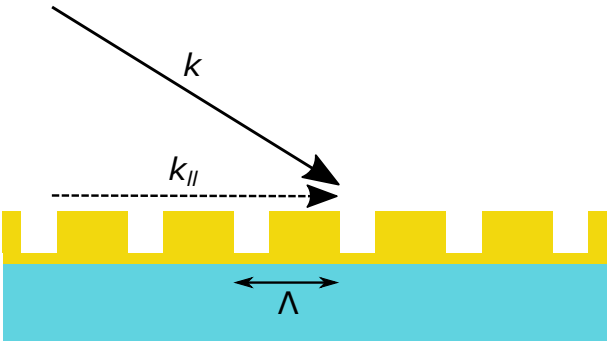

Figure 2.22: Coupling of light into the SPs using a grating mechanism

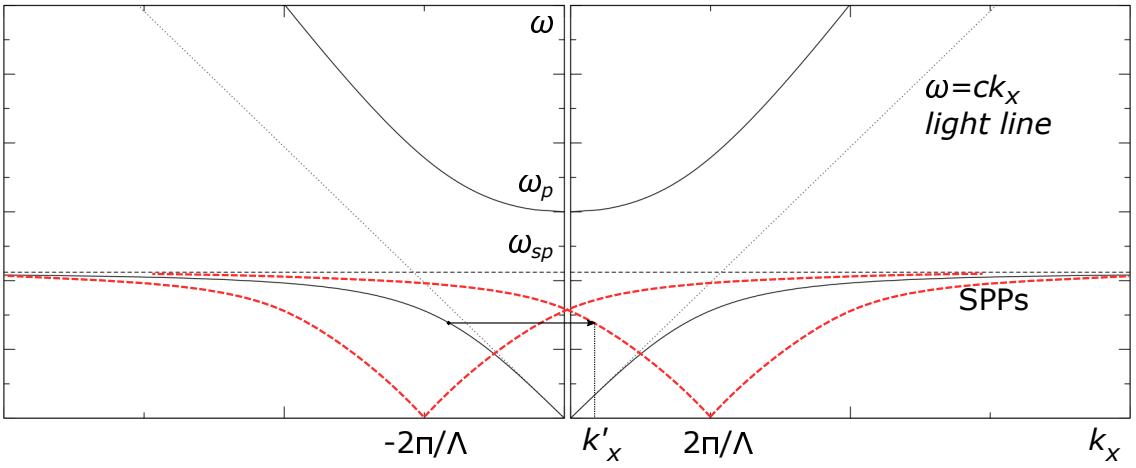

Figure 2.23: Phase-matching technique via a coupling grating on the surface of a metal

From the point of view of SPPs propagating along a surface modulated with a grating the SPPs can couple to light and become *radiative*. The same effect can be also obtained on metallic layers with a random surface roughness which will then represent an irregular grating. This mechanism of SPPs excitation via the metallic gratings explains the above described EOT effect through sub-wavelength periodic apertures (Section 2.6) both for 1D or 2D structures. The presence of SPPs is therefore denoted as a dip in a measured reflection spectrum or a peak in a transmission spectrum (Fig. 2.17).

2.6.2 Surface Plasmons Polaritons in THz Range

The confinement of EM field by SPPs to the interface between a metal and a dielectric is obtained in the range where the frequency of the EM wave is close to the intrinsic plasma frequency of the metal. Since most of the metals have this plasma frequency in the visible or ultraviolet range, the cardinal part of plasmonic applications is usually limited to these spectral bands. The most important metals for plasmonic structures like gold or silver are in the frequencies up to the visible range highly reflective and thus no EM wave can propagate through them. This means no **E**-field component parallel to the surface can exist. As is obvious from the dispersion relation (Fig. 2.20), the SPPs have in lower frequencies a nature of grazing-incidence light field and the decrease of the propagation constant ($\beta \approx nk_0$) means that the confinement of EM wave to the interface is not preserved anymore and the field localization disappears. This is caused by the fact that metals have in these low frequencies, particularly in THz, a large negative real part and a large negative imaginary part of permittivity ($\|\varepsilon\| \approx 10^5 - 10^6$), and hence they are represented by a *perfect electric conductor* (PEC) approximation of infinite conductivity. Generally, the existence of SPPs at a plain metal/dielectric interface is not supported in the THz range. One solution how to successfully excite the SPPs is the use of highly doped semiconductors, e.g. InSb or InAs which can have their plasma frequency in mid-infrared (MIR) or FIR range and therefore support the SPPs at lower frequencies [129, 142, 170].

Another solution was presented by Pendry *et al.* [82] and Garcia-Vidal *et al.* [83] who showed that it is possible to obtain bound EM surface waves even at low frequencies by periodically structuring the metal surface. Such a structured surface significantly slows down the group velocity of SPs and brings the frequency of SPs into the THz range. These SPPs-like surface waves have been named *spoof plasmons* or *designer plasmons* and can exist for PEC as well. The explanation lies in the fact, that a medium periodically structured by sub-wavelengths motifs optically behaves in the long wavelength limit as an effective medium which can

be described by an effective permittivity (and permeability) with the plasma frequency ω_p determined only by the structural parameters. Therefore by proper structuring of the metal surface it is possible to obtain highly confined surface waves due to the finite penetration of the field into the effective surface layer, as shown in Fig. 2.24a. In the case of 1D periodic structure the characteristic

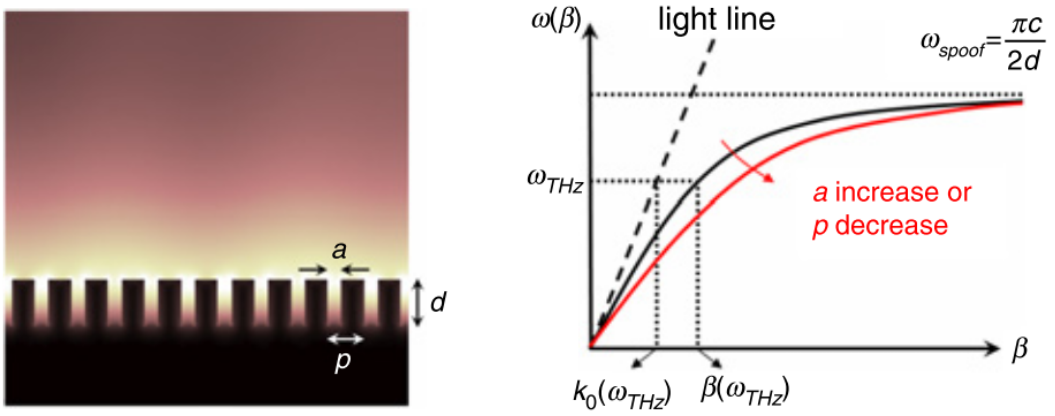

(a) 1D structured surface of PEC

(b) Dispersion diagram

Figure 2.24: 1D structured surface of PEC for spoof SPPs with a distribution of **E** field and corresponding schematic dispersion diagram for THz spoof SPPs [170].

frequency of SPs acquires the form [83]:

$$\omega_{sp} = \frac{\pi c}{2d}, \tag{2.187}$$

corresponding to

$$d = \frac{\lambda}{4}, \tag{2.188}$$

where d stands for the groove depth. Eq (2.187) corresponds to the standing wave along the depth of the grooves providing the phase accumulation during each roundtrip. Consequently, the accumulation of energy in the cavity for ω close to the asymptotic frequency ω_p leads to the small group velocity.

As is drawn in Fig. 2.24b, the dispersion curve of the spoof SPPs can be controlled via structural parameters in such a way that the required inequality $\beta \gg nk_o$ signifying confined SPPs at THz frequencies are obtained. Success-

ful confinement of THz spoof SPPs at different 1D periodic metallic structures was presented also by other authors [171, 172]. Another structure presented by Pendry included 2D square holes of a size a in the metal with a periodicity d (Fig. 2.25). Here the characteristic plasma frequency takes the form [82]:

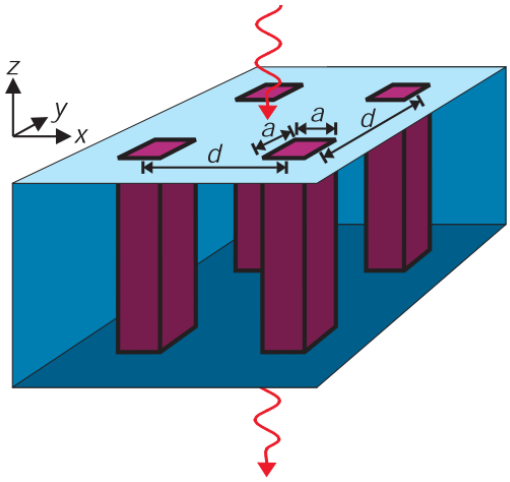

Figure 2.25: Model system for spoof SPPs excitation including $a \times a$ square holes with a periodicity d in a PEC [82].

$$\omega_p = \frac{\pi c}{a\sqrt{\varepsilon_h \mu_h}}, \tag{2.189}$$

where ε_h and μ_h represent the permittivity and permeability of a material filling the square holes, respectively. This frequency corresponds also to the cut-off frequency of a square metallic waveguide of a size a ($\lambda_n = 2a$). It means that all SPPs modes with frequencies higher than ω_{sp} will couple into the waveguide modes. Also here, the dispersion curve of the spoof SPPs can be controlled via the parameters of the 2D structure as shown also in other publications [87, 173, 174, 175].

2.6.3 Surface Plasmon Polaritons for *TE*-polarized Wave

In the Section 2.6.1.2 we saw that it is not possible to excite SPPs at ordinary planar metal/dielectric interface by s-polarized EM wave. It is caused by the fact

that there is no real solution of Eq. (2.181) for *TE* modes due to the different boundary conditions for *TE* and *TM* polarizations. The similar fact stays for the metallic surface patterned by 1D periodic structure. Hence, in order to be able to excite the SPPs with *TE*-polarized wave, some authors started to work with modified structures. Moreno *et al.* [176] showed that by adding of a thin dielectric layer on the metal interface patterned by 1D structure it is possible to create a surface wave that enables the EOT for the *TE*-polarized wave, however without the presence of SPPs. Similar effect was observed also by Chen *et al.* [177]. In 2012 Constant *et al.* [178] demonstrated successful excitation of SPPs

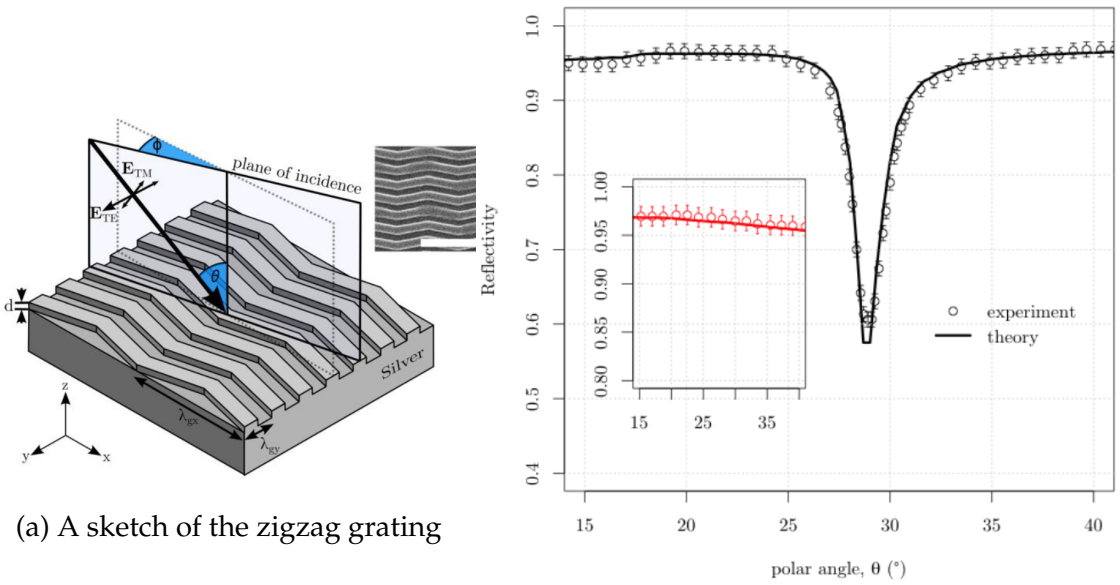

(a) A sketch of the zigzag grating

(b) Reflectivity

Figure 2.26: The coordinate system of a zig-zag grating. Inset: A scanning electron micrograph of a replicated zig-zag surface in a polymer. Specular reflectivity of TE (black) and TM (red) polarized light as a function of polar angle, θ, with a wavelength of 632.8 nm, $\phi = 0°$. Circles: recorded data with error bars of 1%, line: fitted numerical model [178].

for *TE*-polarized visible light on so called *zig-zag* silver grating. This structure, as shown in Fig. 2.26a, supports SPPs propagating in the diffraction plane only for *TE* polarization and for *TM* polarization the excitation of SPPs is forbidden by

the grating's broken-mirror symmetry (confirmed by the reflectivity spectrum in Fig. 2.26b).

The importance of introducing the second dimension of the grating for possible SPPs excitation with *TE*-polarized EM radiation was confirmed by Feng *et al.* [179] who presented pure *TE*-to-plasmon coupling with a designer plasmonic metamaterial as shown in Fig. 2.27. The *TE*-polarized plane wave is coming

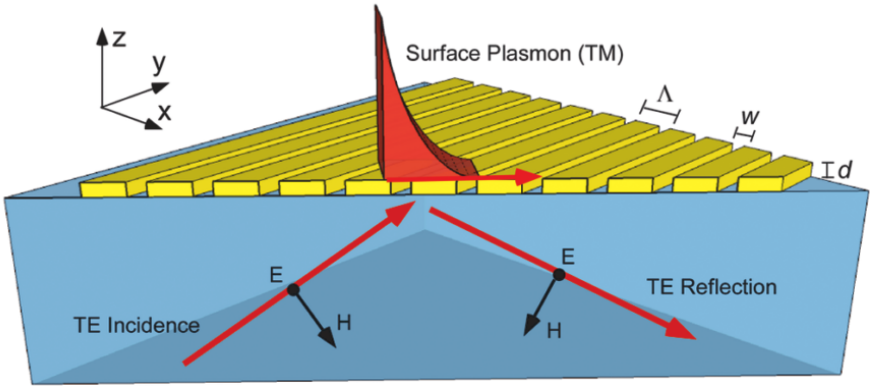

Figure 2.27: Schematic of enhanced pure TE-to-plasmon coupling with the designer plasmonic metamaterial as presented by Feng *et al.* [179].

from a glass substrate with the incident plane as the diagonal cross-section of the metamaterial slab and excites SPPs at the air/metamaterial interface. The FEM simulations show strong field confinement on the surface and exponentially decaying fields into the air, associated with the *TE* mode (Fig. 2.28). Although the polarization of the incident field is pure *TE*, the excited surface mode is almost entirely *TM*-polarized, as $\mathbf{E}_z$ and the magnetic field transverse to the direction of propagation $\mathbf{H}_\perp$ are strongly dominant. This tilting of 1D periodic structure with respect to the incident polarization plane corresponds to an artificial introduction of 2nd dimension of periodicity of the structure, similarly as was done by the zigzag grating in the previous example. In the recent years Yahiaoui *et al.* [94] and Bhattarai *et al.* [89] (Fig. 2.29) presented 2D plasmonic structures for operation at THz frequencies. These structures including circular-hole arrays and supporting excitation of spoof SPPs are insensitive to the polarization of an

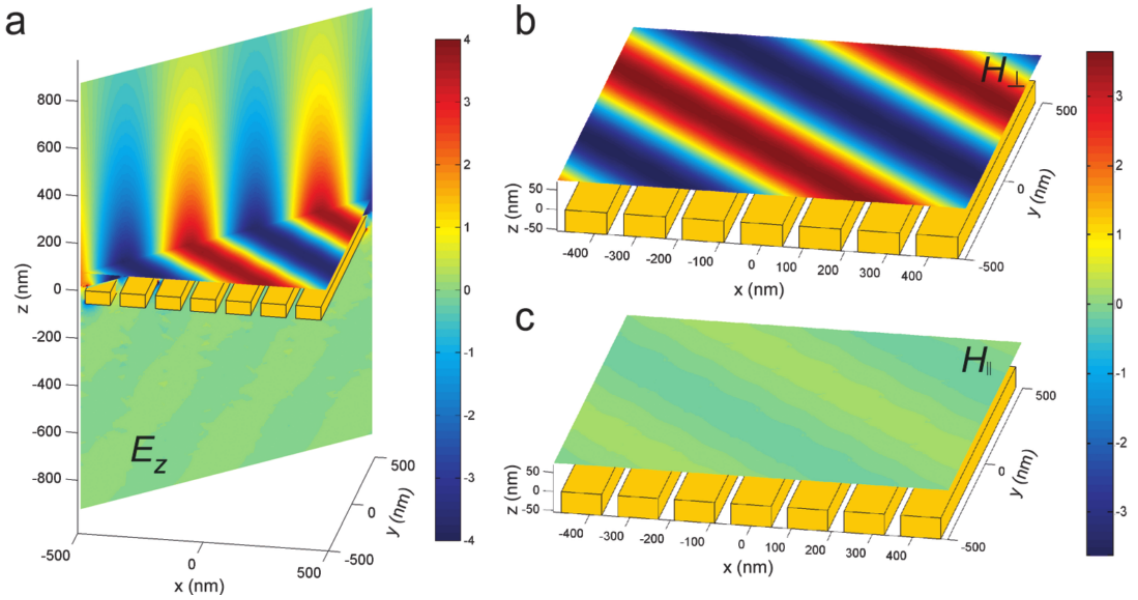

Figure 2.28: FEM simulations of the excited surface mode. (a) Field distributions of $\mathbf{E}_z$ in the diagonal cross-section and $x-y$ plane, respectively. (b) Field mapping of the in-plane magnetic field component transverse to k_{sp}, $\mathbf{H}_\perp$ (TM component). (c) Field mapping of the in-plane magnetic field component parallel to k_{sp}, $\mathbf{H}_\parallel$ (TE component), showing TM characteristics associated with designer SPPs. [179].

incident wave due to their rotational symmetry. The above presented examples confirm the possibility of excitation of spoof SPPs in THz range with incident purely *TE*-polarized EM radiation, as shown in Fig. 2.30.

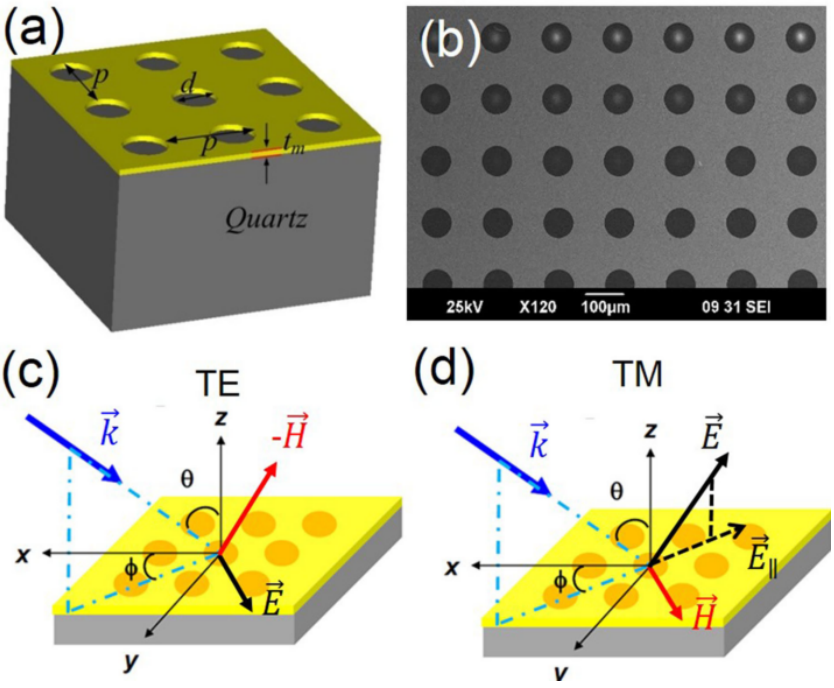

Figure 2.29: (a) Schematic layout and (b) SEM image of metallic hole-array which consists of perforated gold layer on a fused silica substrate. (c) and (d): Configurations of (c) *TE* wave and (d) *TM* wave, where θ and ϕ denote the polar and azimuthal angle for incident wave vector **k**, respectively [89].

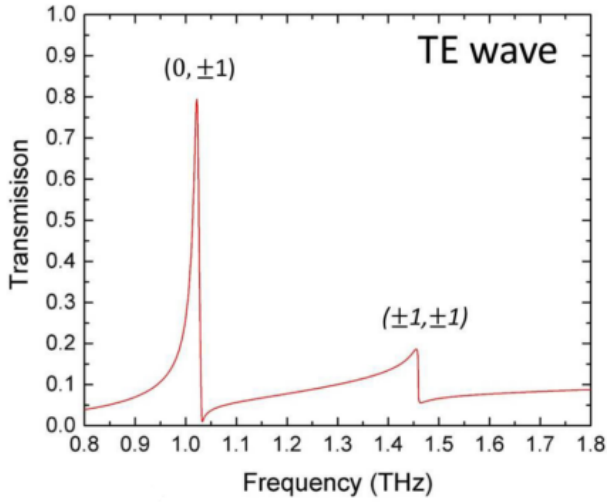

Figure 2.30: Transmission spectra for normally incident *TE* wave [89].

2.7 Conclusion of the Chapter

This chapter summarizes the theory used in the following chapters of the thesis. In the first part we presented properties of THz radiation and Time-domain spectroscopy. This was followed by description of the constitutive relations and material properties important for all the research. Light polarization and Jones calculus required for description of polarization evolution within the measurement system. Magneto-optical effects with a focus on TMOKE, Faraday and Cotton-Moutton effects were described subsequently, together with derivation of eigenmodes for each of these effects. The chapter ended by the description of EOT effect, surface plasmons polaritons and their possible existence for *s*-polarization in THz range. We have seen that even at THz frequencies when metals almost acquire properties of PEC and therefore do not support propagation of SPPs, by proper structuring of their surface it is possible to excite bound surface waves - spoof SPPs which can play an important role in EOT. Moreover, if the structure contains 2nd dimension of periodicity, even *s*-polarized radiation can be coupled with the excited designer plasmons.

CHAPTER 3

Magneto-optical Hexagonal Ferrites

Contents

In this chapter we focus primarily on material parameters of hexagonal ferrites. Precise knowledge of material parameters is crucial for the following design and simulations of the proposed THz isolator as the hexaferrites seem to be ideal candidates for the use as the substrate material.

The first part of the chapter is devoted to their general anisotropy and crystal properties, description of the crystal lattice structure and the source of their high

magnetocrystalline anisotropy energy. We studied the surface quality of different hexaferrites by SEM and AFM techniques as well as the extreme difference in the remanent magnetization among the samples. The origin of permeability tensorial components is presented afterwards. Next part is devoted to the free-space characterization of different crystalline and ceramic hexaferrites. We present an original technique of removing all unwanted Fabry-Perot fringes in the quasi-optical measurement setup. This free-space characterization of non-magnetized samples is followed by a full-tensor characterization of hexaferrite ceramics, as an ideal candidate for THz NRD. The obtained gyrotropic spectra allow to calculate the specific Faraday rotation and the required thickness for use in a Faraday isolator. The last part of the chapter is devoted to the Faraday isolation measurement in a quasi-optical setup in mm-wave range showing a strong isolation even far from the FMR frequency of the material.

3.1 General properties

Magnetic materials have been for already very long time widely used in a high number of applications at microwave frequencies [34, 61, 180]. A growing research interest in sub-millimeter (sub-mm) and millimeter-wave (mm-wave) range has increased a demand for fabrication of novel materials with improved properties active in these higher ranges. Nowadays, we can distinguish several groups of magnetic compounds with strong magnetic properties which have found application close to THz frequencies: ferrimagnetic compounds, anisotropic ferrites with hexagonal structure and anisotropic anti-ferromagnetic materials, all of these having their unique internal properties for possible sub-mm and mm-wave applications. These properties generally depend on the crystal structure, presence and location of metallic ions in the structure and their characteristics and mutual interactions. The interaction of these magnetic materials with propagating EM wave can be described with use of the magnetic susceptibility (Eq. 2.26) coming from spin properties of electrons in the structure. Ferrite

materials, based on iron oxide, have been used primarily for signal processing and control functions such as strong absorbers or EM shielding materials close to their natural magnetic resonance or above and below this range as low-loss NRD due to their intrinsic magnetism. Their low values of anisotropy fields caused by highly symmetric cubic structures suppress their gyrotropic properties above 100 GHz and hence preclude their real application at higher frequencies. However, later created ferrites with hexagonal crystal structure with significantly higher magnetocrystalline anisotropy energies offer possibilities of applications up to sub-mm-wave range due to the increased values of natural ferromagnetic resonance (FMR), as summarized in some high-quality review publications [62, 63, 64, 69, 181]. Nowadays, their common applications are as permanent magnets, magnetic recording or data storage materials.

3.1.1 Anisotropy and Crystal Structure

Gyrotropic hexagonal ferrites are formed by iron, oxygen and one or more other elements, which could be barium, strontium, cobalt, or a combination of these creating a characteristic foliate structure. This hexagonal structure is similar to the structure of magnetic mineral magnetoplumbite, as shown in Fig. 3.1, which was initially described already in 1925 by Aminoff [182]. Depending on their chemical composition and the stochiometry of the metal and oxygen, they are divided into several groups marked by a capital letter, from which the M-type (such as $BaFe_{12}O_{19}$ - BaM ferrite or $SrFe_{12}O_{19}$ - SrM ferrite) are the most known and used and form about 50% of the global manufactured amount of magnetic materials. All of the hexaferrites have complex crystal structures forming close-packed hexagonal crystal lattice (Fig. 3.2a) with two characteristic lattice parameters - the width of the hexagonal plane a and the height of the lattice c. The ratio of the height to width of M-type barium hexaferrite unit cell, which contains an amount of total 64 atoms, is 3.94, signifying a large crystalline anisotropy. They also have high magnetocrystalline anisotropy energy coming from size differ-

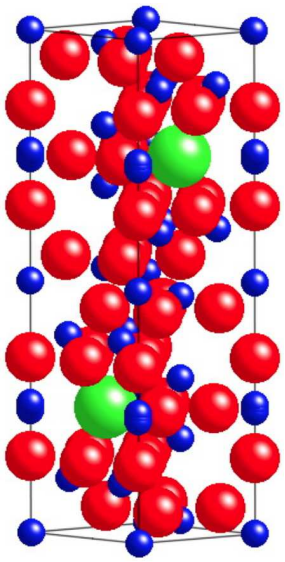

Figure 3.1: Magnetoplumbite structure of $BaFe_{12}O_{19}$ hexaferrite. Different colours represent different atoms: red: O, blue: Fe, green: Ba

ences of ions in the lattice, dipole-dipole interactions and single ion anisotropy. These crystal properties enable the preparation of grain oriented samples with preferred direction of magnetization.

Magnetocrystalline anisotropy energy of all magnetic materials causes a tendency of the magnetic moment vector to strongly prefer to be oriented along some particular crystallographic directions. Hence, if no other forces on the magnetic moment are present, it will be aligned in the preferred crystallographic direction and it can be only moved out of this direction at the expense of the high anisotropy energy. The anisotropy energy for hexaferrite can be expressed as:

$$E_k = K_0 + K_1 \sin^2\theta + K_2 \sin^4\theta + \ldots, \tag{3.1}$$

where K_0 represents the energy to magnetize the easy axis, K_1 and K_2 are the anisotropy constants and θ stands for the angle between crystal's c-axis and magnetization vector $\mathbf{M}$. Because the anisotropy field H_A is proportional to the K_1, the larger value of this constant denotes the large crystalline anisotropy in uniaxial hexaferrites. This is caused by the spin of iron atoms in the structure. Conse-

quently, the stiffness with which the **M** is bound to its preferred direction can be defined as:

$$S = \left(\frac{\partial^2 E_k}{\partial \theta^2} \right)_{\theta=0}. \tag{3.2}$$

The hexaferrites can be according their crystallographic and magnetic properties generally divided into two groups - *uniaxial* or *planar*, also known as *ferroxplana* hexaferrites, as displayed in Fig. 3.2b. The largest part of used hexaferrites have preferred axis of magnetization along *c*-axis of crystals. The planar materials have the preferred direction of **M** in the basal plane perpendicular to the *c*-axis. Figure 3.3 show studied barium and strontium crystalline hexafer-

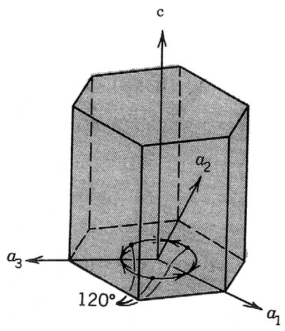

(a) Hexagonal crystal lattice

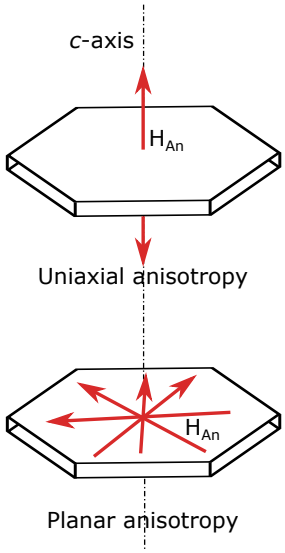

(b) Hexagonal anisotropy

Figure 3.2: Hexagonal crystal lattice and its sheets showing uniaxial and planar anisotropy, $\mathbf{H_A}$ denotes the possible anisotropy field direction

rites ($BaFe_{12}O_{19}$, $SrFe_{12}O_{19}$) grown by the technique of spontaneous germination from a high temperature solution [183] and two types of ceramic strontium hexaferrites $SrFe_{12}O_{19}$ with commercial labels FB6H and FB6N [184] prepared by a wet molding and sintering process. The foliate structure of the monocrystals produces step-like artefacts at the surfaces, making the preparation of a smooth surface for consecutive applications very difficult. This holds particularly for self-

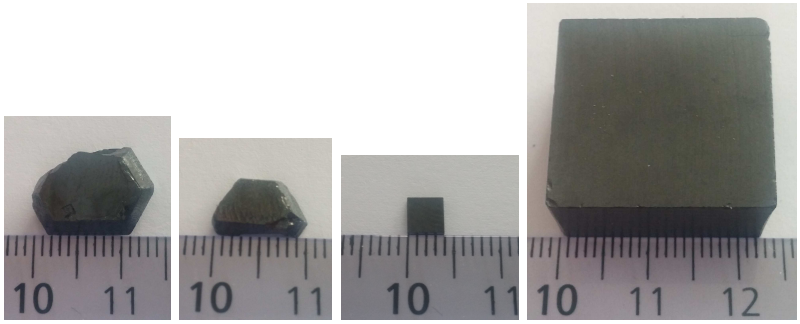

Figure 3.3: Measured samples. From left: crystalline $BaFe_{12}O_{19}$, crystalline $SrFe_{12}O_{19}$, FB6H ceramic, FB6N ceramic.

grown crystalline samples, as displayed in scanning electron microscopy (SEM) pictures (Fig. 3.4). Because the surface quality is critical for later deposition of a metal plasmonic grating, it is important to prepare the hexaferrite with as minimal surface roughness as possible. Luckily, a preparation of hexaferrite ceramics can lead to significantly better surface quality, which can be even improved by subsequent polishing. Figure 3.5 shows pictures from atomic force microscopy (AFM) of FB6N ceramics' surface after different polishing techniques (by water, by Al_2O_3 (alumina) paste and by diamond paste). From measured surface roughness values it is possible to conclude that the best surface quality can be obtained with polishing by alumina paste ($R_q = 14.7\,\text{nm}$) and surprisingly not as good surface was produced by diamond paste polishing ($R_q = 72.2\,\text{nm}$), signifying that the used diamond paste contained too hard particles which created other artificial scratches on the polished surface.

All anisotropy and crystal properties presented here already give a first indication about the possible usefulness of different hexaferrites as substrate material for designed THz NRD. Hexaferrites with planar anisotropy have magnetic moments strongly confined to the plane, however these can be easily switched around in the crystal plane and therefore the total magnetization may be switched even with small driving fields. Since the precise and stable orientation of the magnetization is crucial for functionality of our device, the uniaxial hexaferrites seem to provide better control of this property. Another important characteristics is

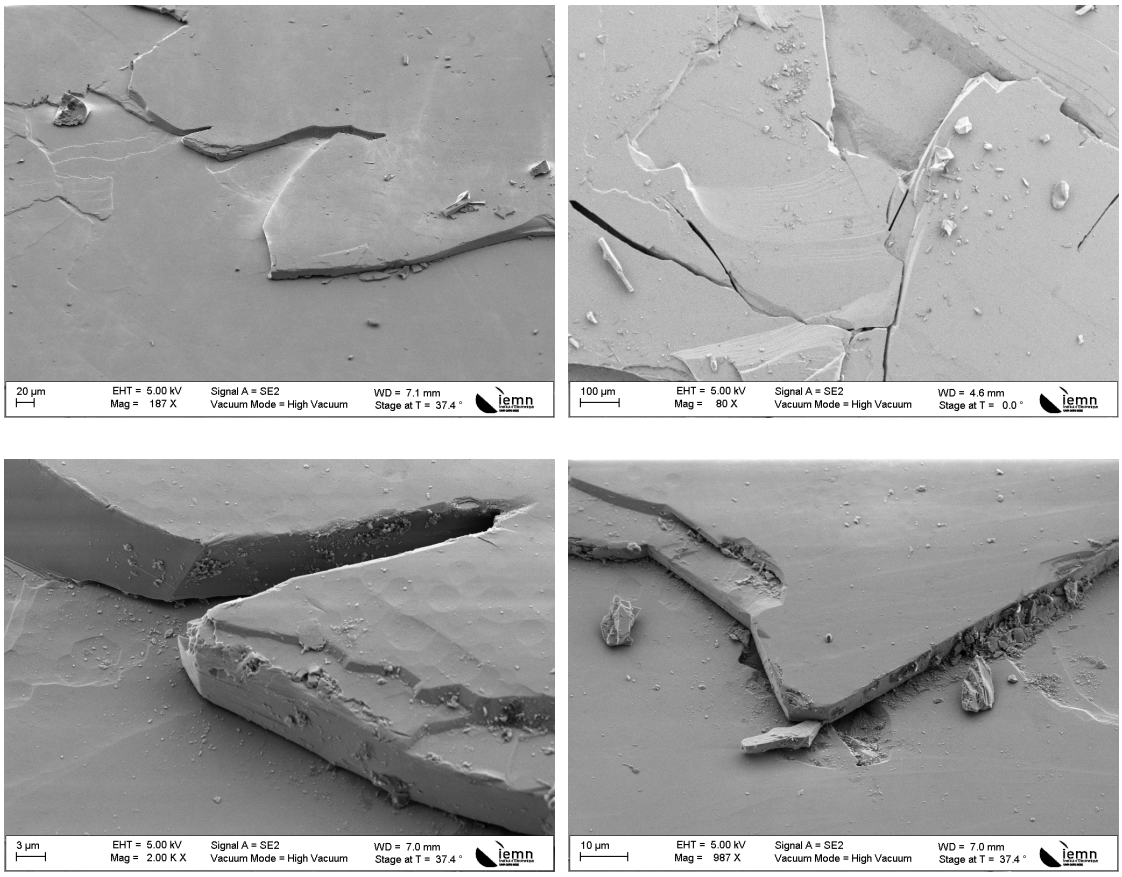

Figure 3.4: SEM pictures of the crystalline hexaferrite $BaFe_{12}O_{19}$ showing step-like artefacts and surface roughness

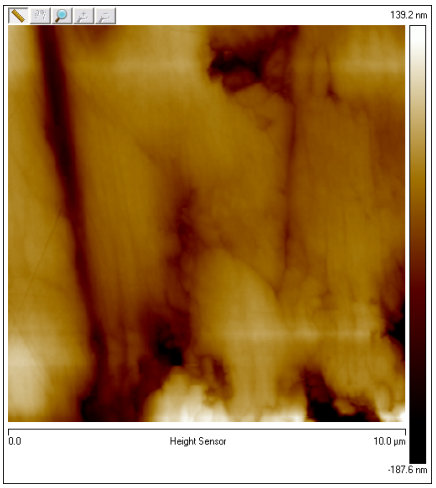

(a) Polished by water

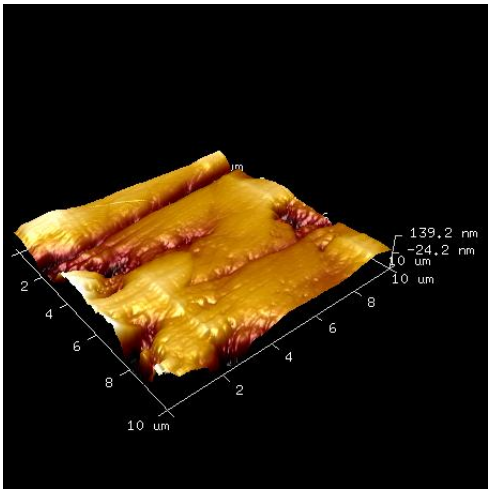

(b) Polished by water - 3D view

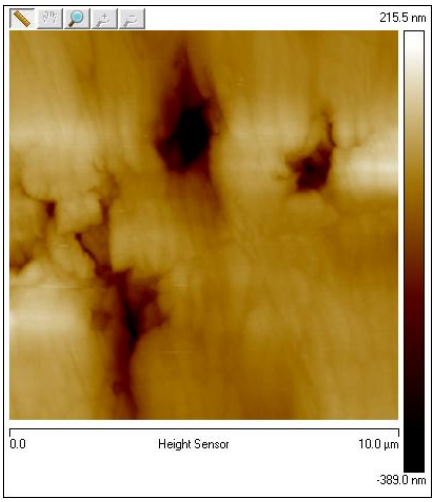

(c) Polished by diamond paste

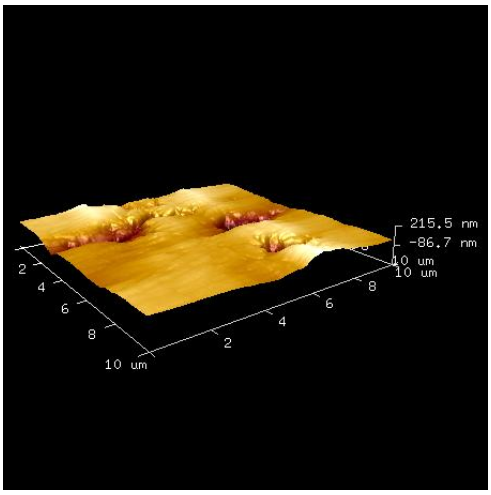

(d) Polished by diamond paste - 3D view

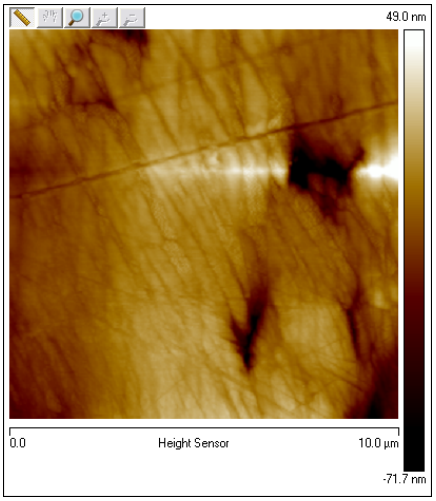

(e) Polished by Al_2O_3 paste

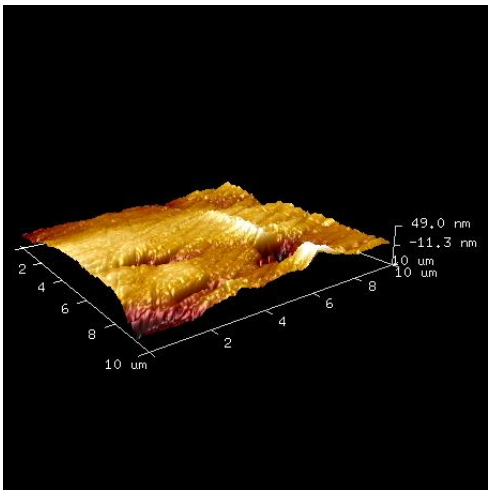

(f) Polished by Al_2O_3 paste - 3D view

Figure 3.5: AFM pictures of FB6N ceramics after three polishing techniques

the surface quality. Any control of the surface quality of self-grown crystalline hexaferrites is very difficult as well as a subsequent surface polishing due to the characteristic foliate structure. On the other hand, ceramic materials, whose controlled preparation enable production of samples with sub-micron surface roughness, are usually commercially available in bulk shapes, which must be processed by a sufficient cutting technique into thin plates. After trying of several cutting techniques we found out that the best way for cutting of a hexaferrite ceramics is a micro-water beam cutting technique. With this water-cutting one is able to prepare samples with thickness of 1–2 mm which is a thickness required for a subsequent deposition of metal structure on the surface by a lithographic process. However all of these materials are very brittle and hence it is very difficult to prepare samples with a high surface/thickness ratio. From all of these facts we can therefore conclude that uniaxial hexaferrite ceramics seem to be the best candidates for substrate materials, however a complete material characterization is yet important for confirmation of this statement.

3.1.2 Magnetic Properties

The gyrotropy in these materials is created by gyromagnetic effects when the saturation magnetization vector precesses nonreciprocally at Larmor frequency $\omega_0 = \mu_0 \gamma H_0$, where $\gamma = 2\pi \times 28\,\mathrm{rad\,GHz\,T^{-1}}$, around hexaferrites' internal magnetic field $H_0 = H_A + H_{ext} + H_d$. This includes the internal anisotropy field H_A keeping the magnetization along certain crystallographic directions, the external applied field H_{ext} and the demagnetization field H_d expressing an anisotropy caused by a material shape. Due to their high magnetic anisotropy field (up to 20 kOe = 2 T, 1000 times higher than classical microwave ferrites with cubic spinel structure [62, 69]), the hexaferrites can have strong gyromagnetic properties well into THz range. The magnetic properties of this material are influenced by presence of magnetic dipole moments arising mainly from spins of electrons. Some of them are unpaired (more left- or right-handed spins) and an applied external

magnetic field can align them in the same direction. This alignment will produce a large total magnetic moment of the material. Due to the presence of exchange forces these spins stay well oriented even when the external field is removed, therefore the material stays permanently magnetized. A hexaferrite with a high coercitive field H_c, which is the field required in reverse direction to decrease the total magnetization back to zero, is known as *hard* ferrite. This material usually has a large value of remanent magnetization M_r approaching 50% of the saturation magnetization value M_s with partially oriented dipole moments and as much as 100% with oriented ones. This high M_r causes a wide, square-shaped hysteresis curve, therefore these hexaferrites are also sometimes known as *square* ferrites.

On the other hand, *soft* ferrites have very narrow hysteresis curve, because even a low applied field can reduce its magnetization to zero. This corresponds to a coercivity which is a strength of the field which must be applied in the opposite direction to the total material magnetization for driving it to zero. This is typically the case for cubic spinel ferrites used in microwave explaining why an external magnet is generally needed for NRD.

3.1.2.1 Hysteresis curve measurement

We measured the hysteresis curves of both types of M-hexaferrites - crystalline (Fig. 3.7a) and ceramic (Fig. 3.7b) in parallel and perpendicular directions to the *c*-axis by vibrating sample magnetometry (VSM). A schematic representation of a typical VSM system is shown in Fig. 3.6. It is used to measure the magnetic properties of materials as a function of magnetic field, temperature, and time. A sample is placed within suitably placed sensing coils, and is made to undergo sinusoidal motion, i.e. mechanically vibrated. The resulting magnetic flux changes induce a voltage in the sensing coils that is proportional to the magnetic moment of the sample. The hysteresis curve is obtained by sweeping the applied magnetic field. From Fig. 3.7 it is apparent that the ceramics belongs to the hard ferrite with square-shaped hysteresis. High coercivity is given by a high crystalline

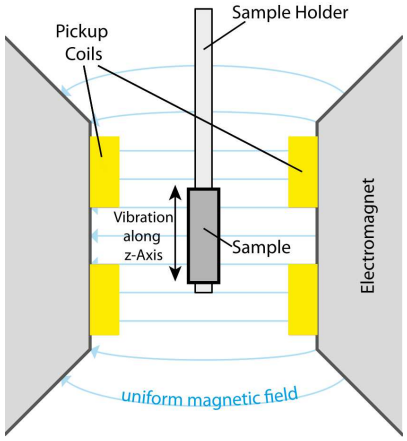

Figure 3.6: Schematic representation of a typical vibrating sample magnetometer

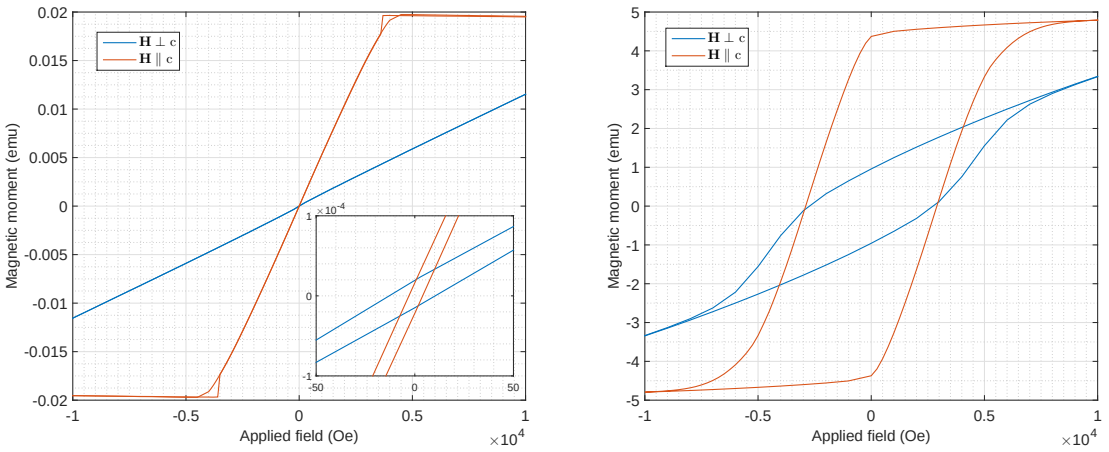

(a) Crystalline $BaFe_{12}O_{19}$ (b) Ceramic FB6N

Figure 3.7: Hysteresis curves of hexaferrites measured by VSM with magnetic field applied in parallel and perpendicular directions of samples. The inset in (a) shows a detail of the central point of the plot.

anisotropy, for example for Sr ceramics the anisotropy constant $K_1 > 3000$ and $K_2 \approx 0$ (Eq. 3.1) which make the ceramics suitable candidates for permanent magnet operation, while crystals show almost zero remanent magnetization. This is probably caused by a complicated domain structure, as was reported by Jalli *et al.* [185] and shown in Fig. 3.8, in which magnetic domains are generally randomly oriented and become well-oriented only when high external magnetic field is ap-

plied. This confirms the main difference between hexaferrite ceramics and single

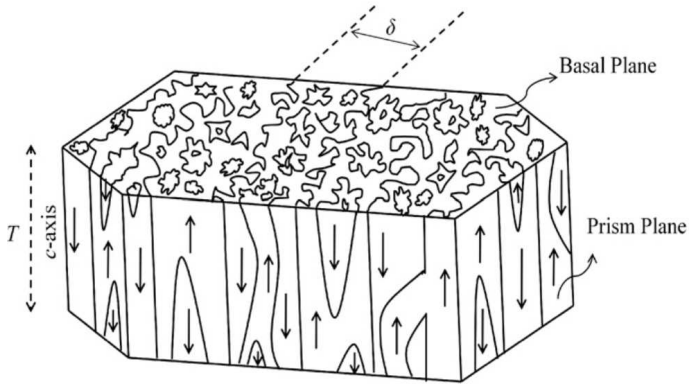

Figure 3.8: Sketch of the domain patterns on the basal plane and the prism plane of a bulk BaM single crystal [185]

crystals [63] in magnetic properties, which is very important for their applications and which can be therefore controlled via the method of their preparation [186]. A variation of magnetic properties is also apparent in different crystallographic directions. The magnetization is saturated more quickly and at lower applied field in the direction of the easy axis than in the perpendicular direction.

3.1.2.2 Permeability Tensor

In this section we will focus on the microscopic behavior of a ferrimagnetic material and its interaction with a signal in order to derive the permeability tensor. This macroscopic description of hexaferrites will be later used to analyze wave propagation through a sample and therefore to determination of anisotropic and gyrotropic material properties. The magnetic dipole moment of an electron due its spin is in the form:

$$m = \frac{e\hbar}{2m_e} = 9.27 \times 10^{-27}\,\mathrm{J\,T^{-1}}, \tag{3.3}$$

where $\hbar$ is the reduced Planck's constant (Eq. 2.2), e the charge of the electron and m_e stays for the electron mass. The electron has a spin angular momentum which

is given in terms of Planck's constant as:

$$s = \frac{\hbar}{2}. \tag{3.4}$$

The vector direction of this momentum is opposite to the magnetic dipole mo-

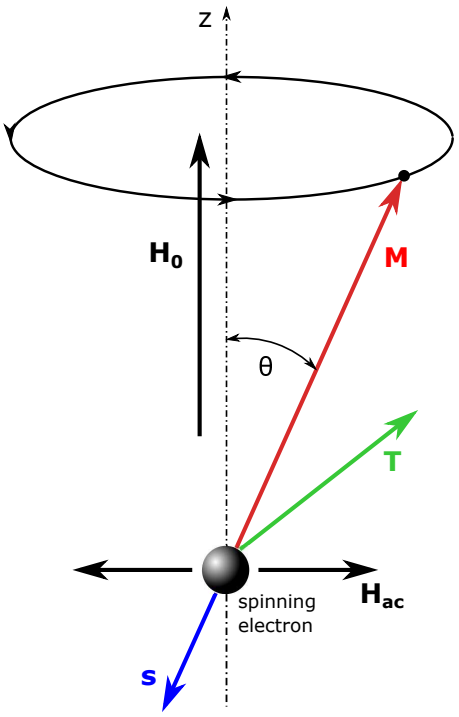

Figure 3.9: Spin magnetic dipole moment and angular momentum vectors for electron precessing around a static magnetic field $\mathbf{H}_0$

ment, as shown in Fig. 3.9. The ratio between the magnetic dipole moment and the spin angular momentum is called *gyromagnetic ratio* and is expressed as:

$$\gamma = \frac{m}{s} = \frac{e}{m_e} = 1.76 \times 10^{11}\,\mathrm{rad\,s^{-1}\,T^{-1}}, \tag{3.5}$$

and in a vector form we can write:

$$\mathbf{m} = -\gamma \mathbf{s}. \tag{3.6}$$

Now we have to consider a torque exerted on the magnetic dipole by the magnetic field $\mathbf{H}_0 = \boldsymbol{\imath}_z H_0$:

$$\mathbf{T} = \mu_0 \mathbf{m} \times \mathbf{H}_0 = -\mu_0 \gamma \mathbf{s} \times \mathbf{H}_0, \tag{3.7}$$

which is equal to the rate of a change of the angular momentum:

$$\mathbf{T} = \frac{\mathrm{d}\mathbf{s}}{\mathrm{d}t} = \frac{-1}{\gamma} \frac{\mathrm{d}\mathbf{m}}{\mathrm{d}t} = \mu_0 \mathbf{m} \times \mathbf{H}_0. \tag{3.8}$$

When the material has been saturated by a sufficiently strong magnetic field, the vector of a total magnetization is given as:

$$\mathbf{M} = N\mathbf{m}, \tag{3.9}$$

where N denotes the number of unbalanced electron spins (magnetic dipoles) per unit volume. The macroscopic equation of motion of the magnetization vector can be therefore obtained with use of Eq. (3.8):

$$\frac{\mathrm{d}\mathbf{M}}{\mathrm{d}t} = -\mu_0 \gamma \mathbf{M} \times \mathbf{H}, \tag{3.10}$$

where $\mathbf{H}$ is the sum of all fields acting upon the magnetization, including the bias field $\mathbf{H}_0$ and interacting RF field $\mathbf{H}_{ac}$ causing a forced precession of the dipole moments around the $H_0 \boldsymbol{\imath}_z$, where $\boldsymbol{\imath}_z$ represents the unit vector in the z-direction:

$$\mathbf{H} = H_0 \boldsymbol{\imath}_z + \mathbf{H}_{ac}. \tag{3.11}$$

This applied field will result in the total magnetization in the material:

$$\mathbf{M} = M_s \boldsymbol{\imath}_z + \mathbf{M}_{ac}, \tag{3.12}$$

where M_s is the DC saturation magnetization and $\mathbf{M}_{ac}$ is the AC magnetization (in the x-y plane). Substituting Eqs. (3.11) and (3.12) into the Eq. (3.10) and

considering

$$\frac{\mathrm{d}\mathbf{M}_s}{\mathrm{d}t} = 0, \tag{3.13}$$

we obtain

$$-\frac{\mathrm{d}\mathbf{M}_{ac}}{\mathrm{d}t} = \mu_0\gamma\left(M_s\boldsymbol{\imath}_z \times \mathbf{H}_{ac} + \mathbf{M}_{ac} \times H_0\boldsymbol{\imath}_z\right). \tag{3.14}$$

where all $M_{ac}H_{ac}$ products have been neglected because magnitudes of the AC components are much smaller than magnitudes of the DC components ($|\mathbf{H}_{ac}| \ll H_0$), and therefore $|\mathbf{M}_{ac}|\,|\mathbf{H}_{ac}| \ll |\mathbf{M}_{ac}|\,H_0$ and $|\mathbf{M}_{ac}|\,|\mathbf{H}_{ac}| \ll M_s\,|\mathbf{H}_{ac}|$. Now we assume that the AC field and AC magnetization have a harmonic dependence on time, $\exp(i\omega t)$, and hence the components of Eq. (3.14) (when $M_i = \mathbf{M}_{ac,i},\ i = x, y, z$) acquires the following form:

$$i\omega M_x = -\omega_0 M_y + \omega_m H_y \tag{3.15}$$

$$i\omega M_y = \omega_0 M_x - \omega_m H x \tag{3.16}$$

$$i\omega M_z = 0, \tag{3.17}$$

where

$$\omega_0 = \mu_0\gamma H_0, \quad \omega_m = \mu_0\gamma M_s \tag{3.18}$$

and ω_0 is called the Larmor ferromagnetic resonance (FMR) frequency defining the precession frequency of the dipole moments and ω_m represents the magnetization frequency. By solving (3.15) and (3.16) for M_x, M_y we obtain set of equations:

$$\left(\omega_0^2 - \omega^2\right) M_x = \omega_0\omega_m H_x + i\omega\omega_m H_y \tag{3.19}$$

$$\left(\omega_0^2 - \omega^2\right) M_y = -i\omega\omega_m H_x + i\omega_0\omega_m H_y \tag{3.20}$$

showing the linear relationship between $\mathbf{H}_{ac}$ and $\mathbf{M}_{ac}$. This set can be written with use of a tensor form of magnetic susceptibility (2.26) $\bar{\bar{\chi}}_m$:

$$\mathbf{M}_{ac} = \bar{\bar{\chi}}_m \mathbf{H}_{ac} = \begin{pmatrix} \chi_{xx} & \chi_{xy} & 0 \\ \chi_{yx} & \chi_{yy} & 0 \\ 0 & 0 & 0 \end{pmatrix} \begin{pmatrix} H_x \\ H_y \\ H_z \end{pmatrix}, \tag{3.21}$$

where the elements of $\bar{\bar{\chi}}_m$ have the following form:

$$\chi_{xx} = \chi_{yy} = \frac{\omega_0 \omega_m}{\omega_0^2 - \omega^2}, \tag{3.22}$$

$$\chi_{xy} = -\chi_{yx} = \frac{i\omega\omega_m}{\omega_0^2 - \omega^2}. \tag{3.23}$$

The permeability tensor (2.19) can be now derived with use of relation between $\mathbf{B}$ and $\mathbf{H}$ (2.27):

$$\mathbf{B} = \mu_0 \left(\mathbf{H} + \mathbf{M}\right) = \bar{\bar{\mu}} \mathbf{H}, \tag{3.24}$$

where the $\bar{\bar{\mu}}$, described by Polder [187], has (for the z-bias field) this form:

$$\bar{\bar{\mu}} = \begin{pmatrix} \mu & i\kappa & 0 \\ -i\kappa & \mu & 0 \\ 0 & 0 & \mu_0 \end{pmatrix}, \tag{3.25}$$

and the elements of the tensor are given by:

$$\mu = \mu_0 \left(1 + \chi_{xx}\right) = \mu_0 \left(1 + \chi_{yy}\right) = \mu_0 \left(1 + \frac{\omega_0 \omega_m}{\omega_0^2 - \omega^2}\right), \tag{3.26}$$

$$\kappa = -i\mu_0 \chi_{xy} = i\mu_0 \chi_{yx} = \mu_0 \frac{\omega\omega_m}{\omega_0^2 - \omega^2}. \tag{3.27}$$

As we can see, the permeability tensor has the anti-symmetric form, and hence, any material having this form of permeability is called *gyrotropic*. This property is required for designing of nonreciprocal devices, because the unequal off-diagonal elements of the tensor are responsible for nonreciprocal effects.

A comment about losses must be given as well. Here we presented an ideal model of FMR without any losses associated with the dipole motion included. However, in real ferrimagnetic materials there exist also damping forces that are responsible for damping out of the precession motion of dipole moments and hence cause a relaxation of magnetization back to the steady-state equilibrium. Consideration of these losses will introduce a damping term into the equation of motion, as was presented in the Landau-Lifshitz [188] form:

$$\frac{\mathrm{d}\mathbf{M}}{\mathrm{d}t} = -\mu_0\gamma\left(\mathbf{M}\times\mathbf{H}\right) - \frac{\mu_0}{\tau M^2}\left[\mathbf{M}\times\left(\mathbf{M}\times\mathbf{H}\right)\right], \tag{3.28}$$

where τ is the relaxation time. Considering the fact, that damping should act not only to the precession motion, but also to the motion induced by the second term in Eq. (3.28), this equation can be written in a more generalized form, presented by Gilbert [189]:

$$\frac{\mathrm{d}\mathbf{M}}{\mathrm{d}t} = -\mu_0\gamma^*\left(\mathbf{M}\times\mathbf{H}\right) + \frac{\alpha}{M}\left(\mathbf{M}\times\frac{\mathrm{d}\mathbf{M}}{\mathrm{d}t}\right), \tag{3.29}$$

where $\alpha = 1/(\gamma\tau M)$ is the damping parameter and $\gamma^* = \gamma(1+\alpha^2)$. Solving Eq. (3.29) analogously to Eq. (3.10) one can find that FMR frequency ω_0 acquires the complex form $\omega_0 \to \omega_0 + i\alpha\omega$ leading to the complex susceptibilities:

$$\chi_{xx} = \Re(\chi_{xx}) - i\Im(\chi_{xx}) \tag{3.30a}$$

$$\chi_{xy} = \Re(\chi_{xy}) - i\Im(\chi_{xy}) \tag{3.30b}$$

including the losses. Moreover, the resonance frequency ω_0 is in a real sample influenced also by other loss mechanisms associated with demagnetization caused by finite sample dimensions, magnetic anisotropy, and crystalline imperfections (polycrystalline structure). Magnetic losses caused by an imaginary part of permeability are however strongest close to the FMR frequency and for a typical Sr-hexaferrite become negligible above 100 GHz, as presented by Kocharyan *et al.* [190] and shown in Fig. 3.10.

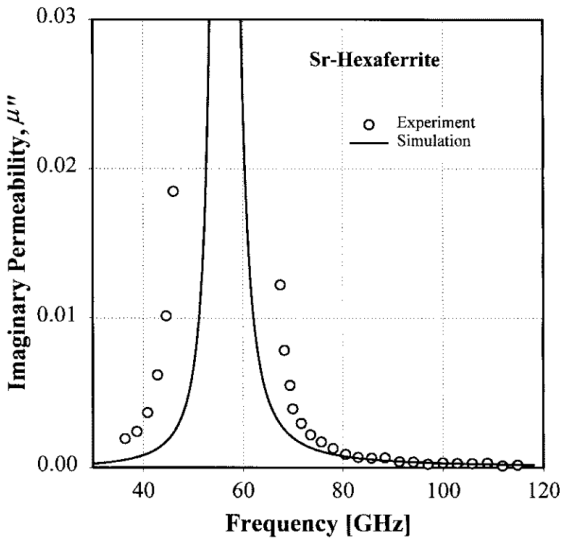

Figure 3.10: Imaginary part of permeability in a non-oriented Sr-hexaferrite ceramics, as presented in [190]

The above introduced gyromagnetic effects are the origin of the permeability tensor and its unequal off-diagonal elements. These are responsible for NR behavior of hexaferrites, which is going to be studied in the following sections, and these processes manifest themselves during interaction with THz waves. The following sections are therefore devoted to a complete characterization of several types of hexaferrites. In the first instance we were interested mostly in the material properties of non-magnetized samples far from the FMR frequency in order to avoid any effects caused by the resonance. This was obtained by a measurement in the sub-millimeter wave range by a Vector Network Analyzer (VNA). In a simplest form, a network analyzer is an instrument used to measure impedance. Today, the VNA generally characterizes high-frequency passive and active devices in their linear mode of operation by measuring their network parameters, called *S*-parameters, as a function of frequency. Through the VNA calibration, impairments of the instrument are completely removed from the measurement. Hence, the *S*-parameters are an accurate representation of the linear behavior of the measured sample. The measurement by VNA was also chosen because it provides significantly faster measurement scans in comparison to a standard TDS

system.

The free-space characterization was followed by a complete full-tensor characterization of magnetized hexaferrite ceramics by a standard THz TDS system. This method provides wide spectral range measurement and therefore gives us a possibility to obtain anisotropic and gyrotropic spectra in the range 0.1–1 THz. Besides the strong anisotropy of hexaferrites, the main goal of this characterization was to determine the Larmor frequency of dipole moments precession and magnetization frequency (3.18) which essentially determine the gyrotropic behavior of ferrites in the measured frequency range.

3.2 Free-space Characterization in the Sub-Millimeter-Wave Range

In this section we present the quasi-optical free-space characterization of magneto-optical hexagonal ferrites in the range between 325 GHz and 500 GHz using the VNA. This method provides us the full complex spectrum of the 2x2 **S**-matrix elements of the sample. Transmission through free air and reflection off a perfect mirror have been used as references. We determined the complex optical indices, permittivities and permeabilities of all samples by fitting a calculated model to measured data. The perturbing effects of multiple reflections between setup components were filtered out by Inverse Fast Fourier Transform (IFFT) of the measured signal and subsequent time gating in the obtained Time-domain (TD) signal. The results presented here show that this processing method reliably deals with all perturbing effects in free-space measurement and therefore can be applied for characterization of various types of magneto-optical (MO) samples with different sizes and significant surface roughness as well. Furthermore it provides convincing indications regarding the usefulness of the different types of hexaferrites for nonreciprocal devices (such as isolators) for sub-mm applications.

Free-space measurement methods are very suitable for material characteriza-

tion because they are contactless; nondestructive and solid samples usually do not need special preparation (any powder samples may be pressed into pellets). For the characterization of materials we used a free-space transmission-reflection method [191] which allows us to determine both complex permittivity and permeability of measured samples.

A proper design of the NRD requires precise material characterization. There is currently a lack of accurate mm-wave hexaferrites data. Most of the research interest is focused on ceramic Sr-hexaferrite material, as a candidate with one of the highest magnetic anisotropy field [69], and there is currently only few conflicting sources reporting dielectric functions of Sr-hexaferrites in the sub-mm-wave band published by Smith *et al.* [73], Shalaby *et al.* [78] and Yang *et al.* [75]. Our motivation is a comparison of material properties of several different types of hexaferrites including crystalline $BaFe_{12}O_{19}$ and $SrFe_{12}O_{19}$, and two types of ceramic $SrFe_{12}O_{19}$ and therefore to help resolve the confusion concerning the correct values. This was done by the free-space characterization which is the main content of this section, structured as follows. Section 3.2.1 covers a description of the measurement system, the used components and the measured samples. Detailed data analysis is included in section 3.2.2. The measured spectra in quasi-optical free-space setup usually contain a combination of several interference fringes originating from multiple sources. Besides the standard Fabry-Perot (FP) interferences from the multiple roundtrips within the material sample, there are also interferences caused by multiple reflections between the sample and the optical components on the beam path (lenses, horns, sample holder, ...). While the FP fringes coming purely from the sample can easily be treated numerically in the data analysis, the other interferences are much harder to discriminate and may seriously hinder a correct interpretation of the data. When performing only a transmission measurement using a perfectly collimated beam and samples with nearly perfectly parallel faces, the detrimental effect of these multiple reflections can be suppressed by slightly tilting the angle with respect to the normal [75] (an angle greater then the angular-width of the incident beam is required). This leads

to diverting signal-power reflected from the sample out of the measurement system and therefore to effective suppression of the residual standing waves. But in case of the transmission-reflection method, where both transmission and reflection data, represented as parameters S_{11} and S_{21}, are measured at the same time, the position and precise alignment of the sample with respect to the incident beam is more critical. Reflections between the horns can not be removed by simple tilting of the sample. Moreover, one often deals with less than ideal samples exhibiting considerable roughness and presenting faces of limited size necessitating strongly focused beams. Hence, angular offsetting the sample in that case does not bring about any improvement in the measured spectra. An elegant way to filter out the presence of all kinds of perturbing FP oscillations in the measured spectra, is by numerically transforming the spectra to the TD and so that only the virtual single-pass contributions can be selected. This technique is described in detail in Section 3.2.2. Section 3.2.3 describes the optical index, permittivity and permeability extraction method. In the last section, the measured results and possible sources of errors are discussed.

3.2.1 Experimental Setup

3.2.1.1 Measurement system

For the characterization we have used a quasi-optical setup using VNA-controlled frequency multipliers and mixers (Rohde and Schwarz ZVA 24) and millimeter heads. A schematic representation and a picture of the setup are shown in Fig. 3.11. It consists of a vector network analyzer, frequency extenders (transmit and receive) for the band 325–500 GHz (201 frequency points), pair of conical horn antennas, four 90-degree off-axis parabolic mirrors with 101 mm focal distance and a sample holder, which was connected to a positioning stage with micrometric screws for precise adjustment of sample position into the beam focal point. Because the frequency resolution determines a time window length after transformation into TD, the number of measurement points (frequency step

$\delta\nu \approx 0.87\,\mathrm{GHz}$) provides in this case an unfolded time window with length of:

$$\Delta T = \frac{1}{\delta\nu} = \frac{1}{8.7 \times 10^8\,\mathrm{Hz}} = 1.15\,\mathrm{ns}. \tag{3.31}$$

The number of measured points (201) was therefore chosen properly with respect to expected optical index and absorptions of measured materials in order to resolve multiple-pass echoes after S-spectra transformation to the TD. Before measurement a conventional waveguide calibration was done, to define the reference measurement plane at the extender outputs [192]. Then, samples were measured in free space by comparing the sample and the air path (differential measurement). The measurement was performed by connecting the horn antennas to the two-port VNA. Both horns can emit and receive only vertically polarized beam.

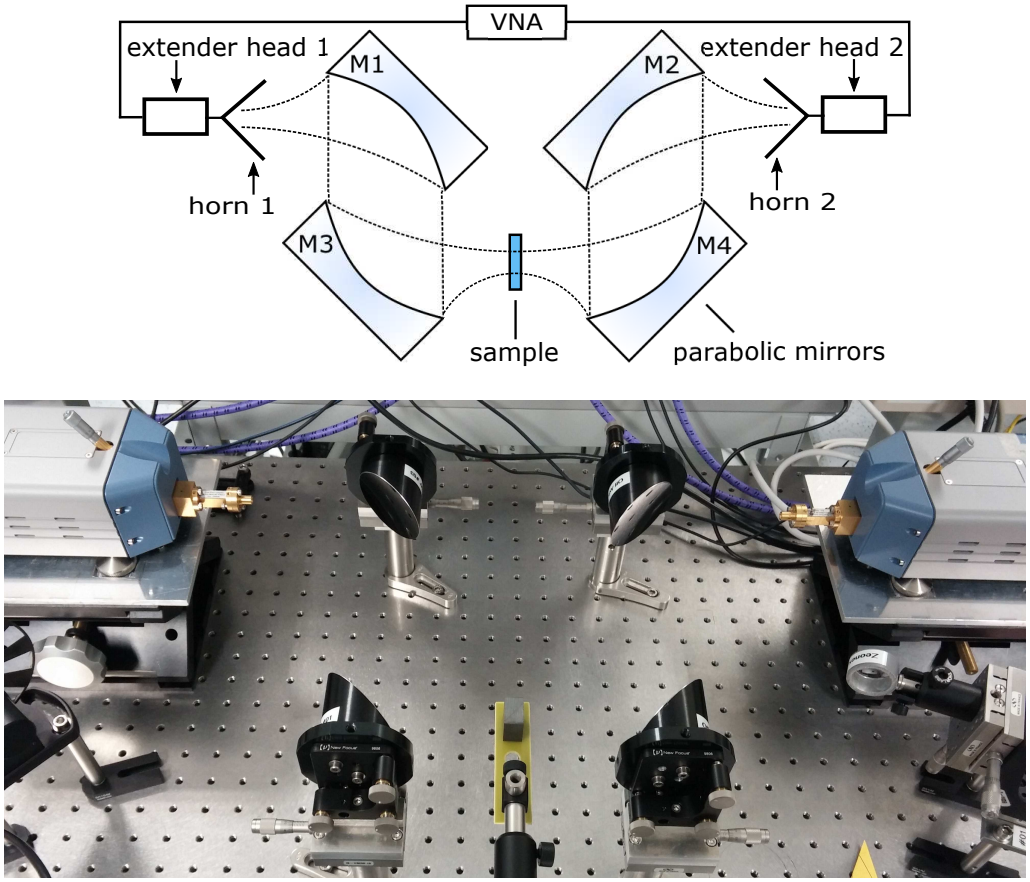

Figure 3.11: A schematic representation (top) and a picture (bottom) of the quasi-optical measurement system with a focused beam.

3.2.1.2 Samples

We have characterized barium and strontium crystalline hexaferrites ($BaFe_{12}O_{19}$, $SrFe_{12}O_{19}$) grown by the technique of spontaneous germination from a high temperature solution [183] and two types of ceramic strontium hexaferrites $SrFe_{12}O_{19}$ with commercial labels FB6H and FB6N [184] prepared by a wet molding and sintering process. The permeability of hexaferrites acquires due to the gyrotropy and anisotropy a tensorial form, as shown in Eq. (3.25) and its unequal off-diagonal elements are responsible for nonreciprocal behavior. The gyromagnetic parameter κ is proportional to the magnetization of the material and the non-zero components of the off-diagonal are determined by the direction cosines of the magnetization (in the form of Eq. (3.25) this corresponds to a z-oriented magnetization). In this study however, the gyrotropic response will be suppressed by characterizing only demagnetized samples. This was verified by measurement in a vibrating sample magnetometer (VSM) done before the free-space characterization. In order to avoid any effects of hexaferrites' crystalline anisotropy, all samples were oriented with the crystal c-axis in parallel direction to the incident beam during measurements. In this case, only the diagonal permeability elements are generally non-zero and the permeability acquires a scalar form $\hat{\mu} = \mu' - i\mu''$. The off-diagonal permeability contributions are the subject of a study in Section 3.3. All measured samples are shown in Fig. 3.3 and a scanning electron microscopy (SEM) image of the $BaFe_{12}O_{19}$ showing the surface roughness is in Fig. 3.4. The free-space measurement technique does not require any special preparation of the samples.

3.2.2 Data Analysis

For the extraction of the complex permittivity and permeability of the materials we used the recorded complex S_{11} parameter representing a reflection from the sample back into horn 1 and the complex S_{21} parameter representing a transmission from horn 1, through the sample into horn 2. The raw measured S-spectra

will therefore contain important FP fringes originating from multiple reflections between the measured sample and setup components and inside the sample itself and complicating the analysis.

3.2.2.1 Transmission

The transmission measurement has been calibrated by the transmission spectrum with the sample removed. Then, the parameter $S_{21} = |S_{21}| \cdot \exp(i\Delta\phi_{21})$ of the sample is obtained from the measurement with and without sample as:

$$S_{21} = \frac{S_{21,\,\mathrm{meas}}}{S_{21,\,\mathrm{ref}}}. \tag{3.32}$$

Amplitude $|S_{21}|$ and phase $\Delta\phi_{21}$ are influenced by multiple reflections. Moreover, due to the periodicity of trigonometric functions, the phase values are wrapped between $\pm\pi$. In case of regular-shaped samples without significant surface roughness it is possible to consider multiple reflections inside the measured sample for extraction of material parameters from the transmission experiment [193]. But because of the irregular shape and significant surface roughness of our crystalline samples it is desirable to extract the single pass contribution from the S-parameter spectra. This was done by unwrapping the phase [194] and transforming the measured spectra of S_{21} by IFFT [195] into the TD. The obtained TD signal is a pure numerical construct that emulates the interaction of a hypothetical pulse with a bandwidth equal to the measurement bandwidth:

$$\delta t \sim \frac{1}{\Delta f} = \frac{1}{175\,\mathrm{GHz}} = 40/7\,\mathrm{ps} \tag{3.33}$$

and with a repetition rate given by the frequency sampling with the sample.

Application of a Time-domain-gating [196] leads to artificially numerically performing a single-pass experiment. This corresponds to selecting a region of interest in the TD, removing unimportant responses and transforming of filtered data by Fast Fourier Transformation (FFT) back into the Frequency-domain (FD).

In this way in principle interference fringes due to multiple round trips are filtered out of the spectrum and only the pure dispersive material properties are probed for. This step is critical in the sense that careless time-gating might introduce artefacts in the frequency spectra or even erase true physical information. Section 3.2.4.1 discusses in more detail possible errors that can arise. In any case, as time-gating gets down to multiplying the obtained time signal by a windowing function, the filtered spectrum is a convolution of the original spectrum and the Fourier transform of the window function. This window needs to be

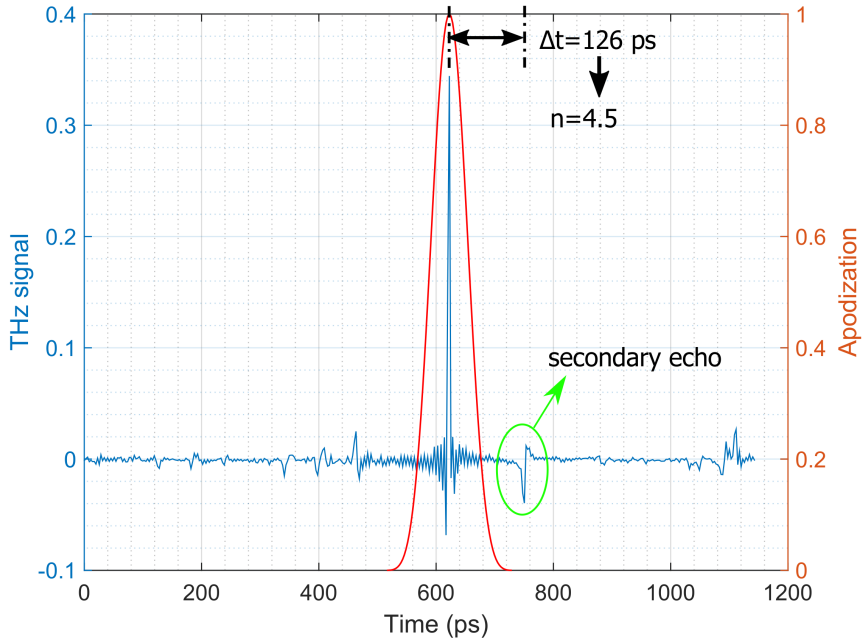

Figure 3.12: Time-domain signal of 4.2 mm thick monocrystal $BaFe_{12}O_{19}$ and applied Blackmann-Harris window on the main echoes. Other parasitic echoes in the detected signal are present around 440 and 1100 ps. The first one arrives before the main echo and thus perhaps represents a part of the beam going aside the sample; the second one corresponds in free-space to a distance of 33 cm, and therefore represents the second roundtrip between horn 2 and the sample.

chosen carefully not only to cover the main TD peak (and remove the echoes at t =440 ps, 1100 ps...; see Fig. 3.12 and Fig. 3.13). Moreover its shape must be such that it minimizes artificial ripple in the spectrum by the convolution opera-

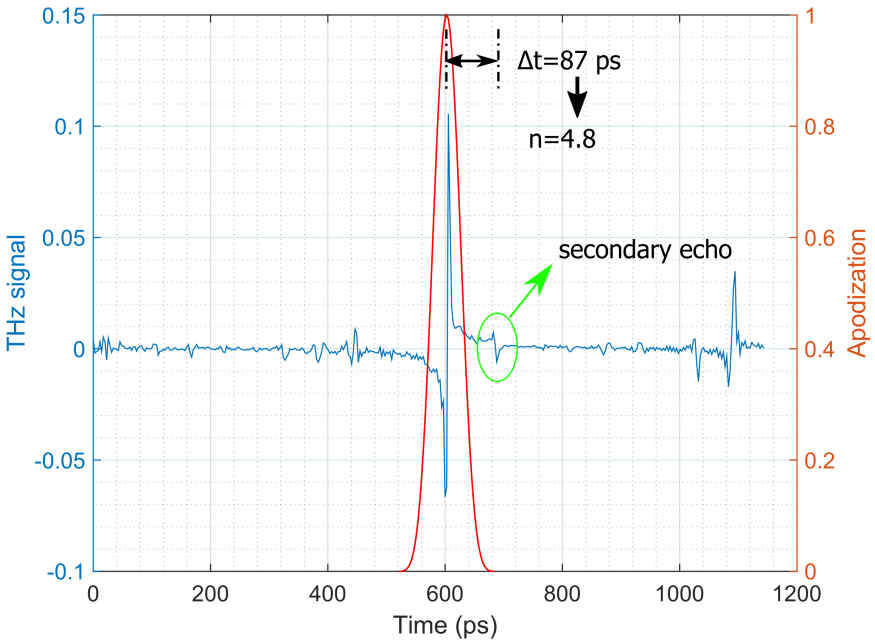

Figure 3.13: Time-domain signal of 2.4 mm thick monocrystal $SrFe_{12}O_{19}$ and applied Blackmann-Harris window on the main echoes. Other parasitic echoes in detected signal are present around 400 and 1100 ps.

tion. Using a Blackmann-Harris apodization window [197] is a typically known technique to minimize edge ripples in the convolution product of the recovered spectrum. Figures 3.12 and 3.13 show the TD transmission signal of monocrystals $BaFe_{12}O_{19}$ and $SrFe_{12}O_{19}$, respectively. The observed time delays between the clearly discernable first echo for the Ba- and the Sr-crystal combined with a first approximate guess of the sample thickness (resp. 4 and 2.5 mm), lead to first estimations of the optical indices (resp. 4.5 and 4.8), confirming a correct order of magnitude [75]. Filtered data were then transformed by FFT back into the FD. In order to minimize the impact of the side lobes of the fourier transform of the apodizing function in the convolution integral [198] that leads to this filtered frequency spectrum, we omit a 15 GHz-wide region in the obtained spectrum for further data analysis[1]. Figures 3.14 and 3.15 compare the real measured

[1] This size more or less corresponds to the bandwidth of the used Blackmann-Harris apodization.

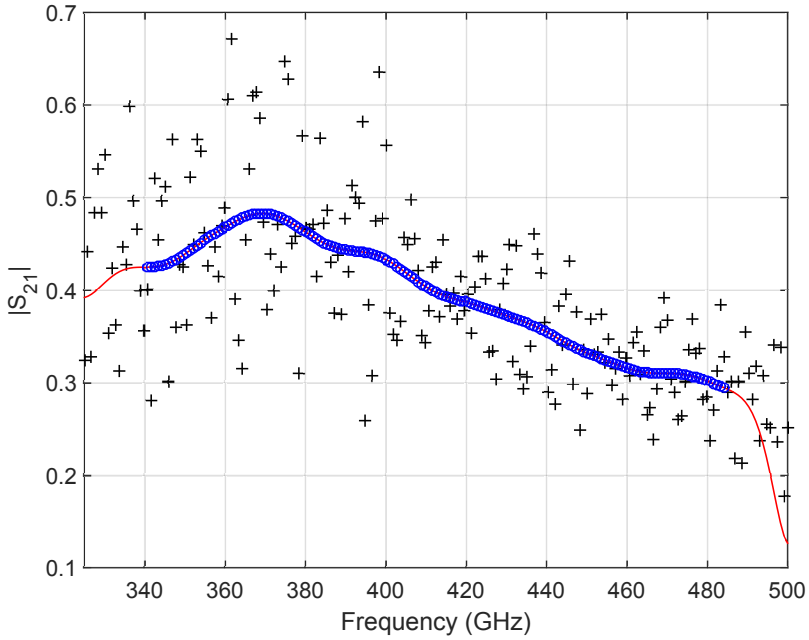

Figure 3.14: Amplitude $|S_{21}|$ of monocrystalline $BaFe_{12}O_{19}$ before (black crosses) and after TD-gating filtering (red lines). Selected range for parameters extraction is highlighted by blue circles.

and TD-gating-processed values of the amplitude $|S_{21}|$ and the phase $\Delta\phi_{21}$ of the crystalline $BaFe_{12}O_{19}$ sample.

3.2.2.2 Reflection

The reflection measurement is calibrated by the reflection signal from a short circuit (perfect conductor). In this case a flat silver mirror has been taken as a reference because of its high reflectivity comparable with gold mirrors [199]. A correctly calibrated S_{11} trace (especially the phase) requires the reference reflection and the sample reflection to be measured at almost identical normal positions with respect to the incident beam. In order to achieve this, a positioning stage was used, equipped with micrometric screws for positioning precision of 100 µm. All measured spectra were then transformed by IFFT into the TD, where the arrival times of main echoes of samples and reference were compared. For the extraction of the complex parameter S_{11}, the sample and reference signals with

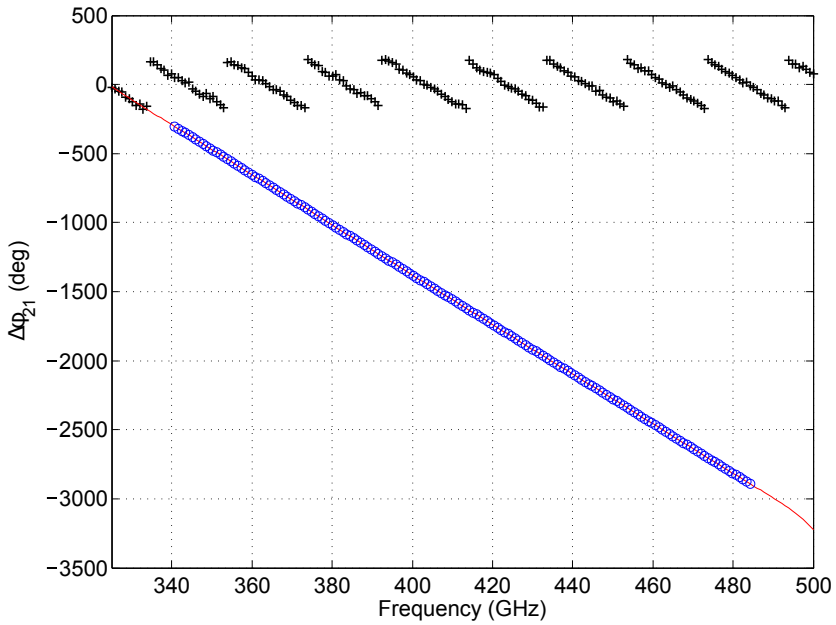

Figure 3.15: Phase $\Delta\phi_{21}$ of monocrystalline $BaFe_{12}O_{19}$ before (black crosses) and after TD-gating filtering (red lines). Selected range for parameters extraction is highlighted by blue circles.

the same arrival time of the main echos were used. This method assures precise agreement between sample and reference positions. Both TD signals of reference mirror (arrival time of main echo $t = 525.94\,\text{ps}$) and sample FB6N (arrival time of main echo $t = 525.94\,\text{ps}$) are shown in Figs. 3.16 and 3.17. This technique (as with the transmission spectra) allows to filter out the signal and keep the influence of just the first interface reflection. In Figs. 3.16 and 3.17 we can again easily discern the presence of parasitic echoes coming from, among others, a reflection inside the emitting horn and additional "cavities" inside the setup (peaks (a) and (b)) such as between the horn and the sample surface. Note that due to frequency sampling, these peaks might be folded by a multiple of $1/\Delta\nu$. All these unwanted effects were removed again by applying TD-gating with a Blackmann-Harris apodization window, similarly as was done for the transmission data. The filtered signals from reference and samples were then transformed by FFT back into the FD and the parameter $S_{11} = |S_{11}| \cdot \exp(i\Delta\phi_{11})$ was obtained from sample

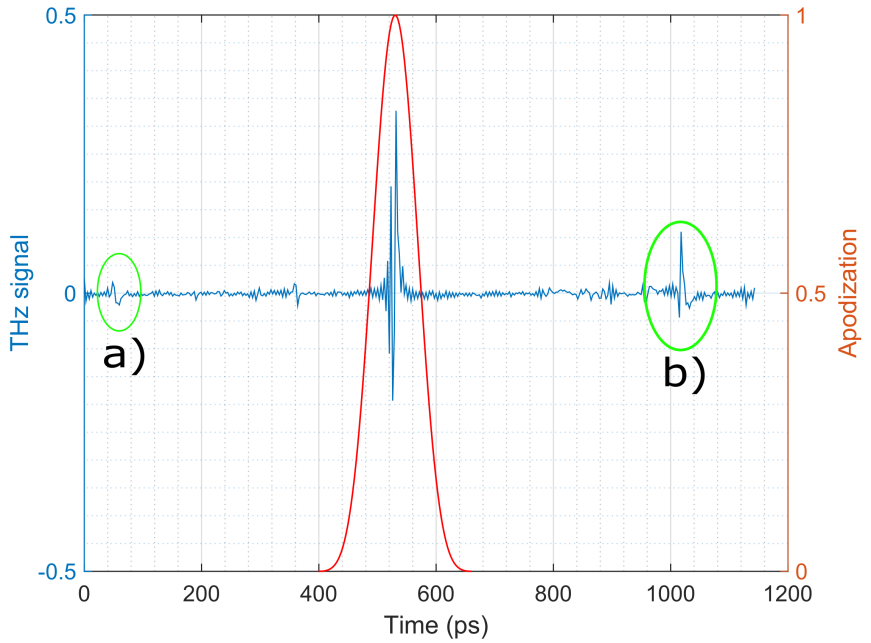

Figure 3.16: Time-domain signal of the reference mirror. Significant echoes coming from reflections in the setup are denoted a) and b).

and reference signal as:

$$S_{11} = \frac{S_{11,\,\mathrm{meas}}}{S_{11,\,\mathrm{ref}}}. \tag{3.34}$$

3.2.3 Permittivity and Permeability Extraction

After extracting the pure single interface reflection and the pure single pass transmission out of the measured S-spectra using the described TD-gating, the material parameters can be extracted using classical Fresnel formulae (see Fig. 3.18). These are given by, for p-polarized light:

$$\begin{aligned} \hat{r}_p &= \frac{\sqrt{\frac{\hat{\mu}_2}{\hat{\varepsilon}_2}}\cos\Theta_t - \sqrt{\frac{\hat{\mu}_1}{\hat{\varepsilon}_1}}\cos\Theta_i}{\sqrt{\frac{\hat{\mu}_2}{\hat{\varepsilon}_2}}\cos\Theta_t + \sqrt{\frac{\hat{\mu}_1}{\hat{\varepsilon}_1}}\cos\Theta_i} \\ \hat{t}_p &= \frac{2\sqrt{\frac{\hat{\mu}_2}{\hat{\varepsilon}_2}}\cos\Theta_i}{\sqrt{\frac{\hat{\mu}_1}{\hat{\varepsilon}_1}}\cos\Theta_i + \sqrt{\frac{\hat{\mu}_2}{\hat{\varepsilon}_2}}\cos\Theta_t} \end{aligned} \tag{3.35}$$

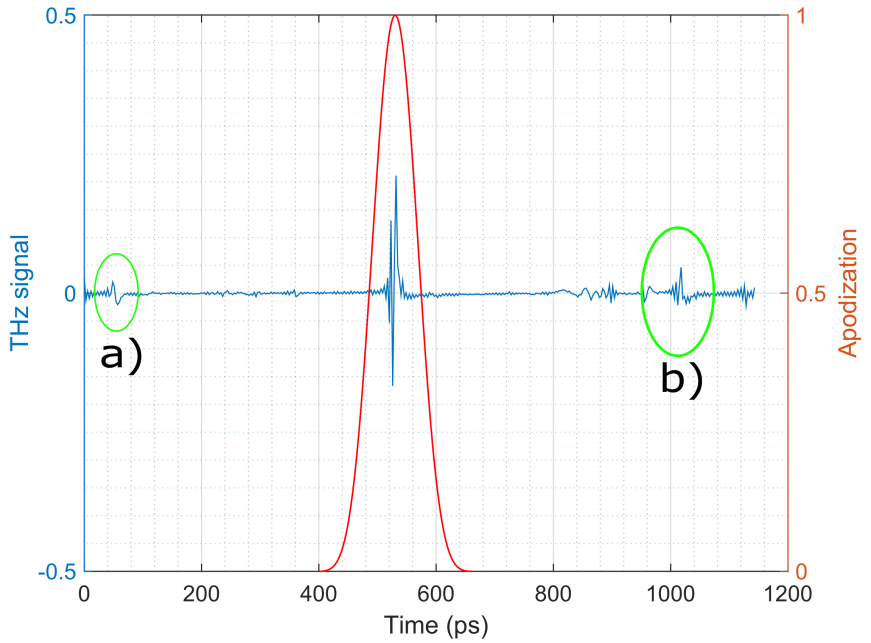

Figure 3.17: Time-domain signal of ceramic sample FB6N (bottom). Significant echoes coming from reflections in the setup are denoted a) and b).

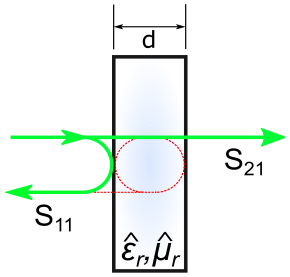

Figure 3.18: Model of the characterized sample, only first transmitted and reflected echoes are considered.

and for s-polarized light:

$$\hat{r}_s = \frac{\sqrt{\frac{\hat{\mu}_2}{\hat{\varepsilon}_2}}\cos\Theta_i - \sqrt{\frac{\hat{\mu}_1}{\hat{\varepsilon}_1}}\cos\Theta_t}{\sqrt{\frac{\hat{\mu}_2}{\hat{\varepsilon}_2}}\cos\Theta_i + \sqrt{\frac{\hat{\mu}_1}{\hat{\varepsilon}_1}}\cos\Theta_t}$$
$$\hat{t}_s = \frac{2\sqrt{\frac{\hat{\mu}_2}{\hat{\varepsilon}_2}}\cos\Theta_i}{\sqrt{\frac{\hat{\mu}_2}{\hat{\varepsilon}_2}}\cos\Theta_i + \sqrt{\frac{\hat{\mu}_1}{\hat{\varepsilon}_1}}\cos\Theta_t} \tag{3.36}$$

where Θ_i and Θ_t represent angles of incidence and of refraction respectively. The measured sample is characterized by a complex relative permittivity $\hat{\varepsilon}_r = \varepsilon'_r - i\varepsilon''_r$, a complex relative permeability $\hat{\mu}_r = \mu'_r - i\mu''_r$ and a complex refractive index $\hat{n} = n - ik = \sqrt{\hat{\varepsilon}_r \hat{\mu}_r}$. The final expressions for the S-parameters assuming a single-pass and normal incidence of vertically-polarized light take the form (with $\hat{\varepsilon}_1 = \hat{\mu}_1 = 1$ for $\hat{r}_p$ and $\hat{t}_{p01}$ and $\hat{\varepsilon}_2 = \hat{\mu}_2 = 1$ for $\hat{t}_{p10}$):

$$S_{11} = \hat{r}_p \left(\Theta_i = \Theta_t = 0\right) \tag{3.37}$$

$$S_{21} = \hat{t}_{p01} \left(\Theta_i = \Theta_t = 0\right) \hat{t}_{p10} \left(\Theta_i = \Theta_t = 0\right) \exp\left(-i\beta d\right), \tag{3.38}$$

where $\hat{t}_{01}$, $\hat{t}_{10}$ are the complex transmission coefficients through the first and second sample interface, respectively, and d represents the sample thickness. Note that the phase factor is corrected by the phase of the reference measurement (free air), hence $\beta = 2\pi\nu \left(\sqrt{\hat{\mu}_r \hat{\varepsilon}_r} - 1\right) / c$.

3.2.4 Results and Discussion

Since the measured frequency band has been relatively narrow and lies far from the expected resonance frequency of hexaferrites (typically around 55 GHz) [75, 200], it is highly unlikely to obtain a reasonable fit using an analytical Larmor model as its distinct features are too far removed [201]. Therefore, both permittivity and permeability of the sample have been modeled by a Kramers-Kronig [202] consistent B-spline (basis-function spline) formulation [203]. In this case, the imaginary part of permittivity and permeability are parametrized by a B-spline curve of 3$^{\text{rd}}$ degree and the real part spectra are analytically calculated using Kramers-Kronig causality relationship. This provides an alternative way to parametrize a dielectric function and allows us to fit all points in the desired frequency range in one time. A B-spline basis function $B_i^k(x)$ is defined by:

$$B_i^k\left(x\right) = \left(\frac{x - t_i}{t_{i+k} - t_i}\right) B_i^{k-1}\left(x\right) + \left(\frac{t_{i+k+1} - x}{t_{i+k+1} - t_{i+1}}\right) B_{i+1}^{k-1}\left(x\right). \tag{3.39}$$

The superscript k of the function denotes the degree of the B-spline, and the subscript i indexes the knot locations t_i. Knots are nodes on the x-axis where the curve transitions from one polynomial segment to another. A spline curve $S(x)$ is then constructed as a linear sum of n basis functions:

$$S(x) = \sum_{i=1}^{n} c_i B_i^k(x), \tag{3.40}$$

where c_i are the spline coefficients for the i-th basis function. If the $\varepsilon_r''(\omega)$ spectra are parametrized by a B-spline curve in the form:

$$\varepsilon_r''(\omega) = \sum_{i=1}^{n} c_i B_i^k(\omega), \tag{3.41}$$

then the $\varepsilon_r'(\omega)$ spectra can be analytically calculated using the Kramers-Kronig causality relationships:

$$\varepsilon_r'(\omega) = \varepsilon_r(\infty) + \sum_{i=1}^{n} c_i \phi_i^k(\omega), \tag{3.42a}$$

$$\text{where} \qquad \phi_i^k(\omega) = \frac{2}{\pi} P \int_0^{\infty} \frac{\omega' B_i^k(\omega')}{\omega'^2 - \omega^2} \mathrm{d}\omega', \tag{3.42b}$$

and where P denotes the Cauchy principal value.

Thanks to the reduced number of fitting parameters the B-spline can improve the robustness of a least-squares data fit (as comparison to a point-by-point fitting procedure). The permittivity and permeability of all samples have been parametrized by 15 and 9 control points, respectively. A simple demonstration of B-spline control points is shown in Fig. 3.19. Note that due to discontinuity of standard B-splines at the end of frequency range it is necessary to include some extra control points in order to handle absorptions outside the considered frequency range [203]. In order to account dispersion due to absorptions that lie far from measured frequency band the terms $\varepsilon_r(\infty)$ and $\mu_r(\infty)$ were fitted as well and then added as a constant offset to the ε and μ spectra. The last fitting parameter was the thickness of a sample. Therefore, we considered 27 fitting

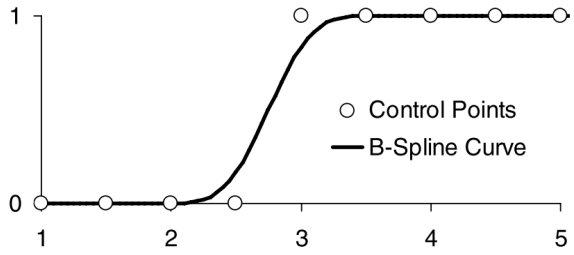

Figure 3.19: Demonstration of B-spline control points [203]

parameters for the extraction procedure (15+9 control points, $\varepsilon_r(\infty)$ and $\mu_r(\infty)$ constants and sample thickness). The model spectra of $|S_{11}|$, $\phi_{11} = \arg(S_{11})$, $|S_{21}|$, $\phi_{21} = \arg(S_{21})$ were then fitted to the measured data. In this procedure the difference between experimental data (E) after time-gating and modeled data (M) is minimized. The objective function χ^2 takes the form:

$$\chi^2 = \frac{1}{n}\sum_{i=1}^{n}\Big(\big||S_{11iM}| - |S_{11iE}|\big|^2 + |\phi_{11iM} - \phi_{11iE}|^2 + \\ + |\phi_{21iM} - \phi_{21iE}|^2 + \big||S_{21iM}| - |S_{21iE}|\big|^2\Big), \quad (3.43)$$

where n represents the number of spectral points. The minimization of the function χ^2 was done by least-square fitting using a Levenberg-Marquardt algorithm [204]. After the fit this residual function had value $\chi^2 < 0.01$ for crystalline and $\chi^2 < 0.0012$ for ceramic samples and 160 frequency points, proof of a reasonable fit. Figure 3.20 compares measured data and the fitted model for the parameters S_{11} and S_{21} for the FB6N ceramic sample.

Final calculated parameters are shown in Fig. 3.21 (permittivity $\hat{\varepsilon}_r$), in Fig. 3.22 (permeability $\hat{\mu}_r$) and in Fig. 3.23 (refractive index $\hat{n} = n - ik$). Table 3.1 summarizes fitted and measured thicknesses of all samples. The values of thicknesses are in accordance with the measured ones (± 0.2 mm for crystalline samples). The measured values were obtained by a sample thickness gauge Mitutoyo at 5 different points of the sample and an averaging of these 5 values. Because the surfaces of all samples are not perfectly parallel, error bars of the measured values are given by a combination of this surface inclination and surface roughness.

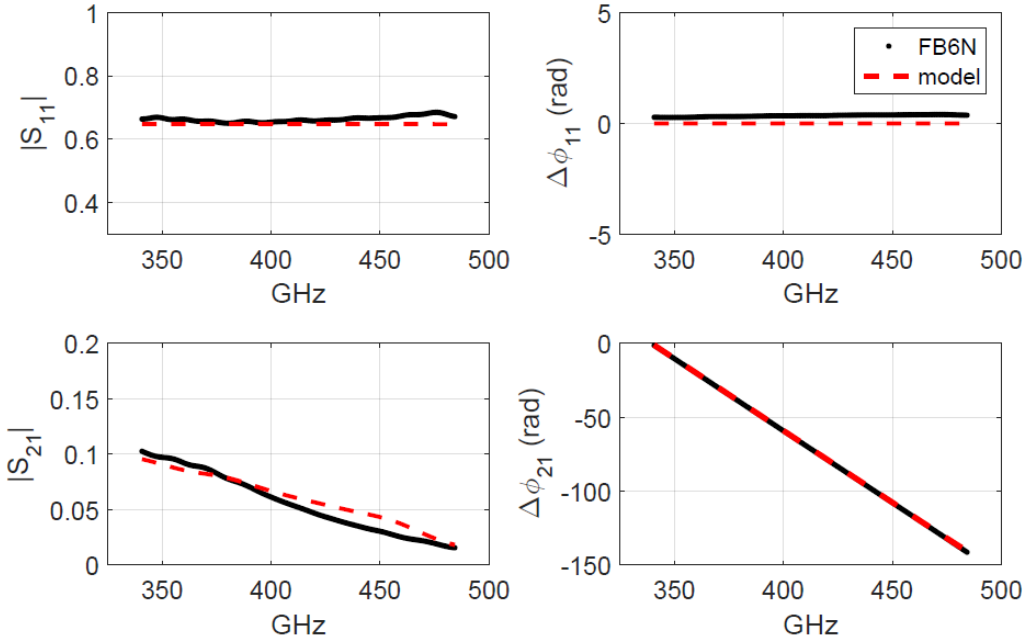

Figure 3.20: Comparison of measured and fitted amplitude and phase of parameters S_{11}, S_{21} of the ceramic sample FB6N.

This is more significant on the crystalline samples where their layered structure causes high surface roughness in the order of tens of μm (as is shown in Fig. 3.4). The calculation of the error bounds Δd of the fitted values is less straightforward. Assuming that all other fitting parameters are errorless, the final residual function χ^2 can be attributed to a thickness variation only. Hence, Δd is calculated from the ϕ_{21} and χ^2 for each sample as: $\chi^2 = (\beta \Delta d)^2$ and therefore: $|\Delta d| = \chi/\beta$. These errors were calculated for the lowest included frequency ($\nu = 340$ GHz). This is, of course, an extreme case because in reality none of the other fitting parameters is errorless and all of them have an impact on the residual χ^2 function. This impact of all parameters is however difficult to quantify, because the entire fit is very complex and robust, and therefore, the presented error bounds of the fitted values are the maximum possible but are expected to be significantly lower.

All measured materials have in this frequency range very similar properties. The real parts of $\hat{\varepsilon}_r$ and $\hat{\mu}_r$ show quasi-dispersionless behaviour confirm-

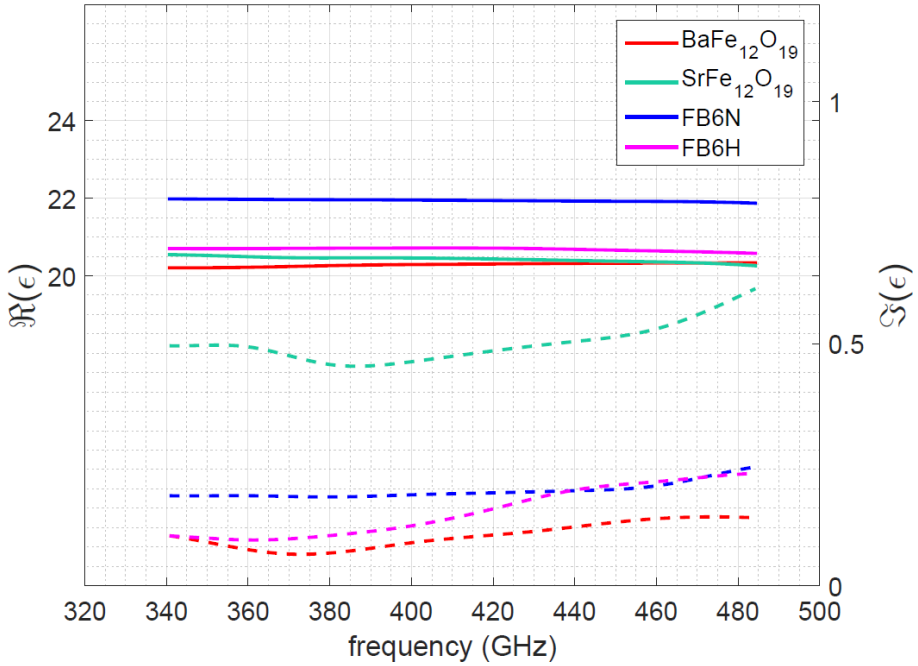

Figure 3.21: Calculated permittivities of all samples, full lines represent the real parts and dotted lines represent the imaginary parts.

Table 3.1: Thicknesses of hexaferrite samples

Sample	$BaFe_{12}O_{19}$ crystalline	$SrFe_{12}O_{19}$ crystalline	FB6H ceramic	FB6N ceramic
Fit (mm)	4.20±0.05	2.70±0.05	1.00±0.02	12.70±0.02
Meas (mm)	4.31±0.28	2.53±0.35	1.03±0.01	12.72±0.01

ing that the Larmor resonance lies well below the measurement frequency range. The lowest losses have been measured in crystalline Ba-hexaferrite ($k = 0.01$ at 400 GHz, corresponding to α =7.28 dB/cm). This hexaferrite, together with the FB6H ceramic ($k = 0.015$, α =10.92 dB/cm at 400 GHz) seem to be better candidates for operation in THz NRD. Imaginary parts of refractive indices of all samples show slowly rising values with frequency. Looking at the ε_r and μ_r spectra, this increase is principally due to the increasing dielectric losses when moving toward the infrared, probably caused by phonon losses. The obtained values of refractive indices and permittivity are also in good agreement with already pub-

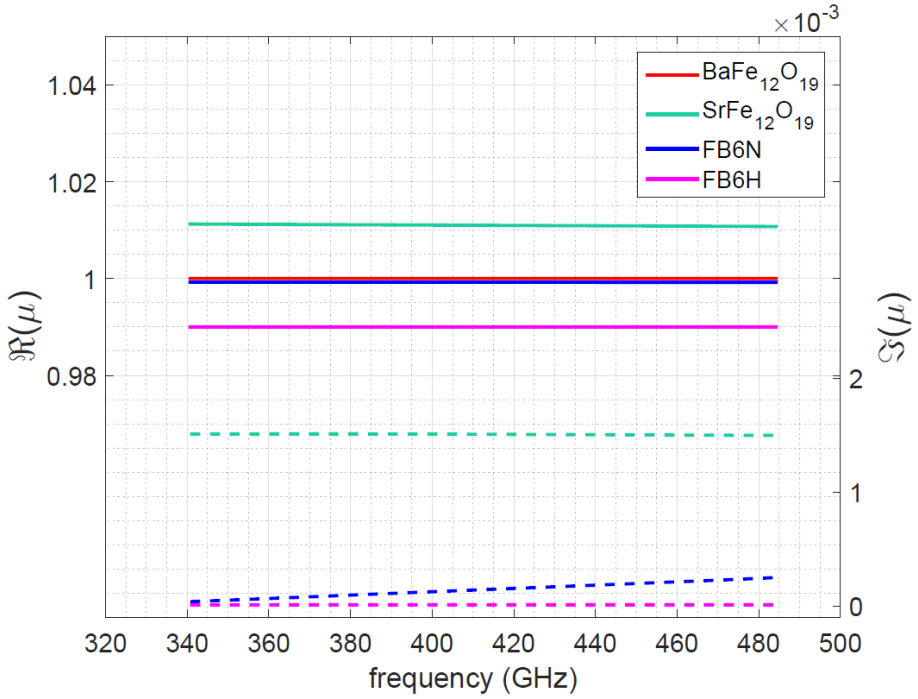

Figure 3.22: Calculated permeabilities of all samples, full lines represent the real parts and dotted lines represent the imaginary parts (red dotted is overlapping with the blue one).

lished ones by Yang et al. [75] for ceramic hexaferrite. The same authors however measured higher losses for FB6H sample ($\alpha \approx 14.5\,\mathrm{dB/cm}$ at 400 GHz). Contrary to these results Shalaby et al. published [78] $n \approx 6$ and $\alpha \approx 43\,\mathrm{dB/cm}$ at 400 GHz. These high values of n and α have not been measured in any of our hexaferrite samples and have also not been observed by Yang et al. Permeabilities of all samples have value very close to 1.0 with negligible imaginary part ($< 2 \cdot 10^{-3}$). It denotes that these hexaferrites have almost dielectric behaviour when they are not magnetized. Kocharyan et al. [200] have reported permeability measurements for non-magnetized ceramic hexaferrites in the frequency range 70–120 GHz. The permeability value increases with increasing frequency from value 0.65 at 70 GHz (close to resonance frequency) up to 0.95 at 120 GHz. Similar values were measured also by Korolev et. al. [205]. We can therefore say that our measured values of permeabilities in higher frequency range are in good

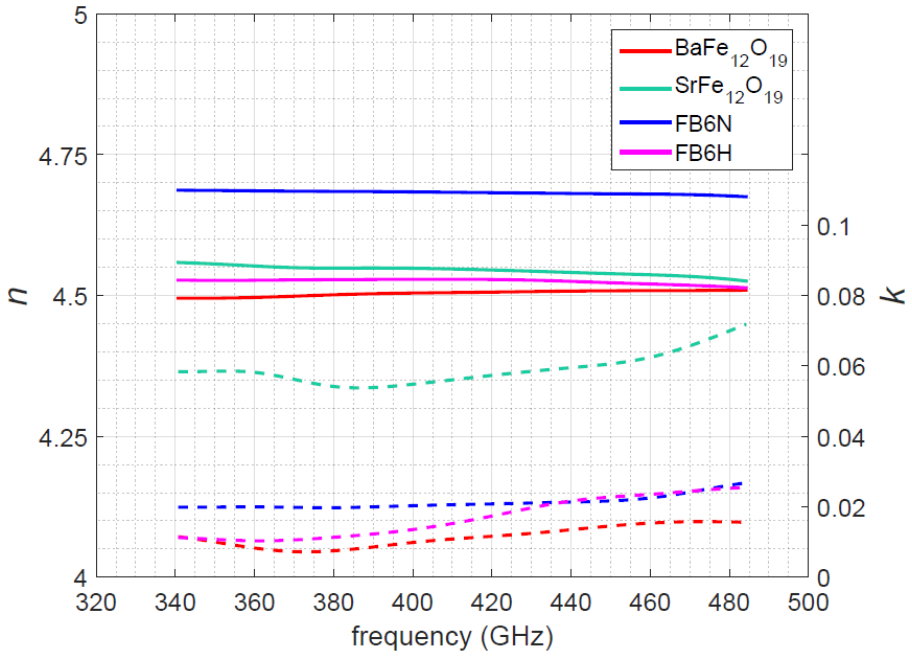

Figure 3.23: Calculated refractive indices of all samples, full lines represent the real parts and dotted lines represent the imaginary parts of $\hat{n}$.

agreement with these published results.

These measurements have provided information about diagonal elements of the hexaferrite permeability tensor in the frequency band relatively far from the ferromagnetic resonance frequency. The following work, presented in Section 3.3, is focused on the characterization in a wider spectral range as well as on the gyrotropic response of magnetized hexaferrites and therefore full permeability tensor determination. This confirms promising gyrotropic properties in the mm- and sub-mm-wave range with a specific Faraday rotation close to 3.8 rad/cm at 400 GHz. We can however already conclude that contrary to the work reported by Shalaby et. al. [78] and Martin et. al. [77], Sr-based hexaferrites are not necessarily the optimal choice for transmissive NRD (from a losses point of view). The work in Section 3.3 on the measured gyrotropic spectra will allow to determine whether gyrotropy creates a trade-off.

3.2.4.1 Sources of errors

There are several possible sources of errors which can influence extracted materials parameters. All the measurements were performed in a dedicated characterization room with controlled humidity and temperature. Moreover, in the considered frequencies bands (close to 300 GHz) the influence of the water absorption lines is very limited. Because of the samples' magnetic character the determination of parameters must be done with both reflection and transmission measurement. The positioning of the samples must be therefore ensured with very high precision. This is described in the section 3.2.2.2. A properly focused beam on the sample in order to avoid any diffraction is also the key requirement for successful measurement. A first systematic error can arise from an ill-conceived fitting model. In the parameters extraction technique we assume the transmission of a pure plane wave through a sample bordered by two perfectly flat and parallel interfaces. In reality, this geometry is obviously a bit different and all samples, the crystalline ones in particular, can have slightly irregular shape with significant surface roughness (as can be seen in Fig. 3.3 and 3.4 and Table 3.1 in measured values of thicknesses). These errors caused by imperfect samples have been minimized by single-pass contribution extraction. But still the experiment variation from the ideal model can bring up some small uncertainties into the extracted data.

The correct choice of time windows applied on main signal echoes during the TD-gating procedure is an important step as well. The time window must be chosen properly in order to cover all contributions from the desired main echo. Moreover the sampling in the frequency domain must also be a good compromise between necessary sweep time and possible confusing effects due to artificial TD folding of parasitic echoes. When the frequency band is too narrow a finer sampling must be performed in order to distinguish echoes (at the cost of sweep time). But when the sample gets too thin (and echoes fundamentally overlap), there is no other possibility than to include multiple reflections into

the model, thereby eliminating the advantage of the time-gating technique. With typical sample indices of the order of 4 and roughly 100 GHz VNA bandwidth, samples must be minimally a few 100 µm thick for the technique here presented to be advantageously useful.

The procedure of fitting model into data must be done with care in order to obtain correct values of fitted parameters. By using the Kramers-Kronig consistent B-spline model for all parameters and therefore fitting all full spectra in one time we greatly reduced the number of fitting parameters and therefore increased the robustness of the fit. But still it is necessary to study the fit convergence and particularly its relation to the input values of parameters. In some cases a correlation between fitted parameters may compensate an error caused by a non-ideal experiment. This was apparently the case for the Sr-crystalline sample. From permittivity (Fig. 3.21) and permeability spectra (Fig. 3.22) it is evident that the imaginary part of permeability of this sample has higher values than of other samples. This small difference ($\approx 1,5 \cdot 10^{-3}$) could cause also the increase of imaginary part of permittivity because of the parameters correlation. Both these errors come from imperfect measurement caused by combination of small sample size and significant surface roughness (Fig. 3.3).

All these errors may be reduced by making many repeated measurement scans and averaging of these measurements before fitting. This step would however rapidly increase the measurement time and thus basically ruin the main advantage of the VNA-driven continuous-wave measurement.

3.3 MO Properties of Hexaferrite Ceramics

This section is devoted to the full-tensor MO characterization of hexaferrites. Since the main goal was a determination of gyrotropic parameters in wide spectral range, the THz Time-domain spectroscopy (TDS) has been for this purpose more suitable than a VNA-driven quasi-optical setup used in the last section. Moreover due to the working principle of TDS spectroscopy, no standing waves

exist in the setup and it enables a direct recording of just a single pass contribution for MO data treatment.

Gyrotropic hexaferrite ceramic materials are showing up themselves as very promising candidates for operation in nonreciprocal devices (NRD) at THz frequencies especially thank to their high remament magnetization (Fig. 3.7). Their strong gyrotropic and anisotropic properties in a wide band (0.1–1 THz) are investigated by an original magneto-optical THz TDS. A general basic experimental scheme of a typical TDS is shown in Fig. 2.6. The following subsections describe a procedure of the complete full-tensor magneto-optical (MO) characterization of the hexaferrite ceramics and a subsequent calculation of unknown parameters by a numerical fitting procedure. The material chosen for this characterization is the commercially available strontium hexagonal ferrite ceramics with commercial label FB6N. While until now research groups focused mainly on the FB6H ceramics [75, 77], the MO properties of FB6N has not been published anywhere else yet. The comparison of FB series ferrite magnets is shown in Fig. 3.24. The

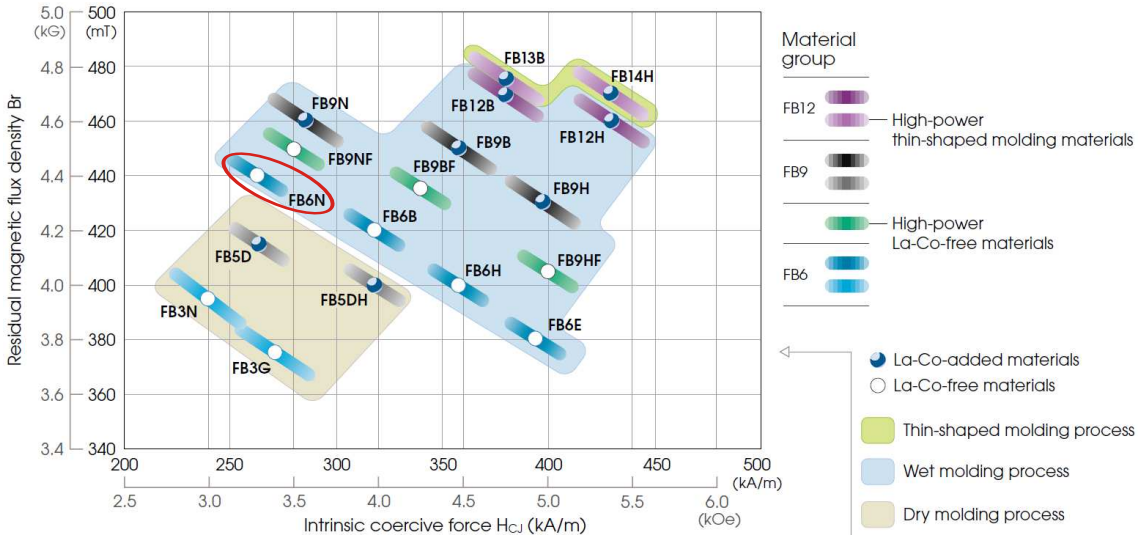

Figure 3.24: Magnetic characteristics distribution charts of FB series as presented by TDK company [184]

ceramics with label FB6N is characterized by higher residual magnetic flux density ($B_r = 440\,\mathrm{mT}$) and lower intrinsic coercitive force ($H_{CJ} = 263\,\mathrm{kA\,m^{-1}}$) with

comparison to the FB6H ($B_r = 400\,\mathrm{mT}$, $H_{CJ} = 358\,\mathrm{kA\,m^{-1}}$). Because gyrotropic properties of magnetic materials are influenced by these intrinsic material parameters, especially by the remanent magnetization value, we expect the FB6N ceramics to have a higher value of magnetization frequency ω_m and thereupon also a higher value of the off-diagonal permeability component κ, determining the gyrotropic properties. Despite this facts, a precise MO characterization is crucial for designing of NRDs.

The whole characterization is divided into two steps. At first the ceramics is characterized in its remanent magnetization state in Faraday configuration, i.e. the magnetization **M** in parallel direction with respect to the incident beam **k**. The second step includes characterization with **M** lying in-plane of the sample, i.e. perpendicularly to **k**. Note that the magnetization direction inside the material is not changed ($\mathbf{M} \parallel c$), we just cut the original bulk material in two different directions. These two configurations provide complete information about on- and off-diagonal permeability tensor components as well as about strong magnetic uniaxial anisotropy along *c*-axis of the hexaferrite ceramics. It is important to mention that all parameters (for both magnetization directions) were obtained in one complete fit which assured the robustness and precision of the procedure. This is strengthened by the fact that both measured sample pieces were initially cut off from one big block of ceramics and therefore some characteristics are identical for both pieces (e. g. ferromagnetic resonance - FMR frequency).

For the characterization we used THz Time-domain Spectrometer TPS Spectra 300 of TeraView Company. This spectrometer allows us to characterize material properties in a wide spectral range (0.1–3 THz). It uses photo-conductive antennas for generation and detection of a THz pulse activated by a femtosecond (fs) pulse from erbium-doped fibre laser with central wavelength of 780 nm and pulse duration shorter than 120 fs. In order to avoid absorptions originating from air, the measurement chamber was during measurement evacuated to residual pressure 0.4 mbar.

3.3.1 Magnetization Perpendicular to the Sample Surface

The hexaferrite ceramics is an uniaxial gyrotropic material with a large spontaneous magnetization **M** with an easy axis along the crystal's *c*-axis (see Fig. 3.2). For the first step of the characterization we chose a sample of size $22.5 \times 21 \times 1.3\,\text{mm}$ with the *c*-axis aligned perpendicularly to its largest surfaces (out-of-plane). Photos of the original block of ceramics and the thin cut, done by a micro-water beam, together with the magnetization direction are shown in Fig. 3.25. Because the M–type hexaferrite ceramics have strong remanent magnetiza-

Figure 3.25: Photos of original block of the Fb6N sample with highlighted preferred magnetization and cut direction and a thin sample after the cut.

tion [69], as shown in Fig. 3.7, the sample was before measurement magnetized by an external electromagnet $(B = 1.6\,\text{T})$ up to its saturation magnetization M_S and characterized in its remanent magnetized state. In this case the resulting spectra are products of pure magneto-optical properties of the hexaferrite itself without influence of any additional external magnetic field which would keep internal magnetic moments perfectly aligned. A linearly-polarized electromagnetic (EM) wave incident perpendicularly on this magnetized sample ($\mathbf{k} \parallel \mathbf{M}$) is then represented as a sum of two counter-rotating circularly-polarized waves, which are characteristic modes of the system. The interaction between one characteristic mode and the precession of magnetic dipoles causes dephasing between both polarizations. These will therefore propagate by different speeds through the gyrotropic hexaferrite, because its refractive indices for right- and left-handed

circularly polarized light are different:

$$\hat{n}_{\pm} = \sqrt{\hat{\varepsilon}_{\pm} \cdot \hat{\mu}_{\pm}} \tag{3.44}$$

and therefore:

$$c/\hat{n}_{-} \neq c/\hat{n}_{+}, \tag{3.45}$$

which is the basic principle of the magneto-optical Faraday effect (as described in section. 2.5.3.1). Because the permittivity $\hat{\varepsilon}_{\pm}$ in Eq. (3.44) is for hexaferrites in THz range same for both polarizations, it is possible to express permeability for these two modes as was explained in Chapter 2 (2.127):

$$\hat{\mu}_{\pm} = \mu \pm \kappa, \tag{3.46}$$

where μ and κ are given by Eqs. (3.26) and (3.27), respectively. Therefore, final expressions for permeabilities become:

$$\hat{\mu}_{\pm} = 1 + \frac{\omega_m}{\omega_0 \mp \omega}. \tag{3.47}$$

One can see that $\hat{\mu}_{+}$ is resonant at FMR frequency ω_0, while $\hat{\mu}_{-}$ is not. This NR Faraday effect causes rotation of a polarization plane when incident light is linearly polarized [114] and it's strongest close to the FMR frequency.

The determination of the complex refractive indices $\hat{n}_{\pm}$ of the hexaferrite ceramics was done by measurement of complex transmittances of the magnetized sample and then subsequent fitting of a model with desired MO parameters into measured data. Because a direct measurement of circularly polarized transmittances over the full frequency band would be rather complicated, we introduced a simpler method including a measurement of linearly polarized transmittances with two mutually perpendicular incoming polarizations and mathematical transforming of these into the circular polarization state. A simple schematic representation of the experiment is shown in Fig. 3.26.

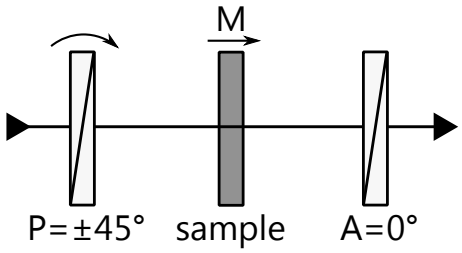

Figure 3.26: Schematic representation of linearly polarized transmittances measurement

Assuming the used polarizers to be quasi-perfect, the MO parameters of the sample are thus determined by measuring time-domain pulses $E_{\pm 45}(t)$ propagating through a polarizer P at positions $-45°$, $45°$, the sample with a thickness d and an analyzer A at $0°$ and a reference pulse $E_{ref}(t)$ through an empty sample holder with both P and A at $0°$. Polarization of an incident THz wave linearly-polarized at an angle given by P is then rotated during the transmission through the gyrotropic sample and the state of outgoing polarization is determined by the analyzer. These measured signals are subsequently transformed into frequency-domain and the linearly polarized complex transmittances $\hat{t}_{-45}(\nu) = E_{-45}(\nu)/E_{ref}(\nu)$, $\hat{t}_{+45}(\nu) = E_{+45}(\nu)/E_{ref}(\nu)$ are then transmitted into circularly polarized transmittances $\hat{t}_{\pm}(\nu)$ with use of Jones formalism, presented in section 2.4.3 as follows:

The incident x-polarized pulse passes through the first polarizer at $\pm 45°$ (its amplitude decreases by factor $\sqrt{2}$ of its initial value) and its polarization state is transformed into circular basis vectors:

$$\frac{1}{2\sqrt{2}} \begin{pmatrix} 1 \pm i \\ 1 \mp i \end{pmatrix} = \frac{1}{\sqrt{2}} \begin{pmatrix} 1 & i \\ 1 & -i \end{pmatrix} \frac{1}{\sqrt{2}} \frac{1}{\sqrt{2}} \begin{pmatrix} 1 \\ \pm 1 \end{pmatrix}, \tag{3.48}$$

the propagation through the sample is represented by **T**-matrix:

$$\frac{1}{2\sqrt{2}} \begin{pmatrix} \hat{t}_+ (1 \pm i) \\ \hat{t}_- (1 \mp i) \end{pmatrix} = \begin{pmatrix} \hat{t}_+ & 0 \\ 0 & \hat{t}_- \end{pmatrix} \frac{1}{2\sqrt{2}} \begin{pmatrix} 1 \pm i \\ 1 \mp i \end{pmatrix}, \tag{3.49}$$

and the product in the circular basis vector is then transformed back into the linear basis vector:

$$\frac{1}{4}\begin{pmatrix} \hat{t}_+(1\pm i)+\hat{t}_-(1\mp i) \\ -i\hat{t}_+(1\pm i)+i\hat{t}_-(1\mp i) \end{pmatrix} = \frac{1}{\sqrt{2}}\begin{pmatrix} 1 & 1 \\ -i & i \end{pmatrix}\frac{1}{2\sqrt{2}}\begin{pmatrix} \hat{t}_+(1\pm i) \\ \hat{t}_-(1\mp i) \end{pmatrix}, \quad (3.50)$$

and the x-component of polarization is detected. Therefore the transmittances $\hat{t}_\pm$ can be expressed as:

$$\frac{1}{4}\begin{pmatrix} (1+i) & (1-i) \\ (1-i) & (1+i) \end{pmatrix}\begin{pmatrix} \hat{t}_+ \\ \hat{t}_- \end{pmatrix} = \begin{pmatrix} \hat{t}_{+45} \\ \hat{t}_{-45} \end{pmatrix}, \quad (3.51)$$

which leads to:

$$\begin{pmatrix} \hat{t}_+ \\ \hat{t}_- \end{pmatrix} = \frac{1}{i}\begin{pmatrix} (1+i) & (i-1) \\ (i-1) & (1+i) \end{pmatrix}\begin{pmatrix} \hat{t}_{+45} \\ \hat{t}_{-45} \end{pmatrix}, \quad (3.52)$$

and therefore to the final relation between $\hat{t}_\pm$ and $\hat{t}_{\pm 45}$ in the form:

$$\hat{t}_\pm(\nu) = (1\mp i)\cdot\hat{t}_{+45}(\nu) + (1\pm i)\cdot\hat{t}_{-45}(\nu). \quad (3.53)$$

These transmittances can be with use of Fresnel formulas (3.35), (3.36) for normal incidence expressed in the form:

$$\hat{t}_\pm(\nu) = t_\pm^{(01)}(\nu)t_\pm^{(10)}(\nu)\exp\left(-\frac{\alpha_\pm(\nu)d}{2}\right)\exp\left(-i\phi_\pm d\right), \quad (3.54)$$

where $t_\pm^{(01)}(\nu)$, $t_\pm^{(10)}(\nu)$ are transmission coefficients of the first and second interface between the air and the sample, respectively. Therefore we can write:

$$\hat{t}_\pm(\nu) = \frac{4n_\pm(\nu)}{\left[n_\pm(\nu)+1\right]^2}\exp\left(-\frac{\alpha_\pm(\nu)d}{2}\right)\exp\left(-i\phi_\pm d\right), \quad (3.55)$$

and real parts of the optical indices and losses of the material for both left- and right-circularly polarized light are respectively given by well-known formulas

[206]:

$$n_{\pm}(\nu) = 1 + \frac{c}{2\pi\nu d}\phi_{\pm}(\nu), \quad \alpha_{\pm}(\nu) = -\frac{2}{d}\ln\left\{A_{\pm}(\nu)\frac{[n_{\pm}(\nu)+1]^2}{4n_{\pm}(\nu)}\right\}, \tag{3.56}$$

where $A_{\pm}(\nu) = \left|\hat{t}_{\pm}(\nu)\right|$ represents the amplitudes and $\phi_{\pm}(\nu) = arg\left(\hat{t}_{\pm}(\nu)\right)$ phases of the circularly polarized transmittances. Figure 3.27 shows measured amplitudes, Fig. 3.28 corresponding calculated extinction coefficient of the ceramics and Fig. 3.29 measured phases for both left- and right- circularly polarized THz radiation, which have been for better illustration of the difference at low frequencies plotted as $\frac{1}{\phi_{\pm}}$ (deg^{-1}).

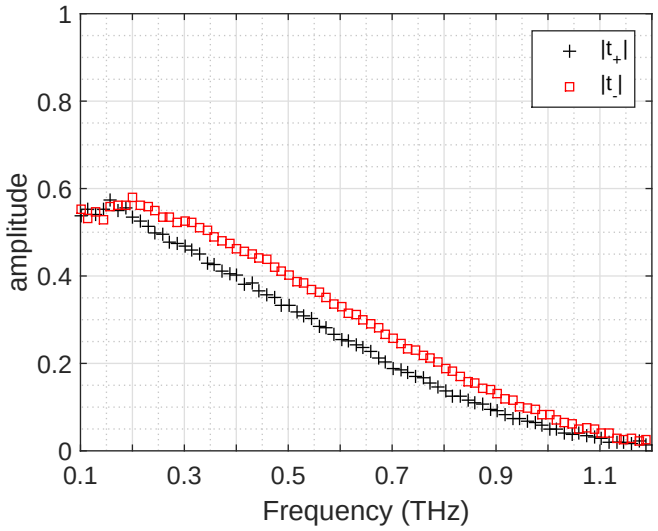

Figure 3.27: Measured amplitudes of circularly polarized transmittances of the hexaferrite for both senses of circularly polarized beam

These figures show increasing losses of the hexaferrite above 200 GHz towards higher frequencies which confirms the fact that the losses in the measured frequency band (which is far form the FMR) originate primarily from dielectric losses. Small increase of losses at frequencies below 200 GHz can come from the imaginary part of permeability, but the measurement sensitivity of the TDS rapidly decreases around 100 GHz, hence it was not possible to extend the measurement range yet to lower frequencies to verify this. However, at higher fre-

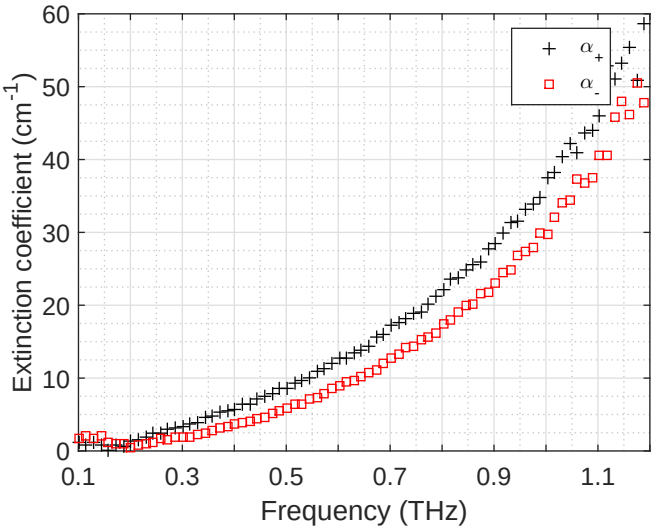

Figure 3.28: Losses of the hexaferrite for both senses of circularly polarized beam

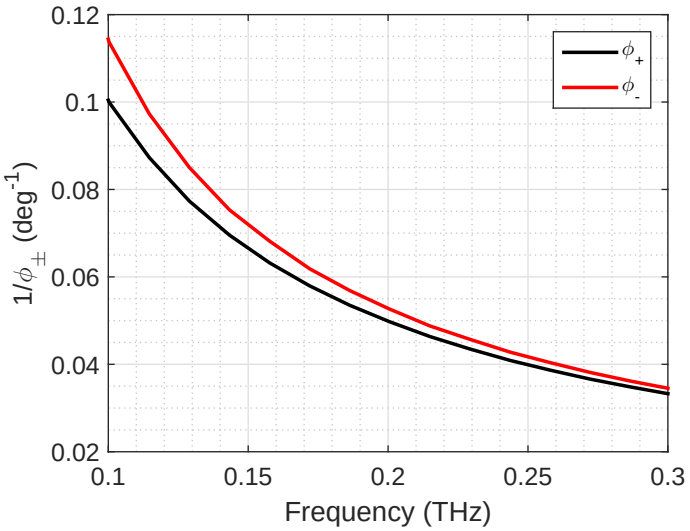

Figure 3.29: Measured phases of circularly polarized transmittances of the hexaferrite for both senses of circularly polarized beam in the range between 100 GHz–300 GHz, plotted as $1/(\phi_{\pm})$

quencies, the imaginary part of $\hat{\mu}$ can be in this study neglected. Because of the expression for the complex optical indices $\hat{n}_{\pm} = \sqrt{\hat{\varepsilon}_r \cdot \mu_{\pm}}$, the observable difference in the measured amplitudes (and thus losses as well) can originate from the term $(\Im(\hat{\varepsilon}_r) \cdot \mu_{\pm})$ as well as from an imperfect experimental setup, for example inaccurate positioning of the polarizers or the measured sample. Final optical indices $n_{\pm}(\nu)$ for both polarizations obtained from the measured transmittances $\hat{t}_{\pm}(\nu)$ and from the fitted model calculated with use of Eq. (3.44) and (3.47) are shown in Fig. 3.30 together with the corresponding model values of tensorial components μ and κ (Fig. 3.31).

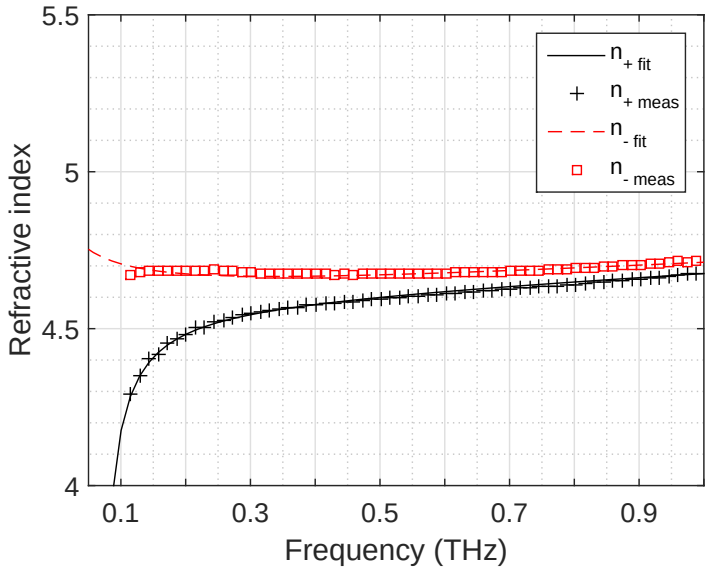

Figure 3.30: Measured and fitted refractive indices for both senses of circular polarization

The numerical fitting of the calculated model was done using MATLAB software and its fitting function *fminsearch* which uses the Nelder-Mead simplex algorithm as described in [207]. The real part of the permittivity was considered to be the same for both polarization orientations and its frequency dependence was described by a simple linear function:

$$\Re(\hat{\varepsilon}_r) = a \cdot (\nu\,[\mathrm{GHz}] - 100) + b \tag{3.57}$$

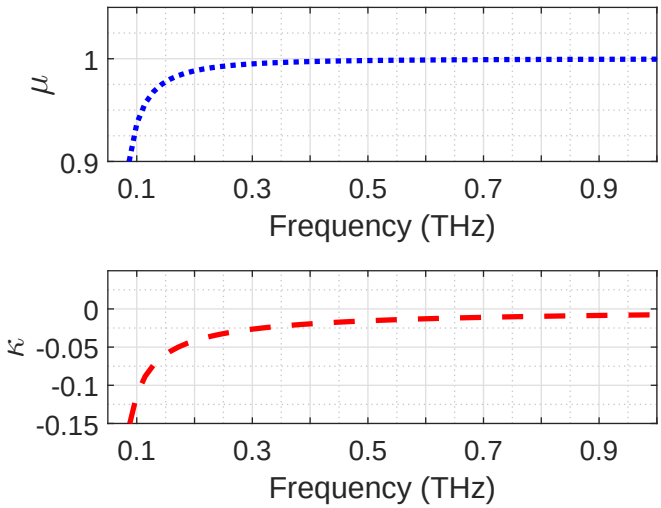

Figure 3.31: Calculated values of the $\bar{\bar{\mu}}$ tensorial components

with two unknown fitting parameters a, b representing an increase of the permittivity with frequency (slope) and its value at 100 GHz, respectively. The linear description of the permittivity has been chosen in order to keep a number of fitting parameters as low as possible, but it still well describes the permittivity behavior in the complete measured frequency band. The permeabilities $\mu_{\pm}$ were determined by fitting of two unknown parameters - the resonance frequency ω_0 and the magnetization frequency ω_m. The final best fit has given these parameters' values:

$$\omega_0 = 2\pi \times 56.3\,\text{GHz},\ \omega_m = 2\pi \times 7.7\,\text{GHz},\ a = 0.001,\ b = 21.1 \tag{3.58}$$

It is possible to see the strong resonance behaviour of the n_+ at lower frequencies while n_- doesn't show that, which corresponds with the permeability description in Eq. (3.47). This difference in the optical indices and the measured sample's FMR (56.3 GHz) give together an indication about strong gyrotropic and hence also nonreciprocal properties of the hexaferrite ceramics in the mm- and sub-mm-wave range, and these parameters will be in the following subsection used for an expression of the frequency-dependent specific Faraday rotation.

3.3.1.1 Faraday Rotation in Hexaferrite Ceramics

The specific Faraday rotation numerically express the angle by which the polarization plane is rotated after a single-pass transmission through an unit of length of the material, when the sample is magnetized in the Faraday configuration, i. e. when $\mathbf{k} \parallel \mathbf{M}$, and is therefore defined as:

$$\Theta_F(\lambda) = -\frac{\pi n_0 Q_m}{\lambda}, \tag{3.59}$$

and with use of Eq. (2.62) for Q_m and Eqs. (3.26), (3.27) for μ and κ we can write:

$$\Theta_F(\nu) = -\frac{n_0 \omega^2 \omega_m}{2c\left(\omega_0^2 - \omega^2 + \omega_0 \omega_m\right)} \tag{3.60}$$

where $n_0 = (n_+ + n_-)/2$. This specific rotation in degrees/mm is shown in Fig. 3.32a. It is possible to observe the largest rotation closer to lower frequencies (and FMR frequency). At high frequencies when $\omega \gg \omega_0 > \omega_m$ this specific rotation can be simplified to:

$$\Theta_{F(\omega \gg \omega_0)}(\nu) \approx \frac{n_0 \omega_m}{2c}, \tag{3.61}$$

and hence it becomes frequency-independent. Because the typical design of a Faraday isolator (as shown in Fig. 2.16) requires rotation of a polarization plane during propagation through a gyrotropic material to be equal to 45°, Fig. 3.32b shows a frequency-dependent required thickness of the ceramics for this 45° rotation. Consequently, we can introduce a figure of merit of the measured ceramics FB6N in order to express the strength of the faraday rotation of the sample combined with the measured material's losses. Hence, this rotation power can be expressed in the form:

$$\Xi(\nu) = \Theta_F(\nu) \cdot d \cdot I(\nu), \tag{3.62}$$

where $d = 1.3\,\text{mm}$ represents the thickness of the ceramics and $I(\nu) = A_{\pm}^2(\nu)$ is the average intensity of the $+$ and $-$ transmitted waves (Eq. (3.56)). The frequency dependent rotation power Ξ is plotted in Fig. 3.33, signifying a possible

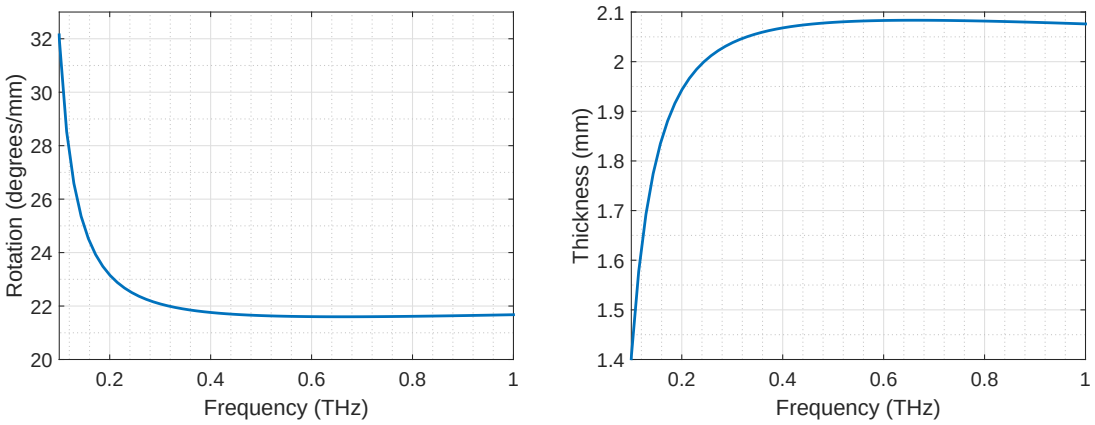

(a) Specific Faraday rotation Θ_F (b) Thickness

Figure 3.32: Calculated specific Faraday rotation and thickness of the ceramics required for 45° polarization rotation

application of the FB6N ceramics in a transmissive THz NRD in the millimeter and sub-millimeter wave ranges.

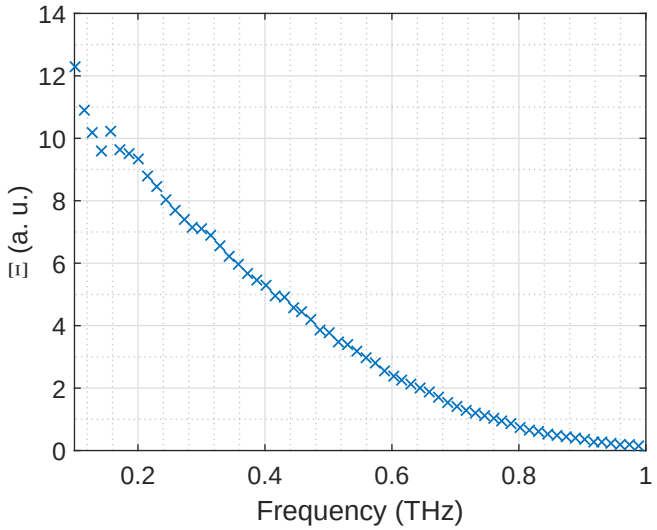

Figure 3.33: Rotation power Ξ of the 1.3 mm thin FB6N ceramics

3.3.2 In-plane Magnetization

Until now we have studied the MO properties of the ceramics magnetized in the direction of the beam propagation **k**. This is of course not a mandatory case when one designs a new THz NRD. Another option is when the magnetization lies in a plane perpendicular to **k**, forming the so-called *transverse* configuration. The second part of the robust magneto-optical characterization therefore included measurement of the ceramics in this transverse configuration. All recorded data, i.e. data from the Faraday and transverse measurements were in the final stage treated together, leading to the one complete and robust fit giving all the important material parameters. The first group of the parameters were presented in (3.58) and the following paragraphs describe a procedure of the transverse characterization. At the end of this second stage we will present all the calculated parameters together.

In the case of the transversely magnetized sample, two different crystallographic directions (a, c) are present in the plane of the hexagonal crystalline lattice. As a result, the MO Cotton-Mouton effect exhibits itself and two normal modes with different optical indices ($\hat{n}_\perp \neq \hat{n}_\parallel$) exist in the material, as was described in section 2.5.3.2. The ordinary wave, characterized by $\hat{n}_\perp$, passes through the material when ($\mathbf{E} \perp c \parallel \mathbf{M} \parallel \mathbf{H}$) and is therefore unaffected by the magnetization of the ferrite. The extraordinary wave with $\hat{n}_\parallel$ is present when ($\mathbf{E} \parallel c \parallel \mathbf{M} \perp \mathbf{H}$) and is affected by the ferrite magnetization. Besides the sig-

Figure 3.34: Photos of original block of the FB6N sample with highlighted preferred magnetization and cut direction and a thin sample with in-plane **M** after the cut.

nificant MO effect, the high crystalline anisotropy of the material plays a key role in the material properties as well, leading to another influence on the optical indices. For the purpose of the MO characterization in the following procedure we chose a sample of size $21 \times 12.7 \times 1.6\,\mathrm{mm}$ which has been by the micro-water jet cutting prepared in a way that the preferred direction of magnetization was aligned inside the sample in parallel with its surface (in-plane) and in perpendicular direction to its longest side, as shown in Fig. 3.34. It was again magnetized at the external electromagnet ($B = 1.6\,\mathrm{T}$, causing alignment of the internal magnetic moments in the direction of the crystal's c-axis) and characterized in its remanent magnetized state. Considering the MO Cotton-Mouton effect together with the high crystalline anisotropy, the ceramics is characterized by two different refractive indices $\hat{n}_{\parallel} \neq \hat{n}_{\perp}$ where subscript denotes a mutual orientation of the c-axis and a polarization of an incident wave. These refractive indices can be expressed as:

$$\hat{n}_{\parallel} = \sqrt{\hat{\varepsilon}_{\parallel}\mu_{\parallel}} \tag{3.63}$$

$$\hat{n}_{\perp} = \sqrt{\hat{\varepsilon}_{\perp}\mu_{\perp}}, \tag{3.64}$$

and the propagation constants for the two perpendicular propagating waves are in the form:

$$\hat{k}_1 = \frac{\omega}{c}\sqrt{\hat{\varepsilon}_{\parallel}\mu_{\parallel}} \tag{3.65}$$

$$\hat{k}_2 = \frac{\omega}{c}\sqrt{\hat{\varepsilon}_{\perp}\mu_{\perp}}. \tag{3.66}$$

It is now apparent, that the effective parameters for the extraordinary wave are $\hat{\varepsilon}_{\parallel}$ and $\mu_{\parallel}$ and for the ordinary wave $\hat{\varepsilon}_{\perp}$ and $\mu_{\perp}$, where permittivities $\hat{\varepsilon}_{\parallel}$ $(\mathbf{E} \parallel c)$ and $\hat{\varepsilon}_{\perp}$ $(\mathbf{E} \perp c)$ can be again described by linear functions:

$$\Re\left(\varepsilon_{\parallel}\right) = a \cdot (\nu\,[\mathrm{GHz}] - 100) + b_{\parallel} \tag{3.67}$$

$$\Re(\varepsilon_{\perp}) = a \cdot (\nu\,[\mathrm{GHz}] - 100) + b_{\perp} \tag{3.68}$$

with the same value of the coefficient a denoting a slope of the linear function

and different values of coefficients $b_{\parallel}$ and $b_{\perp}$ representing the intercepts. The difference in $b_{\parallel}$ and $b_{\perp}$ gives an indication about the crystalline anisotropy, whereas the difference in permeabilities is caused by the Cotton-Mouton effect. The permeability $\mu_{\parallel}$ ($\mathbf{E} \parallel c$) for the one of the EM waves propagating in the ferrimagnetic medium in the direction perpendicular to $\mathbf{M}$ can be expressed as has been demonstrated in Chapter 2:

$$\mu_{\parallel} \equiv \mu - \frac{\kappa^2}{\mu} \tag{3.69}$$

and hence it possesses also a resonant behavior described as:

$$\mu_{\parallel} = \frac{(\omega_0 + \omega_m)^2 - \omega^2}{\omega_{\parallel}^2 - \omega^2}, \omega_{\parallel} = \sqrt{\omega_0 (\omega_0 + \omega_m)}, \tag{3.70}$$

where ω_0 and ω_m have the same values as the sample with the perpendicular magnetization (Eq. 3.58). The ordinary wave with the polarization perpendicular to the c-axis ($\mathbf{E} \perp c$) of a **perfectly saturated** sample is not influenced by magnetization, and therefore the permeability is equal to the permeability of vacuum ($\mu_{\perp} = \mu_0$) and $\hat{k}_2 = \frac{\omega}{c}\sqrt{\hat{\varepsilon}_{\perp}}$, because the magnetization frequency $\omega_{m\perp}$ approaches zero. This second wave therefore propagates as in a nonmagnetic dielectric medium. However in a remanently magnetized sample some of the moments are not anymore well-aligned with the magnetization and can have a non-zero component in any other direction which can influence the ordinary wave. Therefore $\omega_{m\perp}$ has generally a non-zero value which is lower than the remament ω_m and as a consequence the permeability $\mu_{\perp}$ exhibits again a resonance behavior described as:

$$\mu_{\perp} = \frac{(\omega_0 + \omega_{m\perp})^2 - \omega^2}{\omega_{\perp}^2 - \omega^2}, \omega_{\perp} = \sqrt{\omega_0 (\omega_0 + \omega_{m\perp})}. \tag{3.71}$$

This measurement was done by the same setup as the previous one in the similar configuration (Fig. 3.26) with both polarizer P and analyzer A at 0° in order to assure characterization by a vertically polarized beam. Figure 3.35 shows schemes of both measured senses of magnetization $\mathbf{M}$.

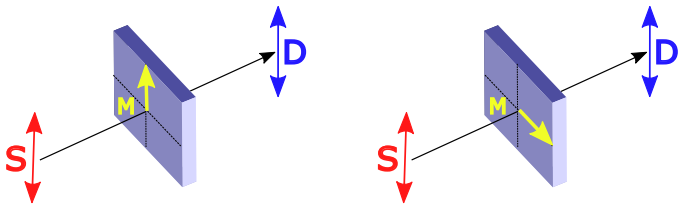

Figure 3.35: Schematic representation of two orientations of the sample with respect to the incident beam's polarization, S and D stay for the source and the detector, respectively

The two measured sample time-domain pulses $E_{\parallel}(t)$, $E_{\perp}(t)$ and the reference pulse $E_{ref2}(t)$ (without sample) are then transformed into the frequency-domain and into the linearly polarized complex transmittances $\hat{t}_{\parallel}(\nu) = E_{\parallel}(\nu)/E_{ref2}(\nu)$, $\hat{t}_{\perp}(\nu) = E_{\perp}(\nu)/E_{ref2}(\nu)$. Figure 3.36 shows the time-domain pulses $E_{\parallel}(t)$ at $t = 34.1\,\mathrm{ps}$ and $E_{\perp}(t)$ at $t = 32.6\,\mathrm{ps}$ and one can see the delay of the $E_{\parallel}(t)$ pulse, which can give a first indication of the difference between real parts of optical indices, $n_{\parallel}$ and $n_{\perp}$, as follows:

$$\Delta t = t_2 - t_1 = \frac{dn_{\parallel}}{c} - \frac{dn_{\perp}}{c} \tag{3.72a}$$

$$\Delta n = \left(n_{\parallel} - n_{\perp}\right) = \frac{c}{d}\Delta t \tag{3.72b}$$

$$\Delta n = \frac{3 \times 10^{8}\,\mathrm{m\,s^{-1}}}{1.6 \times 10^{-3}\,\mathrm{m}} 1.5 \times 10^{-12}\,\mathrm{s} = 0.28. \tag{3.72c}$$

The complex refractive indices of the sample for both mutual orientations of the magnetization and the incident linear polarization are calculated with using of Eq. (3.56) and plotted in Fig. (3.37) together with fitted models, which were calculated using Eqs. (3.63)–(3.71).

These models have been fit together with the perpendicular magnetization and therefore added 3 more parameters into the robust and complex fit: $b_{\parallel}$, $b_{\perp}$ and $\omega_{m\perp}$ which in total with perpendicular magnetization gives 7 fitting parameters. The final values of all parameters from the full measurement procedure are

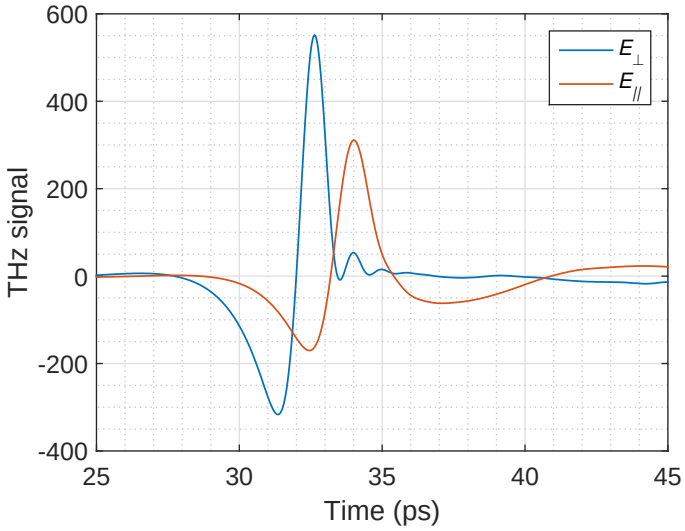

Figure 3.36: Time-domain signal for two orientations of the sample with respect to the incident polarization

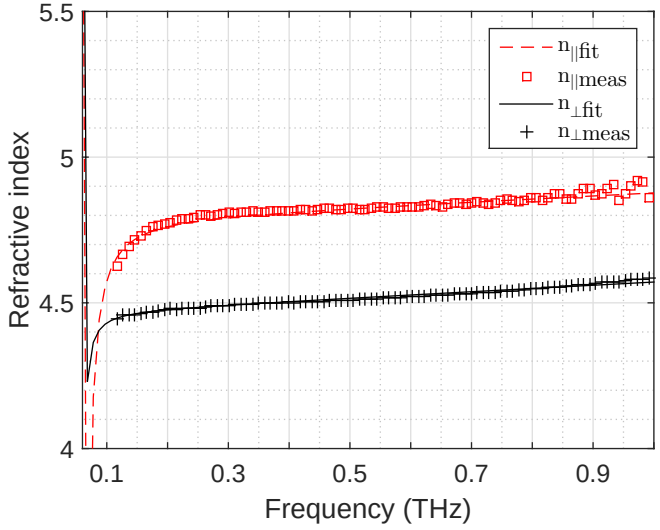

Figure 3.37: Measured and fitted refractive indices for both orientations of magnetization

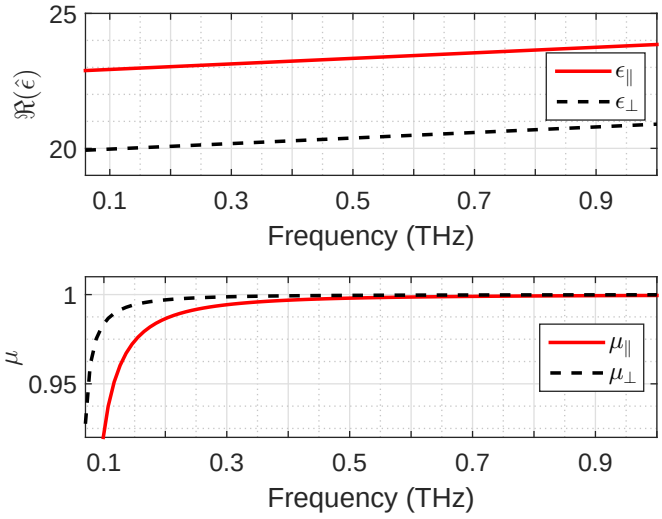

Figure 3.38: Calculated permittivity and permeability for both orientations of magnetization

summarized here:

$$\omega_0 = 2\pi \times 56.3\,\text{GHz},\ \omega_m = 2\pi \times 7.7\,\text{GHz},\ a = 0.001,\ b = 21.1$$
$$\omega_{m\perp} = 2\pi \times 1.9\,\text{GHz},\ b_{\perp} = 20.0,\ b_{\parallel} = 22.9. \tag{3.73}$$

Figure 3.38 shows the calculated permittivities and permeabilities from the fitted parameters. One can see the difference between $\Re(\hat{\varepsilon}_{\parallel})$ and $\Re(\hat{\varepsilon}_{\perp})$ giving a clear proof of the strong crystalline anisotropy of the hexaferrite ceramics when the c-axis lies in the sample plane as well as the difference in $\mu_{\perp}$ and $\mu_{\parallel}$ at low frequencies caused by the MO Cotton-Mouton (Voigt) effect. Both permeabilities show resonant behavior, the $\mu_{\parallel}$ with the same resonant parameters as in the perpendicular magnetization and $\mu_{\perp}$ with the magnetization frequency $\omega_{m\perp} = 2\pi \times 1.9\,\text{GHz}$. This confirms the fact that in the remanent magnetized state some of the magnetic moments can have a small component not perfectly aligned with the total internal magnetization, but still keeping strong permanent magnet properties of the ceramics. These differences in permittivities and permeabilities together have an impact on the difference between the material optical indices (Fig. 3.37).

All the hereby obtained parameters give us complex information about the magneto-optical properties of the hexagonal ferrite ceramics FB6N magnetized both in the direction of **k** or in parallel direction to **k**. Moreover, the fact that two measurement steps were treated together and the important parameters have been obtained by one complex fit, proves the self-consistency of the whole MO characterization procedure.

3.4 Faraday Isolation

After the determination of strong gyrotropic properties of the hexaferrite ceramics in the wide frequency range (0.1 THz–1 THz) we now present an experiment of Faraday isolation with the magnetized sample FB6N in the mm-wave range, thus in the frequency band 210 GHz–335 GHz. The measurement was done by a similar quasi-optical setup as presented in section (3.2.1.1), but now with use of lenses with a longer focal distance instead of parabolic mirrors in order to reduce the angular width of the incident beam and to perfectly control the incident polarization. A schematic representation and a photograph of the setup are shown in Fig. 3.39. It consists of the vector network analyzer, frequency extenders (transmit and receive) for the band 210–325 GHz (401 frequency points), pair of conical horn antennas, four polyethylene lenses for beam focusing, two polarizers (P1, P2) and a sample holder. The polarizers we used for complete characterization of the rotation angle, since the horns can emit and receive only a vertically-polarized wave. The sample was placed in such a way that its magnetization was in the parallel direction to the beam propagation from the horn 1 to the horn 2. In order to reduce multiple reflections from the components and corresponding standing waves in the setup, we placed THz absorbers (A) around the exits of horns, as marked in Fig. 3.39 by green arrows.

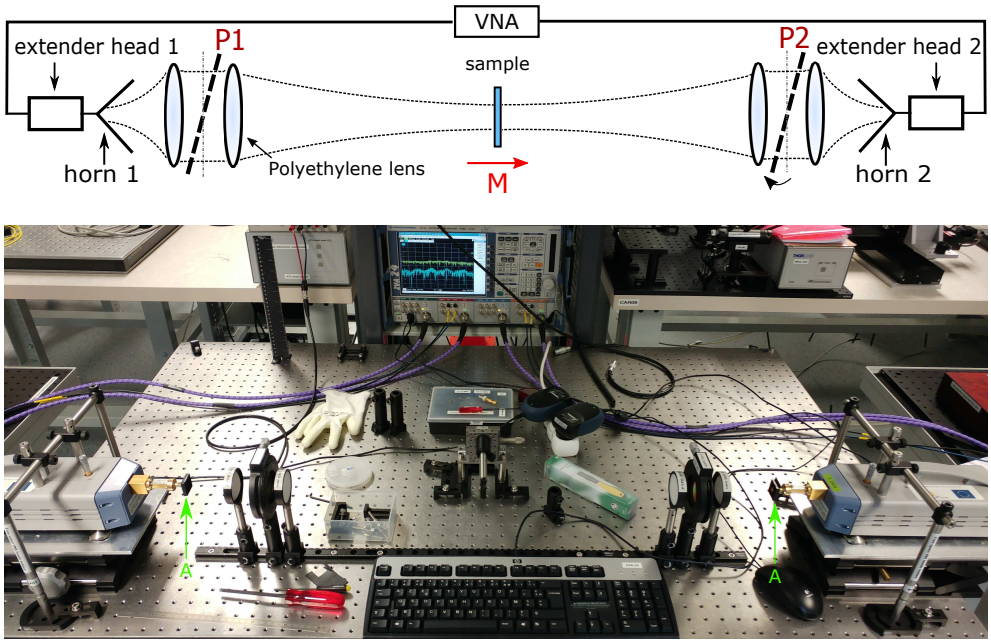

Figure 3.39: A schematic representation (top) and a photograph (bottom) of the quasi-optical setup for Faraday isolation experiment with a focused beam.

3.4.1 Transmission Through a Magnetized Sample

Here we present the calculation of the parameters S_{21} characterizing transmission from the horn 1 through the magnetized sample into the horn 2 and S_{12} describing the transmission in the opposite sense, from the horn 2, through the sample into the horn 1. For this purpose the Jones calculus, presented in section (2.4.3), is used. The measured sample physically represents a single magnetic layer of the thickness d sandwiched between two isotropic half spaces. The Jones transmission matrix $\mathbf{T}$ of this magnetic layer relating the complex electric field amplitudes of the incident (i) and transmitted (t) waves is in the form [208]:

$$\begin{pmatrix} E_x^{(t)} \\ E_y^{(t)} \end{pmatrix} = \underbrace{\begin{pmatrix} t_{xx} & t_{xy} \\ t_{yx} & t_{yy} \end{pmatrix}}_{\mathbf{T}} \begin{pmatrix} E_x^{(i)} \\ E_y^{(i)} \end{pmatrix}, \tag{3.74}$$

where the Jones matrix elements for the gyrotropic material taking into account multiple reflections inside the layer are in the form:

$$t_{xx} = t_{yy} = \frac{1}{2}\left(\frac{t_+^{(01)} t_+^{(10)} \exp\left(-i\beta_+^{(1)}\right)}{1 + r_+^{(01)} r_+^{(10)} \exp\left(-2i\beta_+^{(1)}\right)} + \frac{t_-^{(01)} t_-^{(10)} \exp\left(-i\beta_-^{(1)}\right)}{1 + r_-^{(01)} r_-^{(10)} \exp\left(-2i\beta_-^{(1)}\right)} \right), \tag{3.75}$$

$$t_{yx} = -t_{xy} = \frac{1}{2} i \left(\frac{t_+^{(01)} t_+^{(10)} \exp\left(-i\beta_+^{(1)}\right)}{1 + r_+^{(01)} r_+^{(10)} \exp\left(-2i\beta_+^{(1)}\right)} - \frac{t_-^{(01)} t_-^{(10)} \exp\left(-i\beta_-^{(1)}\right)}{1 + r_-^{(01)} r_-^{(10)} \exp\left(-2i\beta_-^{(1)}\right)} \right), \tag{3.76}$$

with

$$\beta_\pm^{(1)} = \frac{\omega}{c} \hat{n}_\pm^{(1)} d. \tag{3.77}$$

The Fresnel reflection coefficients are expressed as:

$$r_\pm^{01} = -r_\pm^{10} = \frac{n^{(0)} - \hat{n}_\pm^{(1)}}{n^{(0)} + \hat{n}_\pm^{(1)}}, \tag{3.78}$$

and transmission coefficients as:

$$t_\pm^{(01)} = \frac{2n^{(0)}}{n^{(0)} + \hat{n}_\pm^{(1)}}, \tag{3.79a}$$

$$t_\pm^{(10)} = \frac{2\hat{n}_\pm^{(1)}}{n^{(0)} + \hat{n}_\pm^{(1)}}, \tag{3.79b}$$

where $n^{(0)} = 1$ is the optical index of the surrounding medium (air) and the optical index of the gyrotropic material is, considering the permeability given by (3.46), in the form:

$$\hat{n}_\pm^{(1)} = \sqrt{\hat{\varepsilon}_r \cdot (\mu \pm \kappa)} \tag{3.80}$$

and the permeability tensor components μ and κ are presented in Fig. 3.31.

Now we can express the polarization properties of the whole measuring system with use of the multiplication of **T** matrices of all individual components (Eq.

2.56), for the beam direction from the horn 1 into the horn 2 as follows:

$$\underbrace{\begin{pmatrix} E_x^{(2)} \\ E_y^{(2)} \end{pmatrix}}_{\mathbf{J2}} = \underbrace{\begin{pmatrix} \cos\beta^2 & \sin\beta\cos\beta \\ \sin\beta\cos\beta & \cos\beta^2 \end{pmatrix}}_{\mathbf{P2}} \underbrace{\begin{pmatrix} t_{xx} & t_{xy} \\ t_{yx} & t_{yy} \end{pmatrix}}_{\mathbf{T}} \cdot \underbrace{\begin{pmatrix} \cos\alpha^2 & \sin\alpha\cos\alpha \\ \sin\alpha\cos\alpha & \cos\alpha^2 \end{pmatrix}}_{\mathbf{P1}} \underbrace{\begin{pmatrix} 0 \\ 1 \end{pmatrix}}_{\mathbf{J1}}, \tag{3.81}$$

Because the horns can detect only y-polarized component of the electric field, the measured complex transmission parameter S_{21} corresponds to a ratio of the resulting complex amplitude $E_y^{(2)}$ with the sample placed and a complex amplitude $E_{0y}^{(2)}$ of a reference transmission with the sample removed. Similarly it is possible to express the complex parameter S_{12} as the ratio of the resulting complex amplitude $E_y^{(1)}$ and a reference amplitude $E_{0y}^{(1)}$ by changing the wave direction for the opposite one and therefore by an exchange of the matrices **P1** and **P2**, the Jones vectors **J1** and **J2** and the optical indices $\hat{n}_+^{(1)}$ and $\hat{n}_-^{(1)}$ in the **T**-matrix in (3.81). Note, that the rotation angles α, β of P1 and P2, respectively, must be defined with respect to the propagating beam direction.

The whole measurement was done at two positions of the polarizer P1 (0° and −45°) and by changing the position of the polarizer P2 from 0° to 355° with a 5° step, for both P1 positions, all defined from y-axis. In total we measured 144 combinations of the polarizers positions. Figure 3.40 shows measured values of the parameters S_{21} and S_{12} as well as the values calculated with use of Eq. (3.81) for $\alpha = 0°$ and $\beta = 50°$. The parameters are expressed in decibels for which holds:

$$S_{12,21}\,(\mathrm{dB}) = 20\log_{10}\left(\frac{\left|E_y^{(1,2)}\right|}{\left|E_{0y}^{(1,2)}\right|}\right). \tag{3.82}$$

The figure 3.40 confirms the high isolation configuration (more than 15 dB of difference between S_{21} and S_{12}) and confirms the calculated material parameters of the hexaferrite ceramics. The specific Faraday rotation of the ceramics within this

measured frequency range is close to $22\,^\circ\,\mathrm{mm}^{-1}$. Therefore, after the transmission through the sample with the thickness of 1.3 mm, the polarization is rotated by approx. 28°. Then the wave passes through the P2 at 50° and the vertical component of polarization is detected by the horn 2. This causes the forward insertion losses of the parameter S_{21} to be around 10 dB. Both parameters also show typical FP fringes originating from the multiple roundtrips within the measured material and the high-frequency oscillations coming from standing waves between the setup components.

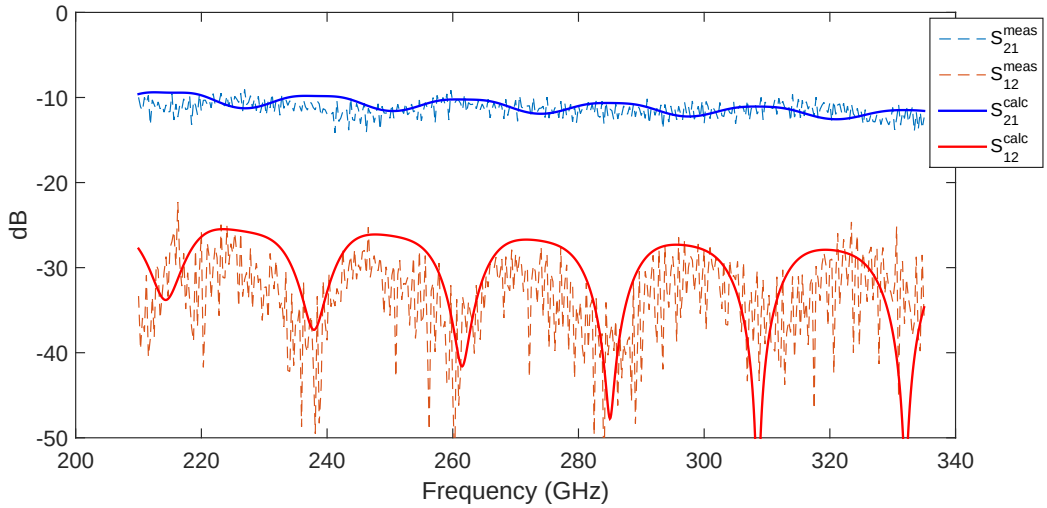

Figure 3.40: Measured (dashed lines) and calculated (full lines) transmission parameters S_{21} (blue) and S_{12} (red) with the P1 at 0 degree and P2 at 50 degree showing a high isolation configuration.

The difference between both S transmission parameters is purely originating from the nonreciprocal behavior of the ceramics, since the measurement system is completely symmetrical. The proof of this is a complete reciprocal transmission with both P1 and P2 at 0°, as shown in Fig. 3.41, where both S parameters acquire the same values (calculated curves are totally overlapping), because the detected vertical components of polarization have the same values for both transmission directions, as schematically depicted in Fig. 3.42.

At this configuration both S parameters acquire lowest forward losses origi-

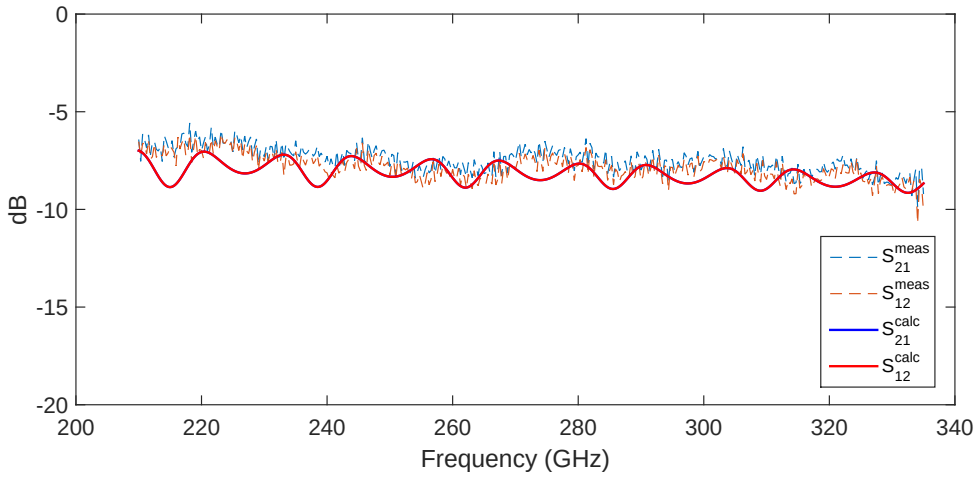

Figure 3.41: Measured (dashed lines) and calculated (full lines) transmission parameters S_{21} (blue) and S_{12} (red) with the P1 at 0 degree and P2 at 0 degree showing a complete reciprocal transmission configuration.

nating purely from the gyrotropic sample and not from the polarizers' misalignment.

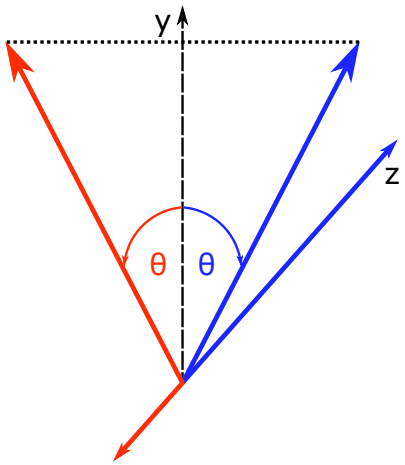

Figure 3.42: Schematic representation of the reciprocal transmission when both P1 and P2 are at 0°. The Faraday rotation in the gyrotropic sample is represented by the angle θ and the vertical polarization components are identical

The measurement of all positions of P2 was done in order to verify a measurement 180° symmetry. A confirmation of this is shown in Fig. 3.43 where we can see the identical S_{12} parameters spectra with P1 at 0° and P2 at 50° and 230°.

This experiment with observed high isolation (more than 15 dB) confirms the cal-

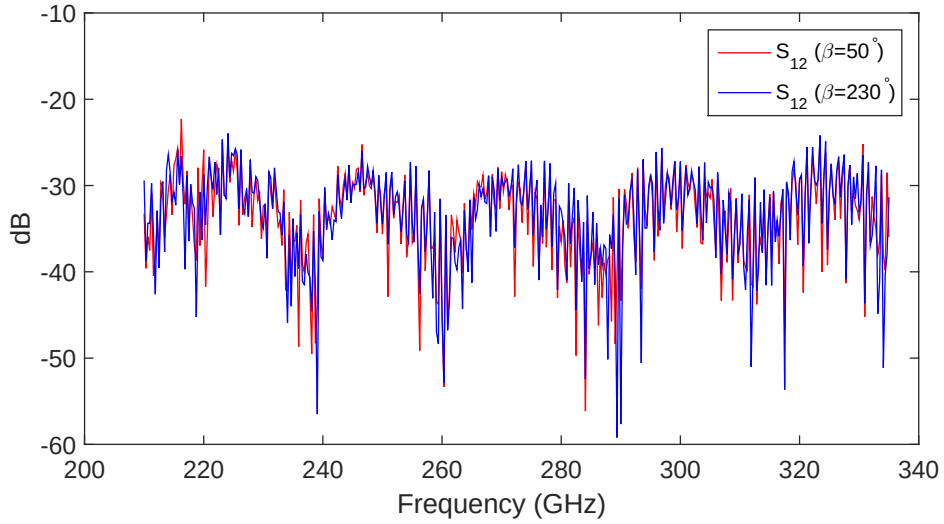

Figure 3.43: Measured transmission parameters S_{12} with the P1 at 0° and P2 at 50° (blue) and 230° (red) showing the 180° polarization symmetry a confirming thus the polarizers' accuracy

culated strong gyrotropic properties of hexaferrite ceramics and its promising potential for application in THz NRD.

3.5 Conclusion of the Chapter

This chapter summarized properties of MO hexagonal ferrites. We presented the crystal structure, anisotropy and magnetic properties as well as the origin of the permeability tensor. In the next part, the procedure of free-space characterization and extraction of $\hat{\varepsilon}_r$, $\hat{\mu}_r$ and $\hat{n}$ of several different types of hexaferrites was presented. The main advantage of the free-space quasi-optical measurement methods in comparison to standard TD terahertz spectroscopy is mainly the higher frequency resolution and higher speed of scans. All unwanted free-space measurement effects such as multiple reflections inside samples or multiple reflections between the setup components and samples were filtered out by the TD-gating technique. Thanks to this method we were also able to measure the reflection with very high precision in order to extract both complex permittivity and complex permeability of the samples. This extraction technique is applicable also for other types of unideal small samples where the precise position of a sample and a reference is crucial and where multiple echoes could negatively influence measured data. The calculated parameters are consistent with some of the published literature on hexaferrites. They give moreover some guidance on the choice of ideal hexaferrite for transmissive NRD. The following part of the chapter is focused on magneto-optical characterization of hexaferrite ceramics FB6N, because it possesses a high remanent magnetization. This material was in the remanent magnetization characterized by THz Time-domain spectroscopy both with **M** out-of-plane and in-plane. The parameters obtained in the one complex fit confirm the strong gyrotropic properties of the ceramics in the millimeter-wave and the sub-millimeter-wave range and allow it to be used for design of a THz NRD. Consequently, we show the specific Faraday rotation of the propagating polarization plane and related thickness of the ceramics which is required for 45° rotation. The introduced figure of merit also showed a possibility of use of the ceramics in a transmissive NRD up to 1 THz. The chapter is finished by an original free-space mm-wave isolation measurement showing a large difference in the

S transmission parameters and confirming therefore a strong Faraday isolation provided by the magnetized hexaferrite ceramics.

CHAPTER 4

Terahertz Nonreciprocal Mirror

Contents

This chapter is devoted to the complete design of the novel THz isolator using a magneto-plasmonic reflecting surface. The transversely magnetized gyrotropic substrate gives rise to the transverse magneto-optical Kerr effect upon reflection of EM radiation. As was discussed in Section 2.5.2, this effect appears for an incident linearly polarized wave, and for gyromagnetic hexaferrites this must necessarily be *s*-polarized. This effect does not provide polarization or mode conversion, what is important for the functionality of the whole device.

For an enhancement of the typically weak MO effect we will make use of the concentration of the local field caused by an excitation of surface plasmons polaritons. In Section 2.6 there was explained that surface plasmons require for their existence an interface between materials with opposite sign of real parts of the permittivity, e. g. metal/dielectric interface. Moreover, for an excitation of SPPs at THz frequencies (*spoof plasmons*) by an *s*-polarized wave, the corresponding metallic layer must be necessarily patterned by a 2-dimensional periodic structure (or with some 2D asymmetry). In our models we will use two kinds of 2D

patterns - square blocks and holes in the layer of gold. For the substrate we use the hexaferrite ceramics and all material parameters were determined in Chapter 3.

The proposed NR device consists of 2 basic elements - the gyrotropic substrate on which there is deposited a structured metallic layer. We will first take a look at the optical properties of gold at THz frequencies, as the material used for the metal layer. The principal part of this chapter is focused on the design of the periodic metal structure for the spoof plasmons excitation. In the Section 2.6 we saw that an EOT effect at metal gratings can be caused both by a presence of SPPs or by FP resonances in the holes. The FP resonances alone however do not interact with a MO substrate and therefore do not provide any (or very weak) enhancement of the TMOKE effect if they are not coupled with the SPPs at the interface [80]. We have to thus focus on the plasmonic resonances as the principal phenomena for the interaction with the substrate gyrotropy and hence for providing of the EOT and TMOKE effects coupling. This proposed isolator, working in a reflection configuration, may significantly reduce insertion losses originating from the gyromagnetic hexagonal ferrite substrate, as there is no need of an EM wave propagation through the magnetized medium.

We also demonstrate the possibility of spoof SPPs excitation by *TE*-polarized incident light using a periodically structured layer of gold fabricated on a crystalline quartz substrate. The presence of SPPs were confirmed both numerically and experimentally with a strong agreement. These results were then used as initial data for designing of a similar structure of holes on the surface of the hexaferrite ceramics.

4.1 Optical Properties of Gold at THz Frequencies

For precise calculations and simulations it is necessary to describe material properties of all used components. Since the hexaferrites characterization was presented in Chapter 3, here we present the optical function of gold which is used as

the metal for the envisaged periodic structure.

The permittivity of gold is according Eq. (2.15) a complex function of an angular frequency ω, which can be described by Drude model, presented in Section 2.6.1.1:

$$\hat{\varepsilon}(\omega) = \varepsilon_1(\omega) - i\varepsilon_2(\omega) = \hat{n}^2(\omega) \tag{4.1}$$

$$\hat{\varepsilon}(\omega) = \varepsilon_\infty - \frac{\omega_p^2}{\omega^2 - i\omega\omega_\tau}, \tag{4.2}$$

and the real and imaginary part of the permittivity take the form:

$$\varepsilon_1(\omega) = \varepsilon_\infty - \frac{\omega_p^2}{\omega^2 + \omega_\tau^2} \tag{4.3}$$

$$\varepsilon_2(\omega) = \frac{\omega_p^2\omega_\tau}{\omega^3 + \omega\omega_\tau^2}, \tag{4.4}$$

where the plasma frequency ω_p can be expressed as:

$$\omega_p\left(\mathrm{cm}^{-1}\right) = \frac{1}{2\pi c}\sqrt{\left(\frac{4\pi N e^2}{m_e\varepsilon_\infty}\right)}, \tag{4.5}$$

where N represents the free electron density, e the electron charge, m_e the electron effective mass and ε_∞ stands for the dielectric constant at high frequencies. The damping frequency ω_τ is then expressed as:

$$\omega_\tau\left(\mathrm{cm}^{-1}\right) = \frac{1}{2\pi c\tau}, \tag{4.6}$$

where τ is the electron lifetime in seconds. For gold the parameters ω_p and ω_τ were presented by Ordal *et al.* [209, 210]:

$$\omega_p(\mathrm{Au}) = 7.28 \times 10^4\,\mathrm{cm}^{-1}, \quad \omega_\tau(\mathrm{Au}) = 2.15 \times 10^2\,\mathrm{cm}^{-1}. \tag{4.7}$$

The real and imaginary parts of the dielectric function of gold at THz frequencies are plotted in Fig. 4.1. It is apparent, that both real and imaginary parts acquires

high negative values $(10^5 - 10^6)$ at 1 THz signifying the PEC-like optical properties of gold at THz frequencies.

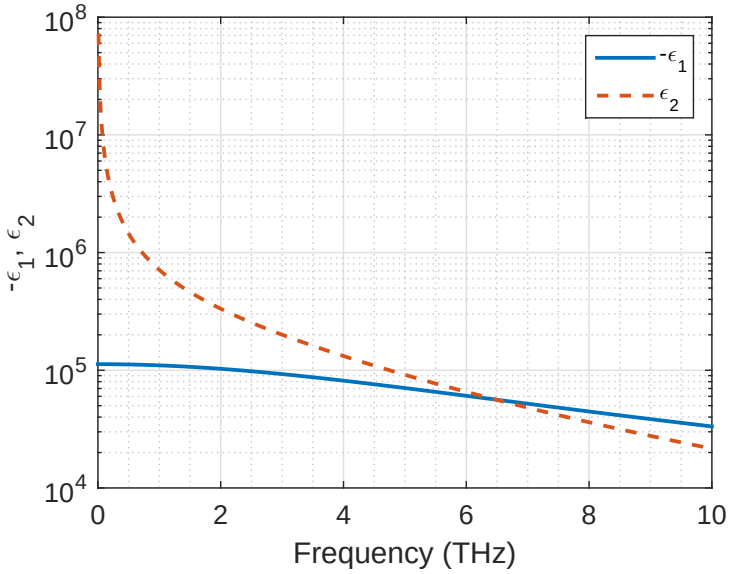

Figure 4.1: Real (ε_1) and imaginary (ε_2) parts of permittivity of gold obtained from Drude model

Another important quantity which influences plasmonic behavior of a metal is a penetration depth of an EM wave. The well-known Beer-Lambert law [211, 212] says that the intensity of an EM wave exponentially decays when propagating through an absorbing medium with a refractive index $\hat{n} = n - i\kappa$:

$$I(z) = I_0 \exp(-\alpha z), \tag{4.8}$$

where $\alpha = 4\pi\kappa/\lambda$ represents the attenuation coefficient and the penetration depth is then in the form:

$$\tau_p = \frac{1}{\alpha} = \frac{\lambda}{4\pi\kappa}. \tag{4.9}$$

This penetration depth quantifies a depth at which the intensity or power of the field decays to 1/e of its surface value. Figure 4.2 shows a dependence of the penetration depth on a frequency for gold. This also denotes a minimal thickness of gold for a proper plasmonic behavior of a structured surface since any

penetration of radiation through the metal into a substrate is not desirable.

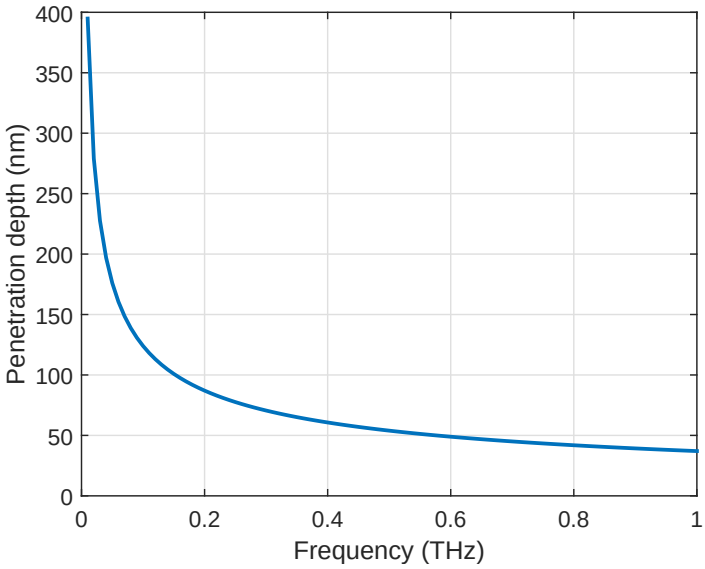

Figure 4.2: Penetration depth in gold

4.2 Design of Plasmonic Structure

In this section we are focusing on the transformation of the proposed isolator concept into a working device. Material parameters of the substrate material - hexaferrite - were presented in Chapter 3 and of the gold in Section 4.1. The idea now is to design a structured gold layer on the surface of the hexaferrite ceramics in order to be able to excite designer plasmons in the mm-wave range. As we saw in Section 2.6, by proper structuring of a noble metal one can be able to excite surface plasmons even when the metal has usually in the THz range PEC-like properties. The presence of SPPs at the interface between the metallic layer and the ceramic appears as a local field enhancement causing an EOT effect of an incident EM wave. When combined with the MOKE caused by the transversely magnetized substrate this can lead into a nonreciprocal shift of the resonant frequency depending on the magnetization direction. For the SPPs excitation we studied two, mutually reversed, structures - 2D holes in the metal layer and 2D

square blocks of the metal (separated by thin slits). In the following sections we describe both designs more in detail and we study the possibility of the plasmons excitation and the behavior of the resonance with varying structural parameters.

4.2.1 2D Holes

This section is devoted to the study of the device design with a metallic layer patterned by 2D holes. First of all we demonstrate the spoof plasmons excitation in the mm-wave range with a patterned gold layer deposited on a low-loss quartz substrate. The real fabricated sample was characterized by THz-TDS and measured data well-fit with our numerical simulations. This was followed up by a designing of a similar gold structure for the use with a hexaferrite substrate. We numerically studied how the resonance frequency behaves when the substrate permittivity changes and also with varying holes size. Numerical simulations then resulted into a design which was fabricated for characterization measurements and the presence of spoof plasmons has been experimentally confirmed.

4.2.1.1 Experimental Demonstration of SPPs in Millimeter-Wave Range

This section presents results of a numerical study and an experimental demonstration of spoof SPPs in mm-wave range with use of our fabricated device which will be then followed by a design of a similar structure on the surface of the hexaferrite ceramics. In their recent work Bhattarai *et al.* [89] presented a structure of a patterned gold layer deposited on a fused silica substrate, which supports an excitation of SPPs at frequencies close to 1 THz. We take up on their work and design a similar structure for plasmons presence close to 250 GHz. In order to avoid high insertion losses of the fused silica, we use low-loss crystalline quartz as the substrate material.

The plasmonic structure for mm-wave spoof SPPs excitation is shown in Fig. 4.3 and consists of a periodic array of holes with a diameter $d = 300\,\mu\text{m}$ and a lattice period $\Lambda = 600\,\mu\text{m}$ in a layer of gold with a thickness $h = 500\,\text{nm}$ fabricated

on the quartz substrate with a thickness $h_{sub} = 240\,\mu\text{m}$. The cut-off frequency of the holes is determined by their diameter:

$$\nu_{\text{cut-off}} = \frac{\chi'_{m,n} \cdot c}{\pi d}, \tag{4.10}$$

where $\chi'_{m,n}$ represents zeros of derivative $J'_m\left(\chi'_{m,n}\right) = 0$, $(n = 1, 2, 3, \ldots)$ of Bessel function $J_m(x)$. For $m = 1, n = 1$ we obtain $\chi'_{1,1} = 1.8412$ and therefore the cut-off of the circular holes is in the form

$$\begin{aligned} \nu_{\text{cut-off}} &= \frac{1.8412 \times c}{\pi d} \\ \nu_{\text{cut-off}} &= \frac{1.8412 \times 3 \times 10^8\,\text{m}\,\text{s}^{-1}}{\pi \times 300 \times 10^{-6}\,\text{m}} \\ \nu_{\text{cut-off}} &= 586.1\,\text{GHz} \end{aligned} \tag{4.11}$$

This cut-off frequency denotes that EM radiation with a frequency lower than $\nu_{\text{cut-off}}$ (and with longer wavelength than $\lambda_{\text{cut-off}}$) cannot pass through the metal layer and all modes in the holes are evanescent.

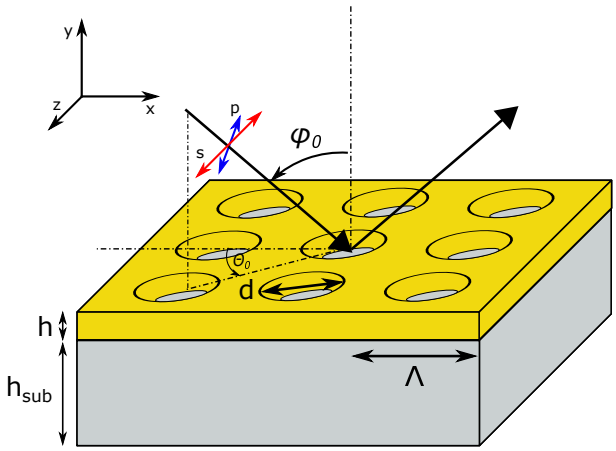

Figure 4.3: Schematic representation of the THz plasmonic device: gold layer patterned by 2D periodic structure of circular holes with period Λ, holes diameter d and thickness h on a quartz substrate of thickness h_{sub} with incident s- or p-polarized plane wave at an angle of incidence ϕ_0 and an azimuthal angle θ_0.

Now we take a look at the calculation of resonant frequencies of this plas-

monic structure. The properties and excitation of SPPs were described in section (2.6.1). For a planar interface between a dielectric and a metal the propagation constant is given by the dispersion relation in Eq. (2.179c), where the dielectric functions of both materials are generally complex:

$$k_{spp} = \beta = \frac{\omega}{c}\sqrt{\frac{\hat{\varepsilon}_1\hat{\varepsilon}_2}{\hat{\varepsilon}_1 + \hat{\varepsilon}_2}}. \tag{4.12}$$

Considering a lossless dielectric medium, this dispersion relation can be expressed in terms of both real and imaginary parts of the optical function of the metal [213]:

$$k_{spp} = \frac{\omega}{c}\sqrt{\frac{\varepsilon_2}{\left(\Re(\hat{\varepsilon}_1) + \varepsilon_2\right)^2 + \Im(\hat{\varepsilon}_1)^2}}\sqrt{\frac{\rho^2 + \sqrt{\left(\rho^4 + \varepsilon_2^2\Im(\hat{\varepsilon}_1)^2\right)}}{2}}, \tag{4.13}$$

where $\rho = \Re(\hat{\varepsilon}_1)^2 + \Im(\hat{\varepsilon}_1)^2 + \varepsilon_2\Re(\hat{\varepsilon}_1)$. Because of the high negative values of $\Re(\hat{\varepsilon}_1)$ and high positive values of $\Im(\hat{\varepsilon}_1)$ of gold at THz frequencies, Eq. (4.13) can approximated by a simple formula:

$$k_{spp} \approx \frac{\omega}{c}\sqrt{\varepsilon_2}. \tag{4.14}$$

This implies that in a structure consisting of a PEC and a lossless substrate material the spectral positions of Wood-Rayleigh (WR) anomaly, which is a minimum in a transmission spectrum occurring when a diffraction order is exactly parallel to the plane of the metal film, is close to the condition for excitation of a SPP on a flat metal-dielectric interface [119]. If we now use the condition for an excitation of SPPs via a metal grating (Eq. (2.186)), for 2D case it takes the form:

$$\mathbf{k}_{spp} = \mathbf{k}_0 \pm m\mathbf{G}_x \pm n\mathbf{G}_z, \tag{4.15}$$

where $|\mathbf{G}_x| = |\mathbf{G}_z| = 2\pi/\Lambda$, m, n are integers and $\mathbf{k}_0 = k\sin\phi_0$, when $\theta_0 = 0°$. Comparing now Eqs. (4.14) and (4.15) it is obvious, that for a square lattice with

a metal considered as a PEC, transmission minima for normal incidence ($\mathbf{k}_0 = 0$) occur at frequencies:

$$\nu_{m,n}^{min} \approx \frac{c}{\sqrt{\varepsilon_2}} \frac{\sqrt{m^2 + n^2}}{\Lambda}. \tag{4.16}$$

For a simplicity we can assume a substrate with $\varepsilon_2 = 4$, which is close to the permittivity of quartz, and a lattice period $\Lambda = 600\,\mu\text{m}$, then the first order transmission minimum (or reflection maximum) for TE wave $[0, \pm 1]$ is present at 250 GHz, which is indeed below cut-off (see (4.11)). The spectral position of surface plasmons is given by Eq. (2.185):

$$\omega_{sp} = \frac{\omega_p}{\sqrt{\varepsilon_2 + 1}}, \tag{4.17}$$

where the characteristic plasma frequency ω_p was for PEC presented by Pendry *et al.* [82] (see Section 2.6.2) and corresponds to the cut-off frequency $f_{\text{cut-off}}$ of the hole with a size d, for circular holes as:

$$\omega_p = \frac{2 \cdot 1.8412 \cdot c}{d} = \omega_{\text{cut-off}}, \tag{4.18}$$

and for square holes as:

$$\omega_p = \frac{\pi \cdot c}{d} = \omega_{\text{cut-off}}. \tag{4.19}$$

Therefore, for a plasmonic structure with circular holes of a diameter $d = 300\,\mu\text{m}$ on the hypothetical substrate with $\varepsilon_2 = 4$, the surface plasmons frequency is present approx. at 262.1 GHz and for a structure with square holes of size d approx. at 223.6 GHz.

Figure 4.4 shows a numerical calculation of a spectrum between 200 GHz–325 GHz after normal incidence reflection of a linearly polarized wave done by rigorous coupled-wave analysis (RCWA) [214]. The simulation considered square-shaped holes of size $d = 300\,\mu\text{m}$ in gold at the quartz substrate. It is possible to observe a strong pronounced minimum at 245 GHz signifying a presence of spoof plasmons polaritons (SPPs) as well as the evident sharp Wood-Rayleigh anomaly close to 250 GHz. The SPPs resonance frequency is slightly shifted from

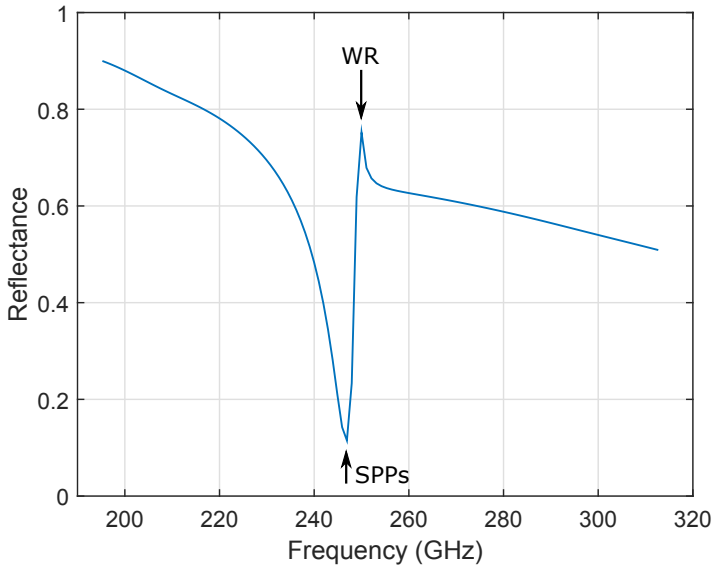

Figure 4.4: Reflection spectrum of the quartz-gold plasmonic structure with square holes after normal incidence of TE-polarized light calculated by RCWA algorithm

the calculated value to high frequencies due to the non-zero losses of the metal and is closely tied with the WR anomaly. These results present the first numerical confirmation of the designer plasmons excitation in the mm-wave range. Note, that due to the normal incidence ($\phi_0 = 0°$, $\theta_0 = 0°$) and 90° rotational symmetry of the 2D grating, this resonance effect will appear for a z-polarized wave as well as for a x-polarized wave.

After the numerical study we focused on fabrication of the real plasmonic structure, as shown in Fig. 4.5a, and its characterization.

Sample preparation included a cleaning of the quartz wafer surface with thickness $h_{sub} = 240\,\mu m$ by acetone and alcohol followed by a development of copolymer and PMMA (polymethyl methacrylate) resists. For a suitable adhesion between gold and the substrate a 5 nm thin layer of germanium was deposited by evaporation. The thickness of this adhesion layer is negligible in comparison to the other structural parameters and working wavelengths and therefore has no

significant impact on the SPPs resonance conditions. After an application of a mask (Fig. 4.5b) by e-beam lithography, the metallizing was done by evaporation of gold after standard pre-etching ($E = 200\,\text{eV}$, $t = 120\,\text{s}$). The excess material and resists were then lifted-off in 2h at $t = 70\,^{\circ}\text{C}$. A real photo of the plasmonic device is shown in Fig. 4.5a.

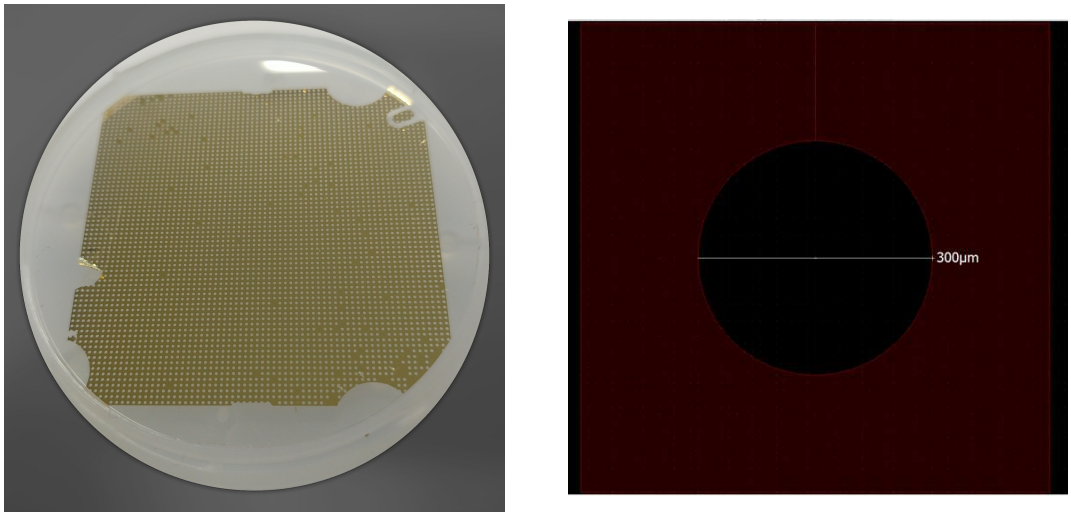

(a) Plasmonic structure

(b) Mask for metalization

Figure 4.5: A photograph of the 2D periodic structure of gold with circular holes of diameter $d = 300\,\mu\text{m}$ and period $\Lambda = 600\,\mu\text{m}$ fabricated on a crystal quartz substrate and a mask for sample metalization with a denoted hole diameter

Because a reflection measurement requires exact positions of the sample and a reference which could complicate the measurement procedure, we characterized the plasmonic device in a transmission configuration. This was done by our THz Time-domain spectrometer and a general TDS experimental scheme is shown in Fig. 2.6. Figure 4.6 shows the plasmonic device placed in the setup during the TDS measurement. The transmittance spectrum after horizontally-polarized normal incidence transmission with a free-air transmission reference together with simulation results obtained by CST Studio Suite software[1] are shown in Fig. 4.7.

The positions of the lowest order SPPs resonance and WR anomaly are

[1] CST Studio Suite: The electromagnetic simulation software, CST - Computer Simulation Technology GmbH, Bad Nauheimer Str. 19, 64289 Darmstadt, Germany

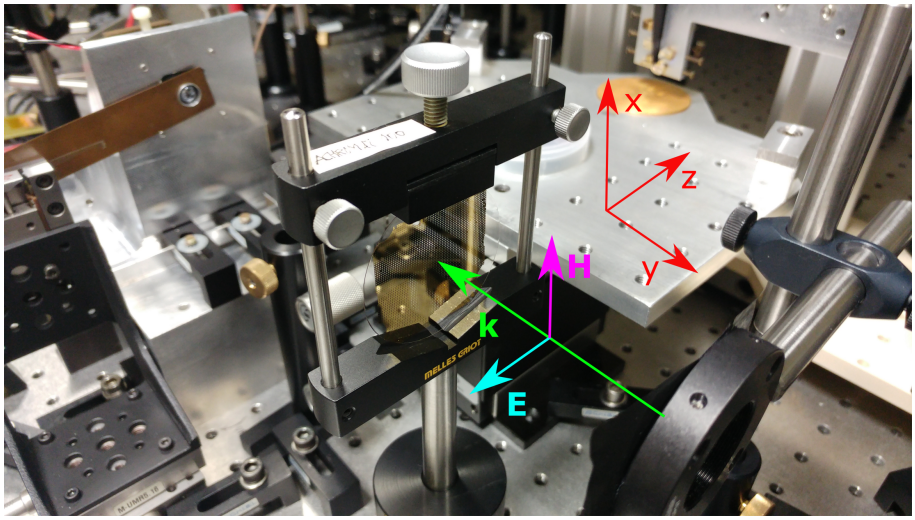

Figure 4.6: A photograph of the plasmonic structure during the TDS transmission measurement with incident horizontally-polarized wave

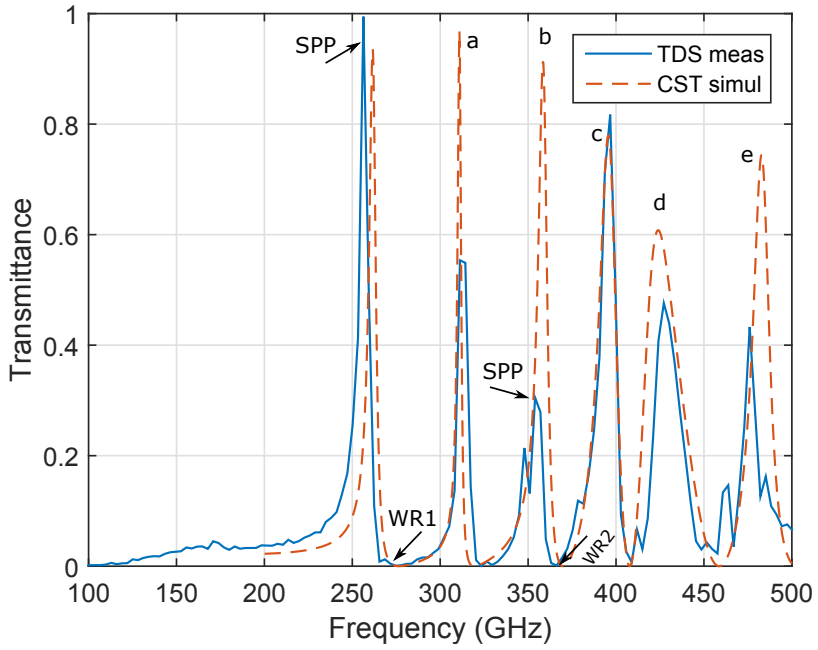

Figure 4.7: Transmittance spectra of the quartz-plasmonic device (Fig. 4.3) obtained by THz-TDS and corresponding calculated spectra obtained by CST Studio Suite, permittivity of the quartz substrate $\varepsilon_2 = 4.41$.

marked. It is possible to observe measured strong resonant transmission maximum at approx. 256 GHz (calculated 261 GHz) followed by a strong minimum at 265 GHz denoting the WR anomaly (calculated 270 GHz). The presence of surface modes is confirmed by the field plot map of $\mathbf{H}_y$ field component at 261 GHz (Fig. 4.8) where we can see strong confinement to sides of the circular holes. The z-polarized electric field excites a two-fold degenerate SPPs resonance modes $[0, \pm 1]$. From the field plot maps of $\mathbf{E}_z$ (Fig. 4.9) and $\mathbf{E}_x$ (Fig. 4.10) implies that the polarization of the surface modes excited with use of circular holes is not strongly determined since they include both $\mathbf{E}_x$ and $\mathbf{E}_z$ component. This was presented and described also in [215]. Field plot maps of the $\mathbf{H}_y$ field component of all other peaks in in the transmission spectrum in are shown in Fig. 4.11a-4.11e. It is apparent, that the transmission peaks *a*, *c*, *d*, *e* correspond to substrate modes, whereas *b* is the higher-order spoof SPPs resonance. This is also confirmed by a presence of WR anomaly, whose frequency can be calculated with use of Eq. (4.16), hence:

$$\nu^{min}_{(\pm 1,\pm 1)} = \nu^{min}_{(0,\pm 1)} \cdot \sqrt{2}, \tag{4.20}$$

where measured $\nu_{WR1} = 260$ GHz and therefore $\nu_{WR2} = 367$ GHz. All the phenomena depicted in Fig. 4.7 are well bellow cut-off what signifies no possibility for FP resonance existence in the holes. We can therefore conclude that these effects are independent of the metal film thickness.

All the above presented results underline the possibility of spoof SPPs excitation at THz frequencies, particularly in the mm-wave range. We will now link the following work on this demonstration and try to obtain excited designer plasmons on a device consisting of the hexaferrite ceramics and a similarly patterned layer of gold.

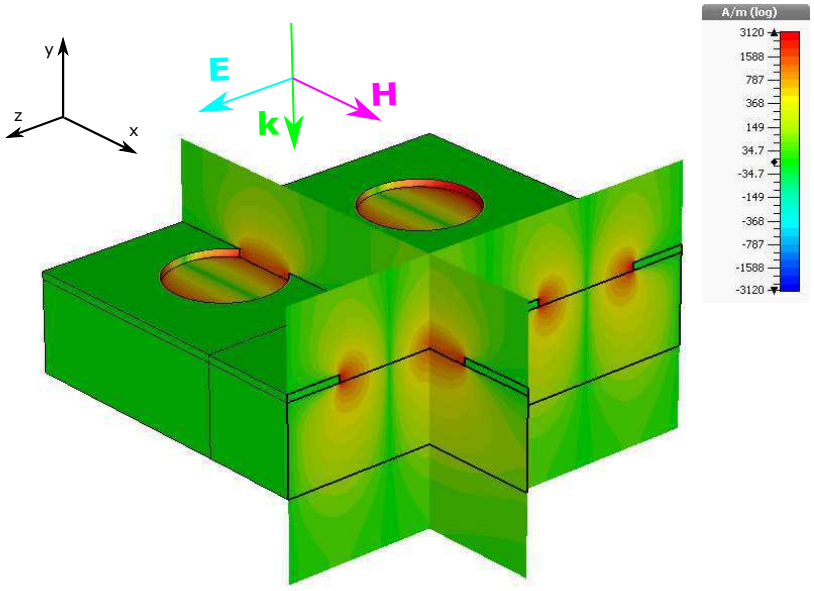

Figure 4.8: Field color map of $\mathbf{H}_y$ field component of the calculated transmittance peak at 261 GHz for 4 unit cells of the plasmonic device. This field color map is a proof of SP behavior since it is observed below WR1 anomaly.

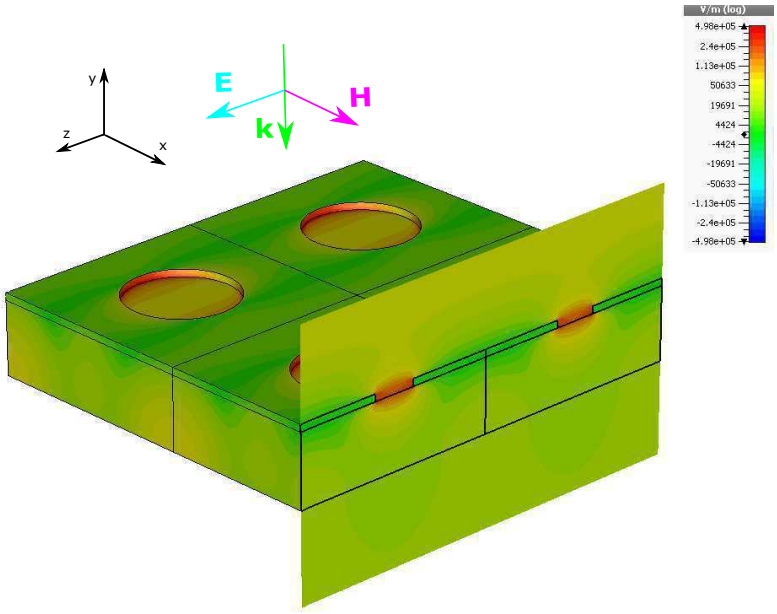

Figure 4.9: Field color map of $\mathbf{E}_z$ field component of the calculated transmittance peak at 261 GHz for 4 unit cells of the plasmonic device.

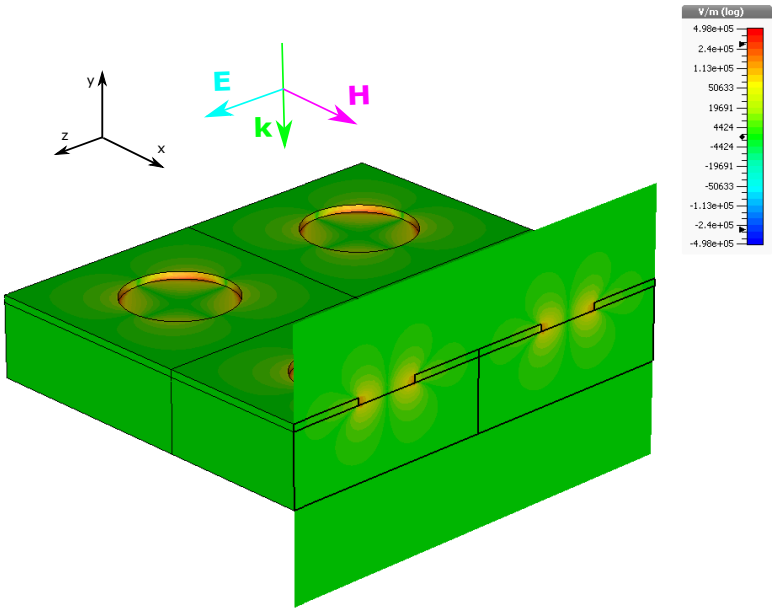

Figure 4.10: Field color map of $\mathbf{E}_x$ field component of the calculated transmittance peak at 261 GHz for 4 unit cells of the plasmonic device.

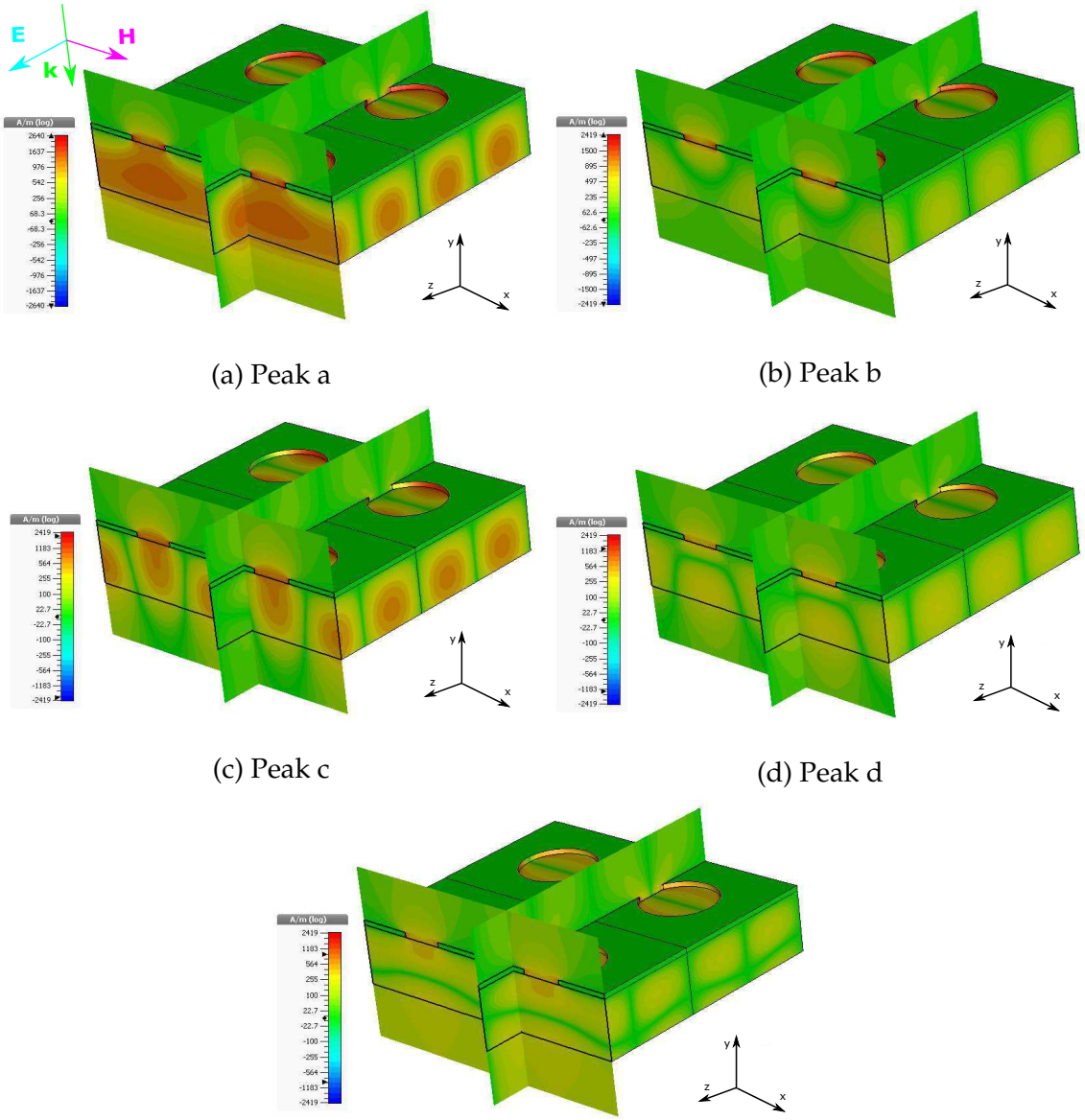

(a) Peak a

(b) Peak b

(c) Peak c

(d) Peak d

(e) Peak e

Figure 4.11: Field color map of $\mathbf{H}_y$ field components of the calculated transmittance peaks a-e for 4 unit cells of the plasmonic device.

4.2.1.2 Spoof Plasmons at Metal/Hexaferrite Interface

After the successful demonstration of spoof SPPs via the quartz-plasmonic structure we will now design a similar device including a patterned gold layer on the surface of the hexagonal ferrite ceramics FB6N. As was presented in Chapter 3, the FB6N ceramics possesses a high permittivity (Fig. 3.38), therefore it is necessary to scale the grating parameters for SPPs coupling on the metal/hexaferrite interface. Because the characteristic frequency of surface plasmons (Eq. (4.17)) as well as the spectral positions of WR anomaly (Eq. (4.16)) depend on the substrate permittivity, an increase of the permittivity value will cause a shift of these phenomena to lower frequencies (longer wavelengths). Therefore, in order to keep them in the mm-wave range between 200 GHz–320 GHz, one has to properly decrease both the grating period Λ and the hole size d. Fig. 4.12 shows reflectance spectra calculated by an in-house developed RCWA algorithm for structures of gold layer with square holes of size d and period λ deposited on substrates with different permittivities. Table 4.1 summarizes parameters of the simulated structures and spectral positions of SPPs and WRs both simulated and calculated via Eqs. (4.17), (4.16), respectively. We are still considering a TE-polarized wave with the normal angle of incidence ($\phi_0 = 0°$, $\theta_0 = 0°$).

Table 4.1: Plasmonic structures simulated by RCWA

	ε_2	$\Lambda(\mu\mathrm{m})$	$d(\mu\mathrm{m})$	SPPs (GHz) (rcwa)	SPPs (GHz) (4.17)	WR (GHz) (rcwa)	WR (GHz) (4.16)
1	4.5	450	200	311	320	314	314
2	10	400	180	235	251	237	237
3	15	300	140	256	267	259	267

One can see that the positions of the lowest order WR anomalies of these structures well follow the Eq. (4.16) and differences in the order of several GHz are present between the SPPs resonances positions calculated by Eq. (4.17) and the RCWA algorithm. These differences perhaps again correspond to the losses of the used metal included in the Drude model as well as with the positions of the WR

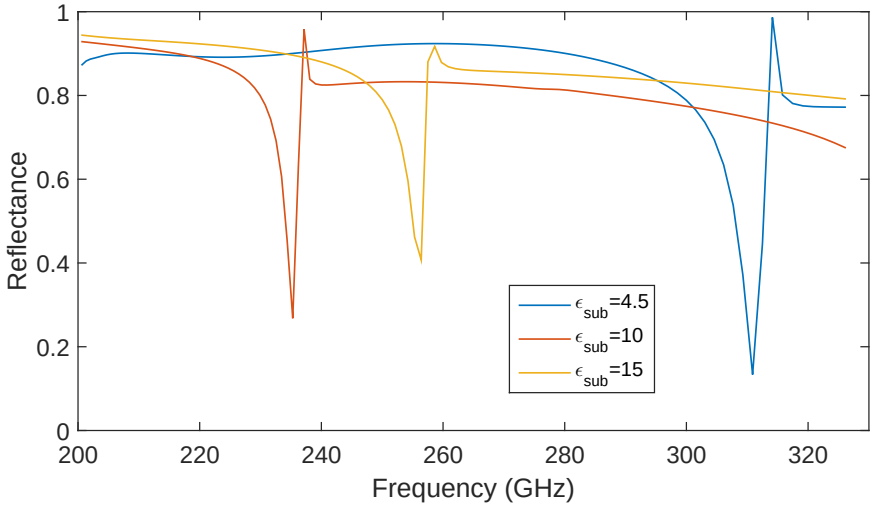

Figure 4.12: Simulated reflectance spectra of plasmonic structures with square holes and increasing substrate permittivity. Blue: $\varepsilon_{\text{sub}} = 4.5, \Lambda = 450\,\mu\text{m}, a = 200\,\mu\text{m}$, red: $\varepsilon_{\text{sub}} = 10, \Lambda = 400\,\mu\text{m}, a = 180\,\mu\text{m}$, yellow: $\varepsilon_{\text{sub}} = 15, \Lambda = 300\,\mu\text{m}, a = 140\,\mu\text{m}$

anomalies. These seem to be present always close to the SPPs resonances and can influence their spectral positions.

After these obtained results we can design a plasmonic structure with the hexaferrite substrate. Contrary to the quartz-plasmonic device we decided to use square holes in the gold layer for the ferrite-based isolator. As was presented and discussed by Qu *et al.* [215], square holes are supposed to incite a higher phase change at the $[0, \pm 1]$ SP resonance frequency than a structure with circular holes. And because the transmission has the derivative shape of the sharp phase changes observed at the SPPs resonance frequencies, as a result the EOT transmission peak is supposed to possess also a higher-quality factor. This is caused by the fact that the polarization of the surface modes excited by circular holes is not strongly determined, as we already observed and demonstrated in Figs. 4.9, 4.10. The schematic representation of the studied THz NR device is therefore shown in Fig. 4.13. The period of the gold grating was calculated as $\Lambda = 250\,\mu\text{m}$. The $[0, \pm 1]$ WR anomaly is for normally incident TE-polarized radiation on this

grating present at

$$\nu^{WR}_{(0,\pm1)} = \frac{c}{\Lambda\sqrt{\varepsilon_2}} = 262\,\mathrm{GHz}, \tag{4.21}$$

where $\varepsilon_2 \approx 21$.

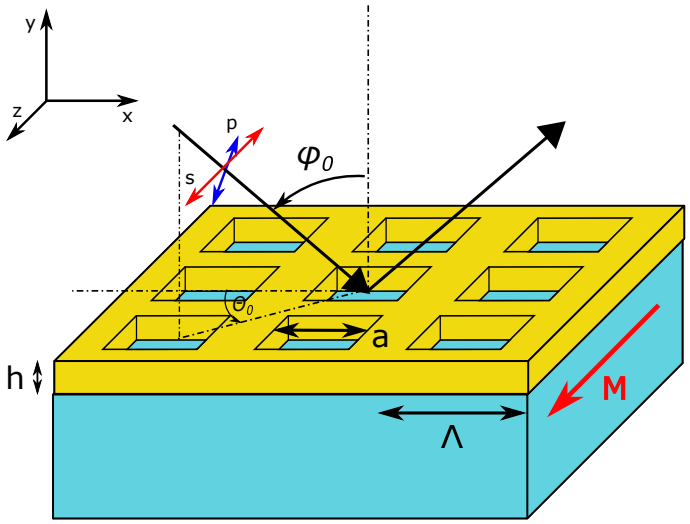

Figure 4.13: Schematic representation of the studied THz nonreciprocal device: gold layer patterned by 2D periodic structure with period Λ, holes size a and thickness h on a magneto-optical hexaferrite substrate magnetized in transverse configuration with incident s- polarized plane wave at an angle of incidence ϕ_0 and an azimuthal angle θ_0.

Mutual spectral positions of the WR anomaly and the SPPs resonance can significantly influence a quality factor of the resonance dip in reflectance spectrum. Since the resonance frequency of SPPs is according the Pendry's theory (Eq. (4.18)) determined primarily by the hole size, we numerically studied several structures with different holes sizes in order to observe the resonance behavior in the spectra. Figure 4.14 shows reflectance spectra of the hexaferrite-plasmonic structure, with nonmagnetized substrate of $\varepsilon_2 \approx 21$ and $\Lambda = 250\,\mu\mathrm{m}$ after normal incidence of *TE*-polarized EM wave calculated by RCWA for holes sizes 100 µm–140 µm. One can see the decreasing quality factor of the resonance, but also minimal change of its spectral position. We can calculate theoretical res-

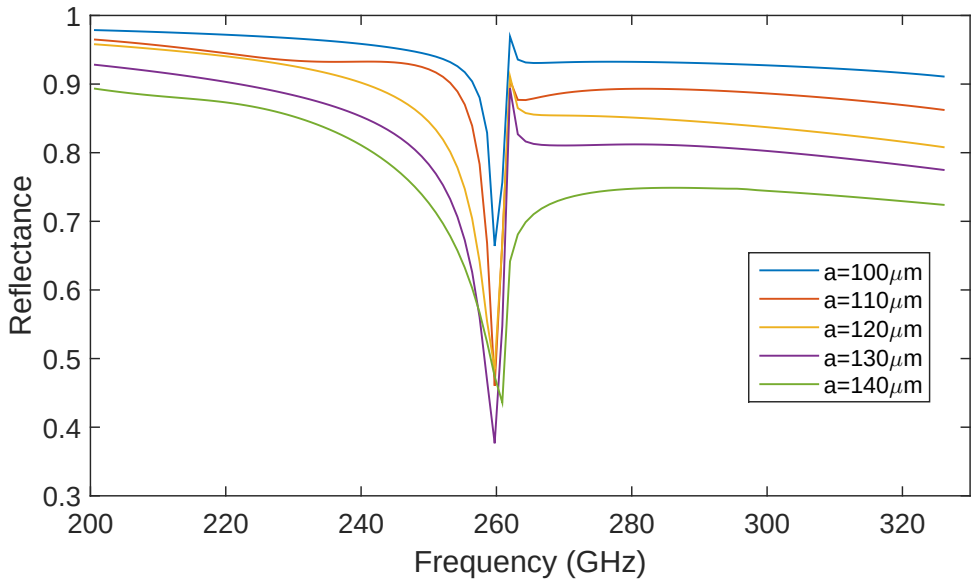

Figure 4.14: Numerical calculation of reflectance spectra of the hexaferrite-plasmonic structure for different holes sizes after normal incidence

onant frequencies of all the patterns for PEC with use of Eq. (4.17):

$$\nu^{SPP}_{(0,\pm1)} = \frac{c}{2a\sqrt{\varepsilon_2 + 1}} \tag{4.22}$$

and these are summarized in Table 4.2 It is possible to observe a strong depen-

Table 4.2: Theoretical SPPs resonant frequencies for structures with different holes sizes

a(μm)	$\nu^{SPP}_{(0,\pm1)}$ (GHz)
100	320
110	291
120	267
130	246
140	228

dence of the resonant frequency on the hole size. However, our RCWA numerical calculations considering a real metal with limited losses did not show that and

the results are consistent with Eq. (4.14). This is important result denoting the fact that in a real metal the position of the resonant frequency is strongly influenced by the position of the adjacent WR anomaly and the hole size influences particularly the quality factor of the resonance. We also concluded that for the device fabrication the holes size of $a = 130\,\mu m$ provides a reasonably strong effect while still keeping a high quality factor required for the high isolation. The design of the gold layer patterned with square holes with the size $a = 130\,\mu m$ and grating period $\Lambda = 250\,\mu m$ was therefore chosen as the optimal one for the fabrication and consecutive studies. The following paragraphs are thus focused on the above described structure.

Sample fabrication included a preparation of the ceramic substrate and a following deposition of the structured gold layer.

Substrate preparation The commercially available bulk ceramics with preferred magnetization direction along the *c*-axis was cut into 1–2 mm thin sheets with the *c*-axis being in plane of the samples. The small thickness is required for subsequent lithography fabrication processes. The cutting was done by a micro-water jet machine which allows to cut even very brittle materials with very high precision. The resulted thin sheets were afterwards polished by Al_2O_3 solution, which was providing the best results from all tried polishing solutions (Section 3.1.1). The procedure of the ceramics preparation and its difficulties are more in detail described at the end of this chapter, in Section 4.2.3.

Fabrication of the metal structure included a cleaning of the polished sample surface followed by an e-beam deposition of a 500 nm thick gold layer by the lift-off technique analogously to the quartz-plasmonic structure. No adhesion layer is now required due to the residual roughness of the ceramic substrate. The dimensions were controlled by SEM and profilometry. Figure 4.15 shows a picture of one and half grating period of the fabricated device captured by SEM and a real photograph of the fabricated device is shown in Fig. 4.16.

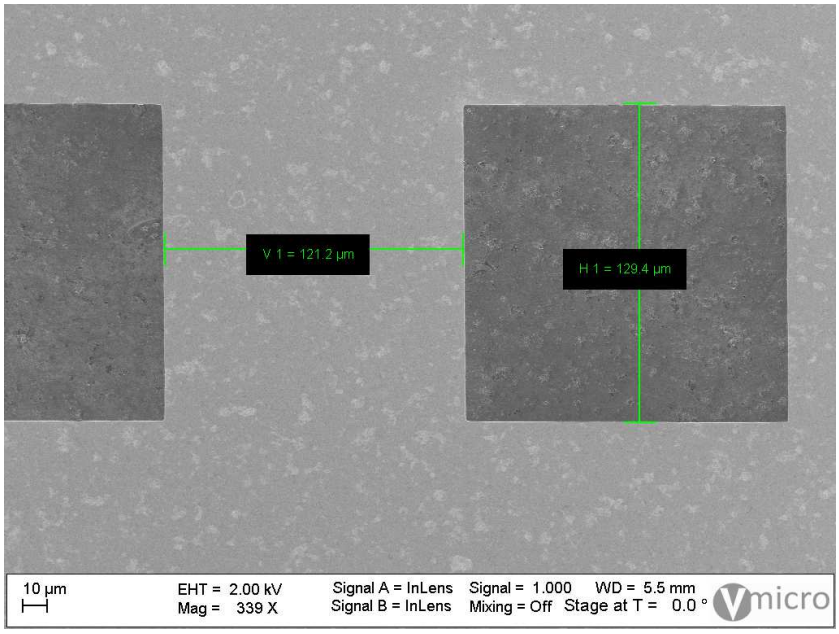

Figure 4.15: SEM image of one grating period of the gold structure on the hexaferrite surface with measured dimensions

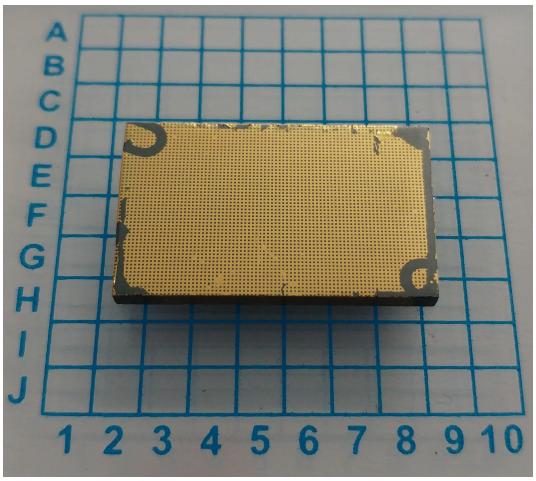

Figure 4.16: A photo of the fabricated gold grating on the hexagonal ferrite substrate

The cut-off frequency of the square holes is determined by their size:

$$\begin{aligned} \nu_{\text{cut-off}} &= \frac{c}{2a} \\ \nu_{\text{cut-off}} &= \frac{3 \times 10^{8}\,\text{m}\,\text{s}^{-1}}{260 \times 10^{-6}\,\text{m}} \\ \nu_{\text{cut-off}} &= 1.15\,\text{THz} \end{aligned} \tag{4.23}$$

Sample characterization The fabricated device has been initially measured by THz-TDS in a normal-incidence transmission configuration. The resulting transmittance spectrum after normalization by a free-space transmission is shown in Fig. 4.17. One can see a resonant maximum signifying presence of SPPs at

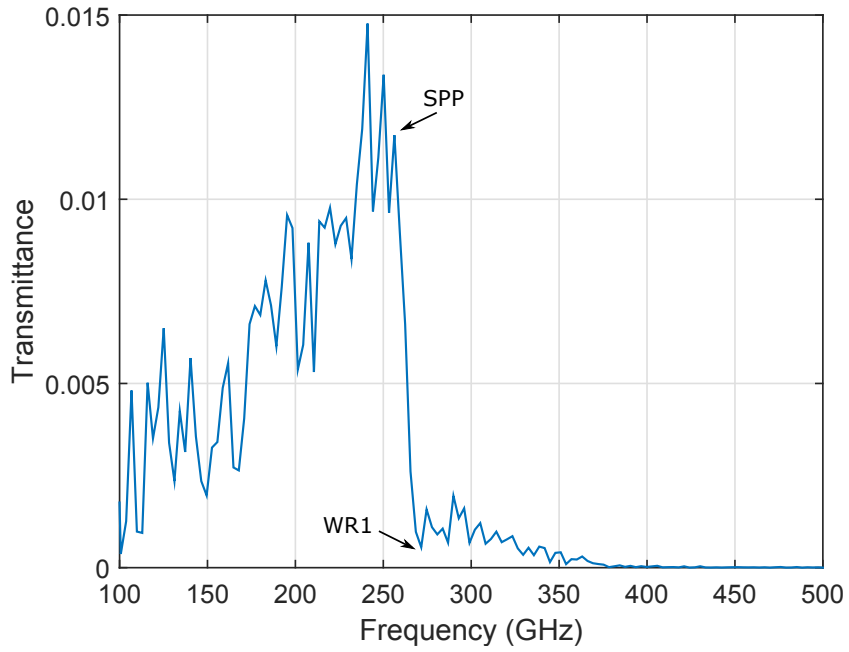

Figure 4.17: Transmittance spectra of the hexaferrite-plasmonic device (Fig. 4.13) obtained by THz-TDS after normal incidence

256 GHz followed by a strong significant minimum denoting the WR anomaly at 271 GHz both with a good agreement with RCWA simulations. The measured intensity is very low particularly due to a combination of losses and thickness (1.7 mm) of the ceramic substrate. These also result in wider SPPs resonant peak as well as in a presence of substrate modes apparent as additional peaks in the spectra (especially at lower frequencies). Besides all these effects complicating the interpretation we can conclude that this measurement confirms the first experimental demonstration of SPPs excitation on the structured metal/hexaferrite interface. Moreover, considering the fact that the transmission configuration is not the principal configuration of the studied NR device, the presence of SPPs

resonance together with already demonstrated strong ceramics' gyrotropy are the crucial phenomena for obtaining a strong isolation.

Until now we studied the plasmonic device under normal incidence of an EM wave. However, for a NR shift of the resonant frequency in the spectra caused by a EOT coupling with the MOKE effect, it is necessary to introduce an angle of incidence $\phi_0 > 0$. Therefore, in the following step we studied the behavior of the SPPs resonance for increasing values of ϕ_0. The dependence of the reflectance spectra on the angle of incidence is shown in Fig. 4.18. As we can see, both

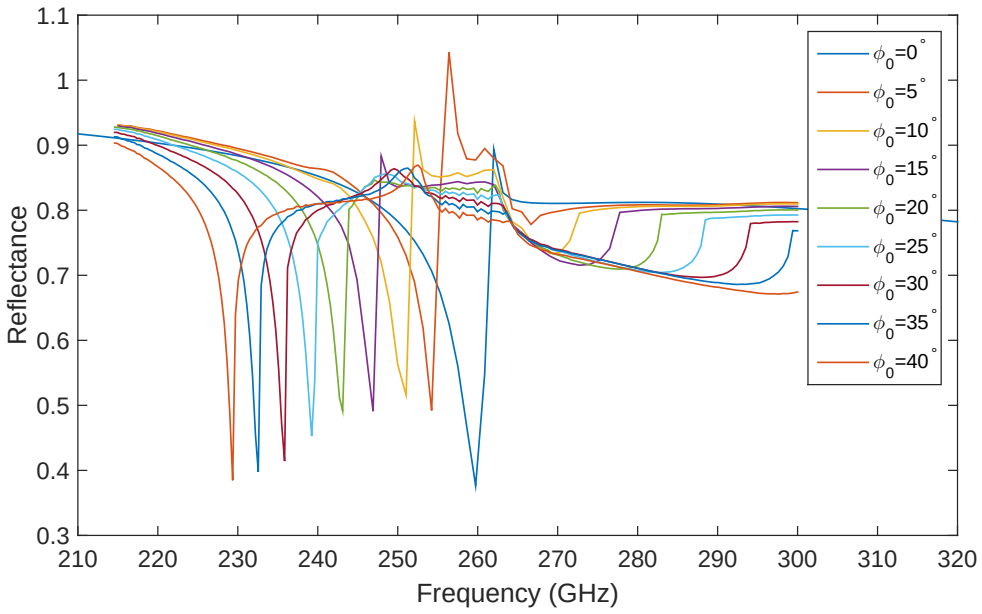

Figure 4.18: Numerical calculation of reflectance spectra of the hexaferrite-plasmonic structure for different incidence angles ϕ_0; $\theta_0 = 0°$.

the SPPs resonance frequency and the WR anomaly frequency are shifted with increasing ϕ_0 to lower frequencies. Considering the condition for SPPs excitation at 2D grating given by Eq. (4.15), for a nonzero angle of incidence ϕ_0 and $\theta_0 = 0°$ it takes the form:

$$\mathbf{k}_{spp} = \mathbf{k}_0 \pm (m\mathbf{G}_x + n\mathbf{G}_z) = (k_0 \sin\phi_0 \pm mG_x)\,\boldsymbol{\imath}_x + (\pm nG_z)\,\boldsymbol{\imath}_z. \tag{4.24}$$

If we now take into account Eq. (4.14), we can express the WR anomaly wavelength at general incidence angle as:

$$\frac{\sqrt{\varepsilon_2}}{\lambda} = \sqrt{\left(\frac{\sin\phi_0}{\lambda} \pm \frac{m}{\Lambda}\right)^2 \pm \left(\frac{n}{\Lambda}\right)^2} \tag{4.25a}$$

$$\frac{\varepsilon_2}{\lambda^2} = \frac{\sin^2\phi_0}{\lambda^2} \pm 2\frac{m\sin\phi_0}{\lambda\Lambda} + \frac{m^2}{\Lambda^2} \pm \frac{n^2}{\Lambda^2} \tag{4.25b}$$

$$0 = \lambda^2\left(m^2+n^2\right) \pm \lambda 2m\Lambda\sin\phi_0 - \Lambda^2\left(\varepsilon_2 - \sin^2\phi_0\right) \tag{4.25c}$$

and general solutions of Eq. (4.25c) for λ at a general incidence angle ϕ_0 are:

$$\lambda_{1,2}^{WR} = \frac{\mp 2m\Lambda\sin\phi_0 \pm 2\Lambda\sqrt{\left[\left(m^2+n^2\right)\varepsilon_2 - n^2\sin^2\phi_0\right]}}{2\left(m^2+n^2\right)}. \tag{4.26}$$

These solutions can be for $[0,\pm1]$ WR anomaly with a TE-polarized incident wave simplified into

$$\lambda_{(0,\pm1)}^{WR} = \Lambda\sqrt{\varepsilon_2 - \sin^2\phi_0}. \tag{4.27}$$

For $\phi_0 = 0^\circ$ this gives $\lambda_{(0,\pm1)}^{WR} = \Lambda\sqrt{\varepsilon_2}$, what is the solution corresponding to Eq. (4.16). Equation (4.27) denotes that with increasing angle of incidence the $[0,\pm1]$ WR anomaly shifts to lower wavelengths (higher frequencies). However our calculations (Fig. 4.18) show that this is true only when $\phi_0 > 10^\circ$. In this case the SPPs resonance and WR anomaly become more separated and both these phenomena are moving to opposite sides of spectra. For $\phi_0 = 40^\circ$ the SPPs resonance is present at $\nu_{SPP} = 229\,\mathrm{GHz}$ and WR anomaly at $\nu_{WR} = 253\,\mathrm{GHz}$. This separation can lead to increase of the resonance quality factor and therefore to the stronger effective isolation. For small angles when $\phi_0 \leq 10^\circ$, only the diffraction about x-axis is affected and the position of WR anomaly is strongly influenced by the SPPs resonance position which shifts to lower frequencies with increasing ϕ_0.

4.2.1.3 Nonreciprocal Response of Magnetoplasmonic Structure

The most important part of the study is devoted to the study of the isolation effect when combining the SPPs resonance with the TMOKE. For this purpose the hexagonal ferrite substrate was magnetized transversely to the plane of incidence, as already shown in Fig. 4.13. We will now focus on a description of the SPPs spectral position shift caused by the coupling with the transverse magneto-optical Kerr effect.

Working principle The TMOKE effect is usually defined as a relative change of reflected intensity of linearly polarized radiation when the magnetization changes its orientation, for s polarization therefore in the form:

$$\delta R_s = \frac{R_s\left(\pm M\right) - R_s\left(\mp M\right)}{R_s(0)}. \tag{4.28}$$

In our case we study the device behavior when the ceramic substrate is in its natural remanence after magnetization of the sample by an external electromagnet at $B = 1.6\,\mathrm{T}$. As it was described in Chapters 1 and 2, the presence of magnetization in the material causes breaking of the Lorentz reciprocity for a TE-polarized wave and the nonreciprocal response of the magnetized device manifest itself as a spectral shift of the resonant effects and anomalies. Therefore the isolation can be expressed using Eq. (4.28) without normalization to the nonmagnetized state:

$$\Delta R_s = R_s\left(\pm M\right) - R_s\left(\mp M\right). \tag{4.29}$$

This spectral shift of the resonance phenomena is described in the following paragraphs.

Considering the transversely ($z-$) magnetized hexaferrite substrate, with the

permeability in the tensorial form:

$$\bar{\bar{\mu}} = \begin{pmatrix} \mu & i\kappa & 0 \\ -i\kappa & \mu & 0 \\ 0 & 0 & \mu_0 \end{pmatrix}, \tag{4.30}$$

and an incident *s*-polarized wave, the wave equation (2.65) can be expressed as:

$$\begin{pmatrix} \hat{n}_y^2 - \mu & -\hat{n}_x\hat{n}_y - i\kappa & 0 \\ -\hat{n}_y\hat{n}_x + i\kappa & \hat{n}_x^2 - \mu & 0 \\ 0 & 0 & (\hat{n}_x^2 + \hat{n}_y^2) - \mu_0 \end{pmatrix} \begin{pmatrix} H_{0x} \\ H_{0y} \\ H_{0z} \end{pmatrix} = 0. \tag{4.31}$$

From the condition for existence of SPPs at the interface (2.177) we for *s*-polarization obtain:

$$\frac{k_{y1}}{\mu_1} + \frac{k_{y2}}{\mu_2} = 0, \tag{4.32}$$

where $k_{y2} = i\sqrt{k_x^2 - \varepsilon_2\mu k_0^2}$, $\mu_2 = \mu - \kappa$. Here we can assume an effective permeability μ_1 as was for structured PEC derived by Pendry *et al.* [82], together with k_{y1} for TE-polarized wave in the form:

$$k_{y1} = i\sqrt{\frac{\pi^2}{a^2} - k_0^2}, \qquad \mu_1^{TE} = \frac{\pi^2\Lambda^2}{8a^2}\left(1 - \frac{\pi^2 c^2}{a^2\omega^2}\right) \tag{4.33}$$

Eq. (4.32) can be therefore expressed as:

$$\frac{k_x^2 - \varepsilon_2\mu k_0^2}{(\mu - \kappa)^2} = \frac{\frac{\pi^2}{a^2} - k_0^2}{\left[\frac{\pi^2\Lambda^2}{8a^2}\left(1 - \frac{\pi^2 c^2}{a^2\omega^2}\right)\right]} \tag{4.34a}$$

$$k_x^2 c^2 = \varepsilon_2\mu\omega^2 + \frac{\left(\frac{\pi^2 c^2}{a^2} - \omega^2\right)(\mu - \kappa)^2}{\left(\frac{\pi^4\Lambda^4 a^2\omega^2 - \pi^4\Lambda^2 c^2}{8a^4\omega^2}\right)^2}. \tag{4.34b}$$

Taking into account the characteristic plasma frequency ω_p for the metal structured by 2D holes given by Eq. (2.189), and considering $\mu \approx 1$ together only with

terms linear in κ, hence $(\mu - \kappa)^2 = 1 - 2\kappa$, we can express Eq. (4.34) into:

$$k_x^2 c^2 = \varepsilon_2 \omega^2 + \frac{64 a^4 \omega^4}{\pi^4 \Lambda^4 \left(\omega_p^2 - \omega^2\right)} (1 - 2\kappa). \tag{4.35}$$

Eq. (4.35) is a dispersion relation for surface plasmon polaritons at the interface between the structured metal surface and gyromagnetic substrate for TE-polarized incident wave. The term 2κ denotes the spectral shift originating from the magneto-optical Kerr effect. Figure 4.19 shows the shift of optical index of SPPs at $\nu = 250\,\mathrm{GHz}$ calculated by Eq. (4.35), where $n_{SPP} = k_x^2 c^2 / \omega_{SPP}^2$.

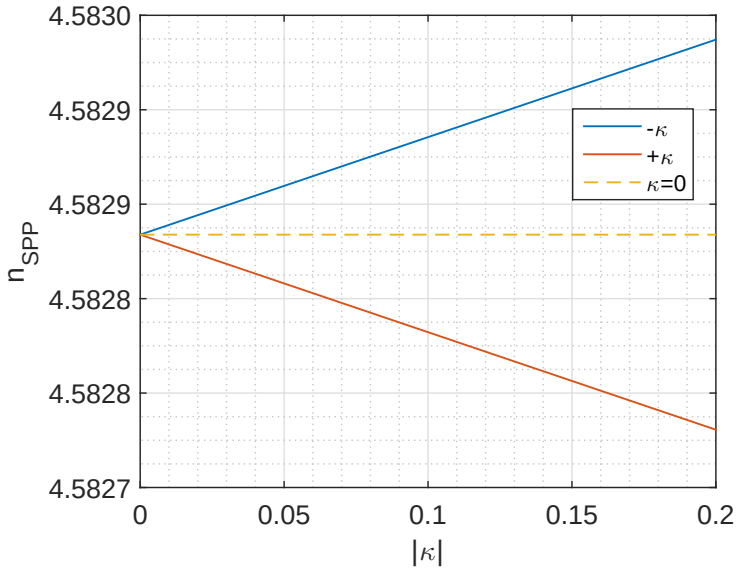

Figure 4.19: Shift of SPPs caused by coupling with transverse MO Kerr effect calculated with use of Eq. (4.35) at $\nu = 250\,\mathrm{GHz}$ for opposite magnetization orientations. Pure SPPs without MO effect are represented by the yellow dashed line.

For numerical studies we included a magnetized layer of the finite thickness $h_{sub} = 200\,\mu\mathrm{m}$ representing the hexaferrite with the permeability tensor (Eq. (4.30)) and the permittivity described by a linear function as shown in Fig. 3.38. The magnetic layer was underlaid by a thin dielectric layer of the identical permittivity at which perfectly matched layer (PML) boundary conditions were ap-

plied. The PML is an artificial absorbing layer for wave equations, commonly used to truncate computational regions in numerical methods to simulate problems with open boundaries. This layer strongly absorbs outgoing waves from the interior of a computational region without reflecting them back into the interior [216]. Figure 4.20 shows simulated reflectance spectrum of the isolating device after an incidence of a TE-polarized wave at $\phi_0 = 30°$. Different curves represent different directions of the magnetization: $+\mathbf{M}$, $\mathbf{M} = 0$, $-\mathbf{M}$.

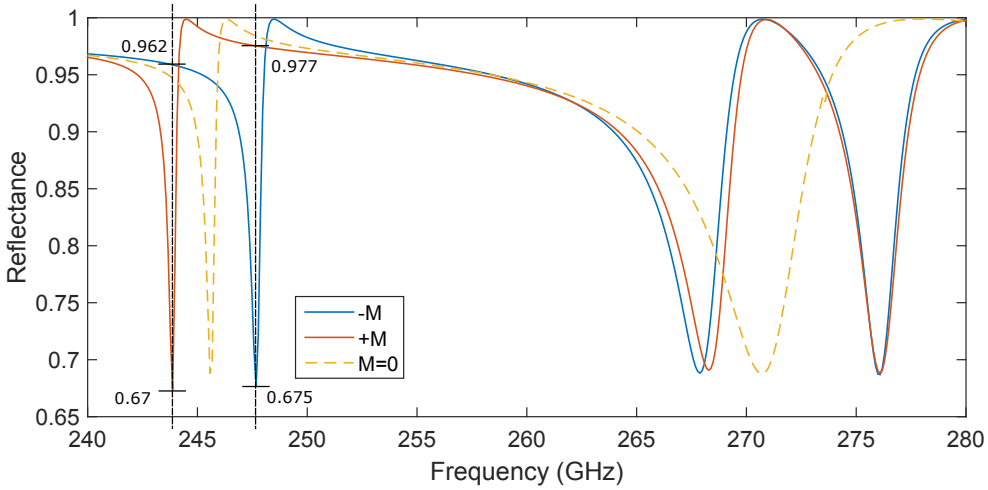

Figure 4.20: Simulated spectra obtained by CST Studio after reflection of TE-polarized wave incident at $\phi_0 = 30°$, $\theta_0 = 0°$ on the transversely magnetized THz NR reflecting device with gold patterned by square holes, where $\Lambda = 250\,\mu m$, $a = 130\,\mu m$, $h = 500\,nm$. Full lines correspond to the opposite magnetization directions and dashed line represent the case when $\mathbf{M} = 0$. The isolation ranges are marked by black dashed vertical lines.

This figure shows several important features. First of all, one can see shifts of the dip representing the SPPs resonance, originally present at $\nu = 245.5\,GHz$ when the substrate is not magnetized, according the magnetization direction to $\nu = 243.8\,GHz$ and $\nu = 247.7\,GHz$. The isolation range of the device is therefore present at these frequencies where radiation is highly reflected for one sense of $\mathbf{M}$, whereas for the opposite direction is weakly reflected, as denoted in the fig-

ure. The isolation can be expressed as a difference of reflectance for the opposite magnetization direction, therefore in the form of Eq. (4.29) and in decibels as:

$$\Delta R_s\,(\mathrm{dB}) = 10\left[\log_{10}\left(R_s\left(\pm M\right)\right) - \log_{10}\left(R_s\left(\mp M\right)\right)\right] = 10\log_{10}\frac{R_s\left(\pm M\right)}{R_s\left(\mp M\right)} \quad (4.36)$$

and hence we obtain the isolation at corresponding frequencies:

$$\Delta R_s\left(\nu = 243.8\,\mathrm{GHz}\right) = 1.57\,\mathrm{dB} \quad (4.37a)$$

$$\Delta R_s\left(\nu = 247.7\,\mathrm{GHz}\right) = 1.61\,\mathrm{dB}. \quad (4.37b)$$

These values are theoretical ones given by depth of the resonance dips which can be influenced by a chosen frequency resolution in the simulations. Higher frequency resolution however significantly increases calculation time which already reaches several days at powerful computer with 12 cores, 128 GB RAM.

Because the opposite magnetization directions correspond to the opposite incidence angles, the same isolation mode is obtained when light is incident at $\phi_0 = 30^\circ$ and $\phi_0 = -30^\circ$ on the device magnetized in one direction. The presence of spoof SPPs is confirmed by the field color map of $\mathbf{H}_y$ field component at $\nu = 245.5\,\mathrm{GHz}$ in the case with $\mathbf{M} = 0$. This plot shows strong confinement of modes to the edges of square holes.

These evanescent modes are strongly *TE*-polarized, as shown by the field color map of the $\mathbf{E}_z$ field component in Fig. 4.22, but a weak $\mathbf{E}_x$ component is present as well (Fig. 4.23). We can therefore conclude, that square holes do not preserve 100 % of the input polarization, however the $\mathbf{E}_x$ field component seems to be weaker than in the case of circular holes.

Another calculated reflectance minimum, originally present at $\nu = 270.7\,\mathrm{GHz}$ when $\mathbf{M} = 0$ is splitted into two minima at $\nu = 268\,\mathrm{GHz}$ and $\nu = 276\,\mathrm{GHz}$ when the substrate is magnetized. These minima however do not change their position when the $\mathbf{M}$ direction is reversed (a minimal shift of the dip at $\nu = 268\,\mathrm{GHz}$ is perhaps caused by shifts of the SPPs resonances at lower frequencies). This

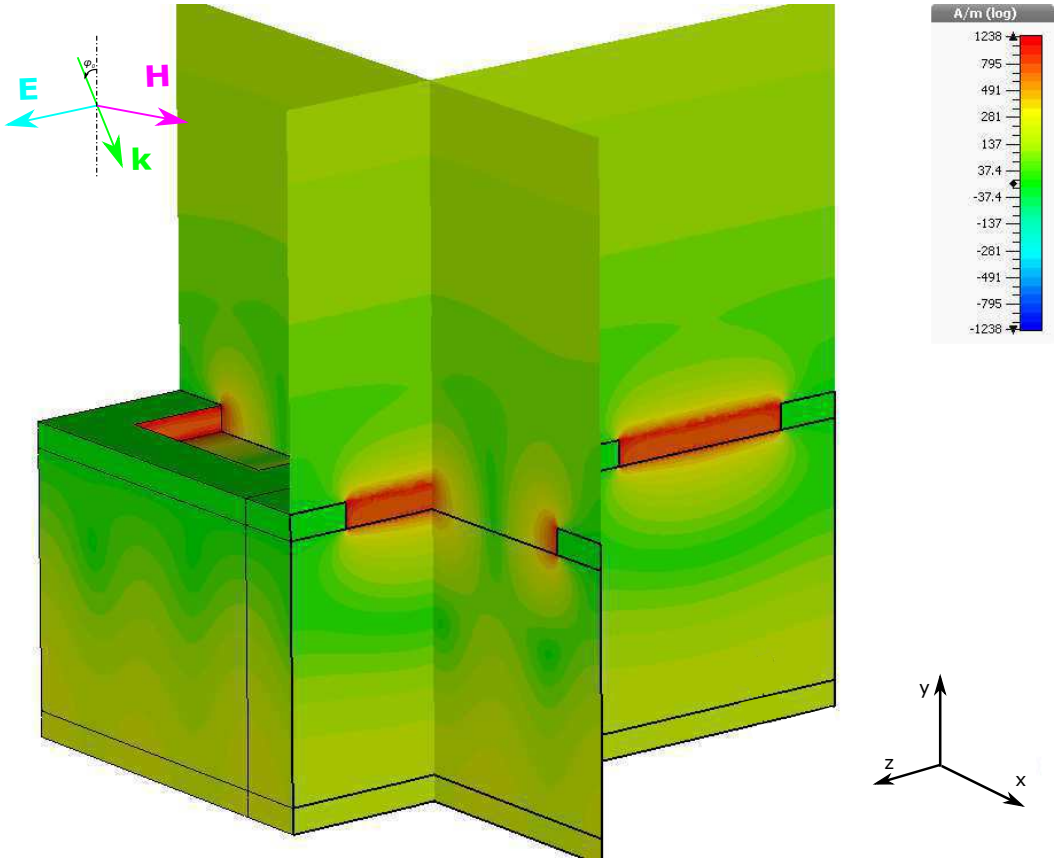

Figure 4.21: Field color map of $\mathbf{H}_y$ field component of the device with non-magnetized substrate at 245.5 GHz for 4 unit cells

signifies the fact that they are caused by guided modes in the substrate which are not active during the TMOKE effect, as confirmed also by the field color map of the $\mathbf{H}_x$ field component shown in Fig. 4.24. Because they were not initially present at spectra calculated by RCWA algorithm (Fig. 4.18) considering a semi-infinite substrate, they are now a result of the finite substrate thickness and their spectral position will on the thickness strongly depend.

The here presented design with square holes in a gold layer seem to be very promising for use as nonreciprocal mirror, however the strong isolating properties are yet to be confirmed by an experimental demonstration. Now we focus on a device with a reversed metal structure - with square blocks of gold on the hexaferrite substrate.

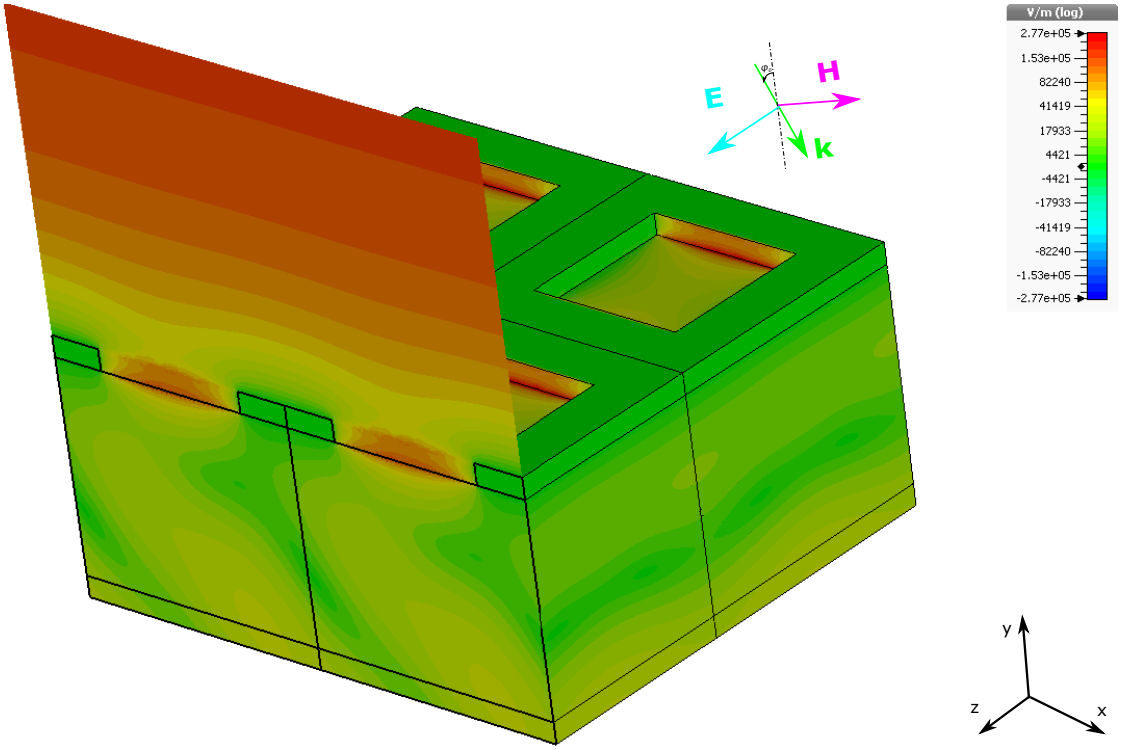

Figure 4.22: Field color map of $\mathbf{E}_z$ field component of the device with non-magnetized substrate at 245.5 GHz for 4 unit cells

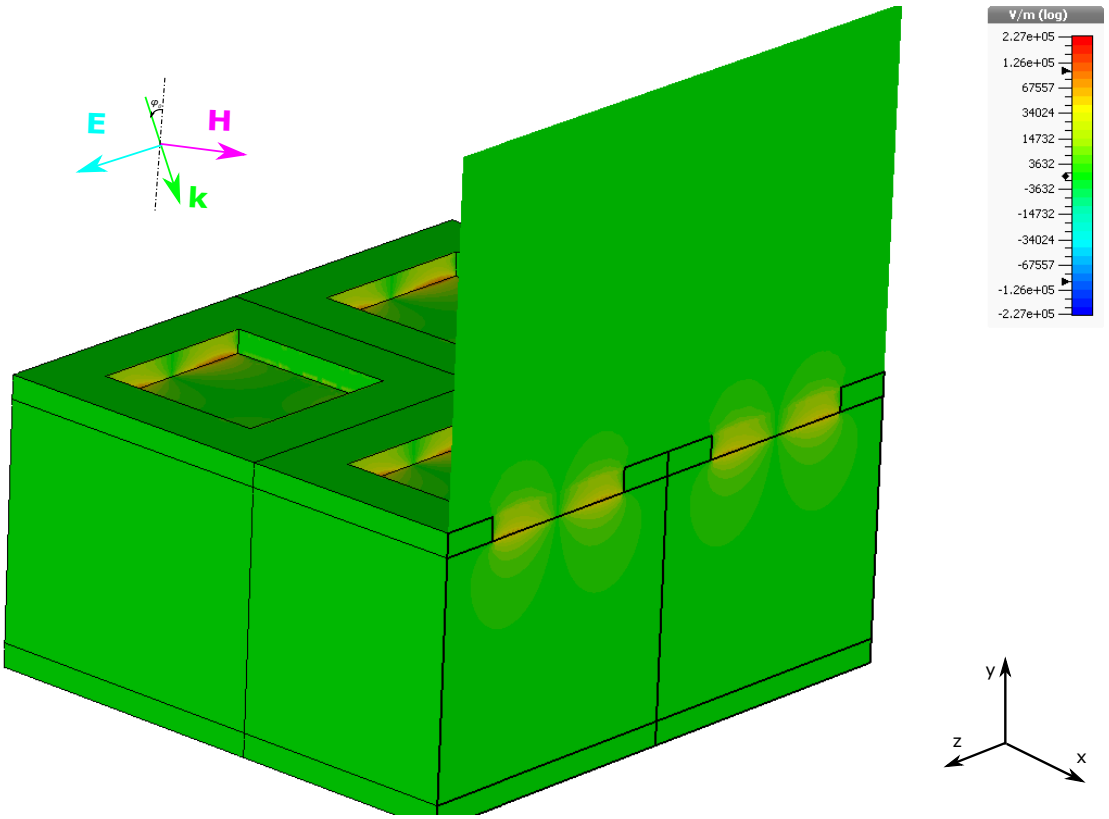

Figure 4.23: Field color map of $\mathbf{E}_x$ field component of the device with non-magnetized substrate at 245.5 GHz for 4 unit cells

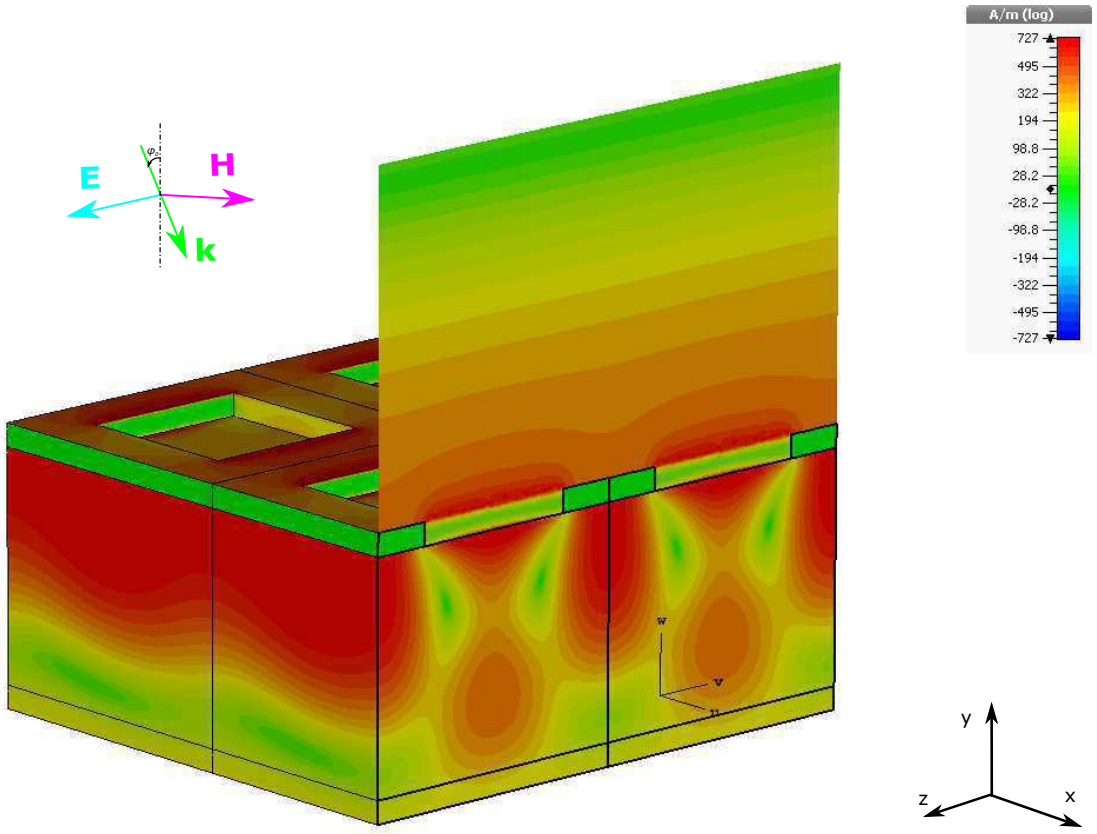

Figure 4.24: Field color map of $\mathbf{H}_x$ field component of the substrate mode at 270.7 GHz for 4 unit cells of non-magnetized device

4.2.2 2D Square Blocks

Even before the study of the design with 2D holes in the metallic layer we considered the reversed structure which is described in this section. The original idea was to extend techniques of NR resonant effects shift working at optical frequencies with use of 1D periodic metallic grating (1D thin infinite slits in the gold layer) [80, 115, 217] and transform this design into 2D. It therefore means to keep the 1D-infinite thin slits and introduce them also into the second perpendicular dimension. The studied device is shown in Fig. 4.25 and consists of the hexaferrite ceramics substrate on which there is deposited the gold structure of a thickness h with square blocks with a period Λ and slits of the size r with an incident TE-polarized wave at an incidence angle ϕ_0.

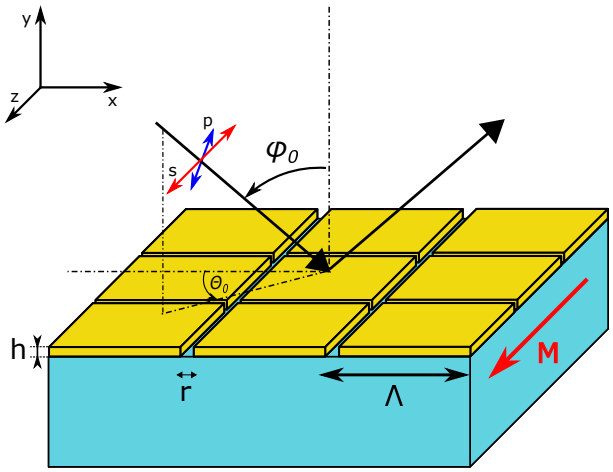

Figure 4.25: Schematic representation of the studied THz nonreciprocal device: gold layer patterned by 2D periodic grating with period Λ, slit width r and thickness h on a magneto-optical hexaferrite substrate magnetized in transverse configuration with incident s- or p-polarized plane wave at an angle of incidence ϕ_0 and an azimuthal angle θ_0.

The initial study was focused on the possibility of obtaining of guided modes, representing surface plasmons, in the structure. These guided modes are described by the dispersion relation given by Eq. (4.12). The phase constant β is

a function of frequency (for a plane wave in a free space $\beta(\omega) = \omega\sqrt{\varepsilon_0\mu_0}$) and the phase velocity v_p and group velocity v_g can be defined as:

$$v_p = \frac{\omega}{\beta}, \qquad v_g = \frac{\mathrm{d}\omega}{\mathrm{d}\beta}. \tag{4.38}$$

For surface waves in a periodic structure there may exist several different propagation constants β at the same frequency, each one describing a specific mode with its own phase velocity, group velocity and field distribution [218]. The relation between β and ω is known as a *dispersion diagram*. For a periodic structure, the field distribution of a surface wave is also periodic with a phase delay given by the wavenumber k or phase constant β and periodicity Λ.

Because the dispersion curve is for a periodic structure also periodic along the β-axis with a periodicity $2\pi/\Lambda$, one needs to plot the dispersion relation within one single period, which is in a reciprocal space also known as the *Brillouin zone*. In 2D period structures, with periodicity in the $x-z$ plane, the Brillouin zone becomes a two-dimensional square area with:

$$0 \leq \beta_{xn} \leq \frac{2\pi}{\Lambda}, \qquad 0 \leq \beta_{zn} \leq \frac{2\pi}{\Lambda}. \tag{4.39}$$

Figure 4.26 shows a dispersion diagram obtained by the Eigenmode solver in CST Studio of the studied nonmagnetized 2D structure with $\Lambda = 50\,\mu\mathrm{m}$, $r = 20\,\mu\mathrm{m}$, $h = 60\,\mu\mathrm{m}$, where the metal of the grating was for a simplicity considered as a PEC and the substrate was characterized by $\varepsilon_2 = 21$. The three main directions in the 2D Brillouin zone are labeled as Γ–X, X–M and M–Γ. This dispersion relation shows that there may exist guided surface plasmons in the given structure, however the considered grating thickness was too high for real fabrication. Therefore we decreased the grating thickness to 30 µm and calculated reflectance spectrum of a TE-polarized wave incident at $\phi_0 = 5°$, which is shown in Fig. 4.27.

One can see the sharp resonance dip at $\nu = 1.62\,\mathrm{THz}$ signifying the presence of SPPs which is accompanied by the characteristic reflectance maximum, denoting the Wood-Rayleigh anomaly. This result serves as the first numerical proof of

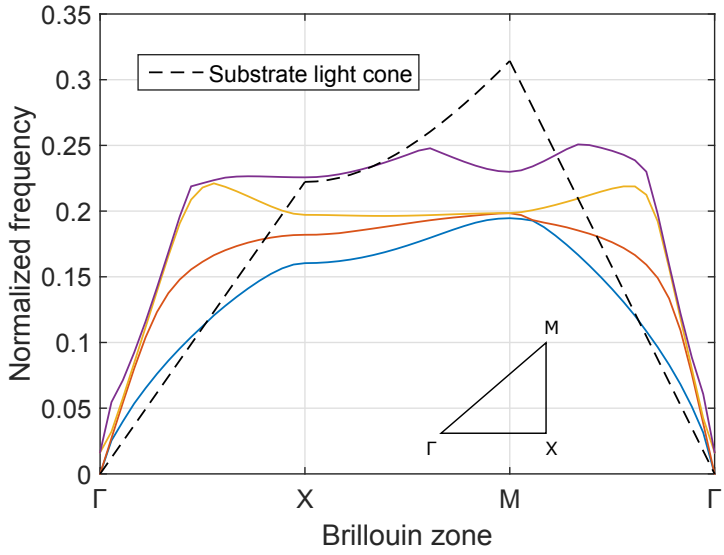

Figure 4.26: Dispersion diagram of the studied structure with 2D gold grating with the parameters: $\Lambda = 50\,\mu m$, $r = 20\,\mu m$, $h = 60\,\mu m$, black dashed line represents the light cone of the substrate.

the SPPs excitation at THz frequencies with use of the 2D-blocks grating, which was also confirmed by a field color map of $\mathbf{H}_y$ field component, shown in Fig. 4.28. This field color map shows the presence of SPPs and their strong localization at the grating/substrate interface. The reflectance minimum present at $\nu = 1.36\,THz$ comes from a low-quality FP resonance in the slits of the grating, as confirmed by a field color map of $\mathbf{E}_z$ field component, shown in Fig. 4.29. The spectral position of the WR anomaly at lower frequency than SPPs resonance is caused by the large thickness of the metal grating.

The following step of the design development was focused on a scaling the grating dimensions for SPPs excitation close to the ferromagnetic resonance frequency of hexaferrites. The structural dimensions were increased to $\Lambda = 1410\,\mu m$, $r = 202\,\mu m$ and thickness of the grating yet decreased to $h = 1\,\mu m$. This grating thickness would be already easier to fabricate by classical deposition techniques. Figure 4.30 shows simulated reflectance spectra obtained by CST Studio after a TE-wave incident at 45° at the above described device. The metal is

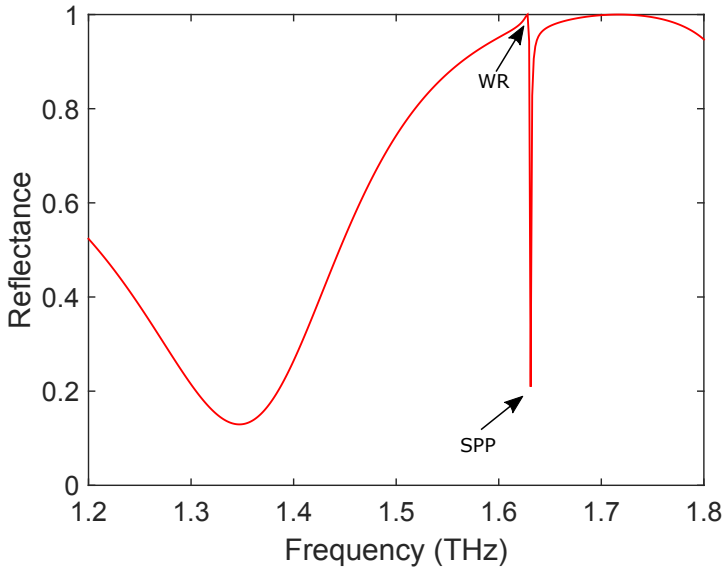

Figure 4.27: Numerical calculation of TE-polarization reflectance spectra ($\phi_0 = 5°$, $\theta_0 = 0°$) of the structure consisting of nonmagnetized hexaferrite substrate ($\varepsilon_2 = 21$) and a 2D PEC grating with the parameters: $\Lambda = 50\,\mu m$, $r = 20\,\mu m$, $h = 30\,\mu m$

still considered as a PEC, but in this case the substrate was already magnetized, with the gyrotropy parameters obtained by the MO characterization presented in Chapter 3. The full lines therefore correspond to the opposite direction of magnetization (in the $x - z$ plane, transverse to the plane of incidence) and the dashed line represent the case when $\mathbf{M} = 0$. One can observe the NR shift of the SPPs resonances caused by a coupling with the TMOKE effect. Different directions of the shift for both resonant frequencies are caused by the opposite sign of the SPP resonance modes, e. g. $[-1, \pm 1]$, $[+1, \pm 1]$. The isolation ranges are marked by vertical dashed lines and the obtained isolation can be calculated with use of Eq.

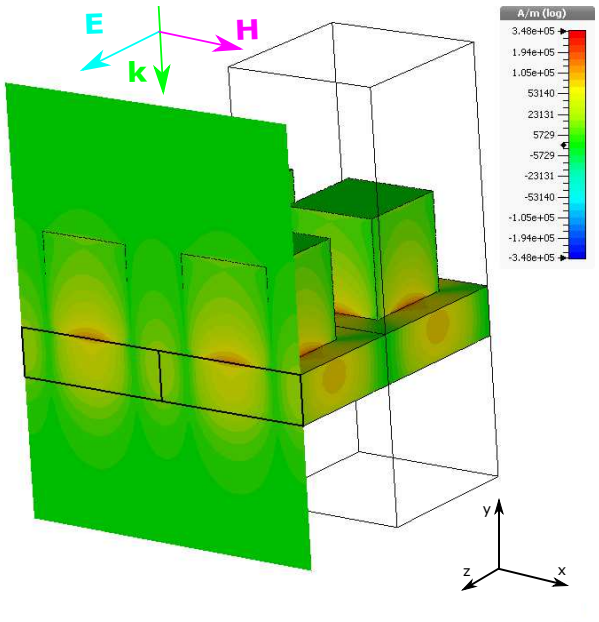

Figure 4.28: Field color map of $\mathbf{H}_y$ field component of the structure with 2D grating of PEC on a nonmagnetized hexaferrite substrate $\varepsilon_2 = 21$ at 1.62 THz showing a confinement of SPPs to the interface

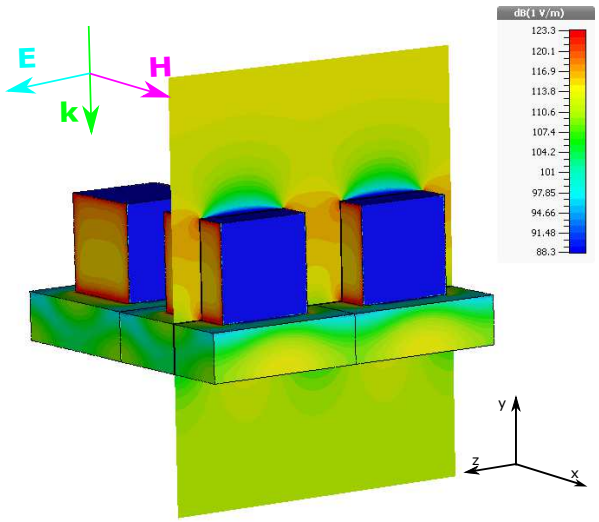

Figure 4.29: Field color map of $\mathbf{E}_z$ field component of the structure with 2D grating of PEC on a nonmagnetized hexaferrite substrate with $\varepsilon_2 = 21$ at 1.36 THz showing low-Q FP resonance

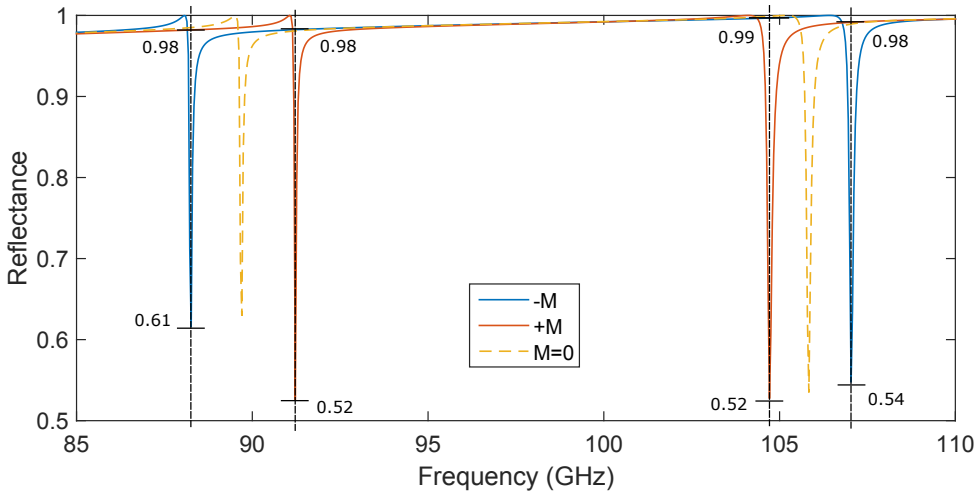

Figure 4.30: Simulated spectra (CST Studio) after reflection of TE-polarized wave incident at $\phi_0 = 45°$, $\theta_0 = 0°$ on the transversely magnetized THz NR reflecting device with square grating made from perfect electric conductor, where $\Lambda = 1410\,\mu m$, $r = 202\,\mu m$, $h = 1\,\mu m$. Full lines correspond to the opposite magnetization directions and dashed line represents the case when $\mathbf{M} = 0$. The isolation ranges are marked by black dashed vertical lines.

(4.36). This gives the following values:

$$\Delta R_s\,(\nu = 88.2\,\mathrm{GHz}) = 2.06\,\mathrm{dB} \tag{4.40a}$$

$$\Delta R_s\,(\nu = 91.2\,\mathrm{GHz}) = 2.75\,\mathrm{dB} \tag{4.40b}$$

$$\Delta R_s\,(\nu = 104.6\,\mathrm{GHz}) = 2.80\,\mathrm{dB} \tag{4.40c}$$

$$\Delta R_s\,(\nu = 107.0\,\mathrm{GHz}) = 2.59\,\mathrm{dB}. \tag{4.40d}$$

This isolation proof-of-principle at low frequencies supported our further study of the design which was consequently scaled for SPPs excitation in the desired mm-wave range, as shown in Fig. 4.31. Here we can see the characteristic resonance phenomena again for a TE-polarized wave incident at $\phi_0 = 45°$ on a device with structural parameters $\Lambda = 560\,\mu m$, $h = 1\,\mu m$ and with 3 different slits sizes r =60 µm, 80 µm and 100 µm. In order to experimentally characterize resonance

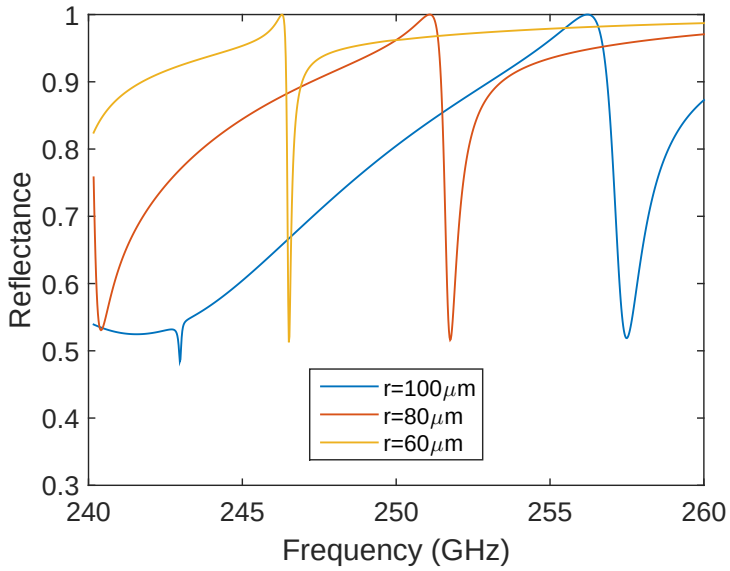

Figure 4.31: Simulated spectra after reflection of TE-polarized wave incident at $\phi_0 = 45°$ on structures with $\Lambda = 560\,\mu m$, r =60 µm, 80 µm and 100 µm, $h = 1\,\mu m$, with nonmagnetized hexaferrite substrate.

behavior of the device as a function of the grating period and slits size, we decided to fabricate structures with 3 different lattice periods and each of this period with 6 different slit dimensions. Because our particular aim was to obtain NR behavior in the mm-wave range, the proposed grating periods were Λ =700 µm, 560 µm and 460 µm which were supposed to support plasmonic resonance close to ν =200 GHz, 250 GHz and 300 GHz, respectively. Table 4.3 summarizes all fabricated grating dimensions. The space factor included in the table corresponds to a ratio r/Λ.

Table 4.3: Dimensions of fabricated gold gratings

hexaferrite (i)	Λ (µm)	space factor (%)	R	S_1	S_2	S_3	S_4	S_5
			0	2	5	10	20	25
1	700	r (µm)	0	14	35	70	140	175
2	560	r (µm)	0	11	28	56	112	140
3	460	r (µm)	0	9	23	46	92	115

We prepared 3 hexaferrite substrates and on each of them there were deposited 6 grating structures with an identical lattice period. A schematic representation of the gratings positioning on a hexaferrite is shown in Fig. 4.32. Here R represents a reference structure with a pure gold layer without slits and S_1–S_5 are the grating structures with different slit size, in accordance with Table 4.3.

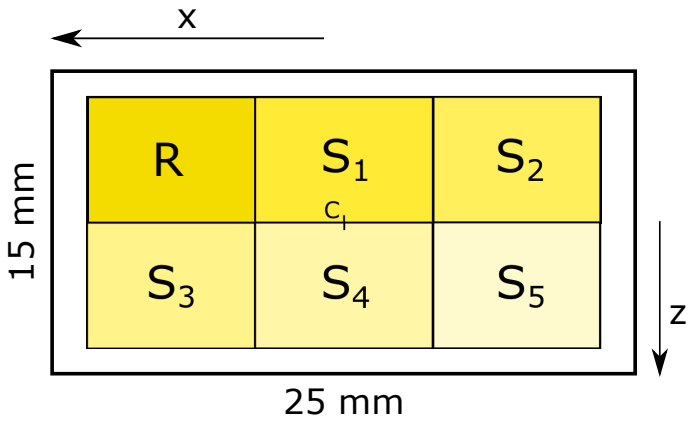

Figure 4.32: Schematic representation of fabricated structure on ceramics surface. Each sample contains 6 grating structures with different r/Λ ratio, R denotes a reference structure with no slits, S_{1-5} represent 2%, 5%, 10%, 20% and 25% of the ratio, respectively, C is the central point for a measurement position calibration at (0,0,0).

The fabrication process of the gratings was similar to the previous structures, the structured gold layers were deposited by lift-off technique. As it was already mentioned, due to the high ceramics natural adhesion, there is no need for an additional adhesion layer between the substrate and structured layer for the gold deposition. Dimensions of all the grating structures were after fabrication controlled by scanning electron microscopy, as one can see for samples with $\Lambda = 700\,\mu m$ in Fig. 4.33a ($r = 14\,\mu m$) and in Fig. 4.33b ($r = 175\,\mu m$). Dimensions of the ceramic substrate are $25 \times 15\,mm$, however the fabrication process did not allow to cover the full sample surface and required $\approx 1\,mm$ of uncovered space at each side. Therefore, each grating structure had dimensions $7 \times 7\,mm$,

which gives an area larger then a focused beam spot size at 200 GHz ($\lambda = 1.5\,\text{mm}$, $d_{beam} \approx 5\,\text{mm}$). A photo of a real sample with 6 fabricated structures, where

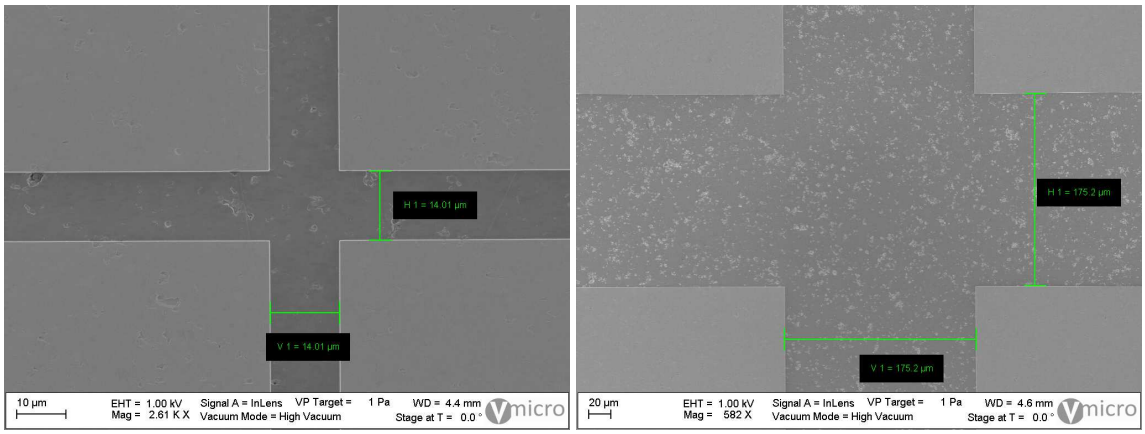

(a) $r = 14\,\mu\text{m}$ (b) $r = 175\,\mu\text{m}$

Figure 4.33: SEM images of fabricated 2D gratings on hexaferrite surface with period $\Lambda = 700\,\mu\text{m}$ and slit size $r = 14\,\mu\text{m}$ and $r = 175\,\mu\text{m}$ confirming the desired dimensions.

$\Lambda = 700\,\mu\text{m}$, is then shown in Fig. 4.34.

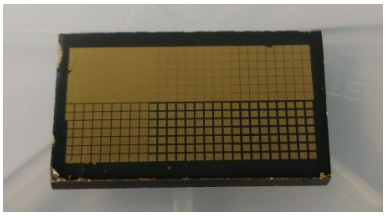

Figure 4.34: Photograph of the real fabricated sample with 6 different gold structures

4.2.2.1 Isolator characterization

For the purpose of the samples characterization we prepared the VNA-driven quasi-optical setup for a reflection measurement with a focused beam incident on the sample under an angle $\phi_0 = 45°$, $\theta_0 = 0°$, as shown in Fig. 4.35. Here, the reflected signals from the sample under scan are represented by S_{21} and S_{12}

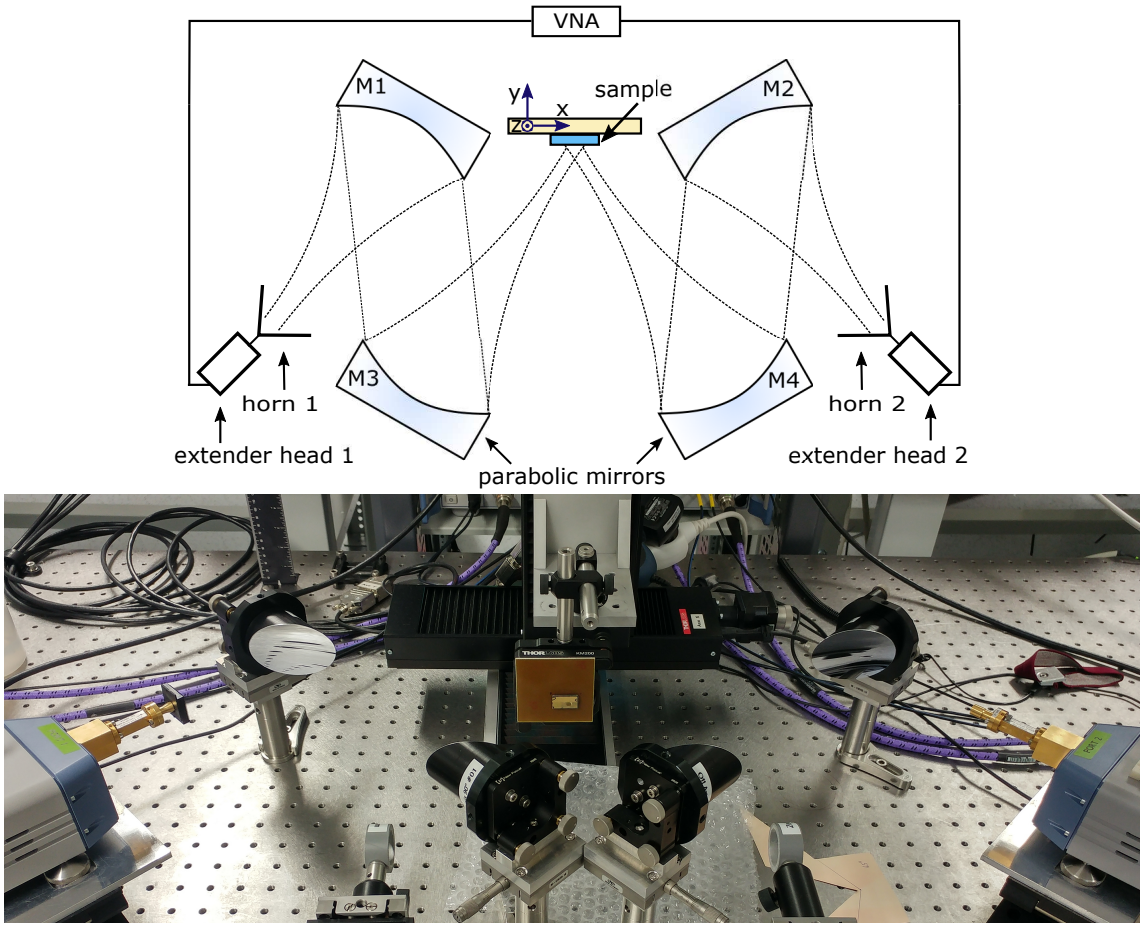

Figure 4.35: Schematic representation (top) and a photo (bottom) of the quasi-optical setup for reflection measurement with angle of incidence $\phi_0 = 45°$, $\theta_0 = 0°$. The measured sample is hold on the positioning stage in order to characterized different positions on the sample surface.

parameters measured by the horns. Because the goal of the measurement was to characterize responses of all the grating designs on the sample, the latter was tacked on a 3D $x - y - z$ positioning stage which enables to move with the sample in a desired direction. The position was after each scan moved by 1 mm in x or z direction (as depicted in Fig. 4.32) in order to scan over the full sample surface and therefore also over all the grating structures. Because the expected SPPs resonance is manifested as a very sharp feature in a reflectance spectra, the VNA setup was calibrated with 12001 measurement points in the frequency band

200–325 GHz giving therefore a high frequency resolution $\delta\nu \approx 10.4$ MHz. All the samples were before the characterization magnetized by an external electromagnet at $B = 1.6$ T and measured in their remanent magnetization state.

Figure 4.36 shows measured S-parameters at the central points of the 6 grating structures with $\Lambda = 560\,\mu$m. The positions of the plots corresponding to structures with different slits sizes is in agreement with the positions in Fig. 4.32. One

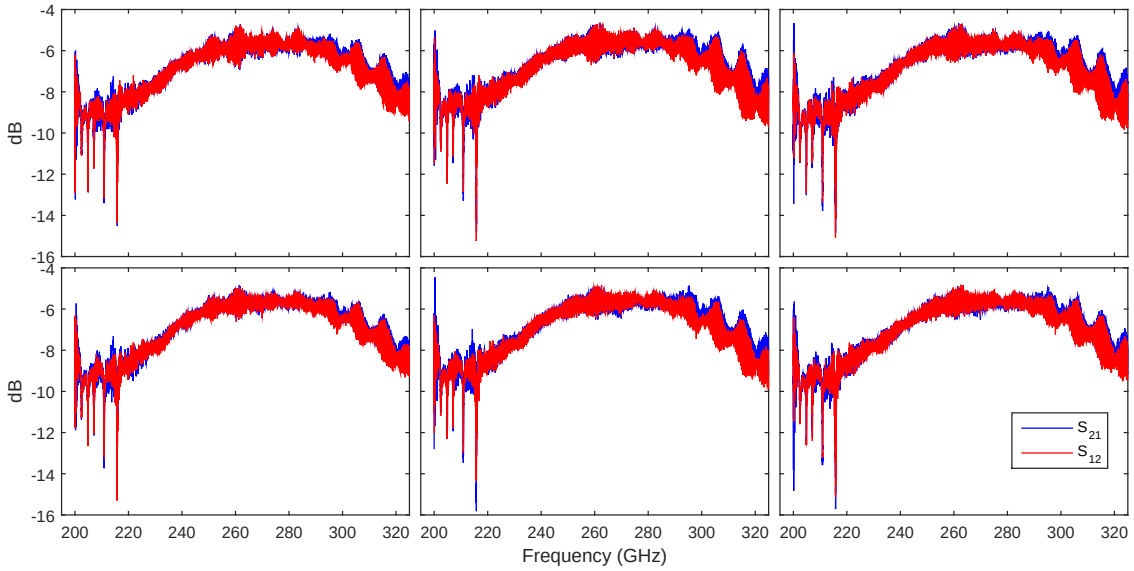

Figure 4.36: Measured S_{21} and S_{12} parameters at central points of all 6 grating structures fabricated on ceramics surface with $\Lambda = 560\,\mu$m. The positions of structures with different filling factor corresponds to the positions shown in Fig. 4.32 - from top, left: R, S_1-S_5.

can see that there is almost no difference between both S parameters of all six structures. Moreover, measured data are again influenced by a presence of standing waves in the setup, causing high-frequency resonances in the measured S-spectra. In the following step of the data treatment we applied the time-domain-gating procedure, as was already explained and used in Section 3.2.2, in order to remove all unwanted detected parasitic contributions. For this purpose a measured signal from a given grating structure was normalized to the signal of the reference structure (R) and then the TD gating procedure was applied. The fil-

tered S-spectra of one particular grating structure ($\Lambda = 560\,\mu m$, $r = 56\,\mu m$) is shown in Fig. 4.37. It is apparent, that there is a very little difference between

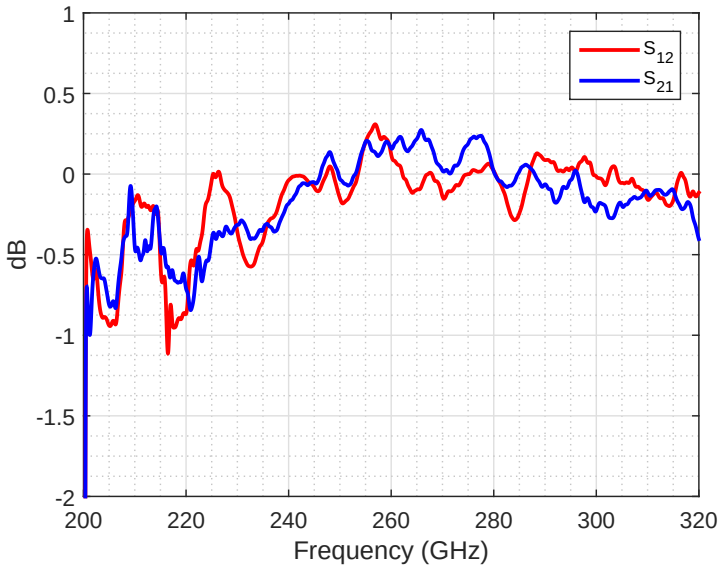

Figure 4.37: Normalized S_{21} and S_{12} parameters of the grating with $\Lambda = 560\,\mu m$ and $r = 56\,\mu m$ after time-domain gating procedure for removing all unwanted echoes.

both S-parameters, e.g. at 227 GHz or around 270 and 300 GHz, however no evident resonance phenomena can be observed. After a further study we concluded that this unsuccessful measurement, which was obtained also with the other 2 prepared samples, can be caused by several reasons, described in the following paragraphs.

First of all, we primarily wanted to compare resonant behavior of structures with different grating parameters. This was the reason why we put 6 different grating designs at an one ceramic substrate. However, in that case a single grating included a low number of periods (7 periods in z-direction for $L = 700\,\mu m$). This is perhaps one of the main reasons why SPPs were not excited, since the whole structure then did not behave like an effective medium. Consequently to the small single structure area, we had to use a strongly-focused beam with as small spot size as possible. This however led into a large beam diffraction and

large angular-width of the beam incident at a sample. Since the SPPs resonance phenomena are typically very sensitive to the angle of incidence, these effects could cause a decreasing of a resonance quality. Finally, we wanted to see how the S_{21} parameter changes with various slits size, and for this purpose we plot a mapping of the S_{21} measured amplitude over the full sample surface ($\Lambda = 560\,\mu m$) at one particular frequency $\nu = 260\,GHz$, and this mapping is shown in Fig. 4.38.

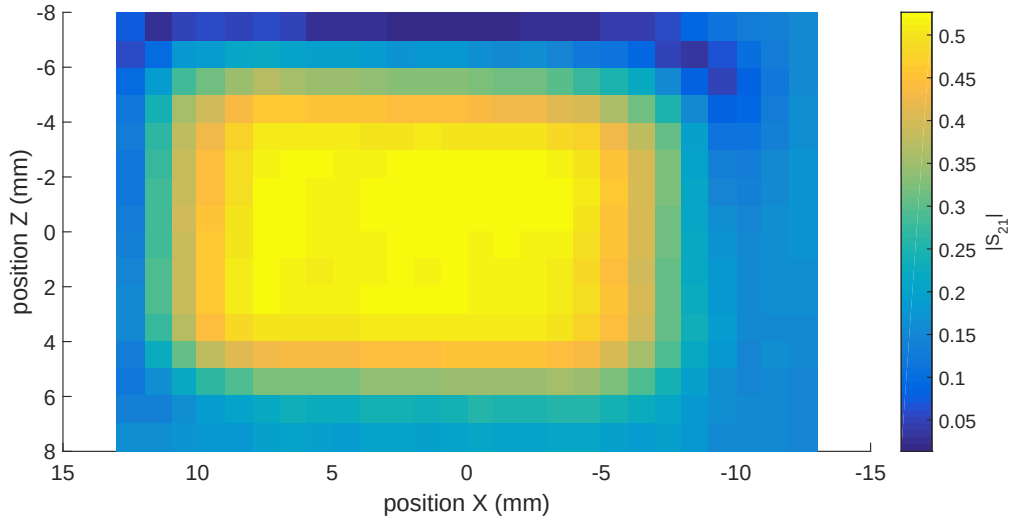

Figure 4.38: Mapping of the S_{21} amplitude over full sample surface with $\Lambda = 560\,\mu m$, for $\nu = 260\,GHz$.

One can see that there is no significant difference in the measured S parameter while moving with the sample position. All the sample behaved as a single reciprocal mirror without any difference in various grating structures, and therefore without SPPs excitation. From these results we can conclude that there are two main requirements which must be fulfilled for future experiments: First of all, the reflection characterization must be done with a collimated beam in order to reduce the beam angular-width and diffraction effects and this is leading immediately to the second condition - a larger area of a gold grating with an increased number of periods for successful excitation of SPPs.

In the last section we will describe the procedure of the ceramics substrate preparation, as this process is not as straightforward as it could appear and there are some difficulties which have to be solved for a preparation of a suitable hexaferrite substrate.

4.2.3 Difficulties in Fabrication

The first, and also one of the most important step in the device fabrication procedure is the preparation of the ferrite substrate. The hexaferrite ceramics is commercially available usually as bulk material, which is difficult to fabricate with a high surface/thickness ratio. Because the ensuing deposition of a structured metal layer requires a maximum thickness of the substrate between 1–3 mm and the working principle of the periodic structure for mm-waves asks for surface dimensions to be larger than $10 \times \lambda_{max}$, where λ_{max} is the maximum wavelength of the operation bandwidth, we had to find a way how to properly cut a fabricated block of ceramics (see Fig. 3.34) into desired thin sheets. After trying of several different cutting methods we found out, that the best one, and perhaps also the only one, process which can be applied for the ceramics is the technique of cutting by a water jet.

Micro-water-beam cutting uses high pressures (~ 4 kbar) for pressing a solution of water with an abrasive material through a thin jet. The diameter of the obtained cutting jet can be reduced up to 0.2 mm and has enough energy to be able to cut even very hard materials. Because the movement of the beam is driven by a computer, a high positioning accuracy in the order of μm is ensured.

Advantages of the water-jet cutting

- Cutting is obtained without a contact of the material with the cutting machine
- No thermal strain or internal tension in the material

- Minimum of unused material waste
- No new cracks in the material around the cut
- Water jet cutting does not cause the air-borne dust to be formed from the split material
- It is possible to cut soft materials as well as hard and brittle ones of various physical and chemical properties
- No chemical changes in the resulting material

Cutting of our samples was done in co-operation with VŠB - Technical university of Ostrava[2] who dispose of the water-jet cutting machine at the Institute of Geonics (Czech Academy of Sciences).

The following step of the ceramics preparation is the polishing of the cut sheets. In order to reduce its surface roughness we applied three different polishing techniques, as explained in Section 3.1.1. The best results have been obtained with use of Al_2O_3 polishing with resulting average surface roughness $R_q = 14.7\,\text{nm}$. For the polishing procedure the ceramics must be glued on a glass substrate and the full ceramics/glass structure is then moved on a polishing surface.

During the whole cutting-polishing procedure we were dealing with the brittleness of the ceramic material. Several cutting attempts resulted into broken samples, as shown in Fig. 4.39. Some of the samples survived the cutting process, but were broken during an application of a high pressure gluing for the subsequent polishing or during the final metallic structure deposition. We found out, that in some of the fabricated ceramic blocks there were small defects and cracks present increasing the natural ceramics brittleness, and resulting in cleavages at the same place of cut samples (see Fig. 4.39). Figure 4.40 shows one of the cleavage which in the fabrication process led to the sample destruction. The

[2] VŠB - Technical university of Ostrava, 17. listopadu 15/2172, 708 33 Ostrava–Poruba, Czech Republic

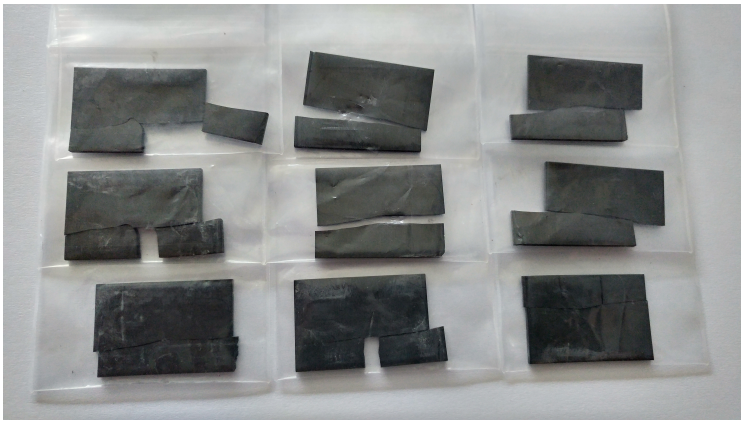

Figure 4.39: Ceramics broken during cutting or polishing procedures

ceramic blocks are typically prepared from a ferrite powder by molding and sintering processes. With an increasing sample size it is therefore not easy to assure a high-quality of the produced material without intrinsic defects, and one has to thus take into account this difficulty when designing the ceramics for the device substrate application.

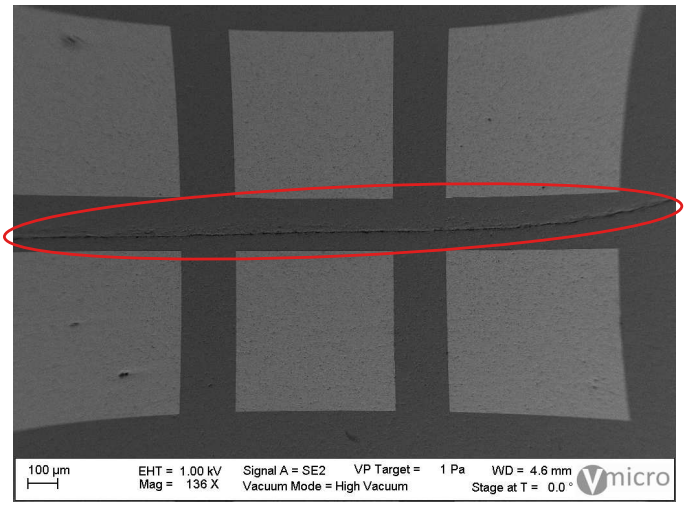

Figure 4.40: SEM image of the ceramics with fabricated gold grating. The highlighted cleavage caused the sample break-up during subsequent fabrication process.

4.3 Conclusion of the Chapter

This chapter was focused mostly on the design of the proposed THz nonreciprocal magneto-plasmonic mirror. After presenting the material properties of gold in THz range, we studied both numerically and experimentally an excitation of spoof SPPs via structuring of a gold grating deposited on a quartz substrate. The obtained good agreement between measured and simulated data confirmed the first experimental observation of SPPs at mm-wave frequencies. These results were followed up by two different designs of gold structures on the surface of hexaferrite ceramics, including square holes in the gold layer and square blocks separated by thin slits. We numerically studied a behavior of the SPPs resonant frequency in dependence on the substrate and grating parameters and the angle of incidence. We observed a first SPPs excitation on the designed and fabricated hexaferrite/plasmonic device and numerical simulations confirm a strong isolation potential at reflection configuration of both the studied designs.

We can therefore conclude that by a proper structuring of a metal on the surface of hexaferrite it is possible to excite spoof SPPs by an incident TE-polarized wave which is a crucial phenomena for functionality of the proposed THz isolator. Moreover, the shape of the holes in the gold layer can influence a polarization preservation of the evanescent modes.

For the envisioned experimental demonstration of the isolation there is a need for fabrication of samples with larger area of a gold grating. This can be complicated by a proper preparation of the hexaferrite substrate, which was described at the end of the chapter.

General Conclusion

This thesis was focused on the study of nonreciprocal effects using hexagonal ferrites and all important results of the work are summarized in the following paragraphs.

Free-space characterization - published in [79] - of 4 different non-magnetized hexagonal ferrite materials in the sub-millimeter wave range has been done using a VNA-driven quasi-optical setup (Chapter 3, Section 3.2). The obtained results show that the optical functions and losses can vary among different hexaferrites and all non-magnetized materials behave in this frequency range almost like dielectric materials. However, our expectation that ceramic materials should possess high insertion losses was not confirmed, as the highest losses have been measured in the crystalline Sr-hexaferrite (Fig. 3.23).

Magneto-optical characterization - submitted for publication [219] - in the wide frequency band using THz-TDS was done with FB6N hexaferrite ceramics. This ferrite material has shown up itself as the most promising candidate for the operation in THz NR devices particularly due to the highest value of remanent magnetization from all measured samples. The obtained gyrotropic and anisotropic spectra show indeed its strong nonreciprocal behavior in the full measured band (Chapter 3, Section 3.3). This material can be used to design **nonreciprocal** Faraday isolators and its highest efficiency is obtained in the mm-wave range, where losses originating both from the imaginary part of permeability and permittivity are minimal, as was shown by calculated rotation power in Fig. 3.33. The strong Faraday isolation was then measured using two polarizers relatively tilted in the mm-wave band (Chapter 3, Section 3.4).

Demonstration of spoof plasmons excitation in the mm-wave band was done by designing, fabricating and measuring a gold grating on a low-loss quartz sub-

strate (Chapter 4, Section 4.2.1.1). The obtained transmission spectra by THz-TDS agree well with our calculated results and confirm the possibility of SPPs existence at THz frequencies (Fig. 4.7). While the SPPs excitation at frequencies close to 1 THz had been already demonstrated by few authors, at the moment there is little literature describing this in the lower, mm-wave, band. This is a very important result for the proposed novel THz isolator design.

THz isolator using an one-way reflecting surface has been studied theoretically, numerically and experimentally. This isolator builds up on the enhancement of the magneto-optical transverse Kerr effect by local field concentration caused by the presence of spoof plasmons. For plasmons excitation at metal/hexaferrite interface we studied two different gold grating structures - 2D holes and 2D square blocks with various structural parameters (Chapter 4, Section 4.17). Both designs enable the spoof plasmons excitation as well as the coupling with the gyrotropy of the hexaferrite substrate and therefore confirm the principle of the proposed isolator. The plasmons excitation at the gold/hexaferrite interface via the 2D holes structure has been confirmed experimentally by transmission measurement of the fabricated sample done by THz TDS (Fig. 4.17). Further characterization is ongoing as the TDS is not suitable for the isolation demonstration due to the low frequency resolution and a quasi-optical characterization by the VNA setup is complicated by standing waves and the large beam divergence in the setup.

Perspectives

The achieved results in this thesis bring up a number of areas which could be interesting for a potential future study and research.

In the first place, obviously, there must be mentioned the proper characterization of the fabricated isolators. Even though that the spoof plasmons existence at the metal/hexaferrite interface has been demonstrated by THz TDS, the experimental demonstration of the isolation in a reflection measurement is very important, however also a rather challenging. From all the performed experiments with the fabricated isolators we have understood that this isolation experiment must be done using the VNA-setup calibrated for a high frequency resolution with a perfectly collimated beam in order to avoid diffraction as much as possible. Also the present standing waves must be limited as much as possible using THz absorbers and subsequent TD gating for an extraction of just a single reflection pass.

The envisioned experiment with a collimated beam for the mm-wave range may require a larger grating area for proper plasmons excitation. This necessitates a fabrication of larger samples, however, as was explained in Section 4.2.3, the brittleness of the hexaferrite ceramics makes the preparation of a substrate with a high surface/thickness ratio very challenging.

For the SPPs excitation at the metal/substrate interface we studied two types of gold structure - 2D holes and 2D square blocks. While the EOT effect with use of a metal layer with holes has been well described in literature, the resonance phenomena of the structure with blocks is rather new and requires yet more study and better understanding. Consequently, it would be interesting to study also other structures, especially holes and blocks with different shapes, e. g. rectangle holes and blocks, circular blocks, or even more complicated structures. Due to the high anisotropy of hexaferrites, this can lead into stronger resonance effect and hence also to the total isolation enhancement. Therefore, the total optimization of the structure is still required and offers a number of possible approaches.

Regarding the choice of the hexaferrite for the use as a substrate, the ceramic samples seem to be the best candidates especially due to their high remanence and comparable losses with other hexagonal ferrites. We chose the FB6N ceramics, however modern fabrication processes enable to preparation much more types of ferrite ceramics (Fig. 3.24). It would be very interesting to study also other samples, since the materials of FB 9, 12, 13, 14 series should possess higher values of remanence and coercitive force and therefore also higher values of FMR and stronger gyrotropy are expected. However, all these materials must be properly characterized, since intrinsic losses may vary due to different fabrication processes.

List of Abbreviations and Symbols

Abbreviations

AFM	Atomic force microscopy
CW	Continuous-wave
EM	Electromagnetic (radiation)
EOT	Extraordinary optical transmission
FD	Frequency domain
FEM	Finite elements method
FFT	Fast Fourier transformation
FIR	Far-infrared
FMR	Ferromagnetic resonance
FP	Fabry-Perot
FT	Fourier transformation
IFFT	Inverse fast Fourier transformation
IR	Infrared (radiation)
LHCP	Left-hand circular polarization
LMOKE	Longitudinal magneto-optical Kerr effect
MCB	Magnetic circular birefringence
MCD	Magnetic circular dichroism
MIR	Mid-infrared

MLB	Magnetic linear birefringence
MLD	Magnetic linear dichroism
MO	Magneto-optical (effect)
MOKE	Magneto-optical Kerr effect
NOP	Nonlinear optical process
NR	Nonreciprocal
NRD	Nonreciprocal device
NSOM	Near-field scanning optical microscopy
PC	Photoconductive
PEC	Perfect electric conductor
PML	Perfectly matched layer
PMOKE	Polar magneto-optical Kerr effect
RCWA	Rigorous coupled-wave analysis
RHCP	Right-hand circular polarization
SEM	Scanning electron microscopy
SPPs	Surface plasmons polaritons
SPs	Surface plasmons
TD	Time-domain
TDS	Time-domain spectroscopy
TE	Trasverse electric (polarization)
THz	Terahertz

TM	Trasverse magnetic (polarization)
TMOKE	Transverse magneto-optical Kerr effect
UV	Ultraviolet (radiation)
VNA	Vector Network Analyzer
VSM	Vibrating sample magnetometer
WR	Wood-Rayleigh (anomaly)

Greek symbols

β	Propagation constant
γ	Gyromagnetic ratio
δ_{ij}	Kronecker delta
$\varepsilon_{s,p}$	Kerr ellipticity for s and p polarization
$\bar{\bar{\varepsilon}}$	Permittivity tensor
ε_0	Vacuum permittivity
ε_r	Relative permittivity
η	Impedance
θ_0	Azimuthal angle of incidence
Θ_F	Faraday rotation
$\Theta_{s,p}$	Kerr rotation for s and p polarization
κ	Off-diagonal permeability component
Λ	Lattice period
λ	Wavelength

λ_c	Cut-off wavelength
$\bar{\bar{\mu}}$	Permeability tensor
μ_0	Vacuum permeability
μ_r	Relative permeability
ν	Frequency
$\tilde{\nu}$	Wavenumber
ρ	Volume electric charge density
χ^2	Objective minimization function
$\bar{\bar{\chi}}_e$	Electric susceptibility tensor
$\chi'_{m,n}$	Zeros of derivative of Bessel function
$\bar{\bar{\chi}}_m$	Magnetic susceptibility tensor
ϕ_0	Angle of incidence
φ_x, φ_y	Phase of complex envelope components
Ξ	Rotation power
ω	Angular frequency
ω_0	Larmor ferromagnetic resonance frequency
ω_m	Magnetization frequency
ω_p	Plasma frequency
ω_{sp}	Surface plasmons frequency

Latin symbols

a_x, a_y	Magnitudes of complex envelope components

c	Speed of light
d	Sample thickness
g	Gyroelectric constant
h	Planck's constant
i	Imaginary unit
$\mathbf{j}$	Electric current density
k	Imaginary part of a complex refractive index
$\mathbf{k}$	Wavevector
$\mathbf{k}_{SPP}$	Wave vector of SPP
n	Real part of a complex refractive index
$\hat{n}$	Complex refractive index
n_+	Refractive index for right-handed circularly polarized light
n_-	Refractive index for left-handed circularly polarized light
$\hat{r}_p, \hat{r}_s$	Complex reflection coefficient for p and s polarization
$\mathbf{r}$	Position vector
$\hat{t}_p, \hat{t}_s$	Complex transmission coefficient for p and s polarization
t	Time
$\mathbf{A}$	Complex envelope
$\mathbf{B}$	Magnetic flux density
$B_i^k(x)$	B-spline basis function
$\mathbf{D}$	Electric displacement

E	Energy
$\mathbf{E}$	Electric field vector
E_0	Electric field amplitude
$\mathbf{G}_x, \mathbf{G}_y$	Reciprocal lattice vectors
H_0	Internal magnetic field amplitude
$\mathbf{H}$	Magnetic field vector
H_A	Magnetic anisotropy field amplitude
H_d	Demagnetization field amplitude
H_{ext}	External magnetic field amplitude
H_0	Magnetic field amplitude
$\mathbf{J}^+$	Hermitian conjugated vector
$J_m(x)$	Bessel function
$\mathbf{M}$	Magnetization vector
M_r	Remanent magnetization
M_s	Saturation magnetization
$\mathbf{P}$	Dipole moment density
Q	Magneto-optical (Voigt) parameter for permittivity
Q_m	Magneto-optical (Voigt) parameter for permeability
R_q	Surface roughness (root mean squared)
V	Verdet constant
Y	Wave admittance

Other symbols

$\boldsymbol{\imath}_i$	Unit vector in i-direction
$\Im$	Imaginary part of a complex number
$\nabla\cdot$	Divergence operator
$\nabla\times$	Curl operator
∂	Partial derivation
$\Re$	Real part of a complex number

List of Figures

List of Tables

List of Publications

International Journals

1. **T. Horák**, G. Ducournau, M. Mičica, K. Postava, J. Ben Youssef, J.-F. Lampin and M. Vanwolleghem, "Free-Space Characterization of Magneto-Optical Hexaferrites in the Submillimeter-Wave Range," *IEEE Trans. on Terahertz Science and Technology*, vol. 7, no. 5, 2017.

2. **T. Horák**, G. Ducournau, O. Stepanenko, K. Postava, J.-F. Lampin and M. Vanwolleghem, "Terahertz Nonreciprocal Components Using Hexagonal Ferrite Ceramics," *Optics Express*, Submitted.

3. M. Mičica, K. Postava, M. Vanwolleghem, **T. Horák**, J.-F. Lampin, J, Pištora, "Terahertz material characterization for nonreciprocal integrated optics", Proc. SPIE 9516, Integrated Optics: Physics and Simulations II, 951615 (2015/05/01).

Conferences

1. **T. Horák**, M. Vanwolleghem, G. Ducournau, K. Postava, P. Koleják and J.-F. Lampin. "Magneto-optical Hexaferrites for Terahertz Isolating Applications," *International Conference on Infrared, Millimeter, and Terahertz Waves, IRMMW-THz 2016*, 7758377, 2016.

2. O. Stepanenko, **T. Horák**, J. Chochol, K. Postava, J.-F. Lampin and M. Vanwolleghem. "Compact mid-IR isolator using nonreciprocal magnetoplasmonic InSb mirror," *International Conference on Infrared, Millimeter, and Terahertz Waves, IRMMW-THz 2016*, 7758556, 2016.

3. **T. Horák**, M. Vanwolleghem, G. Ducournau, M. Mičica, K. Postava, J. Ben Youssef and J.-F. Lampin, "Free-space Characterization of Magneto-optical

Hexaferrites in the Millimeter-Wave Range," *7th International Conference on Spectroscopic Ellipsometry (ICSE-7)*, Berlin, 2016.

4. **T. Horák**, G. Ducournau, O. Stepanenko, K. Postava, J.-F. Lampin and M. Vanwolleghem. "Compact THz Nonreciprocal Components Using Hexagonal Ferrite Ceramics", *9th THz Days, GdR NanoTeraMIR 2017*, Dunkerque, 2017.

5. O. Stepanenko, **T. Horák**, J. Chochol, K. Postava, J.-F. Lampin and M. Vanwolleghem. "THz Isolator Using Nonreciprocal Magnetoplasmonic InAs Mirror," *9th THz Days, GdR NanoTeraMIR 2017*, Dunkerque, 2017.

6. **T. Horák**, G. Ducournau, O. Stepanenko, K. Postava, J.-F. Lampin and M. Vanwolleghem. "Compact THz Nonreciprocal Components Using Hexagonal Ferrite Ceramics", *NanoOstrava 2017*, Ostrava, 2017.

7. O. Stepanenko, **T. Horák**, J. Chochol, K. Postava, J.-F. Lampin and M. Vanwolleghem. "THz Isolator Using Nonreciprocal Magnetoplasmonic InAs Mirror," *NanoOstrava 2017*, Ostrava, 2017.

8. **T. Horák**, M. Vanwolleghem, G. Ducournau, O. Stepanenko, K. Postava and J.-F. Lampin. "Compact THz Isolator Using Nonreciprocal Magnetoplasmonic Mirror," *GdR NanoTeraMIR 2016*, Paris, 2016.

9. O. Stepanenko, **T. Horák**, J. Chochol, K. Postava, J.-F. Lampin and M. Vanwolleghem. "Nonreciprocal Magnetoplasmonic InSb Mirror for Mid-IR Isolation," *GdR NanoTeraMIR 2016*, Paris, 2016.

10. **T. Horák**, M. Vanwolleghem, G. Ducournau, O. Stepanenko, K. Postava and J.-F. Lampin, "Compact THz Isolator Using Nonreciprocal Magnetoplasmonic Mirror," *Journées du CCT-CNES et du GT2-GdR Ondes*, Toulouse, 2016.

11. O. Stepanenko, **T. Horák**, J. Chochol, K. Postava, J.-F. Lampin and M. Vanwolleghem. ”Nonreciprocal Magnetoplasmonic InSb Mirror for Mid-IR Isolation,” *Journées du CCT-CNES et du GT2-GdR Ondes*, Toulouse, 2016.

12. **T. Horák**, M. Vanwolleghem, G. Ducournau, M. Mičica, K. Postava, J. Pistora, J. Ben-Youssef and J.-F. Lampin, ”Terahertz Isolating Device Using Hexaferrites,” *GdR NanoTeraMIR*, Aussois, 2015.

Bibliography

[1] L. Deák and T. Fülöp, "Reciprocity in quantum, electromagnetic and other wave scattering," *Annals of Physics*, vol. 327, no. 4, pp. 1050–1077, 2012. (Cited on page 1.)

[2] H. Weyl, *Symmetry*. Princeton University Press, 2015. (Cited on page 2.)

[3] G. G. Stokes, "On attractions and on clairaut's theorem," *Camb. Dublin Math. J*, vol. 4, no. 1, 1849. (Cited on page 2.)

[4] H. Von Helmholtz, *Handbuch der physiologischen Optik*, vol. 9. Voss, 1867. (Cited on page 2.)

[5] H. Lorentz, "On the radiation of heat in a system of bodies having a uniform temperature," *Koninklijke Nederlandse Akademie van Wetenschappen Proceedings Series B Physical Sciences*, vol. 8, pp. 401–421, 1905. (Cited on page 2.)

[6] R. J. Potton, "Reciprocity in optics," *Reports on Progress in Physics*, vol. 67, no. 5, p. 717, 2004. (Cited on page 2.)

[7] D. Jalas, A. Petrov, M. Eich, W. Freude, *et al.*, "What is - and what is not - an optical isolator," *Nat. Photonics*, vol. 7, no. 8, pp. 579–582, 2013. (Cited on pages 2 and 9.)

[8] Z. Yu and S. Fan, "Complete optical isolation created by indirect interband photonic transitions," *Nature photonics*, vol. 3, no. 2, pp. 91–94, 2009. (Cited on page 3.)

[9] C.-H. Dong, Z. Shen, C.-L. Zou, Y.-L. Zhang, *et al.*, "Brillouin-scattering-induced transparency and non-reciprocal light storage," *Nature communications*, vol. 6, p. 6193, 2015. (Cited on page 3.)

[10] K. Gallo and G. Assanto, "All-optical diode based on second-harmonic generation in an asymmetric waveguide," *JOSA B*, vol. 16, no. 2, pp. 267–269, 1999. (Cited on page 3.)

[11] C. G. Poulton, R. Pant, A. Byrnes, S. Fan, *et al.*, "Design for broadband on-chip isolator using stimulated brillouin scattering in dispersion-engineered chalcogenide waveguides," *Optics express*, vol. 20, no. 19, pp. 21235–21246, 2012. (Cited on page 3.)

[12] D. L. Sounas, C. Caloz, and A. Alu, "Giant non-reciprocity at the subwavelength scale using angular momentum-biased metamaterials," *Nature communications*, vol. 4, p. 2407, 2013. (Cited on page 3.)

[13] A. Metelmann and A. Clerk, "Nonreciprocal photon transmission and amplification via reservoir engineering," *Physical Review X*, vol. 5, no. 2, p. 021025, 2015. (Cited on page 3.)

[14] C. Sayrin, C. Junge, R. Mitsch, B. Albrecht, *et al.*, "Nanophotonic optical isolator controlled by the internal state of cold atoms," *Physical Review X*, vol. 5, no. 4, p. 041036, 2015. (Cited on page 3.)

[15] H. Lira, Z. Yu, S. Fan, and M. Lipson, "Electrically driven nonreciprocity induced by interband photonic transition on a silicon chip," *Physical review letters*, vol. 109, no. 3, p. 033901, 2012. (Cited on page 3.)

[16] Z. Yu and S. Fan, "Integrated nonmagnetic optical isolators based on photonic transitions," *IEEE Journal of Selected Topics in Quantum Electronics*, vol. 16, no. 2, pp. 459–466, 2010. (Cited on page 3.)

[17] R. M. White, *Quantum theory of magnetism: magnetic properties of materials*, vol. 32. Springer Science & Business Media, 2007. (Cited on page 5.)

[18] M. Faraday, "Experimental researches in electricity. nineteenth series," *Philosophical Transactions of the Royal Society of London*, vol. 136, pp. 1–20, 1846. (Cited on page 6.)

[19] J. Kerr, "On the magnetism of light and the illumination of magnetic lines of force," *Report of the British Association for the Advancement of Science S*, vol. 5, 1876. (Cited on page 6.)

[20] J. Kerr, "Xliii. on rotation of the plane of polarization by reflection from the pole of a magnet," *The London, Edinburgh, and Dublin Philosophical Magazine and Journal of Science*, vol. 3, no. 19, pp. 321–343, 1877. (Cited on page 6.)

[21] J. Kerr, "Xxiv. on reflection of polarized light from the equatorial surface of a magnet," *The London, Edinburgh, and Dublin Philosophical Magazine and Journal of Science*, vol. 5, no. 30, pp. 161–177, 1878. (Cited on page 6.)

[22] P. Zeeman, "Measurements concerning the influence of a magnetization, perpendicular to the plane of incidence on the light reflected from an iron mirror," *Leiden Commun*, vol. 29, no. 3, 1896. (Cited on page 7.)

[23] P. Zeeman, "Xxxii. On the influence of magnetism on the nature of the light emitted by a substance," *The London, Edinburgh, and Dublin Philosophical Magazine and Journal of Science*, vol. 43, no. 262, pp. 226–239, 1897. (Cited on pages 7 and 53.)

[24] R. M. Bozorth, "Ferromagnetism," *Ferromagnetism, by Richard M. Bozorth, pp. 992. ISBN 0-7803-1032-2. Wiley-VCH, August 1993.*, p. 992, 1993. (Cited on page 7.)

[25] S. Geller and M. Gilleo, "The crystal structure and ferrimagnetism of yttrium-iron garnet, y3fe2 (feo4) 3," *Journal of Physics and Chemistry of solids*, vol. 3, no. 1-2, pp. 30–36, 1957. (Cited on page 7.)

[26] S. Geller and M. Gilleo, "Structure and ferrimagnetism of yttrium and rare-earth–iron garnets," *Acta Crystallographica*, vol. 10, no. 3, pp. 239–239, 1957. (Cited on page 7.)

[27] J. Smit and H. P. J. Wijn, *Ferrites: physical properties of ferrimagnetic oxides in relation to their technical applications*. Philips, 1959. (Cited on page 7.)

[28] B. Lax and K. J. Button, *Microwave ferrites and ferrimagnetics*. McGraw-Hill, 1962. (Cited on page 7.)

[29] M. Sugimoto, "The past, present, and future of ferrites," *Journal of the American Ceramic Society*, vol. 82, no. 2, pp. 269–280, 1999. (Cited on page 7.)

[30] N. Keller, J. Mistrik, Š. Višňovskỳ, D. Schmool, *et al.*, "Magneto-optical faraday and kerr effect of orthoferrite thin films at high temperatures," *The European Physical Journal B-Condensed Matter and Complex Systems*, vol. 21, no. 1, pp. 67–73, 2001. (Cited on page 7.)

[31] J. Chang, J. Dillon Jr, and U. Gianola, "Magneto-optical variable memory based upon the properties of a transparent ferrimagnetic garnet at its compensation temperature," *Journal of Applied Physics*, vol. 36, no. 3, pp. 1110–1111, 1965. (Cited on page 7.)

[32] H. Dotsch, P. Hertel, B. Luhrmann, S. Sure, *et al.*, "Applications of magnetic garnet films in integrated optics," *IEEE Transactions on Magnetics*, vol. 28, no. 5, pp. 2979–2984, 1992. (Cited on page 7.)

[33] J.-P. Krumme and H. Schmitt, "Ferrimagnetic garnet films for magnetooptic information storage," *IEEE Transactions on Magnetics*, vol. 11, no. 5, pp. 1097–1102, 1975. (Cited on page 7.)

[34] M. Pardavi-Horvath, "Microwave applications of soft ferrites," *Journal of Magnetism and Magnetic Materials*, vol. 215, pp. 171–183, 2000. (Cited on pages 7 and 104.)

[35] G. Catalan and J. F. Scott, "Physics and applications of bismuth ferrite," *Advanced Materials*, vol. 21, no. 24, pp. 2463–2485, 2009. (Cited on page 7.)

[36] T. Nagamiya, K. Yosida, and R. Kubo, "Antiferromagnetism," *Advances in Physics*, vol. 4, no. 13, pp. 1–112, 1955. (Cited on page 7.)

[37] W. Marshall, "Antiferromagnetism," in *Proceedings of the Royal Society of London A: Mathematical, Physical and Engineering Sciences*, vol. 232, pp. 48–68, The Royal Society, 1955. (Cited on page 7.)

[38] J. Chochol, K. Postava, M. Čada, M. Vanwolleghem, *et al.*, "Magneto-optical properties of insb for terahertz applications," *AIP Advances*, vol. 6, no. 11, p. 115021, 2016. (Cited on page 8.)

[39] P. Kwiecien, I. Richter, V. Kuzmiak, and J. Čtyroký, "Nonreciprocal waveguiding structures for thz region based on insb," *JOSA A*, vol. 34, no. 6, pp. 892–903, 2017. (Cited on page 8.)

[40] P. Kwiecien, I. Richter, V. Kuzmiak, and J. Čtyroký, "Magneto-optical waveguiding insb-based structures with nonreciprocal properties," in *Laser Science*, pp. JW3A–79, Optical Society of America, 2017. (Cited on page 8.)

[41] P. Kühne, C. Herzinger, M. Schubert, J. Woollam, and T. Hofmann, "Invited article: An integrated mid-infrared, far-infrared, and terahertz optical hall effect instrument," *Review of Scientific Instruments*, vol. 85, no. 7, p. 071301, 2014. (Cited on page 8.)

[42] L. Aplet and J. Carson, "A faraday effect optical isolator," *Applied Optics*, vol. 3, no. 4, pp. 544–545, 1964. (Cited on page 10.)

[43] F. Sansalone, "Compact optical isolator," *Applied optics*, vol. 10, no. 10, pp. 2329–2331, 1971. (Cited on page 10.)

[44] T. Uchida and A. Ueki, "Optical isolator," Dec. 11 1979. US Patent 4,178,073. (Cited on page 10.)

[45] M. Tonouchi, "Cutting-edge terahertz technology," *Nature photonics*, vol. 1, no. 2, pp. 97–105, 2007. (Cited on page 10.)

[46] L. Cong, W. Cao, X. Zhang, Z. Tian, *et al.*, "A perfect metamaterial polarization rotator," *Applied Physics Letters*, vol. 103, no. 17, p. 171107, 2013. (Cited on page 10.)

[47] N. Born, M. Reuter, M. Koch, and M. Scheller, "High-q terahertz bandpass filters based on coherently interfering metasurface reflections," *Optics letters*, vol. 38, no. 6, pp. 908–910, 2013. (Cited on page 10.)

[48] F. Fan, Y. Hou, Z.-W. Jiang, X.-H. Wang, and S.-J. Chang, "Terahertz modulator based on insulator–metal transition in photonic crystal waveguide," *Applied optics*, vol. 51, no. 20, pp. 4589–4596, 2012. (Cited on page 10.)

[49] J. Federici and L. Moeller, "Review of terahertz and subterahertz wireless communications," *J. Appl. Phys.*, vol. 107, no. 111101, 2010. (Cited on page 10.)

[50] J. F. Federici, B. Schulkin, F. Huang, D. Gary, *et al.*, "Thz imaging and sensing for security applications - explosives, weapons and drugs," *Semicond. Sci. Technol.*, vol. 20, no. 7, pp. S266–S280, 2005. (Cited on page 10.)

[51] Y.-S. Lee, *Principles of Terahertz Science and Technology*. Springer Science+Business Media, LLC, 1 ed., 2009. (Cited on pages 10, 29, 31, 32, 33, 49, 234 and 235.)

[52] S. S. Dhillon, M. S. Vitiello, E. H. Linfield, A. G. Davies, *et al.*, "The 2017 terahertz science and technology roadmap," *J. Phys. D: Appl. Phys.*, vol. 50, no. 043001, p. 49pp, 2017. (Cited on pages 10 and 33.)

[53] F. Fan, S.-J. Chang, W.-H. Gu, X.-H. Wang, and A.-Q. Chen, "Magnetically tunable terahertz isolator based on structured semiconductor magneto plasmonics," *IEEE Photon. Tech. Lett.*, vol. 24, no. 22, pp. 2080–2083, 2012. (Cited on page 10.)

[54] B. Hu, Q. J. Wang, and Y. Zhang, "Broadly tunable one-way terahertz plasmonic waveguide based on nonreciprocal surface magneto plasmons," *Optics letters*, vol. 37, no. 11, pp. 1895–1897, 2012. (Cited on page 10.)

[55] S. Chen, F. Fan, X. Wang, P. Wu, *et al.*, "Terahertz isolator based on nonreciprocal magneto-metasurface," *Opt. Express* , vol. 23, no. 2, pp. 8614–8621, 2015. (Cited on pages 10, 11, 12 and 233.)

[56] J. Chochol, K. Postava, M. Čada, M. Vanwolleghem, *et al.*, "Plasmonic behavior of iii-v semiconductors in far-infrared and terahertz range," *Journal of the European Optical Society-Rapid Publications*, vol. 13, no. 1, p. 13, 2017. (Cited on page 12.)

[57] I. Crassee, J. Levallois, A. L. Walter, M. Ostler, *et al.*, "Giant faraday rotation in single-and multilayer graphene," *arXiv preprint arXiv:1007.5286*, 2010. (Cited on page 12.)

[58] M. Tamagnone, C. Moldovan, J.-M. Poumirol, A. B. Kuzmenko, *et al.*, "Near optimal graphene terahertz non-reciprocal isolator," *Nature communications*, vol. 7, 2016. (Cited on page 12.)

[59] D. Polder, "Ferrite materials," *Proceedings of the IEE - Part II: Power Engineering*, vol. 97, pp. 246–256(10), April 1950. (Cited on page 13.)

[60] K. J. Button, "Microwave ferrite devices: The first ten years," *IEEE Trans. Microwave Theory Tech.* , vol. 32, no. 9, pp. 1088–1096, 1984. (Cited on page 13.)

[61] D. M. Pozar, *Microwave Engineering*. John Wiley & Sons, Inc, 4 ed., 2012. (Cited on pages 13 and 104.)

[62] V. G. Harris, A. Geiler, Y. Chen, S. D. Yoon, *et al.*, "Recent advances in processing and applications of microwave ferrites," *J. Magn. Magn. Mat.*, vol. 321, no. 14, pp. 2035–2047, 2009. (Cited on pages 13, 14, 105 and 111.)

[63] V. G. Harris, "Modern microwave ferrites," *IEEE Trans. Magn.*, vol. 48, no. 3, pp. 1075–1104, 2012. (Cited on pages 13, 14, 105 and 114.)

[64] Ümit Özgür, Y. Alivov, and H. Morkoç, "Microwave ferrites, part 1: fundamental properties," *J. Mater. Sci.: Mater. Electron*, vol. 20, no. 9, pp. 789–834, 2009. (Cited on pages 13, 14 and 105.)

[65] J. L. Snoek, "Magnetic and electrical properties of the binary system MO Fe_2O_3," *Physica*, vol. 3, no. 6, pp. 463–483, 1936. (Cited on page 13.)

[66] T. Stijntjes and B. van Loon, "Early investigations on ferrite magnetic materials by J. L. Snoek and colleagues of the Philips Research Laboratories Eindhoven," *Proceedings of the IEEE*, vol. 96, pp. 900–904, May 2008. (Cited on page 13.)

[67] F. Fan, S.-J. Chang, C. Niu, Y. Hou, and X.-H. Wang, "Magnetically tunable silicon-ferrite photonic crystals for terahertz circulator," *Opt. Commun.* , vol. 285, no. 18, pp. 3763 – 3769, 2012. (Cited on page 13.)

[68] E. Moore, "A 300 ghz quasioptical faraday rotation isolator," *International journal of infrared and millimeter waves*, vol. 10, no. 10, pp. 1317–1325, 1989. (Cited on page 13.)

[69] R. C. Pullar, "Hexagonal ferrites: A review of the synthesis, properties and applications of hexaferrite ceramics," *Prog. Mater. Scien.*, vol. 57, no. 7, pp. 1191 – 1334, 2012. (Cited on pages 14, 105, 111, 122 and 144.)

[70] M. Webb, "A mm-wave four-port quasi-optical circulator," *International Journal of Infrared and Millimeter Waves*, vol. 12, no. 1, pp. 45–63, 1991. (Cited on page 14.)

[71] G. Smith, C. Unsworth, M. Webb, and J. Lesurf, "Design, analysis and application of high performance permanently magnetised, quasi-optical, faraday rotators," in *Microwave Symposium Digest, 1994., IEEE MTT-S International*, pp. 293–296, IEEE, 1994. (Cited on page 14.)

[72] M. Raum, "Quasioptical measurement of ferrite material parameters at terahertz frequencies by a new method: Faraday angle resonance," *Interna-*

tional journal of infrared and millimeter waves, vol. 15, no. 7, pp. 1211–1227, 1994. (Cited on page 14.)

[73] G. M. Smith, S. Kang, C. Unsworth, E. Puplett, *et al.*, "Microwave, millimeter wave and sub-millimeter wave free-space faraday rotators," in *Proceedings of 1995 IEEE MTT-S International Microwave Symposium*, pp. 1665–1668 vol.3, May 1995. (Cited on pages 14, 17 and 122.)

[74] R. I. Hunter, D. A. Robertson, P. Goy, and G. M. Smith, "Design of high-performance millimeter wave and sub-millimeter wave quasi-optical isolators and circulators," *IEEE transactions on microwave theory and techniques*, vol. 55, no. 5, pp. 890–898, 2007. (Cited on page 14.)

[75] B. Yang, R. J. Wylde, D. H. Martin, P. Goy, *et al.*, "Determination of the gyrotropic characteristics of hexaferrite ceramics from 75 to 600 GHz," *IEEE Trans. Microwave Theory Tech.* , vol. 58, pp. 3587–3597, Dec 2010. (Cited on pages 14, 17, 122, 128, 133, 138 and 142.)

[76] B. Yang, X. Wang, Y. Zhang, and R. S. Donnan, "Experimental characterization of hexaferrite ceramics from 100 ghz to 1 thz using vector network analysis and terahertz-time domain spectroscopy," *Journal of Applied Physics*, vol. 109, no. 3, p. 033509, 2011. (Cited on pages 14 and 17.)

[77] D. H. Martin and R. J. Wylde, "Wideband circulators for use at frequencies above 100 GHz to beyond 350 GHz," *IEEE Trans. Microwave Theory Tech.* , vol. 57, pp. 99–108, Jan 2009. (Cited on pages 14, 139, 142 and 233.)

[78] M. Shalaby, M. Peccianti, Y. Ozturk, and R. Morandotti, "A magnetic non-reciprocal isolator for broadband terahertz operation," *Nat. Commun.*, vol. 4, no. 1558, 2013. (Cited on pages 15, 16, 17, 73, 122, 138, 139, 233 and 234.)

[79] T. Horák, G. Ducournau, M. Mičica, K. Postava, *et al.*, "Free-space characterization of magneto-optical hexaferrites in the submillimeter-wave range,"

IEEE Trans. Tera. Scien. Tech. , vol. 7, pp. 563–571, Sept 2017. (Cited on pages 17 and 221.)

[80] L. Halagačka, M. Vanwolleghem, K. Postava, B. Dagens, and J. Pištora, "Coupled mode enhanced giant magnetoplasmonics transverse Kerr effect," *Opt. Express*, vol. 21, pp. 21741–21755, Sep 2013. (Cited on pages 18, 19, 57, 170, 203 and 234.)

[81] L. Halagačka, M. Vanwolleghem, F. Vaurette, J. Ben-Youssef, *et al.*, "Experimental demonstration of anomalous nonreciprocal optical response of 1D periodic magnetoplasmonic nanostructures," *Proc. SPIE*, vol. 8988, pp. 89880E–89880E–6, 2014. (Cited on page 18.)

[82] J. B. Pendry, L. Martín-Moreno, and F. J. Garcia-Vidal, "Mimicking surface plasmons with structured surfaces," *Science*, vol. 305, no. 5685, pp. 847–848, 2004. (Cited on pages 20, 94, 96, 177, 195 and 236.)

[83] F. Garcia-Vidal, L. Martin-Moreno, and J. Pendry, "Surfaces with holes in them: new plasmonic metamaterials," *Journal of optics A: Pure and applied optics*, vol. 7, no. 2, p. S97, 2005. (Cited on pages 20, 79, 94 and 95.)

[84] J. F. O'Hara, R. D. Averitt, and A. J. Taylor, "Terahertz surface plasmon polariton coupling on metallic gratings," *Opt. Express*, vol. 12, pp. 6397–6402, Dec 2004. (Cited on page 20.)

[85] C. R. Williams, S. R. Andrews, S. A. Maier, A. I. Fernández-Domínguez, *et al.*, "Highly confined guiding of terahertz surface plasmon polaritons on structured metal surfaces," *Nat. Photonics*, vol. 2, pp. 175 – 179, 2008. (Cited on page 20.)

[86] A. Rusina, M. Durach, and M. I. Stockman, "Theory of spoof plasmons in real metals," *Proc. SPIE*, vol. 7757, pp. 77572R–77572R–6, 2010. (Cited on page 20.)

[87] S. A. Maier and S. R. Andrews, "Terahertz pulse propagation using plasmon-polariton-like surface modes on structured conductive surfaces," *Applied Physics Letters*, vol. 88, no. 25, p. 251120, 2006. (Cited on pages 20 and 96.)

[88] S. A. Maier, S. R. Andrews, L. Martín-Moreno, and F. J. García-Vidal, "Terahertz surface plasmon-polariton propagation and focusing on periodically corrugated metal wires," *Phys. Rev. Lett.*, vol. 97, p. 176805, Oct 2006. (Cited on page 20.)

[89] K. Bhattarai, S. R. Silva, A. Urbas, S. J. Lee, *et al.*, "Angle-dependent spoof surface plasmons in metallic hole arrays at terahertz frequencies," *IEEE J. Select. Top. Quantum Electron.*, vol. 23, pp. 1–6, July 2017. (Cited on pages 20, 98, 100, 174, 236 and 237.)

[90] A. Arbabi, A. Rohani, D. Saeedkia, and S. Safavi-Naeini, "A terahertz plasmonic metamaterial structure for near-field sensing applications," in *Proceedings of IEEE 33rd International Conference on Infrared, Millimeter and Terahertz Waves*, pp. 1–2, Sept 2008. (Cited on page 20.)

[91] K. Song and P. Mazumder, "Active terahertz spoof surface plasmon polariton switch comprising the perfect conductor metamaterial," *IEEE Trans. Elec. Dev.* , vol. 56, pp. 2792–2799, Nov 2009. (Cited on page 20.)

[92] K. Song and P. Mazumder, "Dynamic terahertz spoof surface plasmon polariton switch based on resonance and absorption," *IEEE Trans. Elec. Dev.* , vol. 58, pp. 2172–2176, July 2011. (Cited on page 20.)

[93] Y. Zhang, Z. Hong, and Z. Han, "Spoof plasmon resonance with 1D periodic grooves for terahertz refractive index sensing," *Opt. Commun.* , vol. 340, pp. 102 – 106, 2015. (Cited on page 20.)

[94] R. Yahiaoui, A. C. Strikwerda, and P. U. Jepsen, "Terahertz plasmonic structure with enhanced sensing capabilities," *IEEE Sensors J.*, vol. 16, pp. 2484–2488, April 2016. (Cited on pages 20 and 98.)

[95] B. Ng, J. Wu, S. M. Hanham, A. I. FernÃ¡ndez-DomÃnguez, *et al.*, "Spoof plasmon surfaces: A novel platform for thz sensing," *Adv. Optical Mater.*, vol. 1, no. 8, pp. 543–548, 2013. (Cited on page 20.)

[96] D. Martin-Cano, M. L. Nesterov, A. I. Fernandez-Dominguez, F. J. Garcia-Vidal, *et al.*, "Domino plasmons for subwavelength terahertz circuitry," *Optical Express*, vol. 18, pp. 754–764, Jan 2010. (Cited on page 20.)

[97] A. K. Azad, J. F. O'Hara, R. Singh, H.-T. Chen, and A. J. Taylor, "A review of terahertz plasmonics in subwavelength holes on conducting films," *IEEE Journal of Selected Topics in Quantum Electronics*, vol. 19, no. 1, pp. 8400416–8400416, 2013. (Cited on page 20.)

[98] F. Fan, S. J. Chang, W. H. Gu, X. H. Wang, and A. Q. Chen, "Magnetically tunable terahertz isolator based on structured semiconductor magneto plasmonics," *IEEE Photon. Tech. Lett.*, vol. 24, pp. 2080–2083, Nov 2012. (Cited on page 20.)

[99] A. Degiron and D. R. Smith, "One-way glass for microwaves using nonreciprocal metamaterials," *Phys. Rev. E*, vol. 89, p. 053203, May 2014. (Cited on page 20.)

[100] J. M. Hollas, *Modern spectroscopy*. John Wiley & Sons, 2004. (Cited on page 27.)

[101] M. Walther, B. M. Fischer, A. Ortner, A. Bitzer, *et al.*, "Chemical sensing and imaging with pulsed terahertz radiation," *Analytical and Bioanalytical Chemistry*, vol. 397, pp. 1009–1017, Jun 2010. (Cited on page 28.)

[102] B. Stuart, *Infrared spectroscopy*. Wiley Online Library, 2005. (Cited on pages 28 and 234.)

[103] R. J. Trew, "High-frequency solid-state electronic devices," *IEEE trans. on electron devices*, vol. 52, no. 5, pp. 638–649, 2005. (Cited on page 29.)

[104] M. F. Kimmitt, "Terahertz research - the first thirty years (1895-1924)," in *Infrared and Millimeter Waves, Conference Digest of the 2004 Joint 29th International Conference on 2004 and 12th International Conference on Terahertz Electronics, 2004.*, pp. 69–70, Sept 2004. (Cited on page 29.)

[105] X.-C. Zhang and J. Xu, *Introduction to THz wave photonics*, vol. 29. Springer, 2010. (Cited on page 29.)

[106] G. Grüner, *Millimeter and submillimeter wave spectroscopy of solids*. Berlin, Heidelberg: Springer-Verlag, 1998. (Cited on page 33.)

[107] C. A. Schmuttenmaer, "Exploring dynamics in the far-infrared with terahertz spectroscopy," *Chemical reviews*, vol. 104, no. 4, pp. 1759–1780, 2004. (Cited on page 34.)

[108] H. Merbold, "Terahertz time-domain spectroscopy of aqueous systems in reflection geometry and construction of polarization-sensitive photoconductive terahertz antennas," *Master's thesis, University of Freiburg, Freiburg, Germany*, 2006. (Cited on page 34.)

[109] M. C. Teich and B. Saleh, "Fundamentals of photonics," *Canada, Wiley Interscience*, vol. 3, 1991. (Cited on pages 36, 46, 47, 49 and 235.)

[110] D. S. Jones, *The theory of electromagnetism*. Elsevier, 2013. (Cited on page 36.)

[111] O. Heaviside, "On the forces, stresses, and fiuxes of energy in the electromagnetic field," *Philosophical Transactions of the Royal Society of London. A*, vol. 183, pp. 423–480, 1892. (Cited on page 41.)

[112] P. R. Griffiths and J. A. De Haseth, *Fourier transform infrared spectrometry*, vol. 171. John Wiley & Sons, 2007. (Cited on page 48.)

[113] J. Bransky, "Magneto optic effects and applications," tech. rep., Air Force Wright Aeronautical Labs Wright-Patterson AFB OH, 1981. (Cited on page 54.)

[114] A. K. Zvezdin and V. K. Kotov, *Modern magnetooptics and magnetooptical materials*. CRC Press, 1 ed., 1997. (Cited on pages 57 and 145.)

[115] V. Belotelov, I. Akimov, M. Pohl, V. Kotov, *et al.*, "Enhanced magneto-optical effects in magnetoplasmonic crystals," *Nature Nanotechnology*, vol. 6, no. 6, pp. 370–376, 2011. (Cited on pages 57 and 203.)

[116] P. Schulz, "Broadband faraday isolator," Oct. 1 1991. US Patent 5,052,786. (Cited on page 73.)

[117] T. W. Ebbesen, H. J. Lezec, H. Ghaemi, T. Thio, and P. Wolff, "Extraordinary optical transmission through sub-wavelength hole arrays," *Nature*, vol. 391, no. 6668, p. 667, 1998. (Cited on pages 79 and 81.)

[118] L. Martin-Moreno, F. Garcia-Vidal, H. Lezec, K. Pellerin, *et al.*, "Theory of extraordinary optical transmission through subwavelength hole arrays," *Physical review letters*, vol. 86, no. 6, p. 1114, 2001. (Cited on page 79.)

[119] F. J. Garcia-Vidal, L. Martin-Moreno, T. Ebbesen, and L. Kuipers, "Light passing through subwavelength apertures," *Reviews of Modern Physics*, vol. 82, no. 1, p. 729, 2010. (Cited on pages 79, 81 and 176.)

[120] H. Bethe, "Theory of diffraction by small holes," *Physical Review*, vol. 66, no. 7-8, p. 163, 1944. (Cited on page 80.)

[121] G. Lehman, "Diffraction of electromagnetic waves by planar dielectric structures. i. Transverse electric excitation," *Journal of Mathematical Physics*, vol. 11, no. 5, pp. 1522–1535, 1970. (Cited on page 80.)

[122] D. T. Auckland and R. F. Harrington, "Electromagnetic transmission through a filled slit in a conducting plane of finite thickness, TE case," *IEEE*

Transactions on Microwave Theory and Techniques, vol. 26, no. 7, pp. 499–505, 1978. (Cited on page 80.)

[123] R. Harrington and D. Auckland, "Electromagnetic transmission through narrow slots in thick conducting screens," *IEEE Transactions on Antennas and Propagation*, vol. 28, no. 5, pp. 616–622, 1980. (Cited on page 80.)

[124] A. Roberts, "Electromagnetic theory of diffraction by a circular aperture in a thick, perfectly conducting screen," *JOSA A*, vol. 4, no. 10, pp. 1970–1983, 1987. (Cited on page 80.)

[125] J. Bravo-Abad, L. Martin-Moreno, and F. Garcia-Vidal, "Transmission properties of a single metallic slit: From the subwavelength regime to the geometrical-optics limit," *Physical Review E*, vol. 69, no. 2, p. 026601, 2004. (Cited on page 80.)

[126] A. Degiron, H. Lezec, N. Yamamoto, and T. Ebbesen, "Optical transmission properties of a single subwavelength aperture in a real metal," *Optics Communications*, vol. 239, no. 1, pp. 61–66, 2004. (Cited on page 80.)

[127] W. L. Barnes, A. Dereux, and T. W. Ebbesen, "Surface plasmon subwavelength optics," *Nature*, vol. 424, no. 6950, p. 824, 2003. (Cited on pages 80 and 83.)

[128] E. Ozbay, "Plasmonics: merging photonics and electronics at nanoscale dimensions," *Science*, vol. 311, no. 5758, pp. 189–193, 2006. (Cited on page 80.)

[129] S. A. Maier, *Plasmonics: fundamentals and applications*. Springer Science & Business Media, 2007. (Cited on pages 80, 89, 91, 92 and 94.)

[130] U. Schröter and D. Heitmann, "Surface-plasmon-enhanced transmission through metallic gratings," *Physical review B*, vol. 58, no. 23, p. 15419, 1998. (Cited on page 80.)

[131] J. Porto, F. Garcia-Vidal, and J. Pendry, "Transmission resonances on metallic gratings with very narrow slits," *Physical review letters*, vol. 83, no. 14, p. 2845, 1999. (Cited on pages 80, 81 and 235.)

[132] S. Astilean, P. Lalanne, and M. Palamaru, "Light transmission through metallic channels much smaller than the wavelength," *Optics Communications*, vol. 175, no. 4, pp. 265–273, 2000. (Cited on page 80.)

[133] F. Garcia-Vidal and L. Martin-Moreno, "Transmission and focusing of light in one-dimensional periodically nanostructured metals," *Physical Review B*, vol. 66, no. 15, p. 155412, 2002. (Cited on page 80.)

[134] S. Collin, F. Pardo, R. Teissier, and J.-L. Pelouard, "Horizontal and vertical surface resonances in transmission metallic gratings," *Journal of Optics A: Pure and Applied Optics*, vol. 4, no. 5, p. S154, 2002. (Cited on page 80.)

[135] F. Marquier, J.-J. Greffet, S. Collin, F. Pardo, and J. Pelouard, "Resonant transmission through a metallic film due to coupled modes," *Optics express*, vol. 13, no. 1, pp. 70–76, 2005. (Cited on page 80.)

[136] A. A. Rahman, P. Majewski, and K. Vasilev, "Extraordinary optical transmission: coupling of the Wood–Rayleigh anomaly and the Fabry–Perot resonance," *Optics letters*, vol. 37, no. 10, pp. 1742–1744, 2012. (Cited on page 80.)

[137] E. Popov, M. Neviere, S. Enoch, and R. Reinisch, "Theory of light transmission through subwavelength periodic hole arrays," *Physical Review B*, vol. 62, no. 23, p. 16100, 2000. (Cited on page 80.)

[138] H. F. Schouten, T. D. Visser, D. Lenstra, and H. Blok, "Light transmission through a subwavelength slit: Waveguiding and optical vortices," *Physical Review E*, vol. 67, no. 3, p. 036608, 2003. (Cited on page 80.)

[139] J. Fiala and I. Richter, "Explanation of extraordinary transmission on 1D and 2D metallic gratings," in *Proc. SPIE*, vol. 9450, p. 94501T, 2015. (Cited on page 81.)

[140] D. Crouse and P. Keshavareddy, "Polarization independent enhanced optical transmission in one-dimensional gratings and device applications," *Optics Express*, vol. 15, no. 4, pp. 1415–1427, 2007. (Cited on page 81.)

[141] Q. Xing, S. Li, Z. Tian, D. Liang, *et al.*, "Enhanced zero-order transmission of terahertz radiation pulses through very deep metallic gratings with subwavelength slits," *Applied physics letters*, vol. 89, no. 4, p. 041107, 2006. (Cited on page 81.)

[142] J. G. Rivas, C. Janke, P. H. Bolivar, and H. Kurz, "Transmission of thz radiation through InSb gratings of subwavelength apertures," *Optics Express*, vol. 13, no. 3, pp. 847–859, 2005. (Cited on pages 81 and 94.)

[143] R. Parthasarathy, A. Bykhovski, B. Gelmont, T. Globus, *et al.*, "Enhanced coupling of subterahertz radiation with semiconductor periodic slot arrays," *Physical review letters*, vol. 98, no. 15, p. 153906, 2007. (Cited on page 81.)

[144] H. Ghaemi, T. Thio, D. Grupp, T. W. Ebbesen, and H. Lezec, "Surface plasmons enhance optical transmission through subwavelength holes," *Physical review B*, vol. 58, no. 11, p. 6779, 1998. (Cited on page 81.)

[145] W. L. Barnes, W. A. Murray, J. Dintinger, E. Devaux, and T. Ebbesen, "Surface plasmon polaritons and their role in the enhanced transmission of light through periodic arrays of subwavelength holes in a metal film," *Physical review letters*, vol. 92, no. 10, p. 107401, 2004. (Cited on page 82.)

[146] P. Lalanne, J. Rodier, and J. Hugonin, "Surface plasmons of metallic surfaces perforated by nanohole arrays," *Journal of Optics A: Pure and Applied Optics*, vol. 7, no. 8, p. 422, 2005. (Cited on page 82.)

[147] A. A. Rahman, K. Vasilev, and P. Majewski, "Designing 1D grating for extraordinary optical transmission for TM polarization," *Photonics and Nanostructures-Fundamentals and Applications*, vol. 10, no. 1, pp. 112–118, 2012. (Cited on page 82.)

[148] A. Roszkiewicz and W. Nasalski, "Resonant transmission enhancement at one-dimensional metal gratings," *Journal of Physics B: Atomic, Molecular and Optical Physics*, vol. 46, no. 2, p. 025401, 2012. (Cited on page 82.)

[149] A. Sommerfeld, "Ueber die fortpflanzung elektrodynamischer wellen längs eines drahtes," *Annalen der Physik*, vol. 303, no. 2, pp. 233–290, 1899. (Cited on page 83.)

[150] J. Zenneck, "Über die fortpflanzung ebener elektromagnetischer wellen längs einer ebenen leiterfläche und ihre beziehung zur drahtlosen telegraphie," *Annalen der Physik*, vol. 328, no. 10, pp. 846–866, 1907. (Cited on page 83.)

[151] R. W. Wood, "Xlii. on a remarkable case of uneven distribution of light in a diffraction grating spectrum," *The London, Edinburgh, and Dublin Philosophical Magazine and Journal of Science*, vol. 4, no. 21, pp. 396–402, 1902. (Cited on page 83.)

[152] U. Fano, "The theory of anomalous diffraction gratings and of quasi-stationary waves on metallic surfaces (Sommerfeld's waves)," *JOSA*, vol. 31, no. 3, pp. 213–222, 1941. (Cited on page 83.)

[153] R. Ritchie, "Plasma losses by fast electrons in thin films," *Physical Review*, vol. 106, no. 5, p. 874, 1957. (Cited on page 83.)

[154] E. Stern and R. Ferrell, "Surface plasma oscillations of a degenerate electron gas," *Physical Review*, vol. 120, no. 1, p. 130, 1960. (Cited on page 83.)

[155] E. Kretschmann and H. Raether, "Radiative decay of non radiative surface plasmons excited by light," *Zeitschrift fur Naturforschung A*, vol. 23, no. 12, pp. 2135–2136, 1968. (Cited on pages 83 and 92.)

[156] H. Raether, *Surface Plasmons on Smooth and Rough Surfaces and on Gratings*. Springer, Berlin, Heidelberg, 1988. (Cited on page 83.)

[157] P. Drude, "Zur elektronentheorie der metalle," *Annalen der Physik*, vol. 306, no. 3, pp. 566–613, 1900. (Cited on page 84.)

[158] P. Drude, "Zur elektronentheorie der metalle; ii. teil. galvanomagnetische und thermomagnetische effecte," *Annalen der Physik*, vol. 308, no. 11, pp. 369–402, 1900. (Cited on page 84.)

[159] L. Chusseau, J. Demaison, and J. Coutaz, *Optoélectronique térahertz*. EDP Sciences, 2008. (Cited on page 84.)

[160] S. Lucyszyn, "Investigation of anomalous room temperature conduction losses in normal metals at terahertz frequencies," *IEE Proceedings-Microwaves, Antennas and Propagation*, vol. 151, no. 4, pp. 321–329, 2004. (Cited on page 84.)

[161] G. Goubau, "Surface waves and their application to transmission lines," *Journal of Applied Physics*, vol. 21, no. 11, pp. 1119–1128, 1950. (Cited on page 91.)

[162] C. Powell and J. Swan, "Origin of the characteristic electron energy losses in aluminum," *Physical Review*, vol. 115, no. 4, p. 869, 1959. (Cited on page 91.)

[163] W. Cai, R. Sainidou, J. Xu, A. Polman, and F. J. Garcia de Abajo, "Efficient generation of propagating plasmons by electron beams," *Nano letters*, vol. 9, no. 3, pp. 1176–1181, 2009. (Cited on page 91.)

[164] S. Liu, P. Zhang, W. Liu, S. Gong, *et al.*, "Surface polariton cherenkov light radiation source," *Physical review letters*, vol. 109, no. 15, p. 153902, 2012. (Cited on page 91.)

[165] J. Lambe and S. McCarthy, "Light emission from inelastic electron tunneling," *Physical Review Letters*, vol. 37, no. 14, p. 923, 1976. (Cited on page 91.)

[166] J. Gimzewski, B. Reihl, J. Coombs, and R. Schlittler, "Photon emission with the scanning tunneling microscope," *Zeitschrift für Physik B Condensed Matter*, vol. 72, no. 4, pp. 497–501, 1988. (Cited on page 91.)

[167] K. Kempa, "Plasmonic protection of the hot-electron energy," *physica status solidi (RRL)-Rapid Research Letters*, vol. 7, no. 7, pp. 465–468, 2013. (Cited on page 91.)

[168] F. Ye, J. M. Merlo, M. J. Burns, and M. J. Naughton, "Optical and electrical mappings of surface plasmon cavity modes," *Nanophotonics*, vol. 3, no. 1-2, pp. 33–49, 2014. (Cited on pages 91 and 92.)

[169] A. Otto, "Excitation of nonradiative surface plasma waves in silver by the method of frustrated total reflection," *Zeitschrift für Physik*, vol. 216, no. 4, pp. 398–410, 1968. (Cited on page 92.)

[170] N. Yu, Q. Wang, M. Kats, J. Fan, *et al.*, "Terahertz plasmonics," *Electronics Letters*, vol. 46, no. 26, pp. 52–57, 2010. (Cited on pages 94, 95 and 236.)

[171] L. Shen, X. Chen, and T.-J. Yang, "Terahertz surface plasmon polaritons on periodically corrugated metal surfaces," *Optics express*, vol. 16, no. 5, pp. 3326–3333, 2008. (Cited on page 96.)

[172] J. Wood, L. Tomlinson, O. Hess, S. Maier, and A. Fernández-Domínguez, "Spoof plasmon polaritons in slanted geometries," *Physical Review B*, vol. 85, no. 7, p. 075441, 2012. (Cited on page 96.)

[173] W. Zhu, A. Agrawal, A. Cui, G. Kumar, and A. Nahata, "Engineering the propagation properties of planar plasmonic terahertz waveguides," *IEEE Journal of Selected Topics in Quantum Electronics*, vol. 17, no. 1, pp. 146–153, 2011. (Cited on page 96.)

[174] G. Kumar, S. Pandey, A. Cui, and A. Nahata, "Planar plasmonic terahertz waveguides based on periodically corrugated metal films," *New Journal of Physics*, vol. 13, no. 3, p. 033024, 2011. (Cited on page 96.)

[175] G. Kumar, A. Cui, S. Pandey, and A. Nahata, "Planar terahertz waveguides based on complementary split ring resonators," *Optics express*, vol. 19, no. 2, pp. 1072–1080, 2011. (Cited on page 96.)

[176] E. Moreno, L. Martín-Moreno, and F. J. García-Vidal, "Extraordinary optical transmission without plasmons: the s-polarization case," *Journal of Optics A: Pure and Applied Optics*, vol. 8, no. 4, p. S94, 2006. (Cited on page 97.)

[177] W. Chen, L. Guo, and Z. Sun, "Resonant absorption of TE-polarized light at the surface of a dielectric-coated metal grating," *IEEE Photonics Journal*, vol. 6, pp. 1–6, Aug 2014. (Cited on page 97.)

[178] T. J. Constant, T. S. Taphouse, H. J. Rance, S. C. Kitson, *et al.*, "Surface plasmons on zig-zag gratings," *Optics express*, vol. 20, no. 21, pp. 23921–23926, 2012. (Cited on pages 97 and 236.)

[179] L. Feng, A. Mizrahi, S. Zamek, Z. Liu, *et al.*, "Metamaterials for enhanced polarization conversion in plasmonic excitation," *ACS nano*, vol. 5, no. 6, pp. 5100–5106, 2011. (Cited on pages 98, 99 and 236.)

[180] O. Acher, "Modern microwave magnetic materials: Recent advances and trends," *Journal of Magnetism and Magnetic Materials*, vol. 321, no. 14, pp. 2033 – 2034, 2009. Current Perspectives: Modern Microwave Materials. (Cited on page 104.)

[181] G. R. Harrison, "Hexagonal ferrites for millimeter wave applications," *Proc. SPIE*, vol. 317, pp. 0317 – 0317 – 11, 1982. (Cited on page 105.)

[182] G. Aminoff, "Über ein neues oxydisches mineral aus långban.(magnetoplumbit.)," *GFF*, vol. 47, no. 3, pp. 283–289, 1925. (Cited on page 105.)

[183] J. Desvignes, H. Le Gall, M. Labeyrie, J. Mage, and T. Robinson, "Improvement of hexaferrites crystal growth: Reproductibility and characterization," *Le Journal de Physique Colloques*, vol. 46, no. C6, pp. C6–331, 1985. (Cited on pages 107 and 125.)

[184] "Ferrite magnets - fb series - product guide." Web pages of the TDK Corporation, Tokyo, Japan, Available: http://product.tdk.com/info/en/products/magnet/map/fb.html, 2014. Accessed: 2016-06-30. (Cited on pages 107, 125, 142 and 239.)

[185] J. Jalli, Y.-K. Hong, G. S. Abo, S. Bae, *et al.*, "Mfm studies of magnetic domain patterns in bulk barium ferrite (bafe 12 o 19) single crystals," *Journal of Magnetism and Magnetic Materials*, vol. 323, no. 21, pp. 2627–2631, 2011. (Cited on pages 113, 114 and 237.)

[186] H. Richter and H. Dietrich, "On the magnetic properties of fine-milled barium and strontium ferrite," *IEEE Transactions on Magnetics*, vol. 4, no. 3, pp. 263–267, 1968. (Cited on page 114.)

[187] D. Polder, "Viii. on the theory of ferromagnetic resonance," *The London, Edinburgh, and Dublin Philosophical Magazine and Journal of Science*, vol. 40, no. 300, pp. 99–115, 1949. (Cited on page 118.)

[188] L. Landau and E. Lifshitz, "On the theory of the dispersion of magnetic permeability in ferromagnetic bodies," *Phys. Z. Sowjetunion*, vol. 8, no. 153, pp. 101–114, 1935. (Cited on page 119.)

[189] T. L. Gilbert, "A phenomenological theory of damping in ferromagnetic materials," *IEEE Transactions on Magnetics*, vol. 40, pp. 3443–3449, Nov 2004. (Cited on page 119.)

[190] K. N. Kocharyan, M. Afsar, and I. I. Tkachov, "Millimeter-wave magnetooptics: New method for characterization of ferrites in the millimeter-wave

range," *IEEE Transactions on Microwave Theory and Techniques*, vol. 47, no. 12, pp. 2636–2643, 1999. (Cited on pages 119, 120 and 237.)

[191] N. Gagnon, J. Shaker, P. Berini, L. Roy, and A. Petosa, "Material characterization using a quasi-optical measurement system," *IEEE Transactions on Instrumentation and Measurement*, vol. 52, no. 2, pp. 333–336, 2003. (Cited on page 122.)

[192] H.-J. Eul and B. Schiek, "Thru-match-reflect: One result of a rigorous theory for de-embedding and network analyzer calibration," in *Microwave Conference, 1988. 18th European*, pp. 909–914, IEEE, 1988. (Cited on page 124.)

[193] T. Tosaka, K. Fujii, K. Fukunaga, and A. Kasamatsu, "Development of complex relative permittivity measurement system based on free-space in 220–330-GHz range," *IEEE Transactions on Terahertz science and Technology*, vol. 5, no. 1, pp. 102–109, 2015. (Cited on page 126.)

[194] J. Barroso and U. Hasar, "Constitutive parameters of a metamaterial slab retrieved by the phase unwrapping method," *Journal of Infrared, Millimeter, and Terahertz Waves*, vol. 33, no. 2, pp. 237–244, 2012. (Cited on page 126.)

[195] J. Bates, "Fourier transform spectroscopy," *Computers & Mathematics with Applications*, vol. 4, no. 2, pp. 73–84, 1978. (Cited on page 126.)

[196] J. Dunsmore, "Gating effects in time domain transforms," in *2008 72nd ARFTG Microwave Measurement Symposium*, pp. 1–8, Dec 2008. (Cited on page 126.)

[197] D. A. Naylor and M. K. Tahic, "Apodizing functions for fourier transform spectroscopy," *JOSA A*, vol. 24, no. 11, pp. 3644–3648, 2007. (Cited on page 128.)

[198] D. Rytting, "Let time domain response provide additional insight into network behavior," in *ARFTG Conference Digest-Spring, 23rd ARFTG*, vol. 5, pp. 126–138, IEEE, 1984. (Cited on page 128.)

[199] M. Naftaly and R. Dudley, "Terahertz reflectivities of metal-coated mirrors," *Applied optics*, vol. 50, no. 19, pp. 3201–3204, 2011. (Cited on page 129.)

[200] K. N. Kocharyan, M. N. Afsar, and I. I. Tkachov, "New method for measurement of complex magnetic permeability in the millimeter-wave range, part ii: hexaferrites," *IEEE transactions on magnetics*, vol. 35, no. 4, pp. 2104–2110, 1999. (Cited on pages 133 and 138.)

[201] O. Yalçın, "Ferromagnetic resonance," in *Ferromagnetic Resonance-Theory and Applications*, InTech, 2013. (Cited on page 133.)

[202] C. Kittel, *Introduction to solid state physics*. Wiley, 2005. (Cited on page 133.)

[203] B. Johs and J. S. Hale, "Dielectric function representation by b-splines," *physica status solidi (a)*, vol. 205, no. 4, pp. 715–719, 2008. (Cited on pages 133, 134, 135 and 238.)

[204] D. W. Marquardt, "An algorithm for least-squares estimation of nonlinear parameters," *Journal of the society for Industrial and Applied Mathematics*, vol. 11, no. 2, pp. 431–441, 1963. (Cited on page 135.)

[205] K. A. Korolev, L. Subramanian, and M. N. Afsar, "Complex permittivity and permeability of strontium ferrites at millimeter waves," *Journal of applied physics*, vol. 99, no. 8, p. 08F504, 2006. (Cited on page 138.)

[206] P. U. Jepsen and B. M. Fischer, "Dynamic range in terahertz time-domain transmission and reflection spectroscopy," *Opt. Lett.* , vol. 30, pp. 29–31, Jan 2005. (Cited on page 148.)

[207] J. C. Lagarias, J. A. Reeds, M. H. Wright, and P. E. Wright, "Convergence properties of the nelder–mead simplex method in low dimensions," *SIAM Journal on Optimization*, vol. 9, no. 1, pp. 112–147, 1998. (Cited on page 150.)

[208] S. Visnovsky, *Optics in magnetic multilayers and nanostructures*. CRC Press, 2006. (Cited on page 161.)

[209] M. A. Ordal, L. L. Long, R. J. Bell, S. E. Bell, *et al.*, "Optical properties of the metals al, co, cu, au, fe, pb, ni, pd, pt, ag, ti, and w in the infrared and far infrared," *Applied optics*, vol. 22, no. 7, pp. 1099–1119, 1983. (Cited on page 171.)

[210] M. A. Ordal, R. J. Bell, R. W. Alexander, L. L. Long, and M. R. Querry, "Optical properties of fourteen metals in the infrared and far infrared: Al, co, cu, au, fe, pb, mo, ni, pd, pt, ag, ti, v, and w.," *Applied optics*, vol. 24, no. 24, pp. 4493–4499, 1985. (Cited on page 171.)

[211] J. H. Lambert, *Photometria sive de mensura et gradibus luminis, colorum et umbrae*. Klett, 1760. (Cited on page 172.)

[212] A. Beer, "Bestimmung der absorption des rothen lichts in farbigen flussigkeiten," *Ann. Physik*, vol. 162, pp. 78–88, 1852. (Cited on page 172.)

[213] F. Yang, J. Sambles, and G. Bradberry, "Long-range surface modes supported by thin films," *Physical Review B*, vol. 44, no. 11, p. 5855, 1991. (Cited on page 176.)

[214] M. Moharam and T. Gaylord, "Rigorous coupled-wave analysis of planar-grating diffraction," *JOSA*, vol. 71, no. 7, pp. 811–818, 1981. (Cited on page 177.)

[215] D. Qu, D. Grischkowsky, and W. Zhang, "Terahertz transmission properties of thin, subwavelength metallic hole arrays," *Optics Letters*, vol. 29, no. 8, pp. 896–898, 2004. (Cited on pages 181 and 186.)

[216] J.-P. Berenger, "A perfectly matched layer for the absorption of electromagnetic waves," *Journal of computational physics*, vol. 114, no. 2, pp. 185–200, 1994. (Cited on page 197.)

[217] I. A. Akimov, V. I. Belotelov, A. V. Scherbakov, M. Pohl, *et al.*, "Hybrid structures of magnetic semiconductors and plasmonic crystals: a novel concept

for magneto-optical devices," *JOSA B*, vol. 29, no. 2, pp. A103–A118, 2012. (Cited on page 203.)

[218] H. Němec, P. Kužel, J.-L. Coutaz, and J. Čtyroký, "Transmission properties and band structure of a segmented dielectric waveguide for the terahertz range," *Optics Communications*, vol. 273, no. 1, pp. 99 – 104, 2007. (Cited on page 204.)

[219] T. Horák, G. Ducournau, O. Stepanenko, K. Postava, J. F. Lampin, and M. Vanwolleghem, "Terahertz nonreciprocal components using hexagonal ferrite ceramics," *Optics Express*, 2017. Submitted. (Cited on page 221.)

the end.